DEFORMATION MECHANISMS IN NANOSCALE SINGLE CRYSTALLINE ELECTROPLATED COPPER PILLARS

Thesis by

Andrew T. Jennings

In Partial Fulfillment of the Requirements for the

degree of

Doctor of Philosophy

CALIFORNIA INSTITUTE OF TECHNOLOGY

Pasadena, California

2012

(Defended May 23, 2012)

ACKNOWLEDGEMENTS

I would first like to thank the National Science Foundation for supporting the research presented here through my Graduate Research Fellowship as well as through the NSF CAREER award (DMR-0748267), which paid for the supplies and travel necessary to make this research possible.

My research advisor, Julia R Greer, had the biggest impact on me during graduate school. Julia's boundless energy and enthusiasm for science always kept research fun and exciting. Her tireless efforts made every aspect of my graduate career easier and more enjoyable than it could have been otherwise. I couldn't have asked for a better advisor.

Thanks also to all the past and present members of the Greer Group who have spent their time teaching and training me, as well as those with whom I've bounced ideas back and forth. This thesis would not have been completed without the help and support of everyone in the group. I would specifically like to thank the magical Dongchan Jang who has an incredible ability to explain complicated topics in an easy-to-understand manner. Special thanks to my office mates Steffan, Shelby, Zach, and Joanna, who made every day in the office entertaining and productive through their ability to switch between in-depth scientific discussions and light-hearted conversations.

To my collaborator Chris Weinberger, thank you for all the discussions and phone calls in which I learned more about dislocation physics than I ever wanted to know. I would also like to thank the efforts of Carol Garland, who spent significant amounts of time training me on the TEMs, keeping them working, and fixing the occasional burnt-in image. I want to thank everyone at Nanomechanics for maintaining the SEMentor; especially Mike Drake for taking my phone calls and providing real-time support when bad things happened. I'd like to thank everyone from the KNI, especially Bophan Chin, for keeping things running smoothly. For all the helpful discussions at conferences and visits to Caltech, I'd like to thank: Ju Li, Wei Cai, Ting Zhu, Dan Gianola, and Pratyush Tiwary.

I would like to thank my housemates for keeping life interesting. Along those same lines, I would like to thank Tara, Lisa, and Cass for making Fridays at Luckys a great time.

Last I would like to thank my family, especially my parents, who pushed me until I was ready to stand on my own. Everyday, I reap the rewards of your efforts.

ABSTRACT

Scientific research in nanotechnology has enabled advances in a diverse range of applications, such as: electronics, chemical sensing, and cancer treatment. In order to transition these nanotechnology-driven innovations out of the laboratory and into real-world applications, the resilience and mechanical reliability of nanoscale structures must be well understood in order to preserve functionality under real-world operating environments. Understanding the mechanical properties of nanoscale materials is especially important because several authors have shown that single crystalline metal pillars produced through focused-ion-beam milling have unique properties when the pillar diameter, *D,* approaches nanotechnology-relevant dimensions. The strength, σ, of these pillars is size-dependent and is well described through a power-law relation showing that smaller is stronger: $\sigma \propto D^{-n}$, where *n* is the exponent and is found to be $0.5 \leq n \leq 1.0$ in face-centered-cubic metals. In this work, the fundamental deformation mechanisms governing the size-dependent mechanical properties are investigated through uniaxial compression and tension tests of electroplated single crystalline copper pillars with diameters between 75 nm and 1000 nm. At larger pillar diameters, $D > 125\ \text{nm}$, these copper pillars are shown to obey a similar size-dependent regime, demonstrating that the "smaller is stronger" phenomenon is a function of the pillar microstructure, as opposed to the fabrication route. Furthermore, the dominant dislocation mechanism in this size-dependent regime is shown to be the result of single-arm, or spiral, sources. At smaller pillar diameters, $D \leq 125\ \text{nm}$, a strain-rate-dependent mechanism transition is observed through both the size-strength relation and also quantitative, experimental measures of the activation volume. This new deformation regime is characterized by a size-independent strength and is governed by surface dislocation nucleation, a thermally activated mechanism sensitive to both temperature and strain-rate. Classical, analytical models of surface source-nucleation are shown to be insufficient to describe either the quantitative strength or the nucleation site preference. As a result, a combination of atomistic chain-of-states simulations and semi-analytical continuum models are developed in order to achieve a realistic, intuitive understanding of surface nucleation processes.

TABLE OF CONTENTS

FIGURE LIST

TABLE LIST

Chapter 1: Introduction

A material's mechanical properties describe how it deforms under external loading. One of the most basic of these mechanical properties is strength, how much stress a material can withstand prior to permanent deformation. For common applications, a material's strength is considered independent of a its size; for example, copper bars with diameters of three millimeters and three thousand millimeters have the same strength. However, in 2004, Uchic et al. performed uniaxial compression tests on single crystalline metal pillars produced through focused-ion-beam, FIB, milling with diameters below ten microns and, remarkably, found that a metal's strength increases with decreasing pillar diameter [3]. This observation of *size-dependent* strength has been subsequently observed in multiple other single crystal metal systems spanning face-centered-cubic [3-33], body-centered-cubic [32, 34-43], and hexagonal close-packed [44, 45] crystal structures all the way down to the size-limits of the FIB-fabrication process ~ 200 nm [9]. This thesis explores the source of the size-dependent strength through primarily experimental studies of the influence of fabrication route and microstructure as well as tests to identify the deformation mechanisms. These mechanisms are discussed through simple, semi-analytical models to provide intuition to the necessary deformation physics.

1.1 Summary

This chapter begins with a brief background to the relevant physics necessary to understand the strength of single crystalline metals. First, the experimentally observed deformation behavior of single crystals under uniaxial tension and compression tests are discussed in order to motivate early attempts to quantitatively identify the relevant deformation mechanisms. These initial attempts are shown to be significant over predictions leading to the discovery of dislocations as the deformation mechanism in the deformation of single crystals. The properties and behavior of dislocations are then introduced to provide necessary background.

Then the recent history of size-dependent strength in metals is discussed in order to understand the high-level of interest in understanding the size-dependent strength in uniaxial tests of single crystals. This begins with observations and mechanisms of size-dependent strength due to strain gradients in bulk single crystals, i.e., as a result of bending, torsion, and indentation tests, and ends with the observations of size-dependent strength with no strain gradients: initially with some ambiguity in

thin films and then conclusively in uniaxial compression and tension tests of micro- and nano-pillars explored here.

1.2 Experimental Mechanical Properties

1.2.1 Uniaxial Tension/Compression Test

In a uniaxial tension or compression tests, a load is applied uniformly over the top face of the test specimen and the resulting displacement is measured. Figure 1.1a depicts the material's physical response under load, while Figure 1.1b shows the resulting stress-strain curve where stress, σ, is defined as the force, F per unit area, A or $\sigma = {}^{F}/_{A}$ and strain, ε, is the length change, Δl, normalized by a reference length, l, or $\varepsilon = {}^{\Delta l}/_{l}$. During the initial stages of deformation, the linear elastic regime, the material deformation is reversible and corresponds to stretching atomic bonds in the material. The end of the linear elastic regime is marked by the onset of permanent deformation, defined by the yield point in Fig. 1.1b. During the plastic regime, the material breaks atomic bonds as the material further accommodates the applied load. Figure 1.1a shows a schematic of observations of single crystalline deformation in the plastic regime; whereby, the material slips on preferred crystallographic planes demonstrating that deformation is a shear process. A successive number of these slip events results in the uniform extension of the entire pillar. These observations provide important details as to how a material deforms; however, they do not explain the micro mechanisms governing the observed deformation behavior.

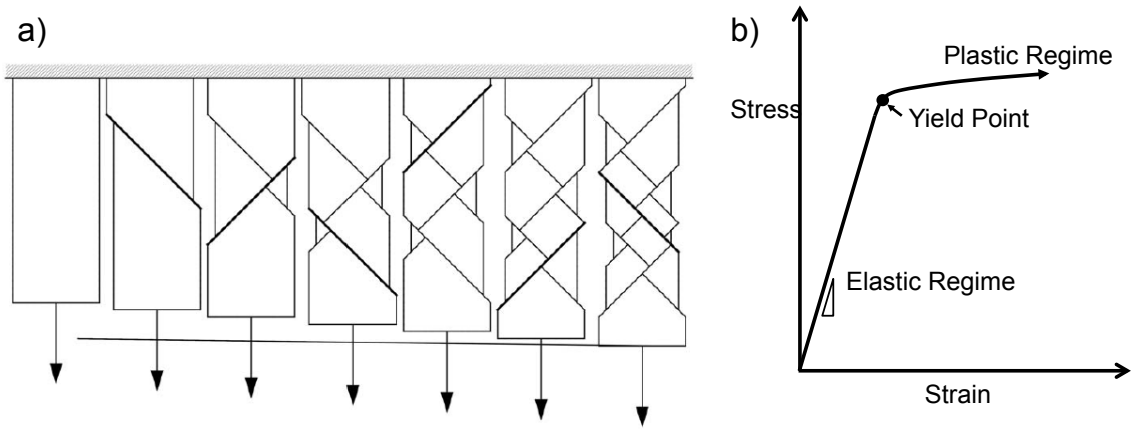

Figure 1.1 a) Schematic of tensile elongation through slip. Adapted from William D. Nix's dislocation notes. b) Schematic of stress-strain curve

1.3 Brief Introduction of Dislocation Plasticity in Metals

1.3.1 Early Estimates of Strength

Early estimates of the strength by Frenkel required to shear entire planes of atoms past each other resulted in large over predictions (~ 100x) of the observed experimental strength [46]. Specifically, the predicted shear strength, τ, corresponds to: $\tau \approx {}^{\mu}/_{2\pi}$ where μ is the material shear modulus. This large discrepancy between theory and experiments demonstrated that shearing whole planes of atoms past each other could not be the mechanism responsible deformation observed in experiments.

1.3.2 Dislocations

In 1934, three researchers: Polayni, Taylor, and Orowan, independently showed that dislocation motion along a slip plane was able to describe the experimentally observed strength [47-49]. In a general sense, a dislocation is a line defect that breaks atomic bonds along the dislocation line. This localized bond breaking requires substantially less applied stress than breaking atomic bonds over an entire plane. Significantly, the predicted stress is similar to that observed in experiments. Furthermore dislocations were subsequently observed through other experimental techniques: both etch pit characterization of material surfaces [50] as well as through direct observation through transmission electron microscope, TEM [50].

Dislocations were first mathematically described by Volterra in the early 1900s as line defects characterized by two vectors: 1) the sense vector, $\vec{\xi}$, describing the dislocation line and 2) the Burgers vector describing the resulting displacement, $\vec{b}$. The Burgers vector shows the atomic displacement caused by a dislocation as can be seen in Figure 1.2. Figure 1.2a shows a prefect crystal subjected to shear, and Figures 1.2b and 1.2c show how two types of dislocations, screw and edge respectively, accommodate the shear stress by slipping the top half of the crystal one Burgers vector relative to the bottom. The types of dislocations in Figures 1.2b and 1.2c correspond to the two extreme cases where the sense vector and Burgers vector are parallel: screw dislocations and perpendicular: edge dislocations respectively. Dislocations with a sense and Burgers vector at an arbitrary angle between parallel and perpendicular are referred to as "mixed" and can be decomposed into a linear combination of screw and edge components.

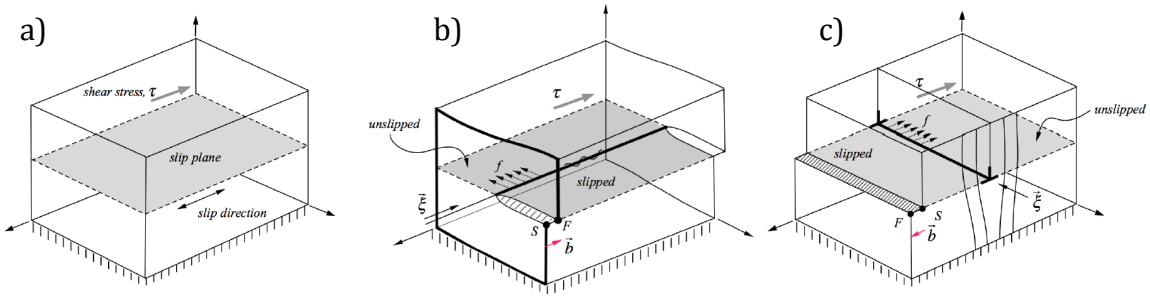

Figure 1.2: a) Reference block with slip plane and shear stress. b) Screw dislocation under an applied shear stress. c) Edge dislocation under an applied shear stress. Adapted from William D. Nix's dislocation notes

1.3.3 Forces on Dislocations

1.3.3.1 Applied Stress

Slip is a shear process, and as a result dislocations responds to stresses resolved onto a dislocation's slip plane and in the direction of the Burgers vector. Under uniaxial tension or compression, the applied uniaxial stress can be resolved simply onto the slip plane in the direction of the Burgers vector through the Schmid factor [51]: $m = \cos(\theta)\cos(\varphi)$ where θ and φ are the angles between the loading direction and the Burgers vector and the slip plane normal, respectively, as seen in Figure 1.3. The resolved shear stress, τ_{rss}, can be described as $\tau_{rss} = m\sigma$ where σ is the applied uniaxial stress. The resolved shear stress results in a force per unit line length of dislocation line of $F/L = \tau b$, and the dislocation will move under this force until it reaches an obstacle of equal or greater strength.

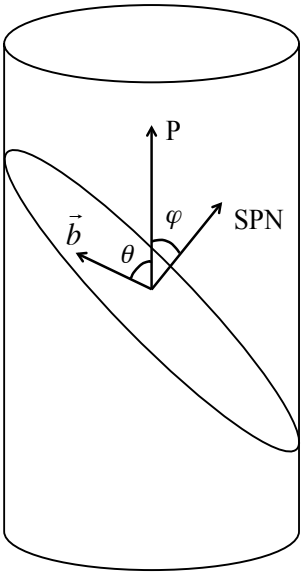

Figure 1.3 Schmid factor schematic

1.3.3.2 General Stress: Peach-Kohler and Dislocation-Dislocation Interactions

The applied stress from external loading is not the only force acting on dislocations. In general, the atoms around a dislocation are displaced from their equilibrium lattice sites and as a result, dislocations have their own stress-fields. These stress-fields are the means in which dislocations can interact with each other inside a crystal. The dislocation stress-fields can be found in Ref. [50].

Under an applied stress, as two dislocations approach each other, the force on each dislocation will be due to both the resolved shear stress and the stress-field of the other dislocation. The force on each dislocation is determined in an analogous manner as in the case of only an external applied stress. The stress acting on a dislocation is resolved onto its Burgers vector, and the corresponding force will be perpendicular to the sense vector. More precisely, the resulting force due to an arbitrary stress field, σ_{ij}, on a dislocation is described through the Peach-Kohler formula: $\vec{F}_1 = \overrightarrow{\xi_1} \times (\sigma_{ij} \cdot \overrightarrow{b_1})$ where $\overrightarrow{\xi_1}$ is the sense vector and $\overrightarrow{b_1}$ is the Burgers vector of the dislocation which feels the force: $\vec{F}_1$. This force can be either attractive or repulsive depending on the orientation and relative position of each dislocation. In a well-annealed single crystal, dislocation-dislocation interactions represent a significant fraction of the material's observed strength. This is because in order for dislocations to move through the crystal, they must break through other dislocation interactions. This strength due to the collective interactions of many dislocations is described via the Taylor relation where $\tau = \alpha \mu b \sqrt{\rho}$, where α is a constant of order unity, μ is the shear modulus, b is the Burgers vector magnitude, and ρ is the dislocation density, which is ~10^{12} m^{-2} for well-annealed metals [52]. The resulting strength is on the order of ~ 10 MPa.

1.3.3.3 Image Stress

A dislocation's elastic field is easily solved for the case of a dislocation in an infinite medium. However, when a dislocation is near a free surface the elastic field becomes more complicated as a result of the requirement to satisfy the surface boundary condition. In general, a dislocation feels a force attracting the dislocation to a free surface; whereas, in the case where the surface is not free, and instead coated with a second material, the dislocation will be attracted to the material with the lower shear modulus and repelled by the material with the higher shear modulus.

1.3.4 Dislocation Energy

The energy required to produce a dislocation is equal to the dislocation's strain energy or work performed by a dislocation on the surrounding crystal. The energy per unit line length of a screw dislocation in an isotropic solid can be written as $\frac{W}{L} = \int_{r_c}^{R} \int_{0}^{2\pi} \frac{\sigma_{ij}(\theta,r)^2}{2\mu} d\theta dr = \frac{\mu b^2}{4\pi} \ln\left(\frac{R}{r_c}\right) + E_{core}$. Here, σ_{ij} is the full stress tensor created by the dislocation and has a $\frac{1}{r}$ dependence where r is the distance from the dislocation line. μ is the shear modulus, *b* is the Burgers vector, *R* is the distance away from the dislocation over which the integral is performed, r_c is the core radius below which this continuum description of a dislocation strain energy is no longer valid, and E_{core} is the energy of the dislocation core. For ease of use, E_{core} can be readily absorbed into the core radius. The resulting function appears as: $\frac{W}{L} = \frac{\mu b^2}{4\pi} \ln\left(\frac{R}{\alpha r_c}\right)$. An edge dislocation has a slightly different line energy corresponding to its slightly different stress field: $\frac{W_{edge}}{L} = \frac{\mu b^2}{4\pi(1-\nu)} \ln\left(\frac{R}{\alpha r_c}\right)$ where ν is the Poisson's ratio, a factor that has a value between 0 and 0.5 and is typically close to 0.3. The net result is the screw orientation is energetically preferred relative to the edge orientation by a factor of ~3.

1.3.4.1 Perfect and Partial Dislocations

As shown above, a dislocation's energy depends on two material constants: the shear modulus, μ, and the Burgers vector magnitude, *b*. In the isotropic approximation performed here, the shear modulus is a constant and independent of direction; however, the Burgers vector represents the interatomic distance over which the dislocation slips the crystal. As a result, dislocations with the smallest Burgers vectors are energetically favorable. In face-centered cubic crystals, the smallest distance between two symmetrically equivalent atoms is $a/\sqrt{2}$<110>, where *a* is the lattice constant. Other perfect dislocations are of course possible; however, their energy will be much larger than and therefore they will be unlikely to be seen.

However, in fcc crystals, perfect dislocations have been observed to dissociate into two partial dislocations. A partial dislocation is one that slips the crystal into non-equivalent lattice sites leaving a stacking fault in between the two dislocations. A schematic representation of this is shown in Figure 1.4. This stacking fault has an associated energy, stacking fault energy (γ_{SF}), as a result of the error in the otherwise perfect stacking sequence. A perfect dislocation will split into two partial dislocations

when energetically favorable, i.e., when the energy of two partial dislocations and the stacking fault is less than the original partial. As shown above, the energy of a dislocation proportional to b^2, so that when $b_{p1}^2 + b_{p2}^2 \leq b^2$ a perfect dislocation will likely split. The width of the stacking fault will then be determined by the additional stacking fault energy, γ_{SF}. In some fcc crystals Ag, Au, and Cu the stacking fault energy is relatively low, so a <110> type dislocation will frequently split into two $\frac{a}{\sqrt{6}} < 112 >$ type dislocations and an accompanying stacking fault

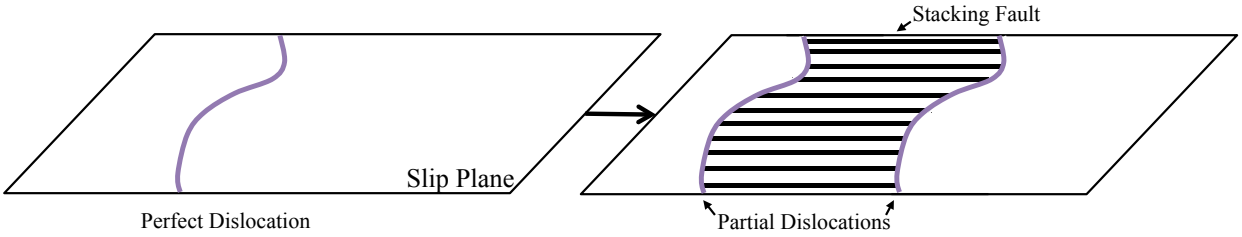

Figure 1.4: Schematic of perfect dislocation splitting into two partials with corresponding stacking fault.

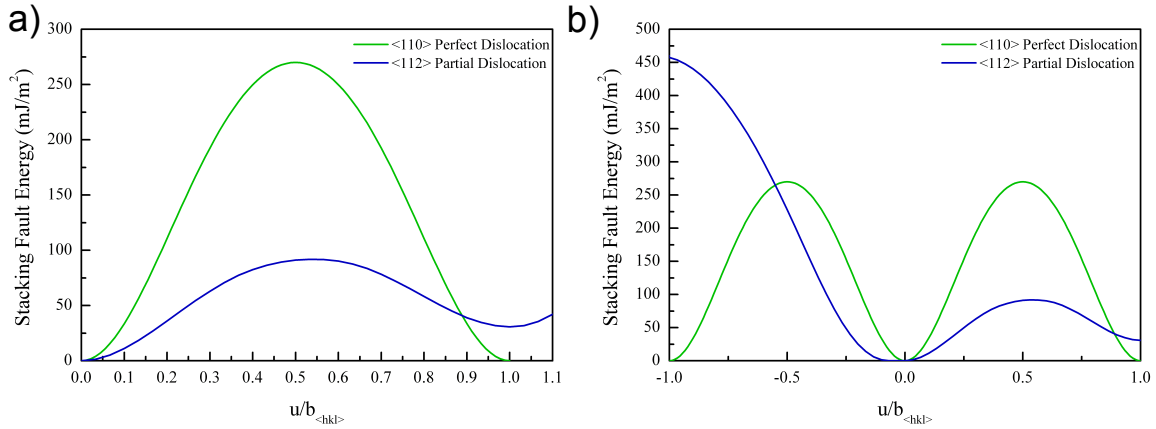

Figure 1.5: a) Au EAM Foiles potential for a perfect and partial dislocation. b) Perfect dislocation stacking fault energy showing symmetry. Partial dislocation showing asymmetric energy landscape for leading, low-energy, and trailing, high-energy, stacking fault

The corresponding stacking fault energy expected for a full partial dislocation slip can be shown for perfect and partial slip in Figure 1.5. These curves are for gold from the EAM Foiles potential for gold [53] on the {111}-type plane in the <110> and <112> directions, respectively. Note that at the distance u/b =1, the perfect dislocation has no stacking fault energy as the stacking order is completely restored; however, in the case of the partial dislocation, the stacking fault is ~40mJ/m^2 resulting from the error in stacking sequence.

1.3.5 Surfaces

1.3.5.1 Ledge Formation

As shown in Figure 1.2, when a dislocation reaches a surface a Burgers vector is deposited creating an extra surface ledge. This ledge has an energetic cost of the order ~1 J/m^2 due to the extra {111}-surface created. In bulk, the energetic cost of producing a surface ledge is relatively small; however, during the nucleation of new dislocations from a free surface, the contribution due to the creation of a surface ledge can be quite large. A more in-depth analysis of surface ledge creation from atomistics and continuum modeling is discussed in Chapter 9.

1.3.5.2 Image Energy

As discussed above, when a dislocation is near a surface, the elastic fields due to a dislocation are altered such that the surface boundary conditions are maintained. This change in the elastic field will affect the energy of a dislocation through the relation: $\frac{W}{L} = \int_{r_c}^{R} \int_{0}^{2\pi} \frac{\sigma_{ij}(\theta,r)^2}{2\mu} d\theta dr$. The integral is left in its general form as the crystal volume will depend on the geometry of the surface. The corresponding mathematics for an arbitrary dislocation is onerous. In general, as a dislocation approaches a free surface, the dislocation's energy will decrease relative to the case of a dislocation in an infinite medium. The results from the special case of a screw dislocation parallel to a free surface are shown in Chapter 9.

1.4 Size Effects in Single Crystalline Metals

This thesis explores the underlying mechanisms governing experimental observations of size-dependent-strength in uniaxial tension and compression tests on sub-micron single crystalline metals. Uniaxial tension and compression tests apply a homogeneous stress across the sample, and in bulk single crystals, these tests show that the strength is size-independent and a function of the dislocation density, which increases with strain. However, bulk single crystals subjected to bending, torsion, and indentation tests demonstrate a clear size-effect where "smaller is stronger". In contrast to tension and compression tests, bending, torsion, and indentation apply an inhomogeneous stress across the sample resulting in strain gradients, which in turn generate the observed size-effect in bulk single crystals. This section briefly discusses the causes of size-effects under strain gradients in single crystals, followed by recent observations and proposed mechanisms governing size-dependent strength in tension and compression tests of micron and sub-micron single crystalline pillars.

1.4.1 Size Effects under Strain Gradients

Under inhomogeneous loading, such as bending, torsion, and indentation tests, a sample's strength is length scale-dependent as the material is subjected to strain gradients. Strain gradients are accommodated through the introduction of geometrically necessary dislocations, GNDs, [54]. A schematic example of GNDs from a bending test can be found in Figure 1.6a. In bending, the top surface expands while the bottom surface shrinks. This increase in length can be accounted for through the introduction of GNDs throughout the bar as these dislocations add extra planes of atoms above the dislocation without corresponding additional planes of atoms below resulting in the shape change necessary for bending. The necessary density of GNDs, ρ_G, for a given macroscopic plastic shear strain, γ, can be described in both bending and torsion through: $\rho_G \approx \frac{4\gamma}{b\lambda}$ where b is the Burgers vector and λ is the material length-scale [54].

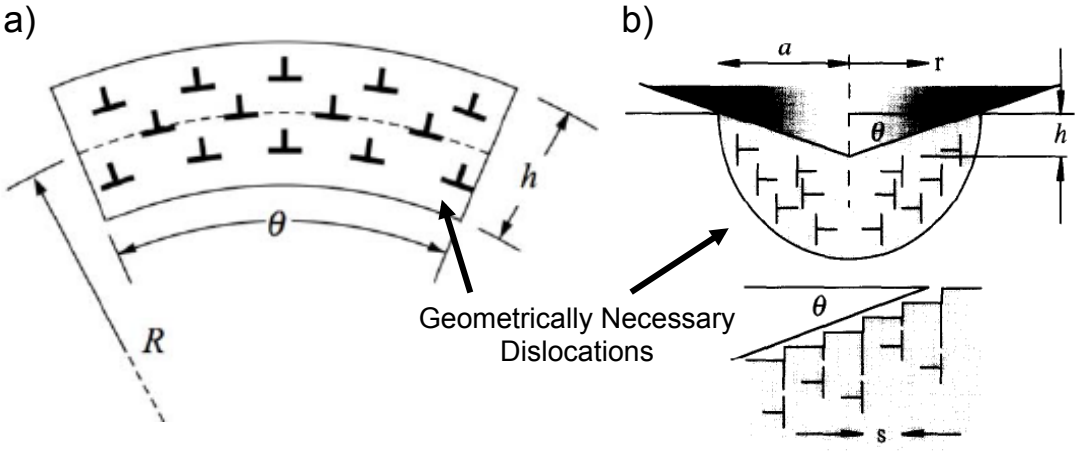

Figure 1.6: Schematic of geometrically necessary dislocations under a) bending and b) indentation. Adapted from Ref. [55] and [56]

Similar to homogeneous compression tests, the material strength is still proportional to the square root of the dislocation density: ρ or $\sigma \propto \sqrt{\rho}$ where σ is the material strength. However, in the case of strain gradients there is also an appreciable GND density, and the total dislocation density now consists of two components: 1) the dislocation density due to strain and 2) the stored GND density due to strain gradients. The strength can now be described as $\sigma \propto \sqrt{\rho + \rho_{GND}}$ where ρ is the crystal's dislocation density due to strain and ρ_{GND} is a related to the inverse length scale resulting in the observed size-dependence of bulk experiments with strain gradients: bending and torsion.

Similar strain-gradient plasticity theory has been used to describe the indentation-size-effect at indents smaller than 1 micron [56]. In these experiments, shallow indents on metal single crystals, show a size-dependent hardness, *H*, that can be accurately described through $H = H_o\sqrt{1 + \frac{h^*}{h}}$ where H_o is the bulk hardness, *h*, is the indentation depth and h^* is a characteristic length. The bulk material strength can be related to the hardness, *H,* through the Tabor relation where $H \approx 3\sigma$. This size-dependent hardness is also explained through the presence of large strain gradients and resulting large geometrically necessary dislocations at shallow indentation depths as seen schematically in Figure 1.6b. Following the simple model in Ref. [56], the geometrically necessary dislocation density is similar to that seen above in bending and is proportional to $\rho_{GND} \propto \frac{1}{h}$, where h is the indentation depth. The resulting material strength is again $\sigma \propto \sqrt{\rho + \rho_{GND}}$ and highest at shallow indents where the strain gradients and corresponding ρ_{GND} are largest.

1.4.2 Size Effects in the Absence of Strain Gradients

Bulk single crystalline metals have strengths proportional to the square root of the dislocation density. When subjected to strain gradients these metals show a size-dependent strength, and in the absence of strain gradients, bulk single crystalline metals show no size-effect. However, in 1956, Brenner noticed that metal single crystalline whiskers grown through halide reduction do not behave like bulk single crystals. In tension, these whiskers have size-dependent, near-theoretical strengths. This behavior is distinct from previously discussed examples of bulk size-effects as tension tests do not generate strain gradients in test samples.

1.4.2.1 Whiskers

In bulk, tension and compression tests on single crystalline metals demonstrate a size-independent strength; however, when the sample diameter is less than or equal to 25μm, Brenner showed that the yield point in thin metal whiskers was on the order of the predicted theoretical strength [57, 58]. Post-yield, the whisker elongation continued at significantly reduced strengths similar to that of bulk single crystals. An example of the stress strain behavior for micron-szied copper whiskers can be found in Figure 1.7a [58]. This stress-strain behavior characterized by a high initial yield point and low flow strength is the result of the very low defect concentrations inside the pillar. In order for plastic flow to start in a crystal with no dislocations, a whisker must first nucleate a dislocation from the surface, an

event requiring very large, near theoretical strengths as observed in the initial yield point. After this first dislocation is produced, it is able to multiply at much lower, bulk-like strengths, a process governing dislocation multiplication in bulk.

Furthermore, the measured strength in these whiskers increases with decreasing wire diameter demonstrating a size-effect as seen in Figure 1.7b. This size effect is thought to reflect the probability of finding an easy nucleation site or surface flaw on the whisker surface[57, 58]. The larger the pillar, the more likely it will be to find a weak surface flaw. This type of deformation has been recently corroborated on VLS grown copper nanowires, Figure 1.7c, and Mo-alloy pillars produced through eutectic solidification [2, 59-61].

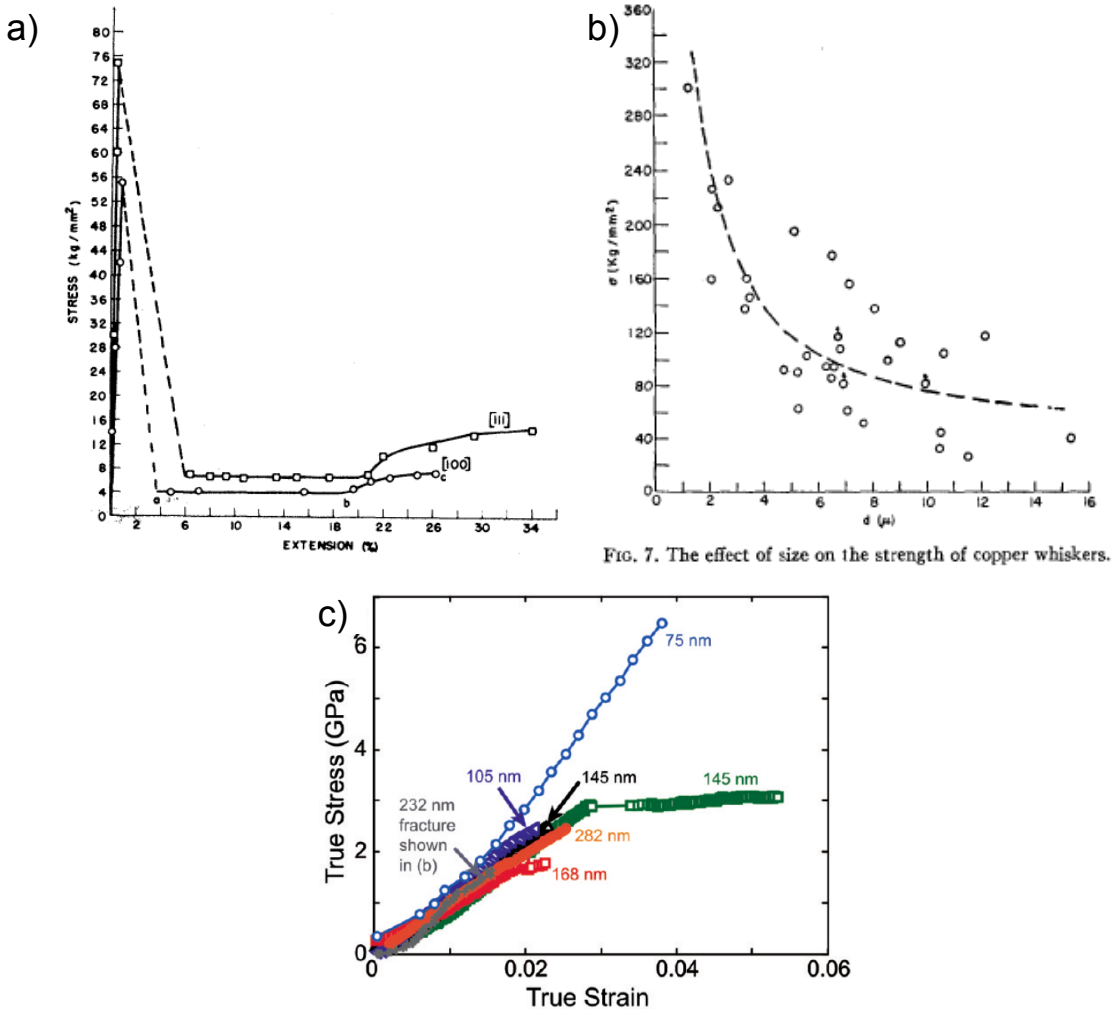

Figure 1.7: a) Stress-strain behavior of copper whiskers in copper adapted from Ref. [57] b) Whisker strength for multiple diameters adapted from Ref. [57]. c) Nanowire strength in copper from Ref. [2]

1.4.2.2 FIB-Fabricated Micron and Sub-micron Uniaxial Pillars

The deformation behavior in FIB-fabricated pillars is distinct from that observed in both dislocation-free whiskers and bulk single crystals demonstrating that FIB-fabricated pillars fall into a previously unexplored deformation regime.

Figure 1.8 shows examples of the mechanical properties and deformation behavior of nanoscale single crystalline gold pillars (1.8a, b adapted from Ref. [9]) and micron-sized single crystalline nickel pillars (1.8c-e adapted from Ref. [4]). Pre-compression and post-compression images of several FIB-fabricated compression pillars are seen in Figure 1.8a,c, and d. The pillars are cylindrical and have a slight taper as a result of the FIB-fabrication procedure. Figure 1.8b and e shows the stress-strain behavior of pillars with diameters between 400nm and 40um. In the larger pillars, the stress-strain signature is continuous and similar to that observed in a standard bulk compression tests; however, in smaller pillars with diameters below ~1um, the deformation behavior is distinct from bulk tests and is characterized by discrete bursts of plasticity corresponding to dislocation avalanches. Furthermore, after a dislocation avalanche, the pillar loads again until a subsequent dislocation avalanche occurs at a similar stress level. The post-compression images (Figure 1.8a,d) show clear slip traces on the pillar surface demonstrating that the deformation mechanism is dislocation-mediated.

Single crystalline pillars have a compressive and tensile strength described by a power-law where $\sigma \propto D^{-n}$. Here σ is a characteristic stress, defined anywhere between the first burst event and a flow strain as high as 15% [62], D is the pillar diameter, and n is the exponent typically found within the range of $0.5 \leq n \leq 1.0$ for fcc metals. The observation of size-dependent strength is ubiquitous across all observed fcc metals as shown in a log-log plot in Figure 1.9 where the x and y axes are normalized by the burgers vector and material shear modulus, respectively.

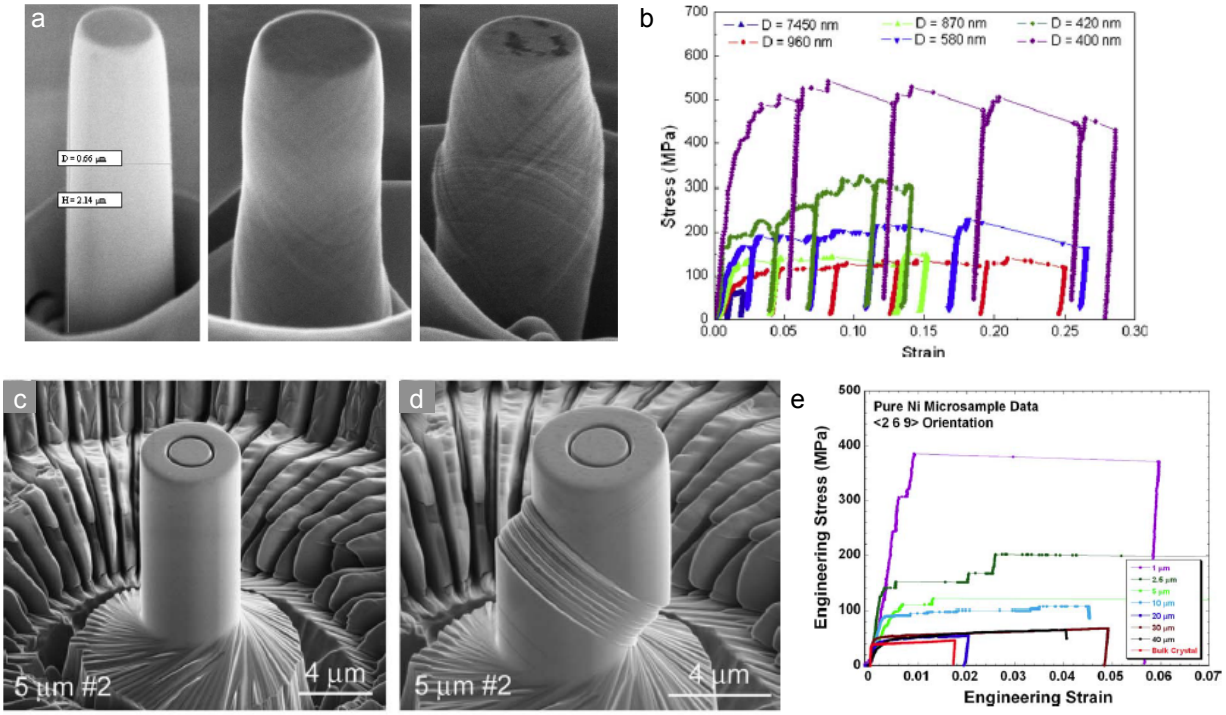

Figure 1.8: a) Pre and post-deformation Au FIB-fabricated nanopillars. b) Stress-strain behavior of Au nanowires of different diameters. a) and b) adapted from Ref. [9] c) & d) Pre- and Post-deformation of a Ni micro-pillar. e) Stress-strain behavior of Ni micro-pillars of a range of diameters. c-e) adapted from Ref. [4]

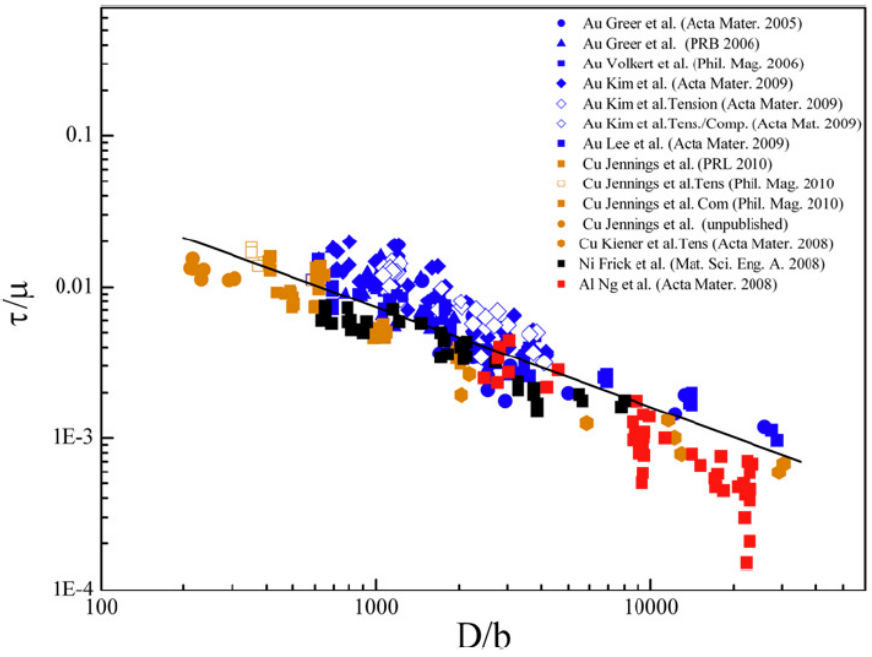

Figure 1.9: Collection of normalized stress vs. diameter data for multiple different FCC pillars, adapted from Ref. [63]

1.4.3 Discussion

1.4.3.1 Deformation Behavior: FIB-fabricated Pillars vs. Whiskers and Bulk

The most obvious difference between pillars, whiskers, and bulk single crystals is the observed stress for plastic flow. Bulk single crystals deform at very low strengths, on the order of 10s of MPa. Sub-micron and micron pillars range in strength from bulk-levels at large pillar diameters to gigapasacals at 200nm, as seen in Figure 1.8; however, in comparison with whiskers, the strengths for the smallest pillars are still significantly lower than similar size whiskers which have near theoretical strengths.

Along with the stress-level during plastic flow, the stress-strain response of FIB-fabricated pillars lies in an intermediate regime between bulk-like and whisker-like properties. In larger pillars, Figure 1.8e, the deformation behavior is continuous and smooth, similar to that of bulk; however, as the sample size decreases the stress-strain behavior transitions from a continuous-type deformation to one characterized by discrete bursts at relatively constant stress levels. These bursts are similar to the initial burst in whisker tensile tests; however, in whiskers after the first burst, deformation becomes bulk-like: smooth and continuous at low flow strengths; whereas, pillar deformation maintains enhanced strengths.

The size-dependent strength observed in pillar compressions is also distinct from both bulk and whisker tests. Bulk, of course, has a size-independent strength except as a result of strain-gradients, which are not present in pillar tension tests. Whiskers show a size-dependent strength; however, the nature of that size-effect is well-reproduced by Weibull statistics that reflect the probability of finding a flaw in a given pillar [64]. Furthermore, the stresses achieved in whisker experiments are significantly larger than those found in FIB-fabricated pillars, further suggesting different in operating mechanisms.

1.4.3.2 Possible Mechanisms

Several theories describing the distinct deformation behavior in sub-micron and micron-sized crystals have been suggested to explain the observed size-effect through the high surface area to volume ratios in nanopillars. For example, the FIB-etching process is known to introduce a surface damage through the introduction of dislocation loops, amorphization, and in some cases precipitation of other phases [18, 61] each of which is a known strengthener in single crystals. As the pillar diameter decreases, the relative volume-fraction of damaged surface increases, as a result leading to size-dependent strengthening-effects.

Another consequence of small pillar diameters is the few absolute number of dislocations contained in the pillar volume. Typical well-annealed single crystalline metals have dislocation densities on the order of $\rho \approx 10^{12} m^{-2}$ [65] which will result in 0-1 dislocations in a 100nm pillar. The few available dislocations will require new dislocations to be nucleated, a process that requires higher strengths. Furthermore, the high relative surface area allows the available dislocations to reach free surfaces more readily resulting in a higher dislocation annihilation rate than one would find in bulk single crystals, a phenomenon known as dislocation starvation [8]. As the annihilation rate increases, the dislocation production rate must also increase as well to maintain plastic flow. As smaller pillars have higher surface area to volume ratios, they will have higher annihilation and corresponding higher dislocation nucleation rates. Larger necessary nucleation rates will require higher stresses to activate sufficient dislocation creation processes such as surface dislocation nucleation.

In summary, FIB-fabricated pillars show distinct mechanical properties in strength, size-effect, and stress-strain behavior from behavior observed in both conventional bulk single crystalline metals and small-scale whiskers. Furthermore, no unified theory exists that can explain all three different regimes. This thesis seeks to identify the operating mechanisms in this sub-micron pillar regime as a means to unify plasticity theory across all length-scales.

1.5 Objective and Outline

This thesis will explore the underlying mechanisms for this size-dependent strengthening trend in sub-micron, $D \leq 1000\ \text{nm}$, pillars through *in situ* and *ex situ* uniaxial compression and tension tests. In order to give a fundamental background and motivation for this work, a brief introduction to plasticity in single crystalline metals is discussed along with the mechanisms for size-dependent strength with and without strain gradients in single crystalline metals (Chapter 1). The experimental methods used to fabricate, observe, and mechanically test specimens are then outlined (Chapter 2). Compression tests on single crystalline, electroplated copper pillars with diameters between 100nm and 500nm are performed, and the results show that that the microstructure as opposed to the fabrication route (FIB-effects) controls the size-dependent behavior in compression (Chapter 3). *In situ* tension tests on similar pillars further show the size-dependent strength as well as demonstrate one of the proposed phenomena: dislocation starvation, as observed through instantaneous necking with minimal homogeneous deformation: a characteristic of negligible strain hardening or dislocation storage (Chapter 4). Further compression tests over a range of strain rates demonstrate two distinct

mechanism regimes through the measured strength and activation volumes corresponding to a size-dependent regime governed by spiral sources (large diameters and fast strain rates) and a relatively size-independent regime governed by surface source nucleation (small diameters and slow strain rates) (Chapter 5). The mechanical properties and resulting dislocation structure of single crystal pillars coated with a hard, ceramic coating are tested in compression to observe the role of the free-surface on the observed strength and operating dislocation mechanisms (Chapter 6). The observed dislocation mechanisms in pillars from Chapter 5 are compared with literature *in situ* TEM studies in pillars and thin films, and proposed analytical models describing surface nucleation are discussed in reference to the measured activation volume and strain rate sensitivities also from Chapter 5 (Chapter 7). Atomistic simulations along with transition state theory are used to predict the surface nucleation strength in experimental conditions and trends in these atomistic results are understood through a simple analytical model of the nucleation process (Chapter 8). The analytical model for surface nucleation is further refined through the introduction of the image stress and the surface ledge to bring the analytical model in closer agreement with atomistic predictions (Chapter 9).

Chapter 2: Experimental Methods

This chapter discusses all the experimental procedures and details used during the completion of this thesis. Pillar fabrication procedures through electroplating are explained in Section 2.1. Followed by the various techniques required to both assess and understand the pillar morphology, Section 2.2, and microstructure, Section 2.3. Both *in situ* and *ex situ* nano-mechanical compression and tension tests are discussed in Section 2.4, and Section 2.5 discusses the data analysis used to understand the nano-mechanical testing data.

Each chapter with experimental results contains its own experimental section for the reader's convenience as well as clarity in regards to the experimental details used in that chapter.

2.1 Sample Fabrication

Most uniaxial tension and compression test samples used to investigate the observed size-dependent strength in micron and sub-micron-sized single crystalline metals are produced through the focused-ion-beam (FIB) [62, 64, 66, 67]. The FIB is the most prevalent tool for pillar fabrication as it offers an easy, repeatable method with a high-level of control over the final sample shape. However, the FIB has limitations: FIB-milling produces a heavily damaged surface layer due to the impacting high-energy Ga^+ ions that may influence or even change the governing mechanisms. For example, similar sized-whiskers initially deform through dislocation nucleation at a free surface [57, 58], a process that is heavily dependent on the surface state, which will be affected through FIB-exposure resulting in the possibility that the FIB-fabrication route alters the mechanism. This provokes the question: how does the fabrication procedure influence the operating deformation mechanisms that govern the observed size-dependent strength in these micron and sub-micron pillars?

As a result of the difficulties associated with the FIB, all of the compression and tension tests performed in this work were performed on samples that are produced though electroplating into patterned templates. These samples are FIB-less: they have never seen the FIB. This section goes through the details of how the templates are fabricated as well as how the pillars are electroplated into the templates as well as listing the corresponding microstructures.

2.1.1 Electroplated Pillars

2.1.1.1 Template Procedure

Adapted from Burek and Greer, Nano Letters *2011. [68]*

Figure 2.1 and 2.2 shows a schematic illustration of the fabrication process for the creation of compressive and tensile mechanical testing specimens. In this work, Cu nanopillars were intentionally chosen; however the technique is not limited to these particular metals and can be applied to a wide variety of electroplatable systems. Nanopillar arrays were fabricated on Si substrates ranging in size from ~1 cm^2 chips to 100 mm diameter wafers. Prior to applying the PMMA resist, a 20 nm thick Ti adhesion layer and a 100 nm thick Au seed layer were deposited on the substrate by electron beam evaporation. This conductive seed layer acts as a cathode in the subsequent electroplating steps. The choice of metal and the thickness of this conductive layer are noncritical, but need to be appropriate for the electrochemical processing, that is, the film does not form an oxide, and for the nanomechanical testing, that is, strong adhesion between the film and the Si substrate. The substrates were spin coated with various dilutions of 950 kD PMMA in anisole (Micro- Chem Corp.). Details of the PMMA resist conditions can be found in Ref. [68]. Generally, pillars meant for compression testing are required to have an aspect ratio of at least 3-to-1 (height-to-diameter) and no greater than 6-to-1. This ensures that nano- pillars are tall enough to experience homogeneous deformation without significant effects of top and bottom constraints, but not so tall as to buckle during compression testing. An aspect ratio of ~4-to1 was selected as the standard for the nanopillars fabricated in this report. Even though the nanopillar aspect ratio is ultimately governed by plating time, it is imperative that the PMMA resist thickness closely matches the intended nanopillar height. This requirement is critical for the fabrication of taper-free pillars with sub-100 nm diameters and also eliminates the use of excessive electron doses. The resist dilutions were selected such that the spin conditions were maintained between 1500 and 4500 rpm, thus ensuring uniform PMMA films. Following spin coating, the PMMA layer was baked at 180 °C for 15 min. The resist was then exposed using a Leica EBPG5000+ electron beam lithography system operating at an acceleration voltage of 100 kV. For all exposures, the beam current was maintained between 650 and 800 pA and the beam step size was 5 nm. The resolution of electron beam lithography is primarily a function of the electron dosage, whose optimal value depends on the resist type and thickness, minimum feature size, and pattern density. Since these relations are inherently nonlinear, a dose matrix was routinely used in order to empirically determine the optimal exposure conditions. Exposure patterns were computer generated and are extremely flexible, allowing for precise isolation of nanopillars and simultaneous fabrication of the

indicator markers, as the individual nano- pillars were routinely spaced up to 50 μm apart. Immediately following exposure, the PMMA was developed for 60 s in a 1:3 solution of methylisobutylketone (MIBK) and isopropyl alcohol (IPA) followed by a 5 s rinse in IPA.

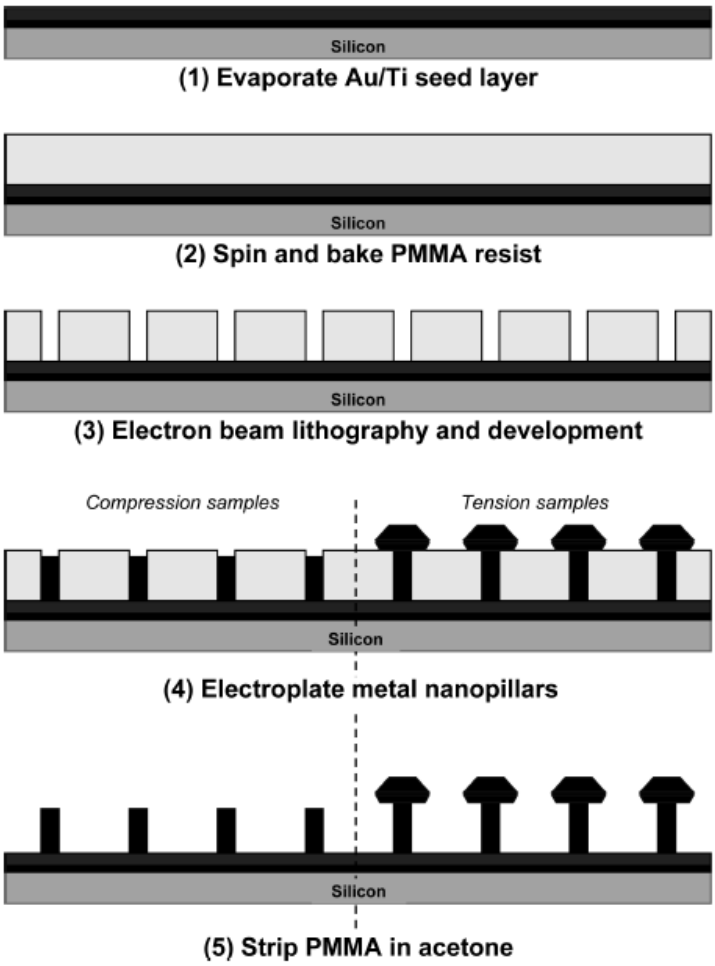

Figure 2.1 Schematic representation of the FIB-less fabrication steps for compression and tension mechanical testing specimens, adapted from Ref. [68]

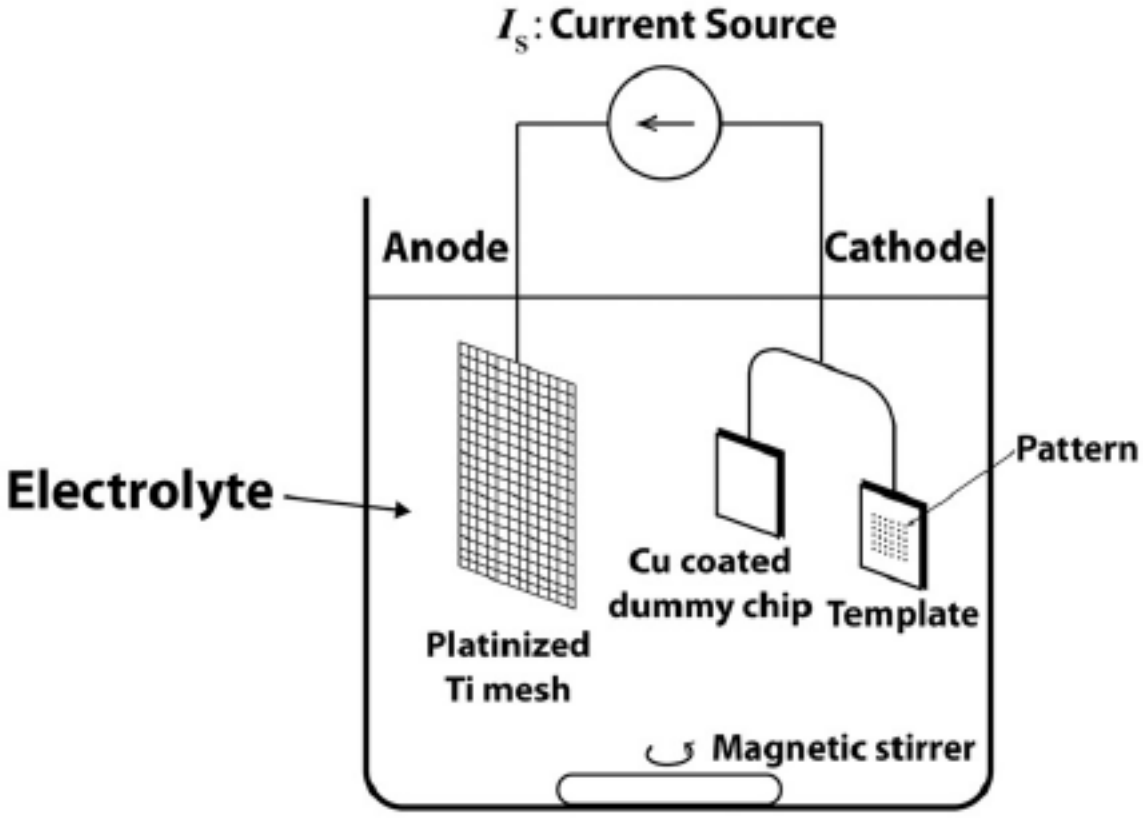

Figure 2.2: Schematic of electroplating setup. Image courtesy of D. Jang

2.1.1.2 Electroplating Procedure

2.1.1.2.1 Copper

Adapted from Burek and Greer, Nano Letters *2011 [68]*

Following development of the PMMA, the resist template was ready for metal electroplating. Electroplating was performed using a two-electrode configuration in a 1.0 L glass beaker. The Au seed layer underneath the resist template acted as the cathode, and a Pt-coated Nb mesh was used as an insoluble anode. The Cu plating solution was made in house using reagent grade 125 g/L $Cu(SO_4) \cdot 5H_2O$ and a supporting electrolyte of 50 g/L H_2SO_4. The homemade Cu plating solution was mixed with deionized water and reagent grade chemicals. The bath temperature was maintained at room temperature for Cu deposition. The plating solution was mechanically stirred and electroplating was performed under both galvanostatic (DC) and reverse pulse (AC) conditions. In DC plating, the

current density for single crystalline pillars with diameters below 250nm was 10 mA/cm2 for Cu electroplating. For AC plating, the cathodic/anodic current was 10 mA/cm2 / 3.5mA/cm2 respectively, and the cathodic pulse was held for 5 s followed by the anodic pulse for 1 s. The electroplating rate was estimated using Faraday's law, and deposition was stopped when the desired pillar height was achieved. Occasionally, fresh electrolytes are used, but in most cases the solutions were preconditioned electrolytes reused from earlier experiments. Following metal deposition, the PMMA resist was stripped in a bath of acetone at room temperature and rinsed in acetone and IPA. In the case of pillars to be used for tension tests, metal was intentionally overplated for a brief period to form a cap on the top of the pillar. Following removal of the resist template, these caps remain and can be accessed by a set of microgrips in order to tense the pillar

2.1.1.2.2 Iron

Similar procedures as used to produce copper nanopillars have been also used to produce single crystalline iron nanopillars. The same electron-beam lithography templates used to deposit copper were also used to deposit iron. Here the bath was made of 100g/L of iron (II) sulfate heptahydrate (Mallinckrodt Chemicals). The plating conditions were an AC square wave of 15mA/cm^2 forward current density for 3 seconds and 0mA/cm^2 reverse current density for 1 second. The zero current density intervals are required to minimize the evolution of hydrogen bubbles at the template interface. The voltage for successful plating experiments was found to be between 1.4V and 1.6V. Sometimes, the observed voltage would rapidly increase to greater than 2V. Under these high voltage conditions, the plating rate increases dramatically, and the resulting pillars contain multiple grains. The high voltage is found to coincide with copper plated alligator clips that contain gaps in the copper plating resulting in rapid bath deterioration. In general, the iron bath is relatively unstable, and the bath quality can deteriorate quickly and without warning. This bath deterioration is observed through the evolution of an orange precipitate, likely an iron oxide, and operating voltages at the above electroplating conditions above 2V. As a result, all electroplating using this iron bath is done within a small time window to preserve consistency in the plating results.

Beyond examples of copper and iron single crystals, this templated electroplating approach has been used to produce pillars of several different materials (gold, copper, nickel, tin, and iron) and microstructures (single crystal, nanocrystalline, nano-twinned). For example, multiple different copper microstructures can be produced through control of the electroplating conditions: higher current

densities promotes the growth of nanocrystalline pillars, while very high pulses separated by long periods of zero current can promote the formation of dense nanotwinned pillars.

2.1.2 Atomic-Layer-Deposition

Adapted from Jennings et al Acta Mat *2012 [69]*

In order to study the influence of a pillar's free-surface on its deformation behavior, a thin, hard ceramic coating was deposited on pillars with several different diameters and subsequently compressed (Chapter 6). Depositing a thin conformal hard coating on high-aspect ratio structures is nontrivial, with atomic-layer-deposition, ALD, being particularly suitable for these types of coatings as it offers atomic-level control of the depositing species one monolayer at a time (Figure 6.1c). Figure 6.1c shows a schematic of this process for an initially uncoated copper pillar whose surface is terminated with oxygen atoms. In the first step (1), a precursor gas is added into an ALD system where the precursor bonds with the oxygen to form a monolayer of the corresponding oxide. The following purge step (2) removes the remaining extra precursor as well as any additional reaction products from the chamber. This surface layer is then functionalized through reaction in a plasma (3) to produce a reactive oxygenated surface. The final step (4) is another purge step to remove the remaining reaction products. This process is repeated until the desired thickness is achieved. All reactions in our process were performed in an Oxford OpAL ALD system (Oxfordshire, UK); whereby 3nm of alumina was deposited with a precursor of trimethyl aluminum (SAFC Hitech, Allentown, PA) and the remaining thickness is titania formed from a titanium tetra-iso-propoxide precursor (SAFC Hitech).

The initial 3nm-thick Al_2O_3 layer was deposited first (1) with a reactant dose of precursor of trimethyl aluminum for 30ms at 120C. This was followed by (2) a 2 second purge followed by (3) a total of 6 seconds in a 300W plasma, 2 seconds for gas stabilization and 4 seconds for plasma power on. Finally, (4) the last purge step also lasted two seconds [70]. This process was repeated until the 3nm layer was complete. The following TiO_2 layer was added with a titanium tetra-iso-propoxide precursor at 200C. The remaining thicknesses of 2nm at pillar diameters, D, 75nm-150nm; 7nm at D~200nm, and 22nm at D ~ 500nm - 1000nm, respectively, were deposited via a process similar to the alumina deposition [71]. In both of these procedures, a remote oxygen plasma functionalized the surface with oxygen atoms such that the surface was identical to the initial conditions. It is expected that oxygen atoms and ozone are the most likely reactive species as there was a showerhead separating the plasma from the substrate.

2.2 Morphology Characterization

2.2.1 Scanning Electron Microscopy

Once samples have been fabricated, the pillar quality is determined through electron microscopy as pillar diameters are between 50nm and 1000nm: sizes too small for optical microscopy to provide sufficient resolution. First, the sample morphology is inspected in a scanning electron microscope, SEM; to check that 1) the pillars are standing upright and otherwise suitable for testing and 2) the deposition was successful, i.e., the desired pillar geometry (height and diameter) was achieved.

(1) Unfortunately, pillars are frequently, successfully produced but are found lying flat on the substrate preventing their use in uniaxial compression or tension tests. If this is the case, the plating rate is determined from the height of the pillars, and a new sample is electroplated with the appropriate time (discussed below).

(2) If the pillars are still standing, the geometry is inspected to ensure that the pillars are suitable for mechanical tests. The first step is to validate the electron-beam lithography write of the PMMA template such that the appropriate height, diameter, and near-zero taper angle, near-zero change in pillar diameter along the pillar length, are achieved. If the templates are successful, then the plating rate can be calibrated through inspection of the plating time and resultant pillar height. While the electroplating process is repeatable, the plating rate is a found to vary with bath age and use. As a result, it is necessary to calibrate the plating rate in order to produce the correct aspect ratio pillars. In compression, the aspect ratio is maintained between 3:1 and 6:1 (height: diameter). The small end of the aspect ratio is chosen in order to prevent dislocation trapping at the top and bottom constraints, diamond tip and substrate, respectively. The high end of the aspect ratio is limited to prevent buckling under compression. In tension, the aspect ratio is determined by the height of the PMMA and the diameter of the pores; however, these tension samples are still sensitive to the plating rate through the size of the tops of the pillars or pillar heads. If the size of the pillar head is too large, the underlying pillar frequently tips over, preventing tensile tests. Furthermore, in the case of pillars that still remain standing, the pillar head has to fit inside the tension grip, which has its own limitations.

If the plating rate is successful, then the next step is to identify pillars suitable for testing by eliminating those that have identifiable surface imperfections such as divots or voids. Also, for compression, the pillar top is evaluated to ensure that it as flat as possible because non-ideal, pointy,

tops result in difficulties during testing arising from problems identifying the point of full contact to pillar bending. If pillars have any of these features, they are excluded from mechanical test samples.

In chips where, overplated, tension pillars are produced, a quick check of the pillar top morphology can be used to ascertain the degree of crystallinity of the pillar below. In the case of single crystalline pillars, the pillar top will show a clearly faceted pillar such as that in Figure 2.3d; whereas, a polycrystalline top will show a spherical top as there is no preferred surface orientation shown such as some of the pillars in Figure 2.3a. Note that the presence of a faceted pillar top is not a sufficient condition for the underlying pillar to be a single crystal; however, it has been found to be a good indicator to suggest that the pillars may in fact single crystals.

2.3 Microstructure Characterization

2.3.1 Focused Ion Beam Imaging

Adapted from Burek and Greer, Nano Letters *2011 [68]*

SEM provides immediate confirmation of nanopillar morphology to validate the template parameters and electroplating process; however, the SEM provides limited microstructural information beyond inspection of the facets of pillar tops. FIB imaging, on the other hand, was employed as a fast, qualitative judgment of nanopillar microstructure. FIB imaging is capable of revealing grain and twin boundary contrast through the use of single-scan ion-beam images thus providing rapid feedback to adjust electroplating parameters to achieve the desired pillar microstructure. Specifically, FIB imaging was extremely useful for determining the electroplating parameters that yielded single-crystal microstructures in copper nanopillars. All FIB images were generated with a 30 kV Ga+ beam with a current of ~50 pA. As an inherently destructive method, FIB imaging is not available as a technique prior to nanomechanical testing. However, the speed of this technique allowed for imaging hundreds of pillars in order to infer the percentage of pillars with acceptable microstructures given a specific set of electroplating parameters. Because of the resolution limitations and the destructive nature of the technique, FIB imaging was limited to pillars with a minimum grain size of ~50 nm (for Cu) and minimum pillar diameter of ~200 nm. Examples of FIB-images are shown in Figure 2.3 (b-i), adapted from Ref. [68].

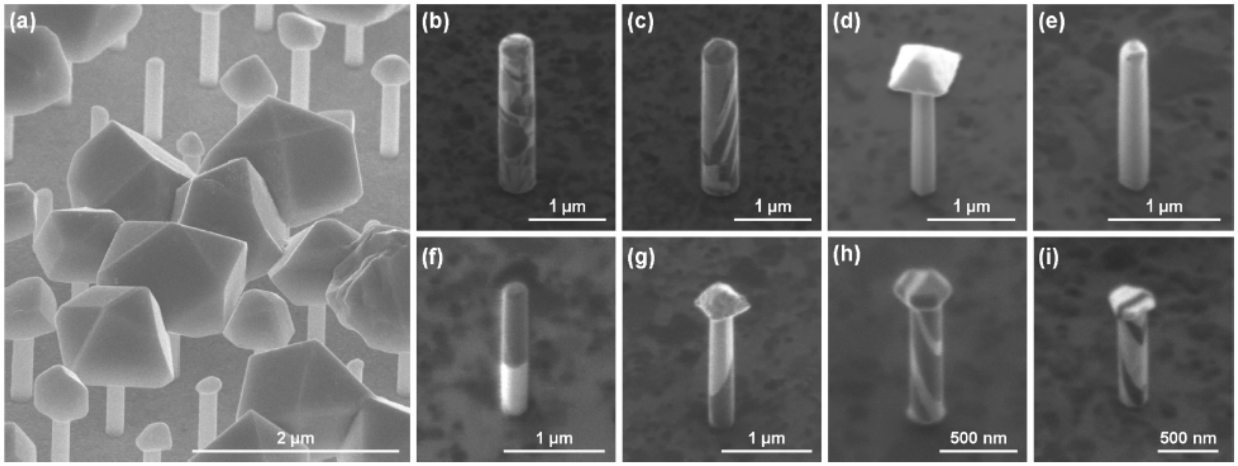

Figure 2.3: SEM image of an array of overplated copper nanopillars with ~175nm diameter and 1000nm heights shown in (a). FIB images showing grain contrast in 500nm diameter polycrystalline copper pillars (b,c). FIB images of single crystal and bicrystal 250nm diameter copper pillars in (d,e) and (f,g), respectively. FIB images of 200nm diameter copper nanopillars showing a unique highly ordered (likely nanotwinned) grain structured shown in (h,i)

2.3.2 Electron Back-Scattered Diffraction

FIB imaging is a qualitative and destructive evaluation method: it is possible to know either a pillar's approximate microstructure or its mechanical properties. Ideally, both pieces of information: a pillar's exact, quantitative microstructure and its mechanical properties would be known. In order to gain this added insight electron back-scattered diffraction, EBSD, was performed on several pre-compression 250nm pillars. EBSD captures crystallographic information from electrons that are back-scattered into a Bragg diffraction condition. The EBSD detector collects these electrons, and the resulting image contrast reveals the available diffracting planes through a Kikuchi pattern [72]. This pattern is used to index the sample, typically performed through an automated look-up table.

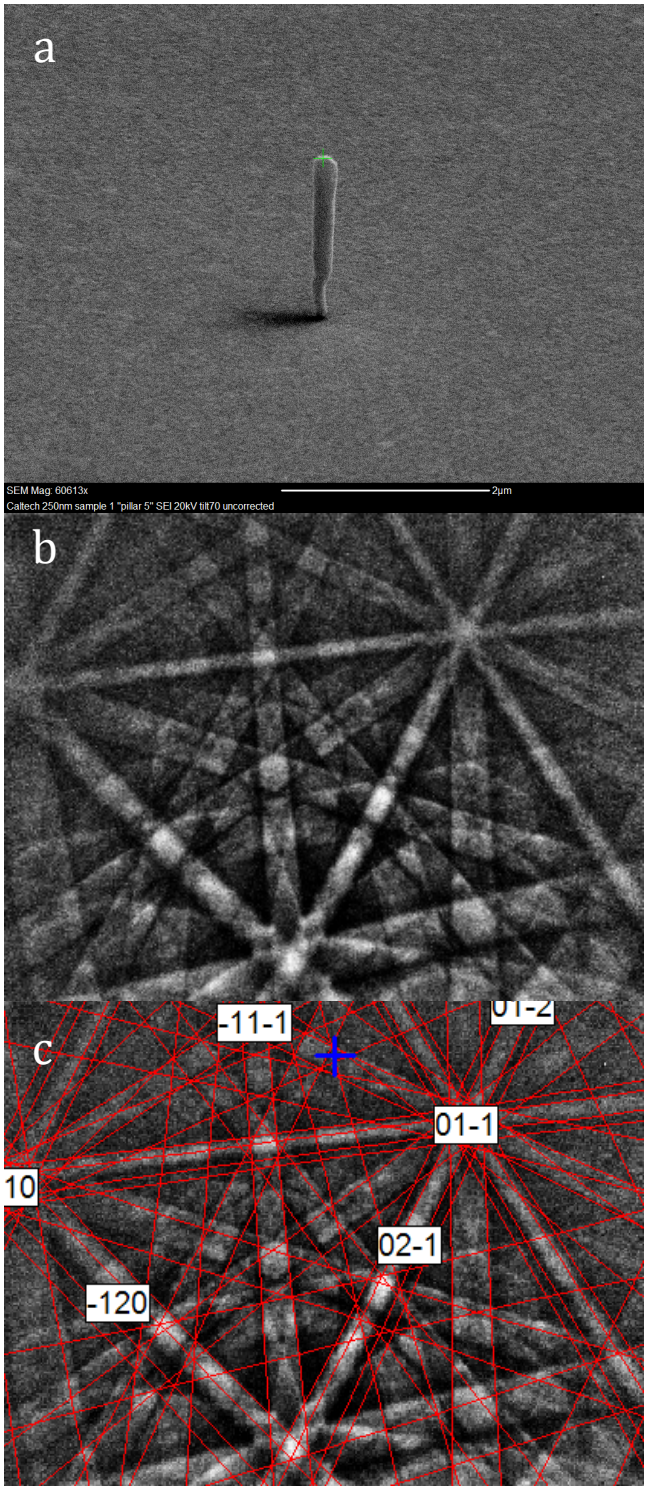

Figure 2.4: a) SEM image of an unsuitable mechanical testing pillar. b) EBSP and c) the resulting automatic indexing of that pattern

Through the help of Scott Sitzman (Oxford Instruments) on a Zeiss (Oberkochen, Germany) 1550 VP FESEM with a HKL (Oxford Instruments, Oxfordshire, UK) EBSD system, a sample containing 250nm electroplated Cu nanopillars was loaded into the SEM and tilted the standard EBSD tilt configuration, 70 degress. The electron beam was focused to a spot and several different electron-backscattered-patterns were taken along the pillar length. It was found that the only clear crystallographic information was acquired towards the top of the pillar, an example of which was seen in Figure 2.4. When scanning the bottom of the pillar, the electrons sampled both the copper pillar and the underlying Au-seed layer. This mix of materials and microstructures obscured the EBSD patterns and prevented pattern identification at the bottom of the pillar. This undesired mixture of signal was found to be unavoidable due to the required geometry between the electron beam, the EBSD detector, and the pillars standing on the Au-seed layer. As a result, this technique is limited to taller pillars with heights greater than 1 micron. In order to have mechanically compressible pillars the aspect ratio limitations confines the pillar diameters to

D > 250nm. Furthermore, EBSD does not accurately capture dislocation information preventing EBSD from aiding in mechanism identification. EBSD helps refine electroplating procedures through identification of crystal structures; however, due to the above limitations, TEM microstructural analysis was also performed on these samples to better understand both the crystal structure and available dislocations.

2.3.3 Transmission Electron Microscopy

In contrast with EBSD, which acquires information from "reflected" electrons, transmission electron microscopy (TEM) acquires its microstructural information from electrons passing through the sample. A variety of techniques can be performed using these transmitted electrons to reveal not only a material's crystallographic orientation, but also a detailed picture of its internal microstructure. For example, TEM provides information related to a material's defect structure such as the presence and orientation of grain boundaries, twins, and dislocations. On the other hand, using transmitted electrons requires that TEM samples must be thin, ~100nm or thinner in order to capture sufficient electrons, information, at the detector. Most conventional samples are initially much thicker than 100nm requiring substantial preparation steps to reach TEM-suitable thicknesses. However, the smallest diameter pillars here are naturally electron transparent due to their very small sizes allowing for unique TEM sample preparation techniques that allow for microstructural detail to be captured before and after deformation along with the mechanical testing data.

2.3.3.1 TEM Sample Preparation

2.3.3.1.1 FIB Lift-outs

Dual beam, FIB/SEM, microscopes can be used as an *in situ* tool to identify specific pillars to examine in the TEM through a procedure known as a "lift-out". The lift-out's site-selectivity is important as the pillars represent a tiny fraction of the substrate. Furthermore, site-selectivity allows for post-deformation microstructures of specific pillars to be examined allowing correlation between the final microstructure and the mechanical response. In a FIB lift-out, both the electron beam and ion beam are used to observe and extract a sample in real-time. Briefly, to lift-out a pillar: (1) first, a pillar is found and identified with the SEM. (2) It is then protected from the ion-beam with an organometallic deposited inside the FIB/SEM. (3) The protected pillar is then removed from the substrate by using the FIB to cut out a lamella from the underlying substrate that the pillar sits on. (4) This lamella is then removed completely from the substrate and (5) subsequently attached to a specialized TEM finger

through the use of a nanomechanical manipulator, Omniprobe (Omniprobe, Dallas, TX). (6) The remaining pillar is then carefully thinned with the FIB until electron-transparency is reached. A detailed walk-through of the procedure is found below.

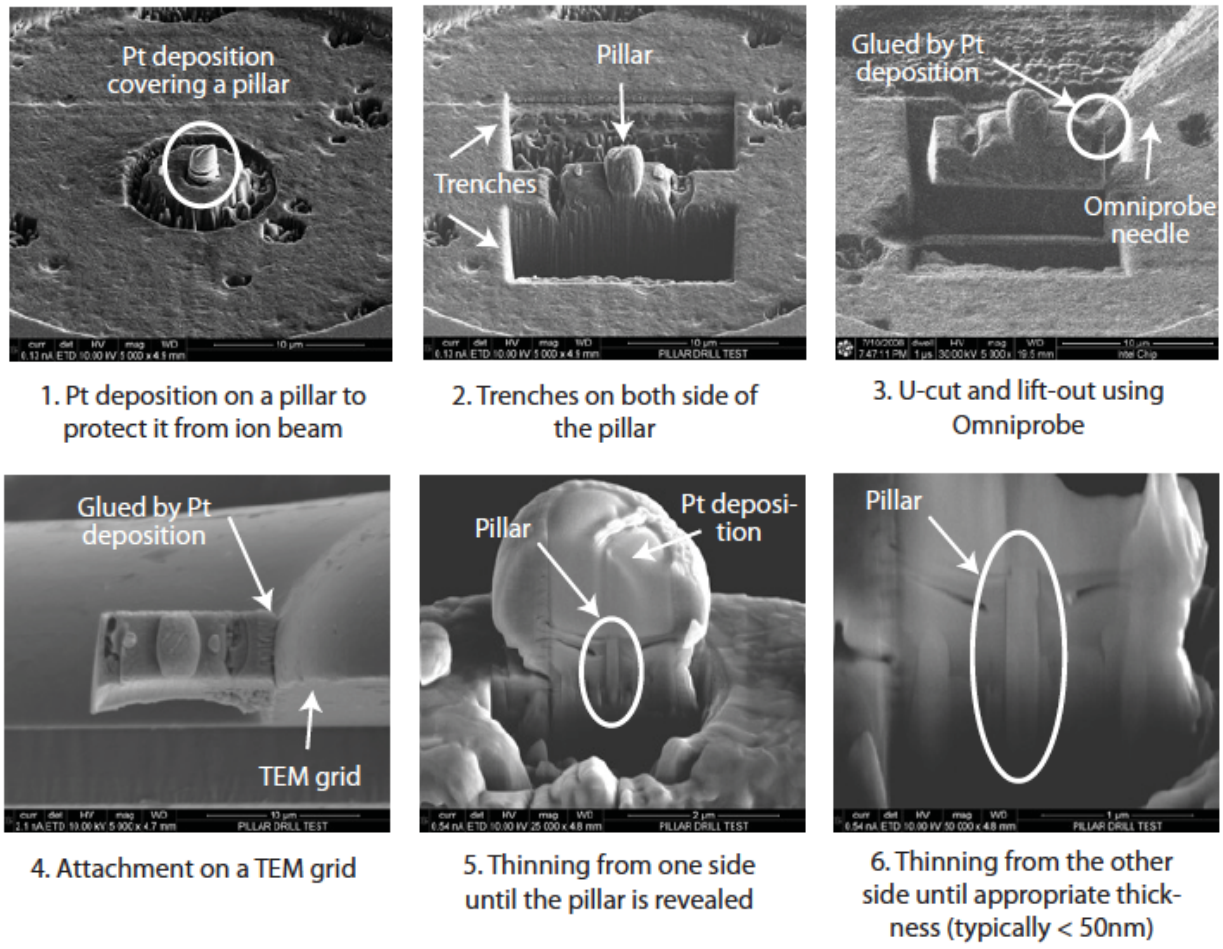

Figure 2.5: FIB lift-out schematic courtesy of D. Jang

General guidelines:

1) NOTE: During any ion-beam milling make sure that the image is scan-rotated 180 degrees to minimize orientation confusion.
2) The ion-beam removes material when it is on. Limit the ion-beam exposures to small periods of time and use the lowest feasible beam current.

(1) Protective Deposition Step

First, the selected pillar is covered in a protective layer of Pt-alloy or W-alloy through the use of an gas-injection-system (GIS) needle and either the electron or ion beam. Deposition works through the release of an organometallic precursor close to the sample surface, ~100um, while the electron or ion-beam rasters over the desired deposition region. When the organometallic comes in contact with the sample surface, secondary electrons coming off the surface react with organometallic to deposit the precursor over only the desired region.

In terms of beam choice, electron deposition is slower than ion-beam deposition as fewer secondary electrons are produced per incident electron than per ion; however, ion deposition induces damage: etching the top most layer as well as depositing material at a faster rate. As a result, electron deposition is used to deposit a thin, 100-200nm, layer first followed by ion-deposition of the remaining thickness. Several other details are listed below:

1) Electron deposition occurs at 0 degree tilt, while ion-beam deposition of occurs at 52 degrees tilt. The tilts listed are such that the deposition always occurs top-down on the pillar.
2) The patterns used are typically circular with radius at least 200nm larger than the pillar and the pattern is centered on the pillar. Subsequent ion-beam deposition will need to be even larger, another ~200nm increase in radius, to ensure that the pillar is coated from all sides.
3) The final height of deposition should be equal to the original pillar height + 2 microns to ensure that there is enough sacrificial deposition for the final thinning steps.

(2) Lamella Milling

Next, the FIB is used to define a lamella. In total, five patterns are used to define the lamella as shown in Figure 2.5.2: three "regular cross-section" patterns and two "rectangular" patterns at 52 degrees tilt. The regular cross-sections are placed parallel to one another and define the width of the lamella. Regular cross-sections are used to cut along the length of the lamella and enable the next step: the undercut. To further aid the undercut and speed up the current step, two cross-sections are placed on the "back side" of the lamella. The rectangular sections are parallel and define the length of the lamella. These two sections are also used to speed up the next step: the undercut. Notice that these

rectangular patterns are not symmetric. One connects each regular cross-section of the lamella; whereas, the other leaves a thin strip connecting the lamella to the rest of the bulk sample.

(3) Undercut Milling and Lift-out

The sample is then tilted back to 0 degrees and the undercut is performed. This cut is a thin ~200nm rectangular pattern extending between both rectangular sections used in the previous step. Concurrently, two rectangles are placed over the previous rectangular cuts on the sides of the lamella. In total, the result of these three cuts is to separate the lamella from the bulk substrate except for a thin region on the left hand side of the ion-beam image. Performing these three cuts in parallel is necessary to prevent redeposition from filling in previously cut sections. The redeposition may behave as a "glue" sticking the lamella to the substrate. These cuts are complete when the ion-beam cut is observed extending through the lamella. This can be seen at 52 degrees tilt in the electron eam.

Still at 0 degrees tilt, insert the Omniprobe. Next, move the omniprobe into alignment above the lamella. X and y positioning can be performed with the electron beam, while z positioning can only be performed with the ion beam. Before making contact with the omniprobe to the lamella, insert a GIS needle (Pt or W) as the act of inserting the GIS needle will cause the Omniprobe to shake aggressively. Bring the Omniprobe into contact with the side that is 100% cut through, the right hand side of the ion-beam image. On contact, the contrast will change as electrons can pass through the Omniprobe as opposed to charging the sample. Add a rectangular pattern to ion-beam deposit ~200nm thick layer of GIS deposition. This will be the glue attaching the Omniprobe to the lamella. After deposition, do not move the omniprobe.

Next, *beam shift* to the opposite end of the lamella, left hand side ion-beam image, and sever the attachment to the substrate with the FIB. While cutting with the FIB, simultaneously watch this procedure with the electron beam to determine when the break occurs. Using the Omniprobe, proceed in the z-direction at 5um/s. If this procedure is done correctly, the Omniprobe will lift out of the substrate. Remove the GIS needle and take the lamella to the "Park" position. If one of the cuts was not completed the glue to the Omniprobe will break first. If this happens, start over on a new sample as the lamella is no longer stable enough to yield a good lift-out. Remove the omniprobe from the chamber.

(4) Attachment to TEM grid

Move the Omniprobe TEM fingers into the electron beam. While simultaneously monitoring the position of the Omniprobe and lamella with the ion-beam and electron-beam, bring the lamella between two TEM fingers and at least ~20um from either finger. Insert the GIS needle. Again the GIS needle will cause the Omniprobe to vibrate. Next, slowly line up the lamella so that the lamella is just out of contact with the TEM finger. Place a small rectangular pattern in order to ion-beam deposit glue to attach the lamella to the TEM finger.

Once the lamella is firmly attached to the TEM finger, *beam shift* to the Omniprobe side of the lamella and cut off the Omniprobe from the lamella. Use care to ensure that the Omniprobe will still be sharp after this cut. This is important as odds are you will be the next user using the Omniprobe for further lift-outs. When the Omniprobe has been detached, carefully retract the Omniprobe and GIS needle from the chamber.

(5) Thinning for TEM

At this step, the pillar is attached to a TEM finger and still coated in a thick layer of protective Pt (or W); however, in order to view your pillar in the TEM the Pt must be selectively removed from the front and back of your sample such that the pillar is $\leq$ 100nm thick. To do this, use "cleaning cross-sections" to slowly etch away the protective Pt layer from the pillar. During this step, it is easy to miss your pillar and accidentally destroy it unless this process happens concurrently with simultaneous imaging in the electron beam. Repeat this process for both sides of the lamella until the pillar is apparent surrounded by Pt and the thickness of this section is thinner than 100nm.

2.3.3.1.1.1 Alternative Chemical Thinning: XeF2

Lift-outs can only give information on one state of the pillar: either before OR after deformation. Another limitation is that, as mentioned previously, FIB techniques introduce damage in the form of surface dislocation loops. However, the thickness of these test specimens is already on the scale of electron transparency thus removing the need to thin one of these samples. As a result of these two factors: 1) limitations of the FIB-lift-out technique and 2) the already electron transparent sample sizes, a second thinning technique was attempted to selectively remove W-protection layer.

All the regular lift-out steps remain the same; however, the W-glue is not completely thinned. When the W-glue thickness is still 100nm larger that the pillar diameter, stop FIB-thinning. Insert the XeF^2 needle and begin performing an electron-beam XeF^2 over the pillar height. XeF_2 is reactive with

W and will form gaseous WF_6, which should then be pumped out of the chamber. Furthermore, XeF_2 is not reactive with Cu and as a result should allow for the selective removal of only the W-deposition. An example of this process can be found in Figure 2.6. Initial attempts at this process showed some success; however, an unknown factor made the etch rate unpredictable. Furthermore, at very long etch times (hours), the copper will be etched away.

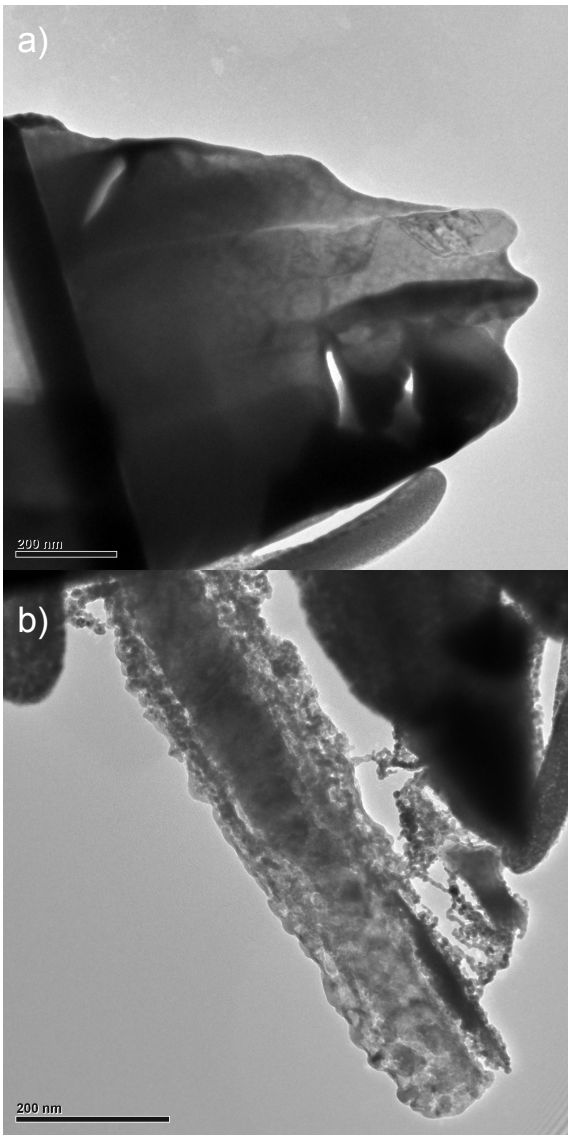

Figure 2.6 XeF_2 etch of pre-thinned pillar before etch: (a) and after two hours of etching with XeF_2 (b)

2.3.3.1.2 Plucking and Gluing

A second technique, plucking, was developed in the Greer lab to study samples that already have electron transparent dimensions. Plucking, in summary, is a tension test inside the SEMentor that takes advantage of the weak as-fabricated interface between the gold surface layer and the bottom of the electroplated pillars. The procedure to pluck is initially identical to a tension test. First the grips are lined up behind the pillar and subsequently the pillar is threaded into the grips. Second, a slight force is applied by the grips with a slight additional substrate perturbation to detach the pillar from the substrate and onto grips. The pillar is now kept in the SEMentor grips as the substrate sample is replaced with a TEM finger. The top of the TEM finger has been previously flattened into a small square pedestal onto which the pillar is slowly lowered. The pillar then detaches from the grips and remains on the TEM substrate. This TEM substrate is then taken to a dual-beam FIB/SEM where the bottom of the pillar is glued through a GIS needle to securely attach the base onto the TEM finger. Figure 2.7 shows an example of the steps in this procedure. The pillar can now be viewed in the TEM before and after a tension test such that a one-to-one correlation between the before and after microstructure can be obtained along with the results of the mechanical test.

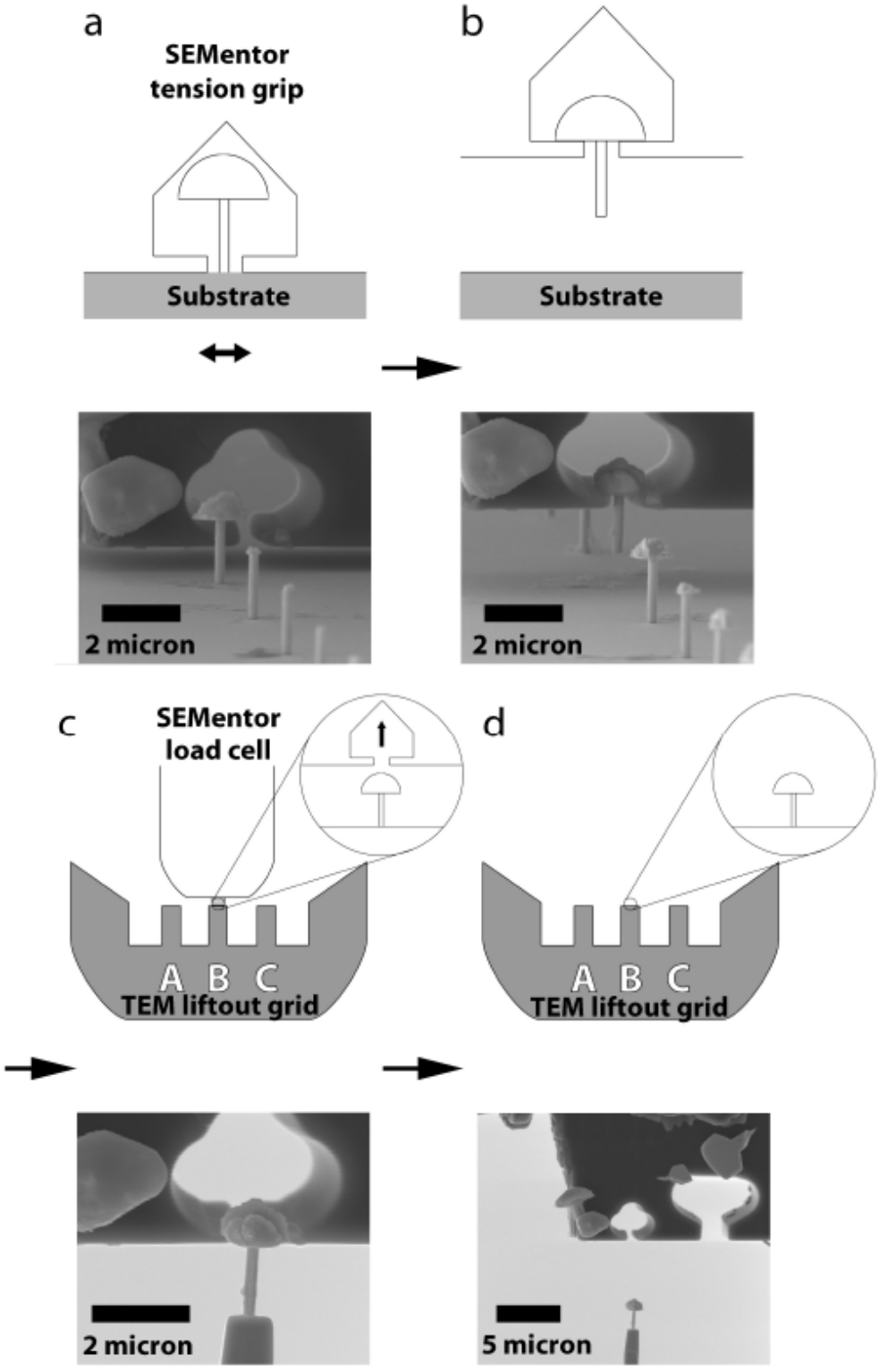

Figure 2.7: Schematic and SEM images of the plucking process. Image courtesy D. Jang

2.3.3.2 TEM - Microstructural Analysis

TEM observation along with diffraction analysis was used to identify the presence of a single crystalline structure after electroplating as well as examine the pre- and post-deformation dislocation structure of nanopillars. Both of which were determined through diffraction techniques.

2.3.3.2.1 Diffraction – Microstructure Determination

In TEM, the incident electrons either pass through the sample or are diffracted by lattice planes satisfying the Bragg condition [72]. In the case of a single crystal at a high-symmetry orientation, these diffracted electrons have a highly symmetric pattern corresponding to the available diffracting planes [72]. The angle and relative distance of these spots can be used to accurately determine the crystal structure and the lattice constant. An example of a single crystalline pattern is found in Figure 2.8b,c, the diffuse rings around the spots are from the protective layer. In the case where multiple crystals are present, other, asymmetric spots are also observed in the diffraction pattern. The presence of these additional diffraction spots demonstrates that multiple crystals exist; however, this information is insufficient to describe the relative extent and size of the other grains. An individual grains size can be determined through a combination of selected area diffraction, SAD, and dark field. Both of these techniques use apertures in the imaging and diffraction planes respectively to show only selected regions. SAD uses an aperture to limit incident electrons to a small region of the pillar such that only these electrons are collected at detector. SAD provides more diffraction contrast by removing unwanted scattered electrons. Dark-field, DF, uses apertures in the diffracting plane to select individual diffraction spots, the resulting pillar image is dark except for the diffracting grain, which is strongly illuminated. An example of SAD patterns and their corresponding dark-field images are shown in Figure 2.2b-e. Through a systematic analysis of the diffraction spots in SAD and DF, the extent of the crystal structure can be determined. The pillars examined in this work had a range of microstructures from pure single crystals to, nanocrystalline; however, only pillars with nominally single crystalline microstructures were tested. An example of a nominally single crystalline pillar ~250nm diameter copper pillar is shown in Figure 2.8. This pillar has one major grain with a very small twin near the base of the pillar.

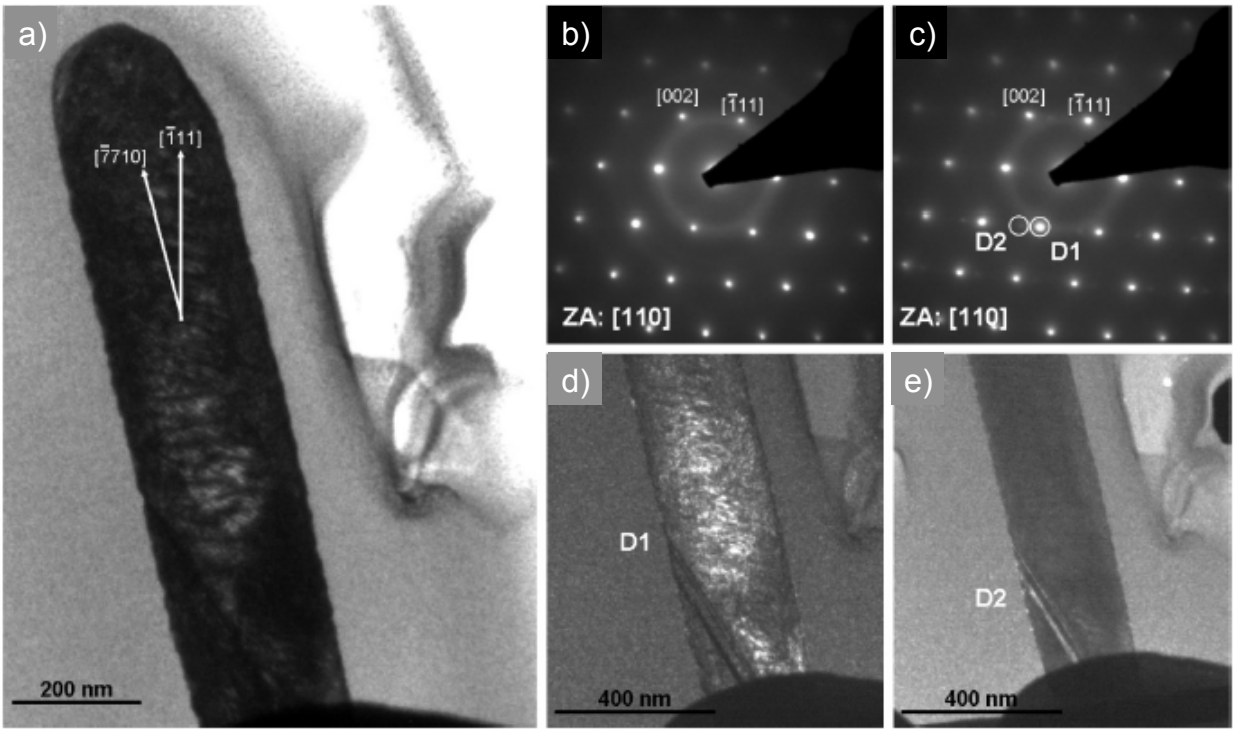

Figure 2.8 a) 250nm diameter single crystal copper pillar. b) and c) SAD patterns of the top and bottom of the pillar respectively. Dark-field images of the spots D1 and D2 in d) and e) respectively

2.3.3.2.2 Pillar Loading Axis Determination

When the crystal is tilted in a high-symmetry orientation, the diffracting beams can be accurately indexed and compared with the image revealing the crystallographic orientation of the specimen. The most important direction to determine is the loading axis or the direction parallel to the pillar's height as this will control the resolved shear stress through the Schmid factor. The procedure is as follows: first the pillar is tilted into several high-symmetry zone axes and the resulting diffraction patterns are indexed. The diffraction pattern is then rotated to correct for the rotation difference between the image and the diffraction pattern. In the FEI Technai TF20 used in this work, this rotation corresponds to ~28 degrees counterclockwise as determined by MoO_3 standards. The high symmetry directions are compared with the resulting image in order to obtain the orientation of the pillar. Furthermore, as the TEM image is a two-dimensional projection, the tilt of the pillar needs to be considered when identifying the loading axis. The resulting single crystalline copper pillars have a loading direction that is found to be within 10 degrees of a <111> orientation.

2.3.3.2.3 Dislocation Structure and Character Determination

Both the dislocation lines and their character, Burgers vector, can be determined through TEM techniques that take advantage of the atomic level displacements around a dislocation. Dislocation lines are visible in TEM because the atomic disregistry at the dislocation core is an efficient electron scatterer. The dislocation character, Burgers vector, can be observed through dark-field or two-beam techniques that selectively image the crystal with only one diffraction vector. A dislocation will only be visible under these conditions if the dislocation's displacement field distorts the selected diffracting planes. If the displacement field does not distort the selected diffracting planes, the dislocation will be invisible. A dislocation's Burgers vector can be determined by selecting multiple different independent diffraction vectors and recording under which diffraction vectors a dislocation is visible and invisible.

2.3.3.2.4 Bright-Field/Zero-Loss Filtered

The most basic method to measure dislocations is through bright-field imaging. In bright field, the central, transmitted beam of electrons, those that do not diffract, are selected for imaging through insertion of a diffraction aperture. Any feature that results in a diffraction or scattering event, for example, the highly strained lattice near a dislocation core, will appear dark in contrast to the much brighter background. Under these conditions, the width of the dislocations can be much broader than otherwise expected for a line defect due to the additional inelastic scattering near the dislocation core

The apparent width of the dislocation core can be narrowed by using an electron energy loss spectroscopy (EELS) technique known as zero-loss filtering. EELS provides extra information over conventional TEM by passing after-sample electrons through a magnetic prism and separating the electrons by their energy. Furthermore, this technique can be used to acquire specimen images or diffraction patterns with narrow energy ranges. By selecting only the electrons that retain their initial incident energy, or have zero energy loss, the inelastic scatter that thickens the dislocation lines can be removed revealing higher dislocation line contrast and in the case of entangled dislocations, more information about the dislocation network. An example of this type of image can be found in Figure 3.4.

2.3.3.2.5 Weak-Beam Dark Field (WBDF)

Another method to provide fine dislocation resolution is weak-beam dark-field. In this technique, the crystal is tilted into a diffraction condition with one weak diffracted beam. When the weak beam is selected through a diffraction aperture, the resulting image is dark as the crystal is far from this

diffraction condition. However, if the image is averaged over long times, 60s or more, dislocation lines appear as thin white lines as dislocation cores are the only regions in the crystal in which the diffraction condition is met due to the high local strain; therefore, the dislocation cores now appear as bright white on a dark background.

2.3.3.2.6 Burgers Vector Analysis (g dot b)

The previous techniques take advantage of the break in lattice periodicity at the dislocation core to image dislocations. These techniques show the dislocation line; however, they provide no information about the dislocation character or Burgers vector. In order to gain insight into the dislocation Burgers vectors present in these crystals, we employ "g dot b" analysis. Burgers vectors can be identified by selectively choosing specific diffraction vectors and when $g \cdot b = 0$ the dislocation will be invisible. When a dislocation's Burgers vector is perpendicular to the selected diffraction vector, the dislocation will be invisible in the image as the Burgers vector shift is in-plane with the diffraction condition. By selecting a series of diffraction vectors, the Burgers vector for an individual dislocation can be determined. This process is especially important in WBDF or more generally two-beam techniques, as imaging with only one diffraction vector may not reveal all the dislocations. A WBDF of a post-compression copper pillar is shown in Figure 3.4.

2.3.3.2.7 Dislocation Density Estimates

The dislocation density in TEM samples is estimated by measuring the apparent dislocation line length through ImageJ (free software) and then dividing that line length by the pillar volume. As TEM produces a two-dimensional projection of a three-dimensional pillar, the depth of the pillar is estimated from the thickness of the lamella after thinning. This dislocation density estimate will always an underestimate of the total dislocation density as this technique cannot resolve dislocation line length that runs parallel to the beam direction.

2.4 Nano-Mechanical Testing

The uniaxial mechanical tests were conducted in two different machines: an *ex situ* Agilent G200 Nanoindenter (Santa Clara, CA) and a custom built *in situ* nanoindenter: SEMentor, Nanomechanics InSEM (Oakridge, TN). Tensile tests were performed only in the SEMentor as tensile tests require *in-situ* alignment; whereas, compression tests were preformed in both machines. This section first explains how both the G200 nanoindenter and the SEMentor work, and then followed by a discussion of the details of the testing procedure.

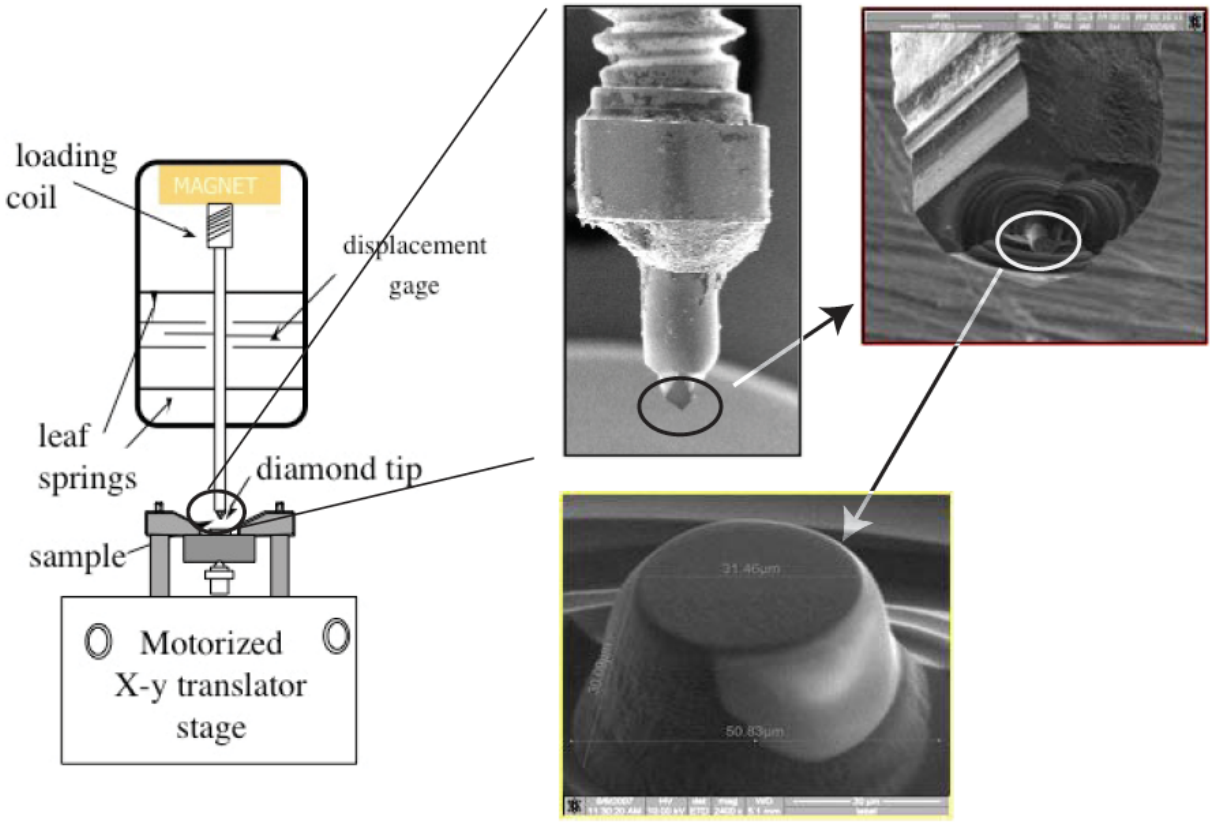

Figure 2.9 Schematic of the DCM load-cell along with SEM images of a diamond flat punch.

2.4.1 G200 DCM Nanoindenter (*Ex situ*)

The nanoindenter used was an Agilent G200 with two different load-cells: 1) the Explorer (XP) and 2) the Dynamic Contact Module (DCM). All the compression tests performed in the G200 were conducted in the DCM as it has a finer load and displacement resolution as well as smaller mass allowing a much quicker response time. The DCM is a load-controlled machine: a voltage is applied to an electromagnetic voice coil and a resultant force, up to 10mN, is then applied through the indenter tip. The displacement, up to 30μm, caused by the force is measured through a capacitive gauge. The displacement signal is inherently noisy and is averaged over 100ms by the machine. For faster tests, the machine is capable of using a faster time constant, 1ms, where displacement signal speed is gained at the cost of increased noise in the data. A labeled schematic of the DCM assembly is shown in Figure 2.9. As can be seen in the image, stability to the nanoindenter shaft is provided through a pair of leaf springs above and below the capacitive gauge. These springs have a very high stiffness perpendicular

to the indenter direction and a low stiffness in the operating direction providing some nominal resistance to the motion of the indenter. This force is calibrated by the machine and subtracted off the results from the tests. In general, the force required to flex the leaf springs over the distance traveled is negligible compared to the nanopillar experiments performed here. The G200 is also equipped with a Continuous Stiffness Measurement capability that allows for the simultaneous measurement of the sample stiffness.

2.4.1.1 Procedure – *Ex situ* Testing

2.4.1.1.1 Identifying and Selecting Pillars

As discussed previously the pillars tested in this work are too small to be evaluated outside of an electron microscope. However, the G200 has a top-down view of the sample with up to a 100x magnification optical microscope. As a result, the desirable mechanical testing pillars cannot be distinguished from those with defects. Therefore, prior to testing, pillars are identified in a GIS-equipped SEM (FEI Nova 200 or FEI Nova 600), and suitable pillars are marked by electron-beam deposition of a large Pt or W annuli. Each annulus has an inner diameter between 6 and 7 microns, width of 1 micron, and height less than 100nm. Examples of these annuli are shown in Figure 2.10. These annuli are visible in the optical targeting system as ellipses as the deposition of circular annuli is performed at 52 degree tilt and the optical microscope observes the pillars at 0 degrees. When drawing annuli, care must be taken to avoid deposition of any precursor on the pillars themselves, this prevents making annuli too close to the desired pillar or the neighboring pillars, should those also be promising.

2.4.1.1.2 Targeting, Surface Find, and Thermal Drift

Sample substrates, $1cm^2$ silicon wafers, are mounted with colloidal graphite to stiff sample pucks in order to prevent additional sample compliance. Prior to loading the puck into the G200, a relatively soft, compliant material needs to be added on top of the silicon to provide a region to perform a microscope to indenter calibration. In this step, an area is targeted with the microscope and a series of indents are made to ensure targeting accuracy. Silicon is too hard for the DCM to effect; therefore, a soft second material, double-sided tape or nail polish, is added. One other critical factor is that this soft material should be as thin as possible to ensure targeting fidelity is preserved between the microscope to indenter calibration and the pillar compressions. Targeting accuracy is important for these tests as the G200 has a random error up to ~1um, so care must be used when using a very small flat punch, 7um used here.

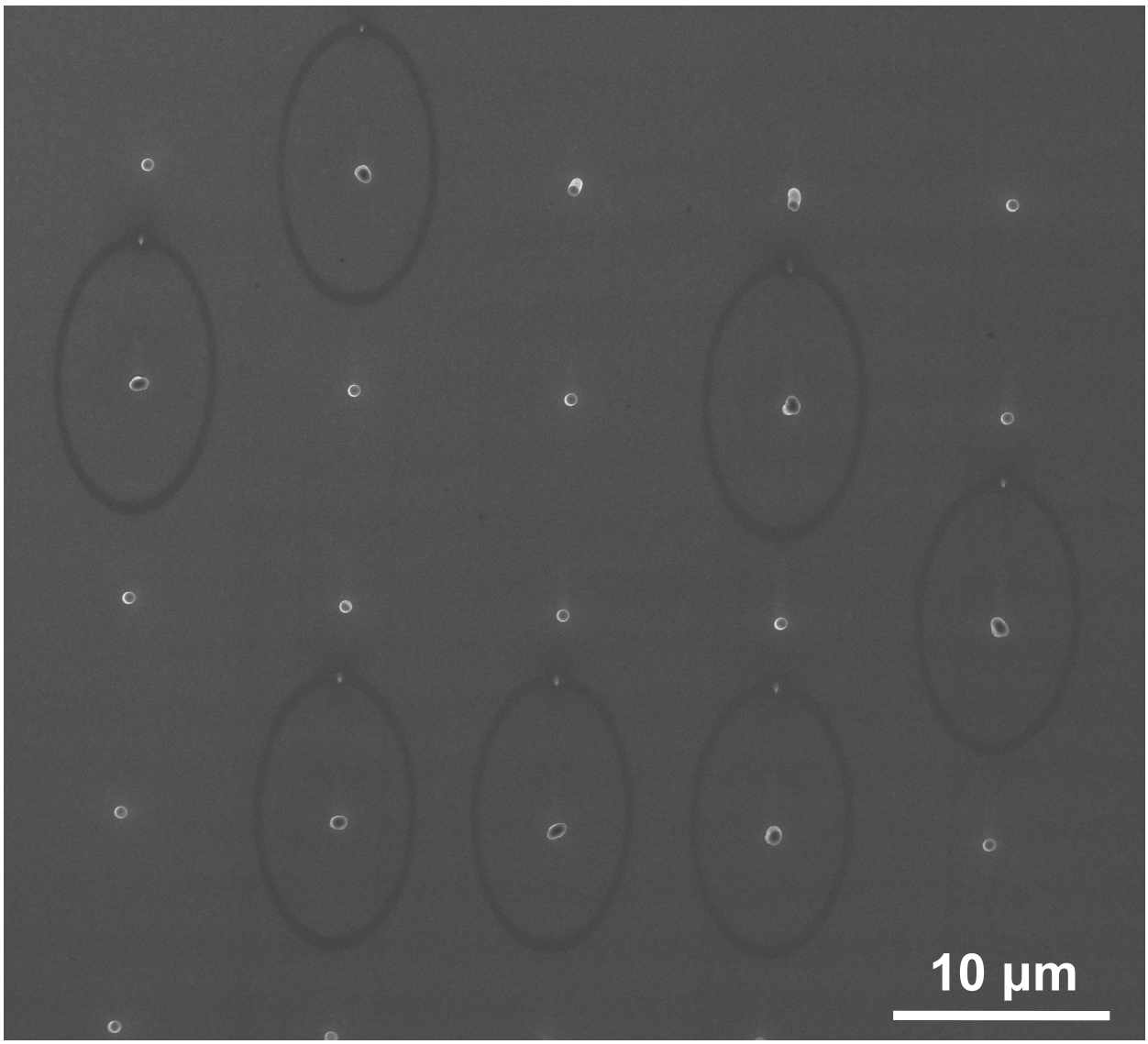

Figure 2.10 Top-down view of 500nm pillars surrounded by rings for identification in the G200.

After the G200 is calibrated, the pillar test locations, x and y positions, and conditions (loading type, rate, etc.…) are programmed into the Test Works/Nanosuite software and are run automatically by the machine. The experimental conditions are similar in both the G200 and the SEMentor and are discussed later in this chapter. Once the test starts, the z-distance is measured at a user-selected surface-find site on the flat silicon surface within 100um of the desired pillar compression to minimize any errors due to subtle sample misalignments. During the surface-find, the DCM extends the tip to near its forward limit and then the whole DCM assembly is lowered until the indenter tip hits the

surface. The DCM iterates this procedure to find an accurate measure of the sample surface. After the surface-find, the machine places the tip on the surface halfway between the test site and the surface-find site and waits until the machine drift, caused by thermal expansion, stabilizes below 0.050 nm/s. Note, that if the surface-find site is poorly selected, the thermal-drift position may be on a to-be-compressed pillar. Once the machine is stabilized, the tip moves above the selected pillar to a height of the surface position plus a user-defined starting position, typically ~2um. The machine then slowly approaches the surface at a prescribed rate, ~10nm/s until it registers a stiffness in excess of a set-threshold, ~100N/m. Once this occurs, the machine pauses and the test proceeds. This procedure occurs before every pillar compression, not just prior to the first compression test.

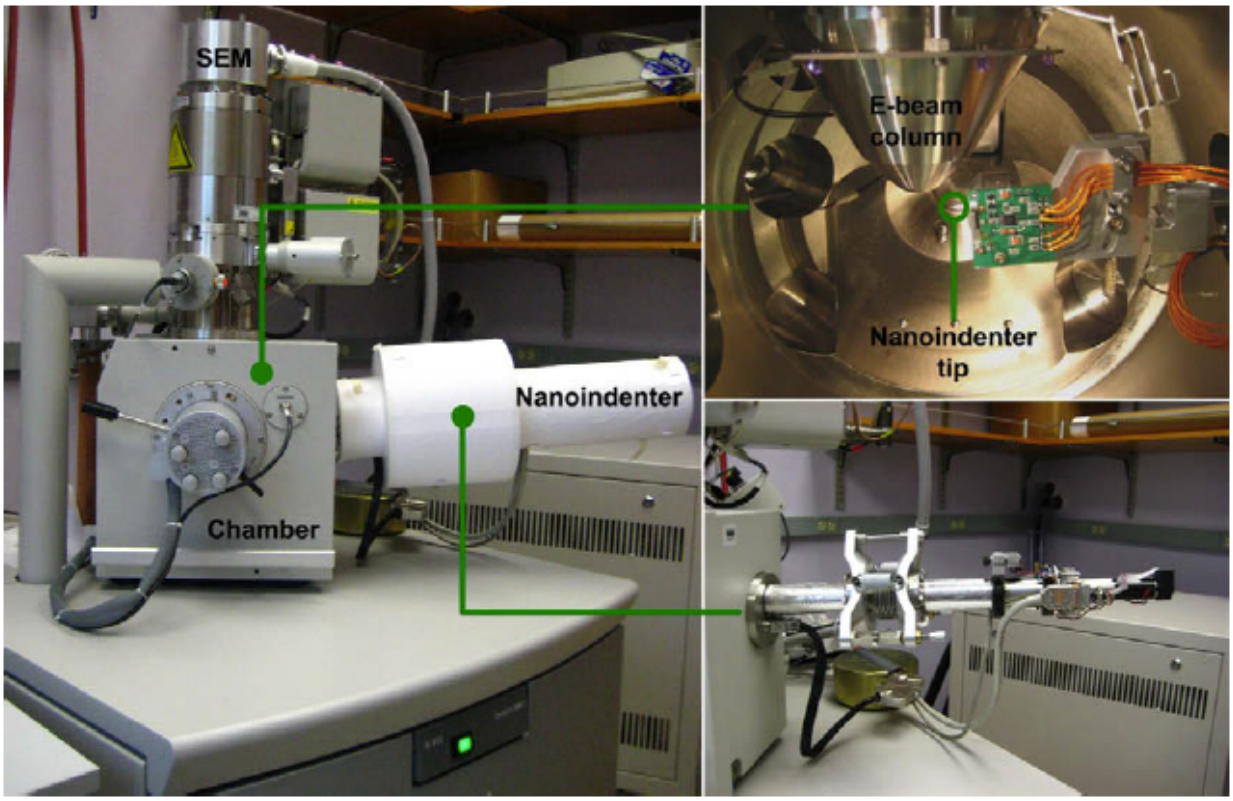

Figure 2.11: Image of the first generation SEMentor installed in Steele 235

2.4.2 SEMentor (*In situ*)

The SEMentor, Nanomechanics InSEM, is a custom built *in situ* DCM, of similar design as the G200, and an SEM that allows for reliable mechanical data as well as real-time observation of nanoscale mechanical tests. Another feature of the SEMentor is that it allows for the three-dimensional

alignment required for tension tests. An image of the SEMentor can be found in Figure 2.11. In contrast to the G200, the SEMentor arm is nearly parallel to the horizontal in order to accommodate the electron beam while allowing the whole sample surface to be visible.

2.4.2.1 Procedure (in-situ testing)

When the SEMentor arm is fully inserted, a polymer block is compressed between the SEM pole piece and the SEMentor arm in order to dampen the observed vibrations. The polymer block is viscoelastic and thus requires several hours to equilibrate. After the drift has subsided, the SEMentor tip can be realigned with coarse adjustment screws outside the chamber. After this realignment, the SEMentor tip position is fixed leaving only 30um of available tip travel along the loading axis.

2.4.2.1.1 Sample Alignment

The sample stage is tilted to 4 degrees such that the indenter arm and the sample surface are perpendicular. Samples are fixed with colloidal graphite onto a conventional SEM sample stub, which is itself affixed to an aluminum SEM cube. Once loaded, the sample is brought near the SEMentor tip with manual SEM stage controls. Depth perception in the SEM image is critical in order to accurately align the tip and sample. There are two main ways to tell depth: 1) the focal plane shows everything at the same depth; therefore by changing the focus, the relative position of the tip and the sample can be understood and 2) when the tip is very close to the surface, the tip casts a shadow on the sample surface providing much more accurate determination of the arrangement between the tip and pillar. Suitable test pillars are typically found in the SEMentor immediately prior to testing as the electron imaging provides excellent resolution. After finding the desired pillar and aligning the tip the test is started.

2.4.3 Experimental Tests/Control

Test conditions in both machines are performed are nominal displacement rate, $\dot{u}$, or strain-rate control, $\dot{\varepsilon}$. The prescribed strain rate is related to a displacement rate through the pillar's initial length, l_o: $\dot{u} = \dot{\varepsilon} l_o$. As the nanoindenter is an inherently load-controlled machine, nominal displacement/strain-rate control is performed via a feedback loop at the outer loop rate (500Hz) controlled through the Testworks (later upgraded to Nanosuite) software. The PID-parameters for the feedback loop were tailored to provide nominally constant displacement/strain-rate control. Slower strain rate tests, $\dot{\varepsilon} < 10^{-1} s^{-1}$ were performed with the long time constant, 100ms to minimize the noise in the displacement signal, while faster strain rate tests, $\dot{\varepsilon} \geq 10^{-1}\, s^{-1}$, used the fast time

constant, 1ms, to provide adequate displacement data. The data acquisition rate varied from 25Hz to 500Hz and depended on the strain rate to provide sufficient resolution in the data.
The mechanical tests stop at a strain of ~25%.

The CSM data is used to verify that the test is successfully applying compression or tension as opposed to bending, buckling, or missing the pillar entirely. The CSM data is compared with the theoretical pillar stiffness defined as $C = \frac{E_{hkl}A_i}{L_i}$ where E_{hkl} is the pillar's Young modulus, A_i is the instantaneous area and L_i is the instantaneous length. During a compression test the pillar area increases and the length decreases resulting in a monotonic increasing pillar stiffness. If the pillar buckles or begins to bend, the stiffness will subsequently decrease. Any data after a decrease in the CSM stiffness is not considered to be part of a successful test and that data is removed from the stress-strain behavior.

2.4.4 Tip Fabrication/Milling

In the case of compression, the diamond indenter tip is originally obtained as a cone or a Berkovich tip and is subsequently milled using the FIB to be a circular flat punch. A larger flat punch is shown in Figure 2.9 and a ~7um in diameter flat punch used in these G200 compression experiments is shown in Figure 2.12. The diameter of the flat punch is first defined through top down milling similar to that required to produce a micro-pillar, and subsequently the tip is mounted on its side so that the tip can be flattened. The ion-beam in the FIB has a Gaussian shape, and as a result milling perfectly edge-on to the flat punch will result in a severely sloped tip. In order to compensate for this, the tip needs to be tilted 2-3 degrees beyond edge-on in order to minimize the slope of the flat-punch. The allowable error in the flat-punch slope depends on the minimum pillar size to be tested. For example in order to test a 250nm-tall pillar to 20% strain in compression, the allowable difference in the tip surface height for repeatable tests can be 50nm. In a 7um tip, this corresponds to a tape angle of 0.4 degrees, a very small variation across the surface.

The SEMentor tip used in compression and tension experiments also is bought as a cone or Berkvoich tip and is milled through the FIB to produce a tip that is capable of both tension in the grips and compression in the flat space. An example of these grips is shown in Figure 2.7. In order to test electroplated pillars, the grips must be milled to be flat in order to match the bottom of the head shape.

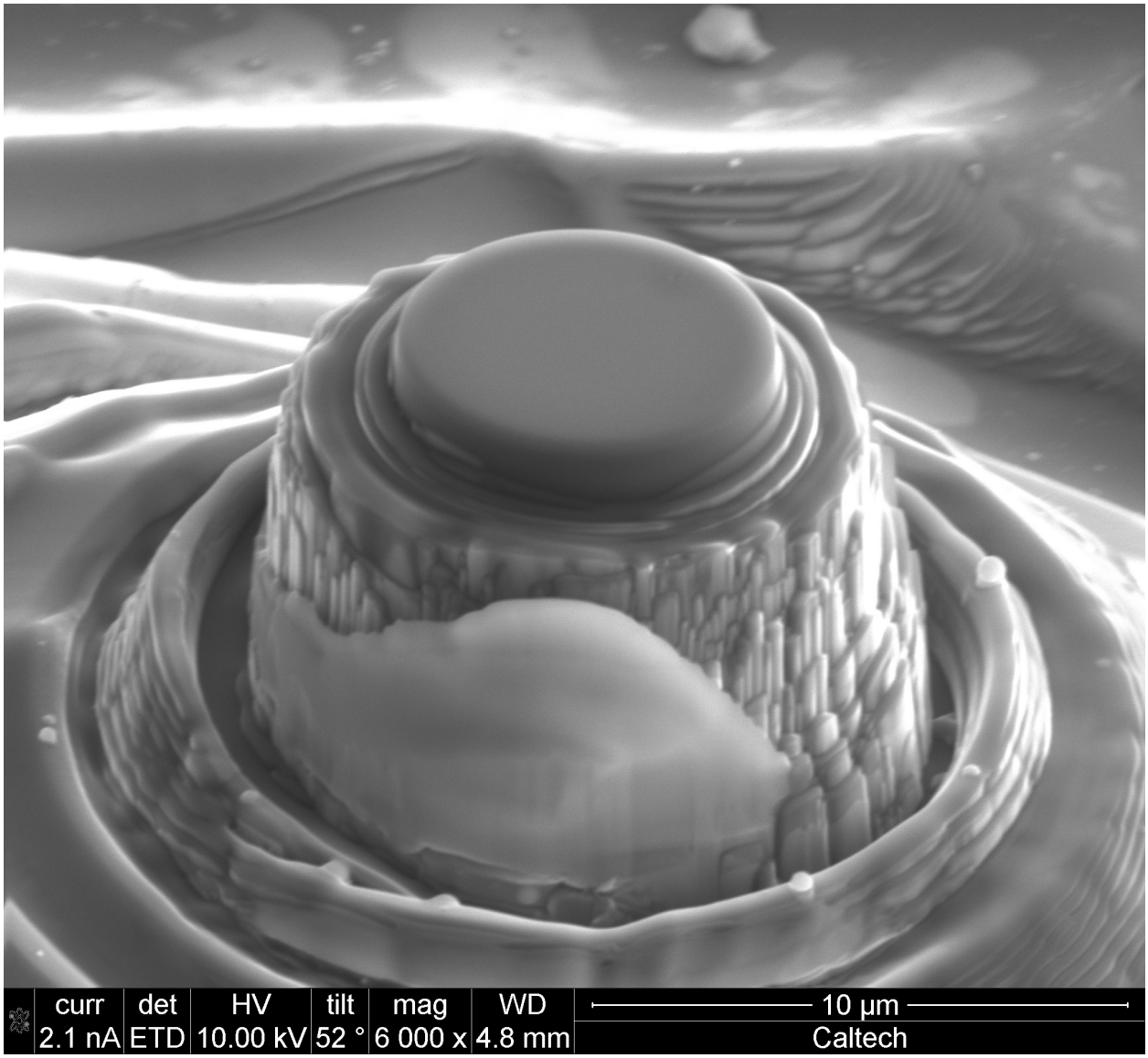

Figure 2.12: 7μm diamond tip used in compression experiments here.

2.5 Data Analysis

2.5.1 Calculation of True Stress – True Strain

The G200 and SEMentor produce both load, P, and displacement, u, as a function of time. In order to generate a detailed understanding of the underlying mechanisms, the data must be converted into stress and strain. In compression, the pillars are near a <111> high symmetry orientation and therefore primarily undergo multiple-slip. The resulting true-stress, true-strain calculations is adapted from Ref. [9]assume that the resulting plastic deformation is homogeneous; i.e., the plastic volume is conserved.

$A_o L_o = A_p L_p$ where A_o is the initial cross-sectional area, L_o is the initial length, A_p is the plastic area, and L_p is original length minus the plastic displacement, u_p, or $L_p = L_o - u_{pl}$.

The measured displacement signal has three components: elastic and plastic deformation of the pillar as well as the elastic indentation of the pillar into the substrate, Sneddon displacement: $u = u_{el} + u_{pl} + u_{Sneddon}$. Here the elastic displacement can be found from Hooke's Law and an assumption of volume conservation. $u_{el} = \frac{1}{E_{<111>}} \frac{P}{A_o L_o} L_p^2$. The sneddon displacement can be found through the solution for the compliance of a cylindrical indenter on a half-space: $u_{Sneddon} = PS_{sneddon}$ where $S_{sneddon} = \frac{\sqrt{\pi}(1-\nu^2)}{2E_{substrate}\sqrt{A_p}}$. The remaining plastic displacement can be found through $u_{pl} = u - (u_{el} + u_{Sneddon})$. Inserting u_{pl} into the definition for L_p yields a complex description of L_p that contains only measured parameters and material constants.

True stress can then be determined through conservation of volume during plastic deformation: $\sigma_{true} = {P}/{A_p} = {PA_oL_o}/{A_p}$. True strain on the pillar is then $\varepsilon_{tot} = \varepsilon_{el} + \varepsilon_{pl} = \frac{1}{E_{<111>}} \frac{P}{A_o L_o} L_p - ln\left(\frac{L_p}{L_o}\right)$. Notice that the total strain subtracts out the displacement of the pillar into the substrate. This displacement can be negligible for low loads and large pillars; however, at higher loads and small pillars the displacement into the surface can become large.

2.5.2 Calculation of Stress and Strain with Hard Coating

In chapter 6, coated pillars are tested in compression in order to understand how the free-surface influences the deformation mechanisms. One consequence of the addition of a coating is a more complicated stress-state inside the pillar. The following, adapted from Ref. [69], discusses the simple models used to evaluate the stress in the copper pillar. In the case where the coating shares load with the copper pillar, we use a simple iso-strain model: $\frac{F}{A_{total}} = \left(A_f + (1 - A_f)\frac{E_{shell}}{E_{pillar}}\right)\sigma_{pillar}$ [73]. Here, F is the applied force, A_{total} is the cross-sectional area of the coated pillar. A_f is the cross-sectional area fraction of the copper pillar or $A_f = {A_{pillar}}/{A_{total}}$, E_{shell} and E_{pillar} are the elastic moduli for the coating and the copper pillar, respectively. This shared load model is most relevant for understanding the stress-state in the copper pillar at small strains, i.e., prior to catastrophic cracking of the coating. On the opposite end of the spectrum, we assume that the coating supports no load, and

therefore the stress in the copper pillar is measured by $\sigma_{pillar} = {}^{F}/_{A_{pillar}}$ where F is still the applied force and $A_{pillar}$is the area of the copper pillar only. This model best estimates the stress-state in the copper pillar after the coating has cracked in multiple locations and is effectively "going along for the ride" as it is not capable of supporting any appreciable elastic stresses.

2.5.3 Influence of Sample Geometry

Adapted from Brinckmann et al. [74]

All of the samples tested here have circular cross-sections; however, comparisons of FIB-fabricated pillars in tension frequently have rectangular cross-sections leading to the following analysis of the influence of the pillar cross-section on the observed stress. We utilize FEM simulations to quantify the elastic stress distribution within the sample to optimize the sample geometry such that the inhomogeneities in stresses and strains within the sample are minimized. The stress concentrations might lead to localized incipient plasticity, and the experiment would not be representative of the general material response at small scales. Flow stresses are often assumed to be homogeneous for nanopillars compressed along high-symmetry crystallographic orientations. However, geometrical constraints at the top and base of the pillar may lead to the elevated local stresses. At the base, the deformation is constrained by the substrate, and friction between the pillar and the flat punch indenter tip restricts the deformation of the pillar top. We use the conventional eight-node linear finite elements (ABAQUS C3D8) and simulate the deformation of square and round cross-sectional samples on a substrate. These elements allow us to quantify the geometrical effects, while allowing for time-efficient simulations. Due to the fourfold rotational symmetry in the sample geometry, it is sufficient to model a quarter of the pillar/substrate combination with 10 three-dimensional elements in the radial direction and 30 in the axial. We assume linear isotropic elasticity to evaluate the overall stress state at 10% strain. Isotropic properties of Au are represented by Young's modulus 79 GPa and Poisson's ratio 0.42. Since the constraint at the pillar top cannot be determined unambiguously, we do not include it in the model. However, the findings due to the constraint pillar base can used to infer a qualitative understanding of the constraints at the pillar top. Figure 2.13 shows the von Mises yield stress distribution inside the pillars of the two described geometries, which is the most appropriate criterion for the incipient yield position in the continuum framework. While the stresses in the two geometries are nearly identical in the plane of symmetry, we find that the maximum axial stress in the circular

column is 1.14 GPa, while that in the square one is 1.80 GPa and is localized in the corner of the square sample decaying away from it. We find that the substrate constraint leads to the formation of higher local stresses in the square-shaped sample, even though the average applied stress is the same. Assuming that the yield is governed by the nucleation of dislocations from the region where the stress state exceeds that of the von Mises yield criterion, this inhomogeneous elastic stress distribution leads to an inhomogeneous dislocation nucleation from the areas of elevated shear stresses, assuming that the dislocation sources are homogenously distributed and require equal activation energy. The post yield stress-strain behavior of the nanopillars consists of multiple discrete slip events indicative of dislocation avalanche propagation, rendering the continuum theory inapplicable to describe this behavior. To model plasticity in these nanoscale volumes with free surfaces, powerful 3-D mesoscopic simulations, such as discrete dislocation simulations [75-80] as well as molecular dynamic simulations [81], are better suited to investigate the post yield behavior of nanopillars.

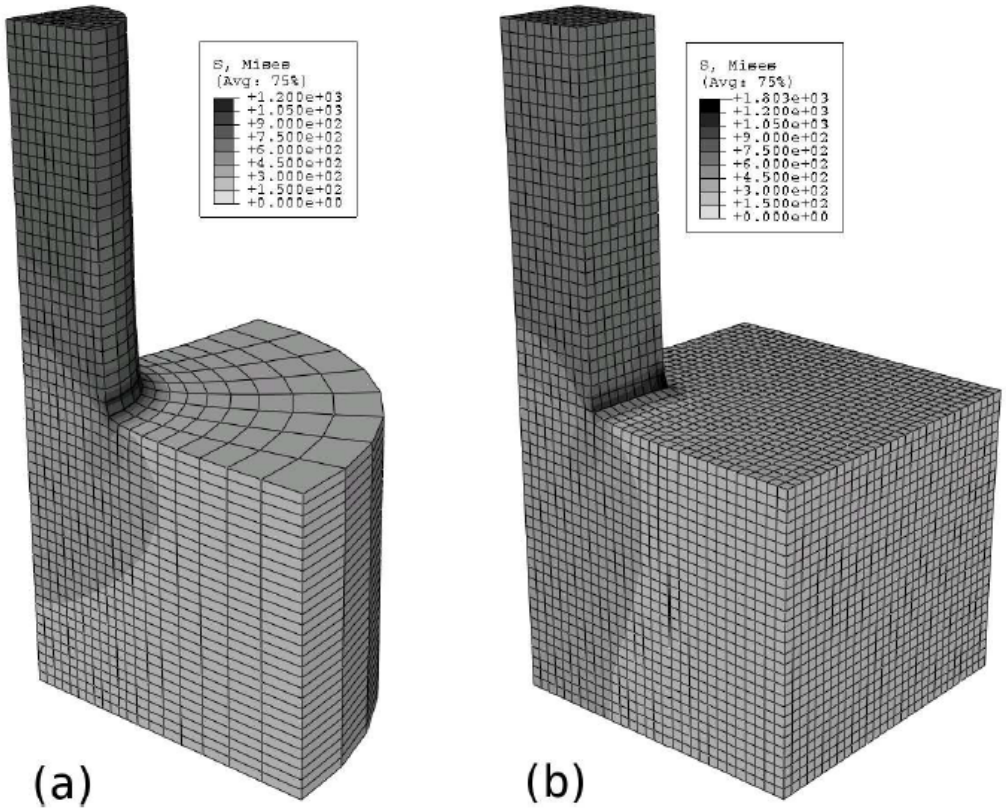

Figure 2.13 Von Mises equivalent stress in MPa at 10% strain determined by finite element method for (a) circular and (b) rectangular cross-sectional samples on substrate due to tension

Chapter 3: Mechanical Properties of FIB-Less Single Crystalline Cu Nanopillars

As introduced in Chapter 1, uniaxial compression and tension tests on FIB-fabricated micron- and sub-micron single crystals demonstrate a size-dependent, sub-theoretical strength. On the other hand, identical tests on similarly sized single crystals produced in non-FIB techniques show theoretical strengths suggesting that the FIB may determine the observed size-dependent strength behavior. In this chapter, adapted from [82], the results of uniaxial compression experiments on FIB-less electroplated single crystalline nano-pillars are shown to have an identical size-effect as FIB-fabricated pillars demonstrating that the FIB-fabrication procedure does not govern the size-effect.

TEM analysis shows that these electroplated pillars contain similar dislocation densities as FIB-fabricated pillars, while other non-FIB-fabricated pillars have near-zero dislocations suggesting that the defect microstructure as opposed to the fabrication technique controls the presence of the size effect. Furthermore, the post-deformation dislocation structure is shown to have Burgers vector in the (111)-plane with no resolved shear stress providing evidence for dislocation starvation; whereby mobile dislocations rapidly escape the pillar.

3.1 Introduction

To date, one of the most common techniques for assessing mechanical properties of materials at the micron and sub-micron scales without imposing strong strain gradients is uniaxial deformation of micro- and nano-pillars [3-5, 9, 11, 12, 16, 17, 20, 23, 25, 28, 32, 34-36, 59, 60, 67, 83-87]. The most prevalent method to fabricate pillars is by focused ion beam (FIB) [3-5, 8, 9, 12, 17, 19, 23, 28, 32, 34-36, 83-88]. Remarkably, at these length scales, face-centered cubic (fcc) metallic nano-pillars exhibit a strong size-dependent strengthening: as the pillar diameter becomes smaller, its flow stress increases as a power law: $\sigma \propto D^{-n}$ where D is the pillar diameter, and n lies between 0.5 and 1.0 [3-5, 9, 19, 20, 23, 36, 67, 83]. Few alternate fabrication techniques, which do not rely on FIB, have also been used to produce nano and micron sized samples. Interestingly, these samples show yield stresses near theoretical strength with limited size effects, contrary to pillars produced by FIB [2, 57, 59]. Attainment of such high strengths has been attributed to the pristine initial microstructure in these pillars, i.e., no initial dislocations [57]. In contrast to any FIB-less technique, Ga^+ ion bombardment inevitably associated with FIB fabrication can introduce surface dislocation loops and precipitates, as

well as instigate surface amorphization [18, 84]. The presence of FIB-induced defects may have led several researchers to deduce that FIB-based fabrication methods may significantly contribute to strengthening. However, studies by Bei et al. [84] and by Lee et al. [20] showed that FIB machining of pristine or annealed Mo and Au pillars, in fact, reduces rather than increases their strengths to those significantly below the theoretical limit. Of note is recent work by Buzzi et al. [89] on embossed rather than FIB-machined sub-micron Ag pillars. While these authors also report a size effect, these Ag pillars are found to also deform through mechanical twinning, resulting in a more complex deformation mechanism than in other previously studied fcc micro-pillars.

All of these studies clearly underline the importance of initial microstructure and its effect on the presence or absence of size effects. So far, FIB-less fabrication methods have only been able to produce features without dislocations, thereby rendering theoretical strengths, regardless of size, not surprising. Pillars fabricated by FIB, in contrast, contain as many as 10^{13} dislocations per m^2 [24]. Therefore, in order to understand what drives the size effect, it is imperative to mechanically test pillars produced via FIB-less fabrication methods yet with non-zero dislocation densities.

Recently, Burek et al. developed a FIB-less method to produce single crystalline Cu nano-pillars by electroplating Cu into an array of electron beam patterned holes in a PMMA matrix [90]. Thin films of electroplated copper have been reported to contain trace amounts (.005% by weight) of carbon from the plating process [91]. Since these contamination are very small, if at all present, we believe that their effect on the attained nano-pillar strengths is likely negligible. In this report, we show the results of uniaxial compression experiments performed on these ~<111> oriented, FIB-less Cu nanopillars with diameters between 100nm and 500nm, with non-zero initial dislocation densities.

3.2 Experimental

3.2.1 Crystal Structure Determination

We determine the pillar microstructure by performing site-specific TEM analysis on individual representative pillars, lifted out of the matrix and transferred onto TEM grids by using Omniprobe (Autoprobe 200, Omni Probe). Details of this procedure can be found in Ref [92] and Chapter 2. Figure 3.1a shows bright field TEM image of a 100nm pillar, with inset corresponding to diffraction pattern at a [211] zone axis, which remained unaffected as the selected area diffraction aperture was moved along the pillar height, thereby demonstrating its single crystalline nature. Analysis of the diffraction patterns' orientation with respect to pillar axes shows that the loading axis is ~ <111>. For

example, the pillar in Fig. 1*A* is oriented in ~$[8\bar{7}\bar{9}]$ direction, 6° from $[1\,\bar{1}\,\bar{1}]$. This initial offset from the high-symmetry <111> orientation causes rotation of the slip planes away from double slip condition (Fig. 3.1b), consistent with our observations that the slightly misaligned pillars deform by single slip. Those samples oriented perfectly along high-symmetry <111> direction deform along multiple slip planes (Fig. 3.2b).

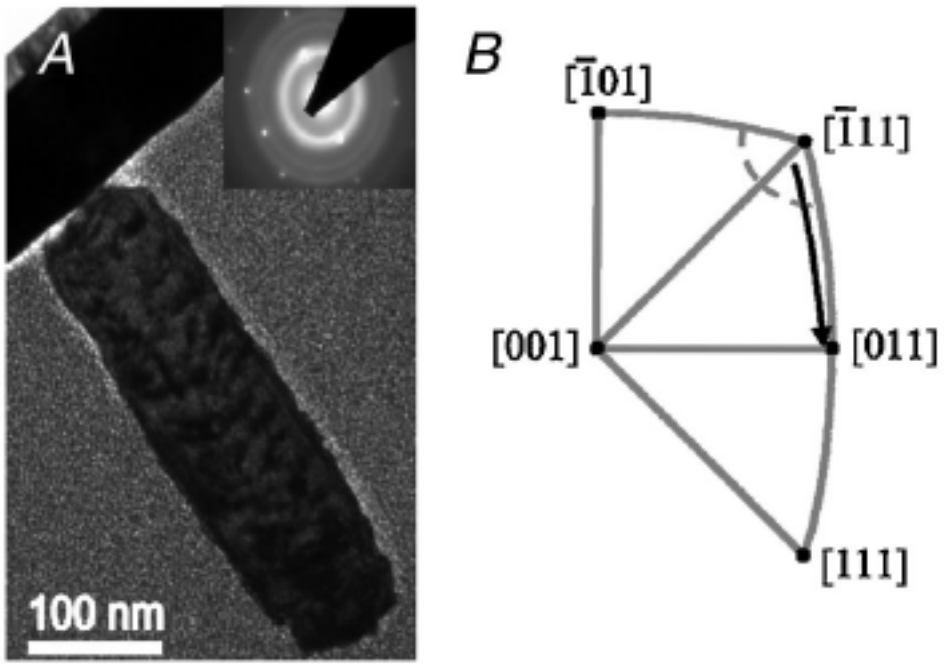

Figure 3.1 (a) Bright-field TEM image of ~100nm diameter single-crystalline copper pillar. Inset diffraction pattern shows [211] zone axis. The rings in the diffraction pattern are from the partially nanocrystalline Pt deposition. (b) Stereographic triangle of [001] pole. Dashed line represents 10^o locus, the maximum deviation from [111] loading axis. Arrow represents rotation of slip planes in compression away from loading axis.

3.2.2 Mechanical Testing

Pillars with diameters above 250nm were compressed with a custom-made flat punch tip in Agilent G200 Nanoindenter. Pillars smaller than 250nm were compressed in SEMentor, a custom-built in-situ mechanical deformation instrument [36]. All compression tests were carried out at a nominally constant displacement rate of 2 nm/s with simultaneous contact stiffness measurements via Continuous Stiffness Measurement (CSM) option. Load-displacement data were converted into stress-strain by methodology outlined in Ref [9] and also found in Chapter 2. Stiffness data was used to filter out tests that deviated from uniaxial behavior. Pillars were fabricated with aspect ratios of ~3:1 to 6:1 in order to avoid any constraint hardening from the compression platens and to prevent buckling. A

typical as-fabricated pillar morphology is provided in Fig. 3.2a and shows some surface roughness as well as the slightly imperfect pillar-substrate interface. Fig. 3.2b shows the same pillar after compression. Slip trace analysis shows that multiple slip systems were activated throughout the pillar volume indicating its likely <111> orientation with respect to the loading direction.

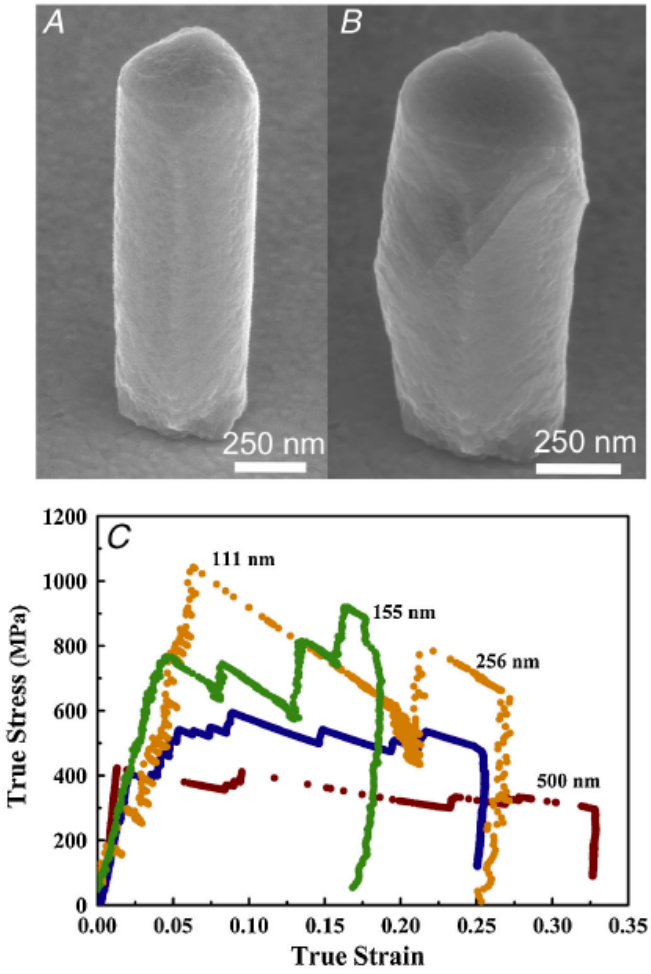

Figure 3.2 SEM images of a ~500nm diameter copper pillar (a) before and (b) after compression. Multiple symmetric slip lines can be seen in (b) corresponding to compression along <111> loading axis. (c) Representative true stress vs. strain curves. Numbers above each curve corresponds to pillar diameter. The plot clearly shows an increase in strength as a function of decreasing pillar diameter.

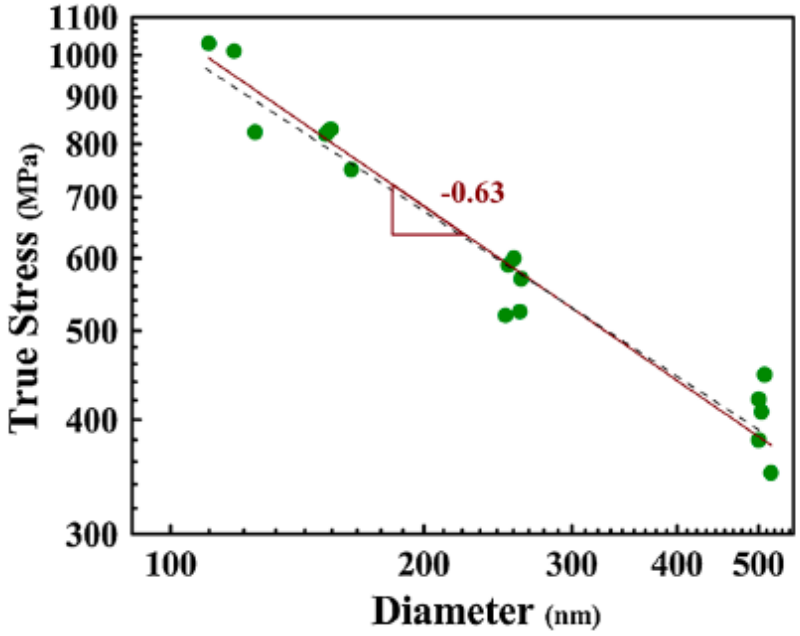

Figure 3.3 Log-log plot of characteristic stresses plotted as a function of pillar diameter. The data show a clear power-law trend (shown by dashed line) with n = -0.63, nearly identical to the trend demonstrated in FCC metals represented by the solid line.

3.3 Mechanical Properties

3.3.1 Stress-Strain Behavior and Size-Dependent Strength

Representative compressive true stress – strain curves corresponding to the deformation of pillars of four different nominal diameters are shown in Fig. 3.2c. Each curve is characterized by nearly elastic initial loading followed by intermittent, discrete strain bursts. At the end of each strain burst, the pillar undergoes a short, nearly elastic loading until the stress is large enough to induce a new strain burst. This sporadic signature has been ubiquitously observed in the deformation of all nano- and micro-scale pillars and is generally attributed to the highly stochastic nature of dislocation avalanches, and therefore, prevalent in source-controlled plasticity [3-5, 9, 10, 12, 17, 23, 25, 27, 28, 32, 34-36, 60, 67, 83, 84, 93, 94]. Importantly, these electroplated pillars share the same flow behavior as those produced by FIB, clearly demonstrating that the same deformation mechanisms likely govern flow behavior of nano-scale samples regardless of fabrication methods. This characteristic of nanoscale flow behavior has been found to share the same statistics of a number of avalanche type behavior such as earthquakes. This analysis can be found in Appendix B. Furthermore, true stress-strain plots in Fig. 3.2c show an unambiguous size effect: smaller pillars attain higher stresses compared to larger ones.

The difference in initial loading slopes between the two smallest and two largest pillars is attributed to the different stiffnesses of the testing equipment (G200 vs. SEMentor). In order to quantify the size-dependent strength, flow stresses at 10% strain of all compression tests plotted against pillar diameter on log-log scale are shown in Fig. 3.3. The compressive strengths of our nano-pillars follow a power-law dependence with the slope of $-0.63 \pm .036$ (s. d.), a result strikingly similar to -0.6, a value widely reported for various FCC metallic FIB-fabricated pillars [67]. These results convincingly eliminate several of the previously conjectured main sources of size-dependent strength in FIB-fabricated nano-scale crystals, namely precipitate strengthening [18, 95] and surface amorphization resulting in dislocation pile-ups and back stresses. Furthermore, the smallest Cu pillars with 100nm diameters tested in this study reach only ~15% of theoretical strength [96], a value significantly lower than that of other FIB-lessly fabricated pillars with zero initial dislocation densities [2, 57, 59], implying that our nano-pillars contain initial mobile dislocations.

Comparing our results on electroplated Cu pillars to those reported for FIB-fabricated Cu samples, two key differences are apparent: our pillars attain lower flow stresses and negligible hardening relative to data in [11, 17, 19]. The authors of Reference [17] demonstrate that both hardening and very high flow stresses attained by their pillars are due in part to the very stiff lateral support of their indenter system [11, 12, 17]. Furthermore, the low pillar aspect ratios used in their study led to the creation of dislocation pile-ups against the wider gripping supports during testing causing additional hardening [16]. Rather, our compression results are consistent with the high aspect ratio tensile results reported by Kiener et al. [12], as the longer sample geometry results in lowering the effective lateral stiffness of the entire system and thereby removing hardening effects due to dislocation pile-ups [11, 12, 17]. Also, the -0.63 slope reported here is larger than that reported by Kiener et al., -0.47, also likely due to previously mentioned differences in lateral stiffness constraints.

3.4 Dislocation Density Determination

3.4.1 Electroplated Vs. FIB

In order to determine the initial dislocation density of our electroplated pillars, we performed site-specific weak-beam dark-field (WBDF) TEM analysis in FEI Tecnai TF20 (200keV). Samples were prepared in FIB by standard lift-out procedures utilizing Omniprobe (details can be found in Ref. [92] and Chapter 2. Importantly, during thinning of the copper samples, only a negligible amount (if at all) of ion damage was introduced since the protective platinum layer remained on their surface. Figs. 3.4a

and b show WBDF images of an uncompressed Cu pillar, and the use of two depicted different diffraction conditions ensures we capture all dislocations within the pillar excluding only those with [110] Burgers vector. It is reasonable to expect that in Cu full lattice dislocations would dissociate into <121>-type partials with a corresponding stacking fault between them; therefore, all dislocations within the pillar should be visible in at least one of the two WBDF images. The estimated total dislocation line length in the boxed region is 317 nm, as shown in Fig. 3.4c. In order to compare this initial dislocation density to that of a FIB-machined pillar, Fig. 3.4d shows energy-filtered bright field TEM images of a typical Au pillar produced in our lab, thinned down to electron transparency with a very low accelerating voltage of 1kV (FEI Hilsboro, OR). Unfortunately, this pillar was bent at the substrate interface in the process of thinning making WBDF, and therefore, Burgers vector analysis, unattainable. Dislocation densities were evaluated by dividing the total dislocation line length (Fig. 3.4c,e) by the volume in which they are contained. We find the initial dislocation density in our Cu nano-pillars to be 1.5×10^{14} m^{-2}, i.e. the same order of magnitude as FIB-prepared Au nano-pillars, $\rho = 3 \times 10^{14}$ m^{-2}. It is important to recognize that these represent an estimate of dislocation density rather than its exact value, as the dislocation length parallel to incident beam is not discernible, the precise distinction between pinned and mobile dislocations for the Au pillar is unavailable, and unambiguous identification of dislocation-based contrast features is challenging. While in bulk, a dislocation density of $10^{14}\ m^{-2}$ corresponds to a heavily cold-worked metal [65], the minimum attainable non-zero dislocation density in these small pillar volumes is $10^{14}\ m^{-2}$, equivalent to the existence of a single 7-atom loop in the entire pillar. A single dislocation line subtending the pillar diameter, for example, would increase the dislocation density by two orders of magnitude, i.e., corresponding to the value reported here.

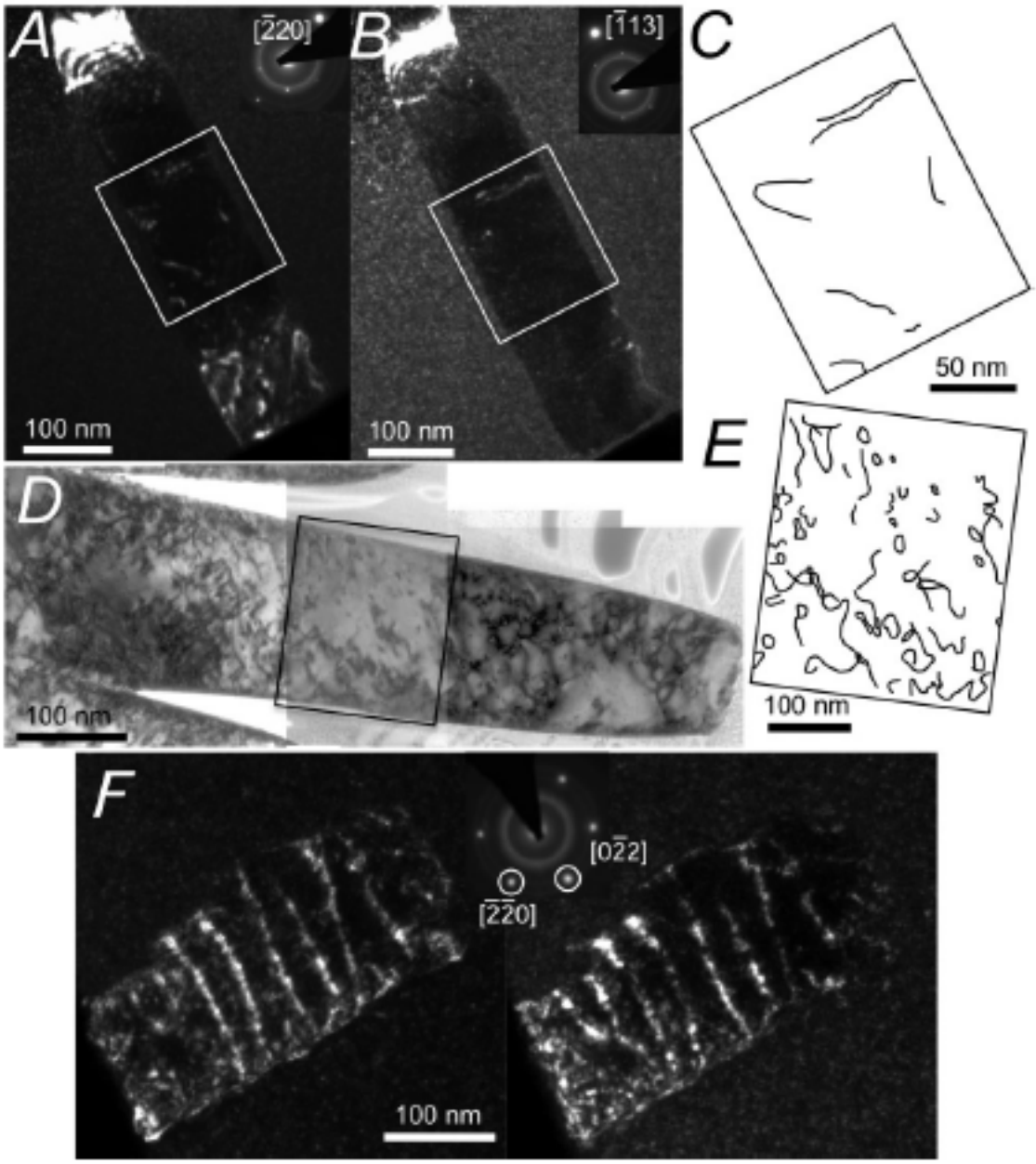

Figure 3.4 WBDF images of ~120nm copper pillar. A layer of platinum was left covering the pillar such that the pillar did not endure any ion damage. Regions for dislocation density measurements are shown as the middle region where the deformation is expected to be homogeneous. (C) A zoomed-in rendition of the boxed region with outlined dislocation lines. (D) Bright-field energy filtered TEM image of a 400 nm gold pillar fabricated with the FIB at 30kV. This pillar was thinned down in successive steps to 1kV (FEI Hillsboro, OR). (E) Enhanced view of dislocation density in the boxed region. (F) Dark-field images of a compressed pillar illustrating that all of the remaining dislocations lie in the {111} plane with no resolved shear stress.

3.4.2 Post-Deformation TEM Dislocation Starvation

Figure 3.4f shows two dark-field images of a compressed pillar, and remarkably, demonstrates that all remaining dislocations lie in {111} planes, which experience no resolved force during deformation, suggesting dislocation starvation as dominant deformation mechanism [8]. Several atomistic and statistical simulations have corroborated this phenomenon in their explanations of size-dependent strengthening [26, 75, 93, 97-99]. A recent review of these and other models can be found in Ref [67].

3.5 Summary

In summary, our results demonstrate that 100nm-500nm-diameter single crystalline Cu nano-pillars created without the use of Ga^+ and containing several initial dislocations exhibit an identical size effect to the ones fabricated by FIB. This size effect manifests itself as "smaller is stronger" in a power law fashion with exponent of ~-0.6, consistent with most values reported to date for different FCC metals. This finding convincingly shows that plasticity at the sub-micron scale is truly a function of microstructure, which in turn defines size effect. At small scales, if the structure is initially pristine, i.e. without any dislocations, the material will yield and deform at close-to-theoretical strengths, revealing no size effects. However, nano-scale crystals with non-zero initial dislocation densities display a remarkable dependence on size, as conveyed by many computational and experimental reports to date, and, as demonstrated here, independently of fabrication technique.

Chapter 4: Tensile Deformation of Electroplated Copper Nano-Pillars

Chapter 3 shows that single crystalline, electroplated copper nanopillars have a size-dependent strength similar to that observed in FIB-fabricated pillars. The mechanical data along with pre-deformation TEM observations of non-zero dislocation density in these pillars clearly demonstrate that the microstructure as opposed to the FIB is responsible for the size-dependent strength in micro- and nano-pillars. In this chapter, adapted from Ref. [100], we perform tensile tests on similar electroplated pillars and show an analogous size-dependent strength in the tensile pillars' ultimate tensile strength, UTS. In tension, the deformation behavior is characterized by limited plasticity followed by a single catastrophic burst during which the pillar either necks or deforms through single slip. The initial large necking event demonstrates that the pillar is unable to strain harden sufficiently to compensate for the reduction in area suggesting a dislocation-starvation type mechanism.

4.1 Introduction

Early work studying the mechanical properties of materials at reduced dimensions has focused on the compression of cylindrical, micro- and nano-pillars fabricated by the focused ion beam (FIB) [3-5, 8-12, 17, 19, 20, 23, 27, 28, 32, 34-36, 40, 67, 83, 85, 87, 101]. A key advantage of this technique over other small-scale testing methodologies is the removal of strong strain gradients during mechanical testing. These compression experiments have been primarily focused on pillars with diameters ranging from ~250 nm up to several microns [3-5, 8, 9, 11, 16, 17, 19, 20, 23, 28, 32, 34-36, 40, 67, 83]. Reports of nano- and micro-scale tensile experiments, however, are significantly scarcer as they require custom-made instrumentation designed specifically for this purpose [12, 25, 35, 36, 101]. Similar to the compression experiments, the majority of the existing tensile experiments have also been performed on samples machined from bulk single crystals through the use of FIB. Significantly, all FIB-fabricated face-centered cubic (fcc) metallic pillars exhibit nearly identical size dependent power-law strengthening with size in both compression and tension, the physical origin of which is still being actively pursued and discussed. As shown in Chapter 3, single crystalline electroplated Cu pillars, which have never been exposed to FIB, obey the same power-law increase in strength with decreasing size as FIB-manufactured fcc pillars, and that this size dependence is a direct result of initial dislocation

density and microstructure [102]. In this work, we present the results of tensile tests on 75-165nm diameter single crystalline Cu samples with non-zero initial dislocation densities, fabricated by e-beam patterning followed by electroplating [68], a process nearly identical to the one used to create the compressive specimens in Chapter 3. Through *in situ* mechanical tests, we correlate physical deformation phenomena with the uniaxial stress-strain response. TEM analysis of pillar microstructure reveals the occasional twin boundary in some pillars. We comment on the geometry of the twin boundaries as well as the complexities of dislocation - twin boundary interactions.

4.2 Experimental

4.2.1 Sample Preparation

Tensile samples were fabricated by electroplating copper into the electron beam patterned holes in a PMMA (poly methyl methacrylate) matrix with intentional overplating to enable subsequent gripping of the pillar tops. Specific details of this fabrication method can be found in Chapter 2 and Ref [28]. Unfortunately, these samples do not adhere well to the evaporated seed Au film on the Si substrate, and initial tests on these as-fabricated nano-pillars resulted in the pillars' fully detaching from the substrate at minute loads. Therefore, in order to perform successful tension tests, we effectively glued the pillar bottoms to the underlying film by using a focused electron (rather than ion) beam with a tungsten hexacarbonyl, $W(CO)_6$, source (FEI Nova 200) to locally deposit a thin layer of organometallic tungsten at the pillar-substrate interface, similar to the procedure described by Richter et al. [2]. Transmission electron microscope (TEM) images of this e-beam deposited W confirm this coating to be amorphous, as evidenced by the diffuse rings in the diffraction pattern in Figure 4.7, suggesting its deformation mode to be of brittle character, without exhibiting any appreciable plasticity prior to fracture. Therefore, the presence of the W-glue is not expected to influence the deformation behavior or accompanying stress-strain response.

Figure 4.1a shows a scanning electron microscope (SEM) image of an as-fabricated 150nm Cu pillar with nearly perfectly vertical sidewalls. As a result of tungsten deposition (Figure 4.1b), the bottom ~600 nm of the pillar becomes non-uniformly wider than its initial diameter due to this coating. In order to deposit the W, rectangular electron beam patterns (1

micron x 100nm) were defined at 52° tilt in the SEM. The top of the rectangle was positioned several hundred nanometers away from the pillar base, and the deposition was performed at .54 nA and 10kV in a FEI Nova 200. This procedure was then repeated on the opposite pillar side to ensure adequate adhesion.

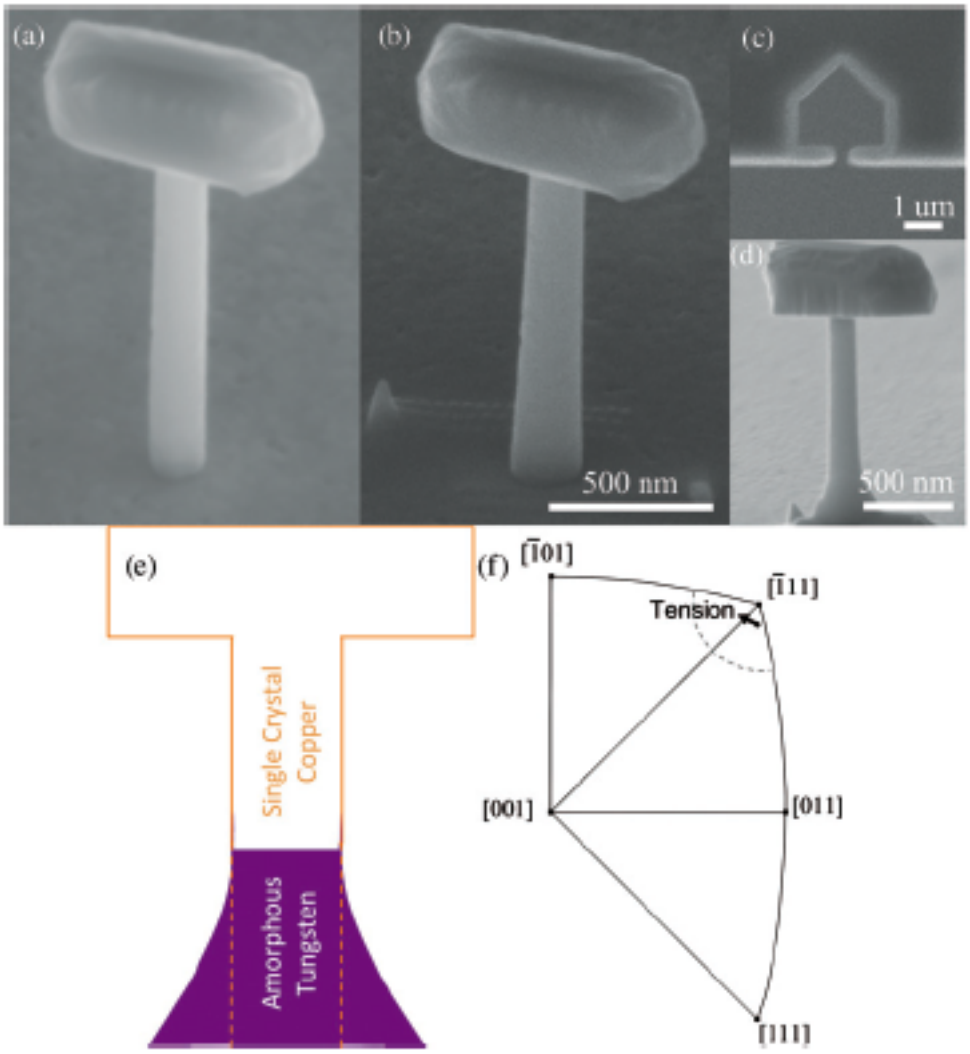

Figure 4.1 SEM images of an initially untapered 150nm tensile pillar before (a) and after (b) electron beam tungsten deposition showing the development of some taper at the pillar-substrate interface (images taken at 52° tilt). (c) custom fabricated diamond tensile grips to accommodate the 90 degree angle of the overplated region shown in (d). (e) A schematic of a tensile sample with the W glue. (f) stereographic projection of the standard face-centered cubic triangle. Arrow represents rotation of slip planes towards a double-slip condition under uniaxial tension.

4.2.2 Mechanical Testing

Tensile tests were performed in the SEMentor, an *in situ* mechanical deformation instrument comprised of SEM and the Dynamic Contact Module (DCM) nanoindenter arm (Agilent Corp.) [36]. While the nanoindenter is an intrinsically load controlled instrument, all of our experiments were performed at a nominally constant displacement rate through a custom-written, feedback loop based software method. In this work, both tension and compression tests were performed at nominal displacement rates of 1-2 nm/s. The diamond indenter tip was custom machined by FIB such that the tops of the copper pillars can be conformally gripped during tensile testing (Figure 4.1c). Figure 4.1d shows a glued pillar in the SEMentor prior to testing, exemplifying the presence of W coating towards the pillar bottom and an unaffected top part of the pillar reflecting no added W in this region. A schematic of the tungsten glue geometry is shown in Figure 4.1e.

In order to evaluate whether the presence of W layer contributes to the measured tensile strength, we also performed compression tests on electroplated Cu pillars with and without the glue. The as-fabricated compressive pillars had aspect ratios between 3:1 and 6:1 while that for the glued pillars was closer to 3:1 after ~600nm of length was subtracted from the overall height since plastic deformation occurred only in the non-coated section of the pillar. Contact stiffness was monitored throughout the experiments by utilizing a Continuous Stiffness Measurement (CSM) option with the harmonic displacement amplitude of 1 nm at 75Hz oscillation frequency in order to validate the quality of compression tests. Only those pillars whose contact stiffness matched theoretical prediction were included in the analysis. Recently it has been shown that dynamic vs. static loading can have an effect on deformation during nanoindentation tests [103], however we believe that this effect is marginal in these tensile experiments since the data under both conditions looks nearly identical. Samples for TEM microstructural analysis were prepared by the now-standard lift-out procedures [92].

4.3 Results

4.3.1 Deformation Behavior and Necking

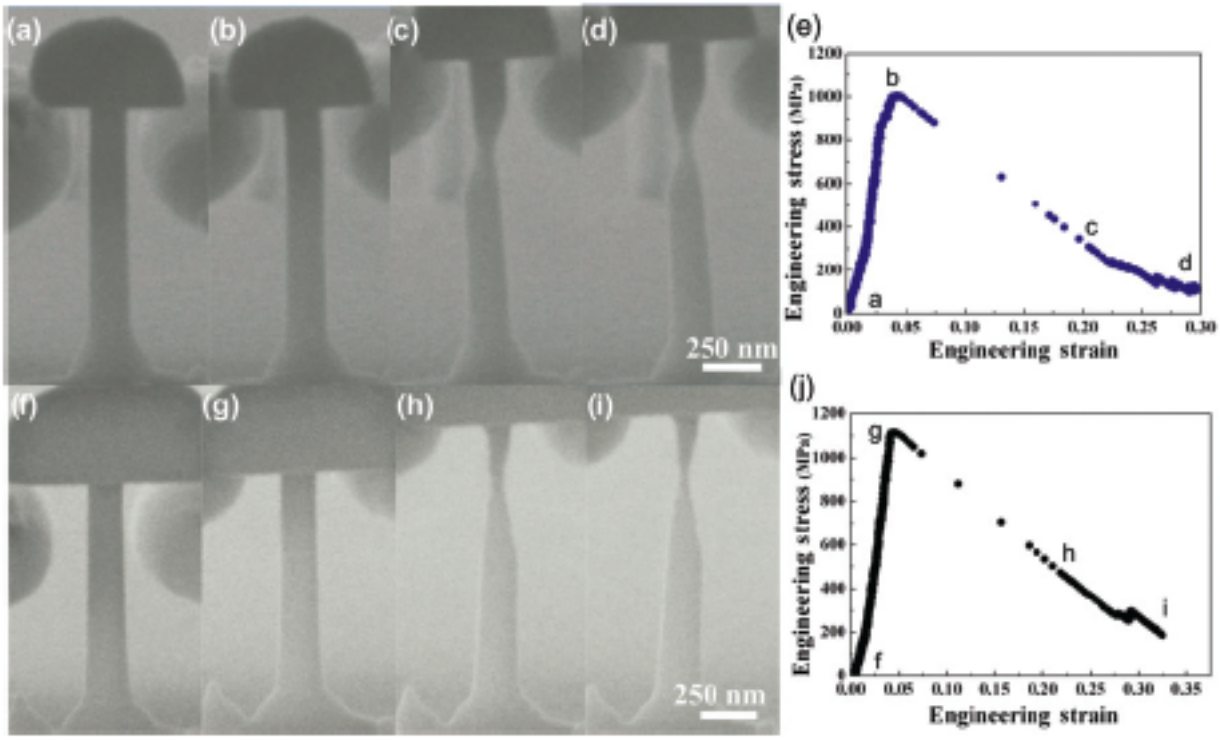

Figure 4.2 Progressive snapshots and engineering stress-strain curves of two nano-pillars during tensile experiments deforming via different mechanisms: single slip (a-e) and necking (f-j). (a) 155nm pillar prior to loading with W deposited at the bottom, (b) the pillar immediately prior to slip, (c) the extent of deformation after the major burst, and (d) final extent of the plasticity. The annotated tensile curve, (e), correlates each snapshot with its corresponding location in the stress-strain response. (f-j) A similar strain series is for a 164nm pillar that deforms by nearly instantaneous necking. Noticeably, most of the plastic strain is accommodated by one major burst; subsequent strain of the deformed region is relatively small. These 150nm pillars exhibit ~30% engineering strain. The true strain in the neck of both of these pillars is ~250%.

Single crystalline copper nano-pillars fabricated by the procedure described above are oriented such that their loading axis is close-to-<111> orientation [68]. The locus of close-to-<111> orientations produced by this process is shown in the conventional stereographic triangle (Figure 4.1f) and illustrates that in tension, the slip planes will rotate towards the double slip condition [104]. As a result, the deformation path for these pillars is mixed: some pillars fail by double slip and necking; whereas others undergo single slip before necking. Figure 4.2 shows progressive series of SEM images for uniaxial tension of two ~150nm diameter representative nano-pillars deforming via different mechanisms: single slip followed by necking (Fig. 4.2a-d) and by necking only (Fig. 4.2f-j). Their corresponding, annotated stress-strain curves are shown in Figure 4.2e,j. Figure 4.2c shows the

pillar initially forming single-slip offsets; however, after the initial single-slip burst, these slip planes rotate towards the loading axes such that multiple slip is activated, as evidenced by the formation of a very thin, on the order of 35nm, neck (Figure 4.2d). On the contrary, a 164nm pillar undergoes minimal homogeneous extension, as evidenced by the instantaneous vertical displacement of the pillar head in favor of forming a neck, quickly reaching its final extension of 33% (Fig. 4.2e-i). We estimate true strain in the neck to be between 236% and 296% by utilizing the reduced area $\varepsilon_T = \ln\left(\frac{A_o}{A_i}\right)$. This somewhat large range for strain is a result of ambiguity in the neck diameter determination due to limited SEM image resolution at the working distance suitable for the mechanical experiments. Nevertheless, this localized deformation is very large and not surprising, as single crystalline pillars oriented for double slip have been shown to draw down to a point in the necked region resulting in very high local strains [36, 73].

Figure 4.3 shows the pre- and post-deformation images of an 80 nm tension sample, as well as its engineering stress-strain curve. As with the larger pillar shown in Figure 4.2e-h, this 80nm pillar necks instantaneously. During the initial loading up to ~1% strain, the pillar "head" slightly tilts to conform to the grips due to their less-than-perfect initial contact. The remaining loading segment reflects nearly elastic response of the whole pillar. At 2.5% engineering strain there is a small amount of plastic deformation followed by further loading until reaching the UTS at 1730 MPa, where the top-most region of the pillar instantaneously necks. Immediately after this neck formation, the pillar was unloaded in order to preserve the neck region for subsequent visual analysis, as shown in the inset of Figure 4.3b.

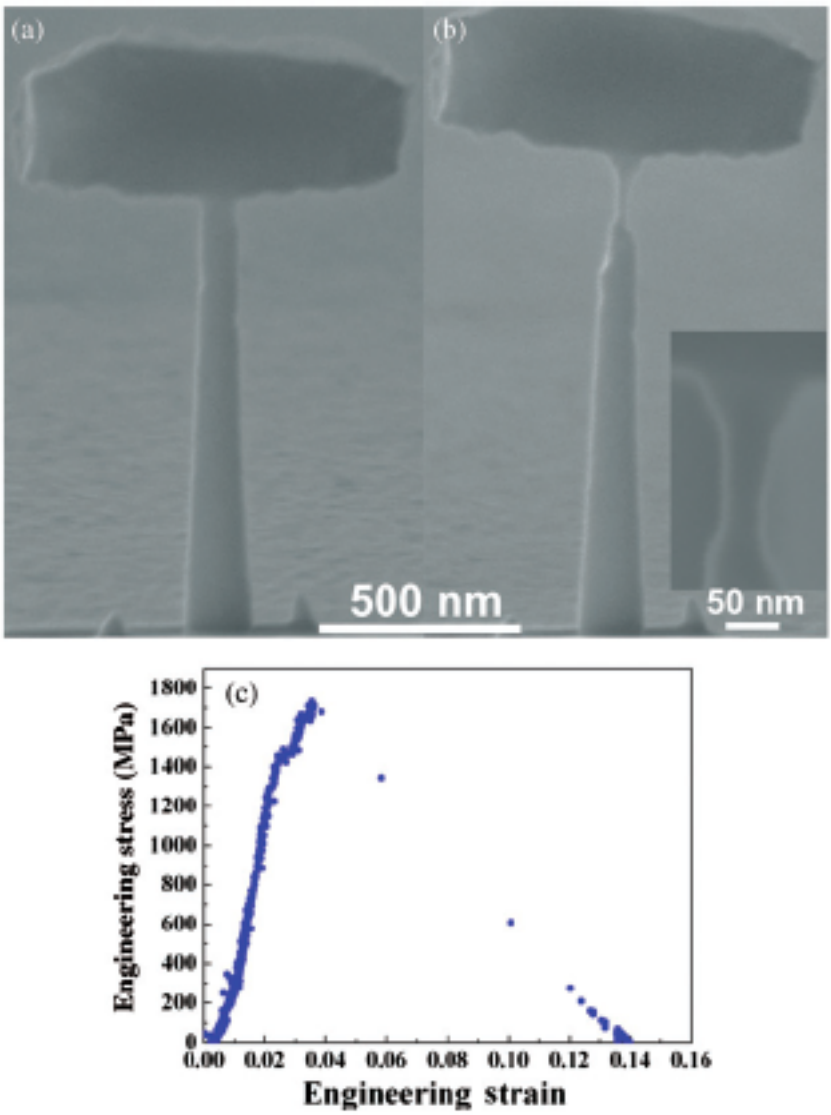

Figure 4.3 (a) Pre- and (b) post-deformation SEM images of a 80nm pillar (diameter measured in the top section as representing the site for subsequent neck formation). Inset in (b) shows a zoomed-in region of the neck. (c) Engineering stress-strain curve showing that the pillar reaches ultimate tensile strength (UTS) at ~1.7 GPa and then rapidly forms a neck, as evidenced by a pronounced strain burst

4.3.2 Stress-Strain Response

Figure 4 shows engineering stress-strain plots for different initial pillar diameters. Each curve shares many similarities: after the initial loading segment, very limited homogeneous deformation takes place prior to reaching the ultimate tensile strength (UTS), followed by a single large burst. This burst corresponds either to the nearly instantaneous necking or to the initial single slip followed by slip plane rotation into a necking condition. Unlike larger pillars (Figure 4.2), which show extended deformation

after the initial burst, during which the neck is further thinned, pillars with diameters of ~100 nm and smaller do not plastically deform after the initial burst (Figure 4.3). Instead, the initial strain burst represents the full extent of plastic deformation, with any subsequent increase in applied load resulting in immediate fracture in the neck.

4.3.3 Size-Dependent Strength

The stress-strain curves in Figure 4.4 clearly show the presence of a size effect, where pillars with the smaller diameters yield at the higher UTS. To examine the size effect, we have plotted the tensile and compressive data from this work on a log-log graph in Figure 4.5. Here, the tension samples are marked by closed circles; whereas, compression pillars are open squares and triangles. The stresses for both types of deformation appear to obey a single power-law dependence with the exponent of -0.63, a value nearly identical to the previously reported one for electroplated copper pillars in compression only [102] and for all other FIB-machined fcc metals to date [67]. This plot also shows that there is no tension-compression asymmetry in the range of diameters tested (75 nm to 165nm): both compression and tension samples of the same diameter appear to deform at similar stresses, as expected for fcc metals.

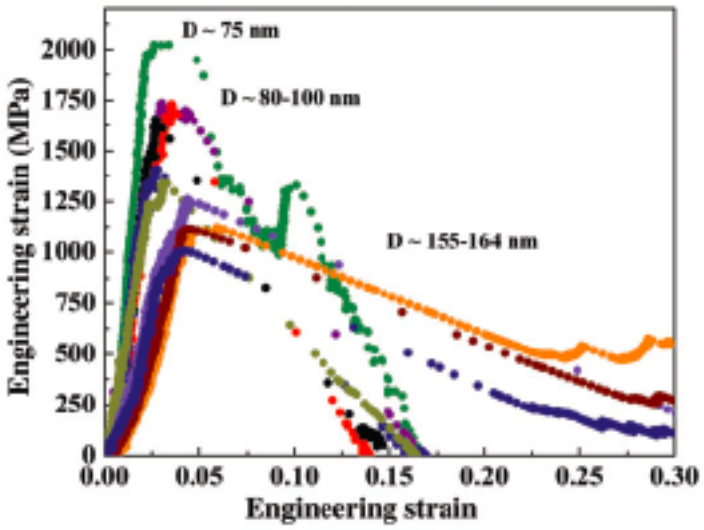

Figure 4.4 Tensile engineering stress-strain curves for all pillars tested in this work. The initial loading slopes are not perfectly overlaid most likely due to an imperfect initial contact between the sample "heads" and the grips. Smaller-diameter pillars reach larger stresses at equivalent strains compared with the larger pillars, which also have extended flow after necking.

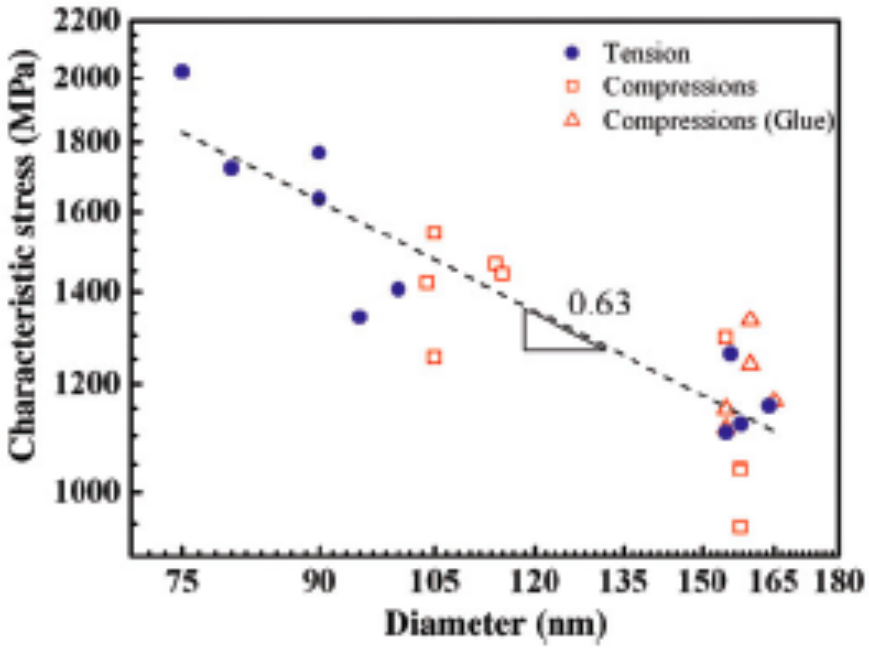

Figure 4.5 Characteristic stress vs. diameter in electroplated Cu pillars: size effect is manifested as "smaller is stronger" through power law relation for compression and tension. The characteristic stress is measured as true stress at 10% flow strain for compression, and is taken as UTS in tension. Closed circles represent tension tests and open symbols are compression tests. Open triangles and squares are compression tests performed with and without the W glue. Each point corresponds to an individual test. The dashed line shows the power-law fit for both the tensile and compressive pillars, showing the slope of -0.63.

4.3.4 Boundary Conditions – W glue

In order to identify any strengthening effects the tungsten glue may cause in tensile tests, we compressed several samples that were glued to the substrate with the same procedure as for tensile testing and compared their strength with the as-fabricated compression samples. Figure 4.6 shows the pre- and post-deformation images of a 155 nm diameter Cu pillar with glue at the bottom. As evidenced from the images, the bottom of the pillar is constrained by the W glue and remains undeformed, serving the role of a stiff substrate while the unconstrained top deforms as typical for nano-pillar deformation. Figure 4.6c shows the representative true stress – true strain curves for 155-nm diameter pillars with and without the tungsten glue. Noticeably, the pillars' strengths calculated at 10% flow strength are equivalent. In Figure 4.6c, the unglued pillar shows a larger initial burst than the glued sample. This is not a characteristic feature of glued versus non glued pillars, but rather is a result

of the natural statistical sample-to-sample variation, as these differences are also present among the as-fabricated samples.

In Figure 4.5, the 150 nm compression samples are separated into open squares and open triangles reflecting those pillars with and without glue at the pillar substrate interface. The log-log plot shows that both glued and non glued pillars sustain the same compressive flow stresses at 10% strain, as well as the UTS of 150nm tensile pillars. Figure 4.6d shows the corrected contact stiffness as compared with the theoretical stiffness for a pillar with this geometry, showing very good agreement. The corrected curve is the measured stiffness of the pillar taking into account the Sneddon correction of the pillar itself acting as a flat punch indenter on the substrate [9]. The theoretical stiffness curve is determined by assuming the conservation of volume during plastic deformation with the height defined as the difference between the original pillar height and the extent of the glue, i.e., the plastically deforming region. The theoretical and corrected stiffnesses deviate from one another at the larger strains due to the top and bottom constraints.

4.4 Discussion

4.4.1 Testing Geometry

It is apparent from Figure 4.4 that the initial loading has some variability, which we believe is a result of the imperfect initial alignment between the pillar "heads" and the grips, generating small elastic bending and possibly torsional moments. However, those pillars that undergo either torsion or bending are easily identified during *in situ* experiments as revealed by the rotation of the anisotropic pillar head. Pillars with identified torsional or bending activity were excluded from the data. Small bending moments are frequently unavoidable due to the roughness of the pillar tops. Noticeably, after the settling process the loading slope is consistent across tensile tests.

Of note is the difference in size between the smallest compression and tensile samples: 105 nm and 75 nm, respectively. This difference is due to the ~1° taper angle present in the smallest pillars. As plastic deformation in tension is dominated by localized necking, the diameter is recorded as the pre-deformation diameter at the site of necking; whereas, in compression the average diameter along the gauge length is used. Furthermore, compression tests were performed on pillars ~ 300 - 600 nm tall to avoid buckling; whereas, tensile samples were ~1,150 nm tall, the height of the PMMA matrix. The associated taper angle causes the shorter compression samples to have slightly larger diameters than the taller, thinner tensile samples.

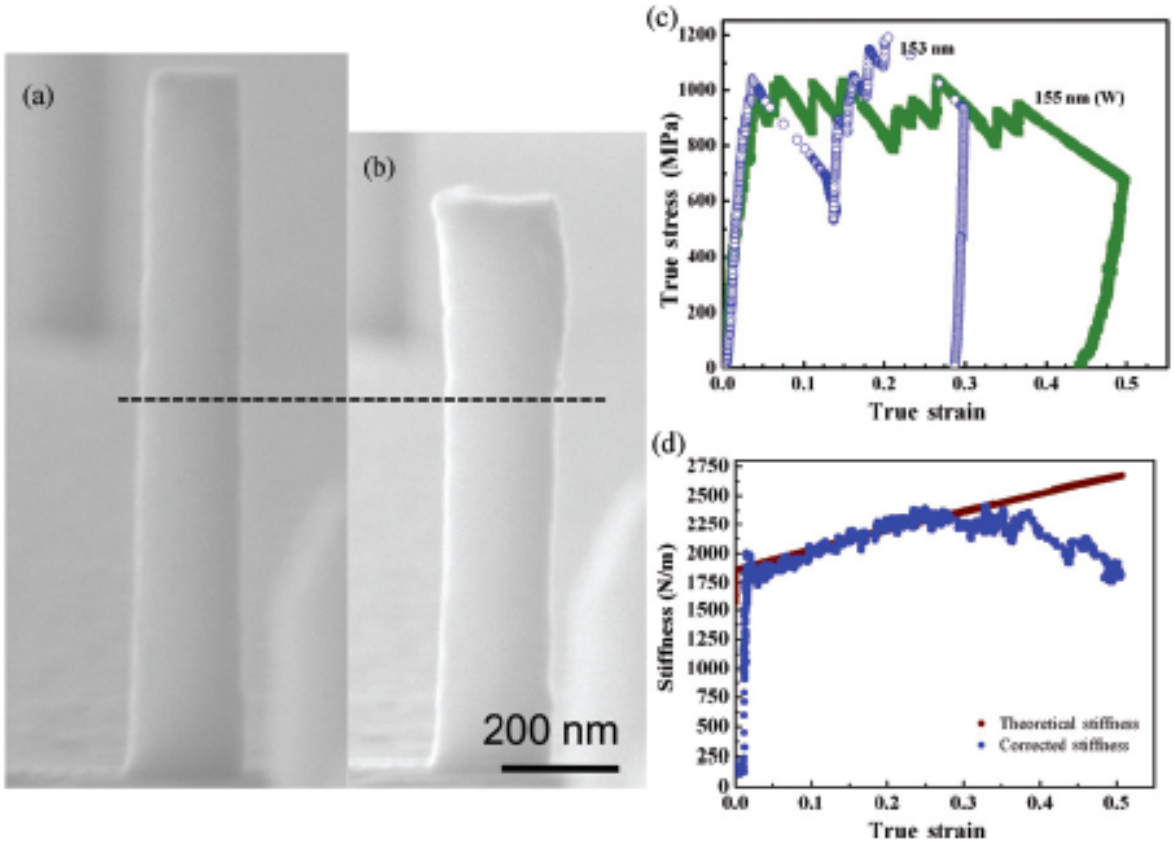

Figure 4.6 SEM images of a 155 nm-diameter pillar that has been glued at the substrate interface (a) before and (b) after deformation. Dotted line represents where the W glue defines the effective substrate. (c) compressive true stress –true strain response from the above glued pillar as compared to a pillar without the glue. (d) theoretical vs. measured contact stiffness as a function of strain showing good agreement.

4.4.2 Strain Hardening and Dislocation Starvation

The lack of homogeneous deformation during tensile loading alludes to the absence of strain hardening in these pillars. This can be shown through the necking criteria: $\frac{d\sigma_T}{\sigma_T} \leq -\frac{dA_i}{A_i}$ which means that when the fractional increase in stress through strain hardening is less than or equal to the fractional decrease in the cross-sectional area, the pillar will form a neck [73]. When this condition is not satisfied the pillar will deform homogeneously. All of the pillars tested here show little to no homogeneous deformation prior to necking, a behavior very different from many previous tensile tests on FIB-fabricated single crystalline micro-tensile samples oriented for multiple slip [36]. In those experiments, necking occurred only in some cases, and only at significant strains of ~20-30%. This discrepancy is likely due to the predominantly micron- rather than nano-sized specimens used in

previous reports, as they were limited by the ion beam resolution during FIB fabrication steps such that the smallest attainable pillar diameter was ~250 nm. Significantly, all pillars tested in this study are below 200 nm, where predominant plasticity mechanism is expected to be hardening through dislocation starvation or "mechanical annealing" [8, 9, 28]. In these nano-sized samples the gliding dislocations have to travel only very short distances before annihilating at a free surface; furthermore, as the pillar necks the deforming diameter further decreases, thereby amplifying this phenomenon. Previous tensile studies specifically on copper micro-pillars oriented for single slip reported homogeneous deformation throughout their gauge length [12]. The smallest pillar diameters tested in that work, however, were 500nm, significantly larger than the largest tension tests reported here, 165nm.

It should also be noted that surface roughness, a source of local stress concentrations, may play a nontrivial role in a pillar's ability to deform homogeneously. In order to maintain homogeneous plastic deformation, any stress concentrator must be neutralized through strain hardening; otherwise, the pillar will neck at the stress concentration. A complete analysis requires a combined experimental and computational approach.

4.4.3 Neck Microstructure

In order to study the developed microstructure in the necked region, we have made several attempts to arrest the tests on smaller pillars prior to their fracture, a challenging task since the neck is very fragile and tends to break soon after the major burst. Such a representative neck with the final diameter of ~35nm prior to fracture is shown in the inset of Figure 4.3b. Studying plasticity in these very thin necks is appealing because at these length scales, surface effects begin to seriously affect several properties, including thermodynamic, i.e. melting temperature.

4.4.4 Boundary Conditions – W glue

Recently Ngan et al. [105] used ion rather than electron beam deposition of a similar tungsten compound to completely coat Al micro-pillars with the purpose of trapping dislocations inside the specimens during compressive testing. They report an increase in strength by 50-300% depending on the micropillar's diameter, as well as a change in the deformation signature: from discrete, burst-ridden curves to continuous, constantly-increasing stress-strain behavior.

Unlike the stress-strain signature present in Ngan et al.'s [105] coated pillars, the compression pillars here with the glue at the interface exhibit no strain-hardening and generally do not differ from

the stochastic behavior of their non-glued counterparts. We observed one pillar, with the aspect ratio below 3:1 above the glued region, exhibit hardening, however in this case the entire pillar, including the region covered with glue deformed, and a stress-strain curve similar to that seen by Ngan et al. was observed.

As opposed to the deformation behavior seen by Ngan et al. [105], the deformation behavior of the glued pillars compressed here is similar to that reported by Lee et al.b[20] on the compression of single crystal Au pillars on stiff MgO. As a result, we postulate that the presence of the W coating effectively raises the substrate and reduces the initial pillar height, as illustrated by the fiducial line in Figure 4.6.

4.4.5 TEM Microstructure

TEM analysis has previously revealed that most electroplated samples are single crystalline; however, we have also observed the presence of nanoscale twins. Figure 4.7 shows several dark-field images of a pillar containing a few twins. The diffraction pattern in Figure 4.7d suggests that this pillar has coherent twin boundaries (CTBs) across the {111} planes, which are also dislocation glide planes [106]. Recently, CTBs in copper thin films have become an interesting topic due to their ability to increase both ductility and strength of the metal [107].The structure of the twins observed here is different than the twins in Cu films as they are stacked along the <111> growth direction in the latter, such that most of the twin boundaries are perpendicular to the growth direction. The twin boundaries in the pillars, as evidenced by Figure 4.7, exist on the inclined {111} planes rather than only those orthogonal to the loading direction. This variation of the CTBs' inclination with respect to the loading direction may have important consequences for the dislocation reactions at these CTBs, especially in the presence of nearby free surfaces.

Several atomistic simulations have begun to identify the complex reactions between dislocations and CTBs in order to describe the increased strengths of nano-twinned metals. Zhu et al., for example, used simulations based on transition rate theory to evaluate the athermal stress for transmission and absorption of a screw dislocation at a CTB and found that the required stress is dependent on the dislocation storage inside the twin boundary [108]. Furthermore, several MD simulations have been performed to evaluate the complex dislocation reactions with twin boundaries in both bulk [109-111] and in nanopillar geometries [112-115] and demonstrated that dislocation reactions are dependent on the dislocation character as well as on the loading condition (pure shear

versus tension). Image stress calculations for a twin boundary in Cu showed that a perfect screw dislocation is repelled by the twin boundary [116] suggesting that dislocations in nanopillars containing twin boundaries may be even more attracted to the free surface, amplifying the tendency for dislocation starvation.

4.5 Summary

We report the results of in-situ uniaxial tensile tests on ~<111>-oriented single crystalline copper nanopillars fabricated without the use of the focused ion beam. In order to perform these tests, we develop a procedure to "glue" the samples to the substrate with a W compound. We compare the ultimate tensile strengths (UTS) with the compressive strengths of nano-pillars with and without the same glue and conclude that the glue process does not substantially contribute to pillar strength. The tensile behavior is characterized by limited homogeneous deformation prior to reaching UTS, followed by a plastic burst. We attribute this lack of homogeneous ductility to the annihilation of dislocations at free surfaces before they have the opportunity to interact. We report size-dependent strength, which scales in a nearly identical power-law fashion with the sample diameter as previously reported size effects in both electroplated and FIB machined face-centered cubic pillars. While most pillars tested are single crystalline, dark-field TEM images reveal the presence of several twins in some samples.

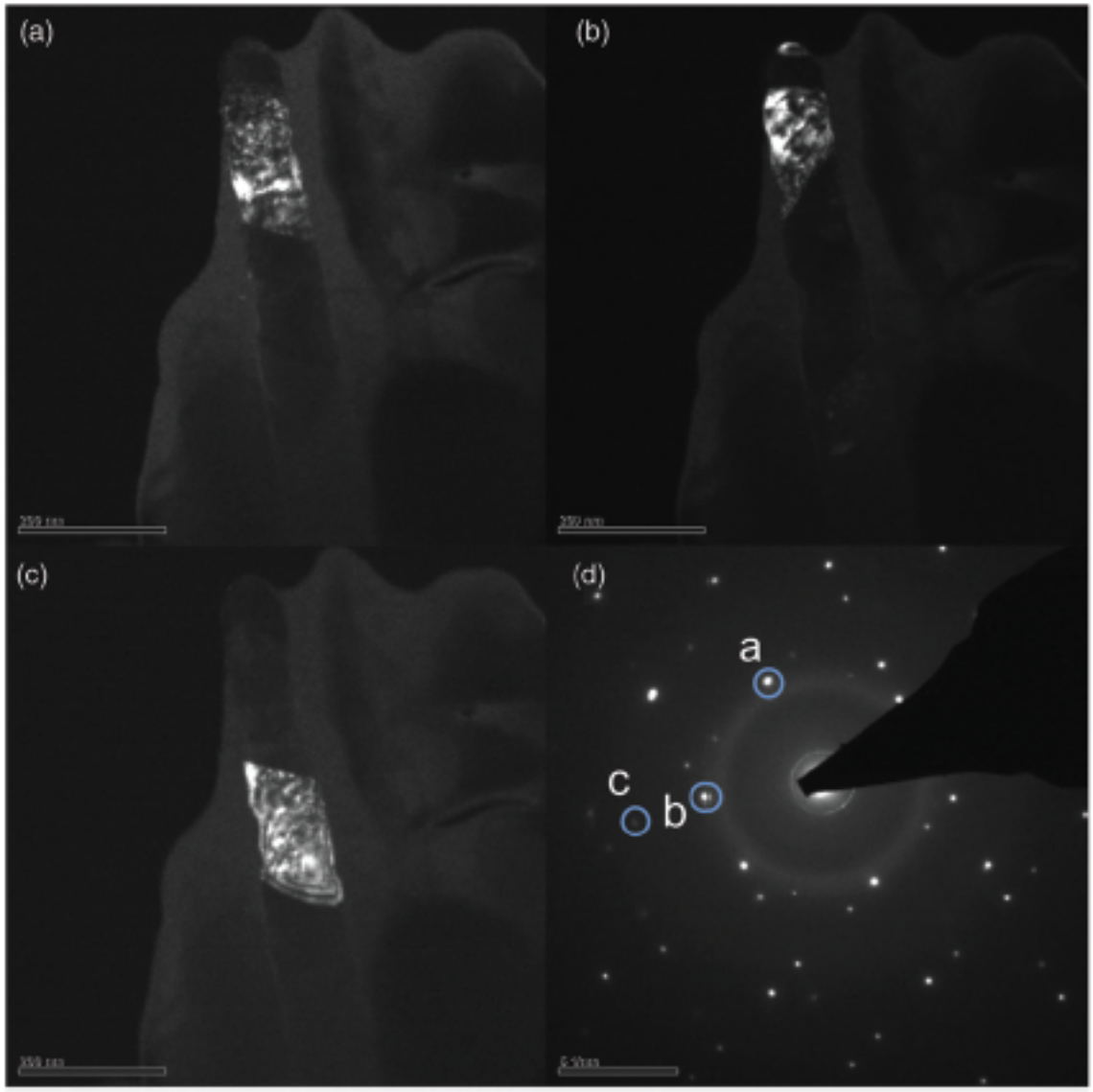

Figure 4.7a-c Dark field TEM images of a Cu nanopillar clearly showing twin boundaries. (d) diffraction pattern associated with dark field images in a-c indicating of the presence of coherent twin boundaries across {111} planes. The protective layer around the Cu pillar is an amorphous W layer – it is deposited in the same manner as is used to glue pillars to the substrate. The diffuse rings in the diffraction pattern show the lack of long range structure and, therefore, the amorphous nature of W layer.

Chapter 5: Experimental Identification of Mechanism Transition from Dislocation Multiplication to Dislocation Nucleation through Strain Rate Effects

Chapter 3 and 4 showed that single crystalline electroplated pillars have a similar size-dependent strength as observed in FIB-fabricated pillars demonstrating that the FIB is not the source of this unique deformation behavior. However, neither set of experiments, compression tests (Chapter 3) and tension tests (Chapter 4), revealed the governing dislocation mechanism(s) at these length scales. In this chapter, adapted from Jennings et al. (*Acta Materialia*, 2012) [117], two different operating mechanisms in nano-pillars are identified through constant strain rate compression tests over a range of pillar diameters, $75\text{nm} \leq D \leq 525\text{nm}$, and strain rates, $10^{-4}\ s^{-1} \leq \dot{\varepsilon} \leq 10^{0}\ s^{-1}$. We find that small diameter pillars at slow strain rates deviate from the observed trend in size-dependent strength and have similar size-independent strength behavior and measured activation volumes as theoretical predictions of surface sources. Larger pillars and faster strain rates obey the widely observed power-law size-effect in micron and sub-micron pillars and are shown to match the predicted strength and activation volume trend expected for single arm sources.

5.1 Introduction

A major current focus in the nano-mechanical community is the investigation of single crystalline strength at reduced dimensions through uniaxial deformation of cylindrical specimens, often referred to as micro- or nano-pillars [3, 9, 64, 67, 83]. Remarkably, the results of all such experiments on face-centered cubic (FCC) crystals with non-zero initial dislocation densities convey that their strengths depend on pillar diameter in a power-law fashion: $\sigma \propto D^{-n}$, where σ is the flow stress and D is the pillar diameter, with $0.5 \leq n \leq 1.0$ [3, 9, 64, 67, 83]. Size-dependent strength is counterintuitive, as crystalline strength in bulk is generally considered to be independent of sample size. In bulk metals, strength is proportional to the increasing-with-strain dislocation density via the Taylor relation: $\sigma \propto \mu b\sqrt{\rho}$ [73] , whereby dislocations multiply via double-cross slip and by operation of pinned dislocation sources [118].

Recent modeling efforts have probed possible types of dislocation sources in pillars at a range of length scales from ~1nm up to several microns. For example, dislocation dynamics (DD)

simulations performed on micron-sized pillars reveal that in these relatively large samples, single-arm, or spiral, dislocation sources generate stochastic stress-strain signatures and unambiguous size effects, in accordance with those observed experimentally [75, 79, 80, 95, 119, 120]. Reducing the pillar dimensions by an order of magnitude, molecular dynamics (MD) simulations of nanowires show the nucleation of partial dislocations from the surface of the wire [121-123]. An important consideration is that neither type of simulation has been able to accurately capture both mechanisms simultaneously: discrete DD simulations cannot accurately describe surface nucleation; whereas, MD simulations are too computationally intensive to accurately describe the collective dislocation dynamics of large systems.

Major advances investigating crystalline plasticity deeply in the sub-micron regime have also been enabled via *in situ* TEM tensile tests. These experiments reveal two mechanisms for dislocation generation in small-scale crystals: (1) via spiral, or single arm sources (SASs), as is the case for ~455nm single crystalline aluminum under tensile loading [25] and (2) via partial dislocation nucleation from the surface, or surface sources (SS), as revealed during uniaxial tension of ~15nm-diameter Au nanowires by Zheng et al. [31, 124]. In the former, dislocations are multiplied as they are generated from an already existing pinned source, while in the latter individual dislocations are nucleated stochastically, from a distribution of surface locations.

Although the precise nature of either type of source is being vigorously pursued, a general agreement exists that in micron-sized FCC pillars dislocations multiply and form complex intertwined networks through the operation of SASs; whereas, nano-sized pillars are characterized by virtually non-existent dislocation multiplication or storage, and deform via dislocation nucleation at the surface (via SSs), glide, and subsequent annihilation at the free surfaces. However, despite this general agreement, the possible coexistence and/or transition between these two mechanisms, as well as their strength, geometry, stability, and thermal nature remain important open questions.

A previously unexplored route in nano-pillar experiments is to probe the presence of a particular type of dislocation source by computing the activation volumes required for their operation. For example, atomistic simulations have predicted the surface sources to have an activation volume of ~1-10 b^3 which would result in a significant thermal contribution to the source's strength [81]. In contrast, a single arm source, often represented as a truncated Frank-Read source, whose activation volume is relatively large, ~100-1000b^3, would have an almost negligible thermal contribution to its

strength [118]. We hypothesize that this wide difference in the activation volumes should manifest itself in vastly different strain rate dependences between the two mechanisms, with SSs being more sensitive to strain rate than SASs [81, 118].

In this work, we present compressive behavior of single crystalline Cu nano-pillars with diameters between 75nm and 525nm, fabricated without the use of focused ion beam (FIB) and deformed at different constant strain rates spanning over ~4 orders of magnitude. The flow stress' dependence on the strain rate is measured to determine the activation volumes for each strain rate and pillar diameter, which are then compared to theoretically-determined activation volumes. Our experiments reveal a discontinuity in the measured strain rate sensitivity and activation volume, suggesting a possible deformation mechanism transition from collective dislocation dynamics to surface dislocation nucleation [125].

5.2 Experimental

5.2.1 Sample Preparation and Resulting Microstructure.

Single crystalline Cu nano-pillars were fabricated by electroplating copper from a copper (II) sulfate bath under an applied voltage. A schematic of the electroplating process can be seen in Figure 5.1a. The cathode, shown in a zoomed-in image in A, is a silicon wafer upon which a ~100-nm thick Au/Ti seed layer was deposited to serve as an electrical contact. The gold seed layer had a columnar grain structure with a <111> texture and an average grain width larger than all pillar diameters tested. A PMMA (poly methyl methacrylate) layer was spun onto the seed layer; the PMMA was then patterned with cylindrical pores corresponding to the pillar diameter in an electron beam pattern generator (EBPG). This chip served as the cathode in the copper bath described above. A voltage was applied between the insoluble anode and cathode depositing copper into the pores. Further details of the sample fabrication process can be found in Ref [68]. Examples of typical 75nm and 525nm pillar morphologies are shown in Figure 5.1b,c. These pillars had a loading axis oriented in ~<111> direction, and as a result of the electroplating process, they contained defects: initial dislocations and surface roughness. By the latter we mean that the surface was not atomically smooth or forcibly reorganized through sample preparation as in FIB pillar fabrication. Analysis of the surface roughness suggested a variation of +/- 2nm for each pillar diameter, resulting in an error in the recorded strength of +/- 4% for 100nm pillars. TEM analysis of these copper electroplated pillars provided estimates of

the dislocation density of ~10^{14} m^{-2} similar to other pillars produced by the Focused-Ion-Beam (FIB) [82]. Most pillars tested had no taper; however, all pillars tested had less than 1 degree of vertical taper.

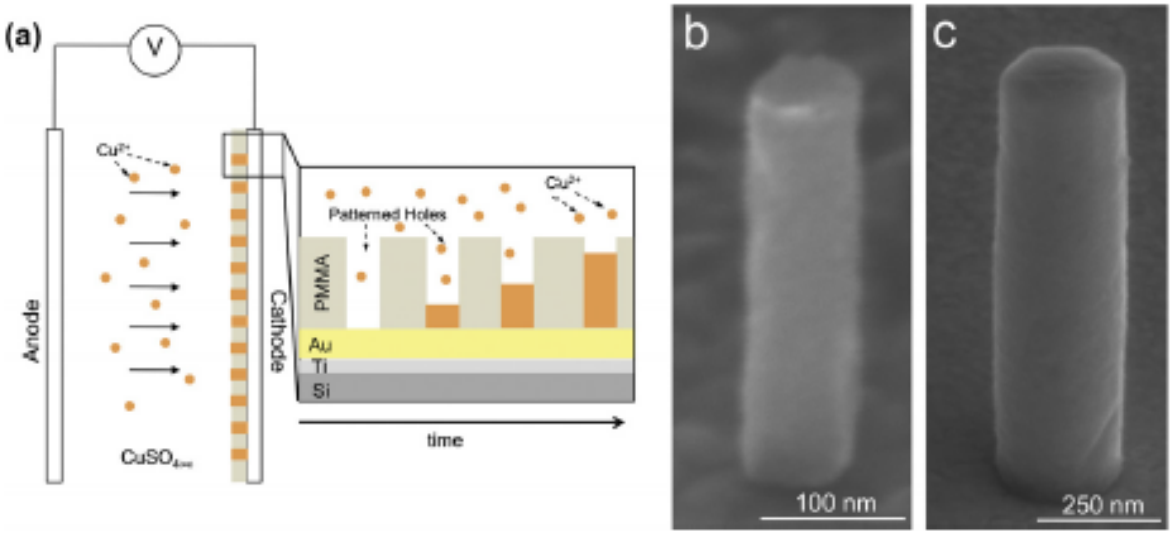

Figure 5.1(a) Schematic of the fabrication process. When a voltage is applied Cu^{2+} is reduced at the cathode. Details of the cathode structure show cylindrical holes patterned in a PMMA layer on top of a gold seed layer. Inset illustrates the holes progressively filling with copper with increasing time; SEM images of (b) 75nm and (c) 525nm diameter Cu nano-pillars fabricated by this technique.

5.2.2 Mechanical Testing

Pillars suitable for compression were identified through the use of a scanning electron microscope (SEM), FEI Nova 200, fitted with a Gas Injection System needle of $W(CO)_6$. Inside the SEM, an annulus of tungsten with an inner diameter of 6-8um and width of 1um was deposited at 52 degrees tilt around each compression pillar in order to identify these pillars in the nanoindenter's optical system. Compression tests for five different nominal sample diameters: 525 nm, 250 nm, 150 nm, 125 nm, and 75nm were performed under nominal constant strain rates in an Agilent G200 nanoindenter and the SEMentor, a custom built *in situ* instrument, comprised of a scanning electron microscope (SEM) and a Dynamic Contact Module (Agilent) [36]. Compressions tests were performed in nominal strain rate control; whereby the desired displacement rates were maintained through an internal feedback loop between a voice coil applying a force and a capacitive plate measuring the resulting displacement. Displacements rates were prescribed through the following equation for a desired strain rate: $\dot{u} = \dot{\varepsilon} l_0$ where l_0 is the initial pillar length.

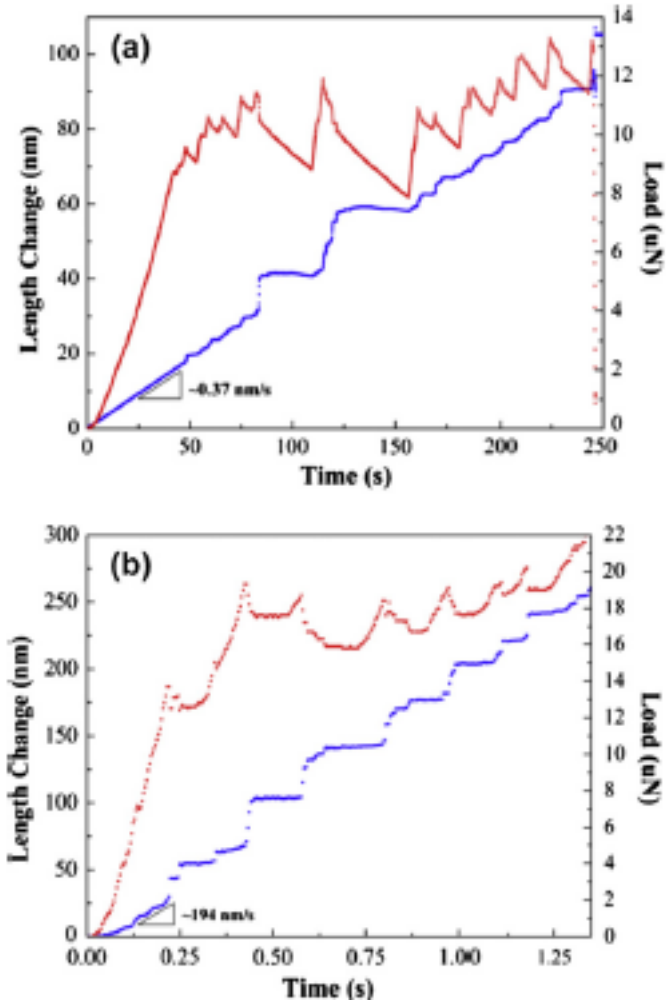

Figure 5.2 Load (red) and length change (blue) vs. Time for two D~125nm pillar compression tests. The measured displacement rates in A and B are 0.37 nm/s and 194nm/s respectively while nominally prescribed ones are 0.38nm/s and 200nm/s respectively. Displacement excursions correspond to load drops as a result of dislocation bursts. The constant displacement sections are due to the feedback loop maintaining a constant average displacement rate.

Actual displacement rates were then measured through the slope of the displacement versus time data for the nearly elastic loading sections as seen in Figure 5.2. The displacement rates ranged from ~0.15 nm/s to ~700 nm/s. While sub-nm displacement rates may seem spurious, the feedback loop was able to perform tests at these very slow speeds. Figure 5.2a,b show the displacement and force versus time for two D~125nm compression tests. The average displacement rate in Figure 5.2a,b were measured to be ~0.37nm/s and 194nm/s, respectively. This displacement rate is relatively constant throughout the test excluding characteristic displacement bursts and subsequent machine response required by the feedback loop. As the minimum aspect ratio of pillar compressions was chosen to be ~3:1 to minimize geometric constraints, there is a natural lower bound to the accessible strain rates. Tests at $\dot{u} < 0.1$ nm/s were not attempted and are not expected to give reliable results. In this study, ~150 successful compression tests were performed resulting in an average of ~5 compressions per data point in Figure 5.5a. Details of the specific experimental attributes in performing nanoscale compression tests including rounding of the pillar tops, misalignment, and geometric constraints are discussed in detail in [6, 7, 67].

5.3 Results

5.3.1 Stress-Strain Behavior

Characteristic stress strain curves are shown in Figure 5.3, where four different stress-strain curves correspond to two distinct diameters, 125nm and 250nm, each of which is deformed under two different strain rates, 10^{-1} s^{-1} and 10^{-3} s^{-1}. The stress plotted here is true stress following the analysis assuming a homogeneously deforming pillar while correcting for the elastic response of the pillar acting as an indenter into the substrate [9]. All of the stress-strain curves have a nearly elastic loading followed by intermittent strain bursts. Noticeably across all pillars tested, there is no appreciable global hardening. In comparing the two different sizes at a constant strain rate, there exists a clear size effect, whereby smaller pillars exhibit strengths much greater thank bulk. Furthermore, at a constant pillar diameter, faster strain rates result in higher stresses with the increase in strength significantly larger for smaller pillar diameters. Interestingly, increasing the strain rate by two orders of magnitude results in only a 15% strength increases in 250nm pillars, while the strength in 125nm pillars increases by almost 100% upon the same strain rate increase, suggesting an increased strain rate sensitivity in smaller pillars (Figure 5.5a). It also appears that the faster strain rate compressions result in one catastrophic strain burst as opposed to the multiple successive bursts characteristic of the slower strain rates (Figure 5.3).

5.3.2 Size-Dependent Strength

Figure 5.4a shows a log-log plot of flow stress at 10% strain as a function of pillar diameter for five different pillar diameters between 75nm and 525nm deformed at three different constant strain rates: from 10^{-1} s^{-1} to 10^{-3} s^{-1}. If a strain burst occurs at 10%, strain the last point in the previous loading region is chosen as the recorded stress. Stresses are not recorded for values inside a burst because as the pillar is deforming the machine is also removing load in order to maintain a constant displacement rate. The two combined effects result in an unclear instantaneous stress level during a burst. This plot reveals that pillars with larger diameters, 150nm to 525nm, obey the widely observed power-law size effect for all strain rates tested, with the power-law slope of ~0.54, well within the previously reported range [67]. Across three different strain rates, the power law slope remains nearly constant despite a noticeable increase in strength with increasing strain rate. This suggests that the power-law slope in this size regime is not significantly affected by strain rate, and therefore by thermal contributions. The results for the fastest strain rate of 10^{-1} s^{-1}, shows this continuous power-law behavior extending down to the smallest diameter tested: 75nm. At the two slower strain rates, however, a transition diameter

exists, below which the pillar strength deviates from the power-law trend continued in a dashed line. This transition diameter, or the smallest diameter unambiguously continuing the power-law trend, is not constant and appears to decrease with increasing strain rate: D_t~150nm for 10^{-3} s^{-1},; D_t ~125nm for 10^{-3} s^{-1}; and $D_t \sim \leq 75$nm for 10^{-2} s^{-1}. Precise identification of the transition diameter is challenging; however, there is a clear trend that faster strain rates result in smaller transition diameters.

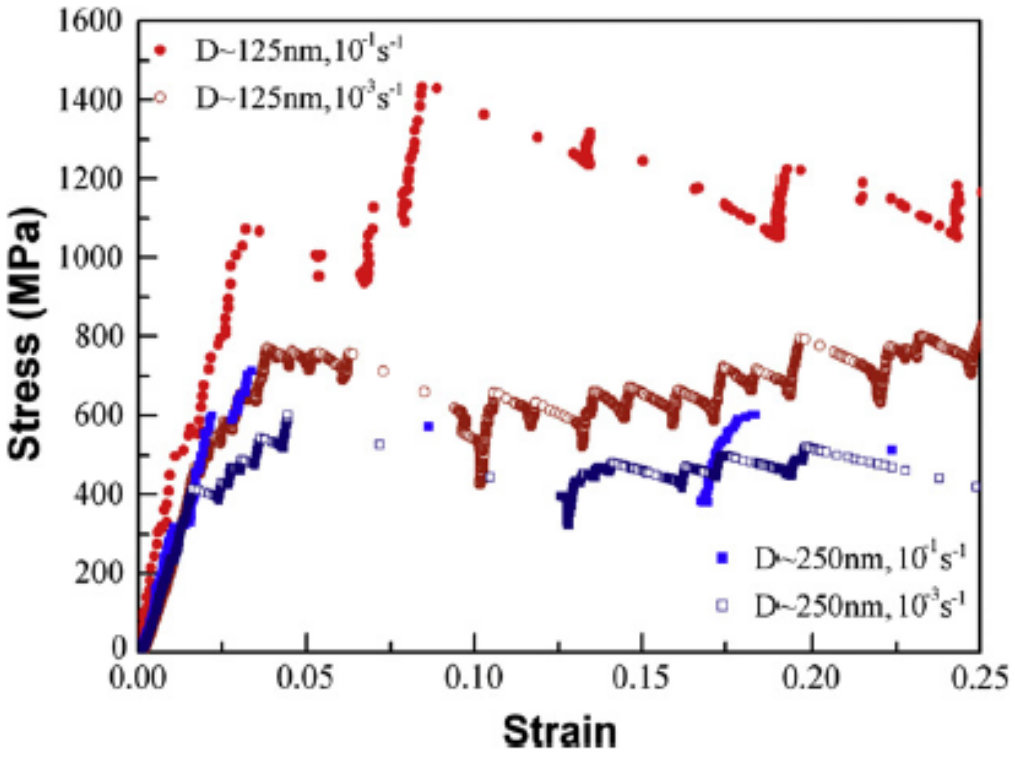

Figure 5.3 Four characteristic stress-strain curves plotted for pillars of two different diameters, 125nm and 250nm, each deformed at two different strain rates, 10^{-3} s^{-1} and 10^{-1} s^{-1}. At a constant strain rate, smaller pillars have higher strengths, whereas, at constant diameter, faster strain rates result in higher strengths. Plastic deformation continues beyond 25% strain followed by unloading in all the compression tests above. Deformation behavior beyond 25% strain is omitted for clarity.

5.3.3 Strain Rate Sensitivity and Activation Volume

A material's strain rate dependence is usually quantified through an empirical fit of $\sigma = \sigma_0 \dot{\varepsilon}^m$ where m is the commonly reported strain rate sensitivity. The strain rate dependence, indicative of the rate controlling mechanism, for dislocation source operation can also be described by an Arrhenius form that connects the shear strain rate, $\dot{\gamma}$, to the applied shear stress, τ [125]:

$$\dot{\gamma} = \dot{\gamma}_o \exp\left(\frac{Q^* - \tau\Omega(\tau,T)}{k_B T}\right)$$ Eq. [5.1]

Here $\dot{\gamma}_0$ is a constant related to the source's attempt frequency, Q* is the activation energy, k_B is Boltzmann's constant, and T is the temperature. The activation volume expressed above describes how the activation free energy changes with shear stress or $\Omega(\tau,T) \equiv \left.\frac{\partial Q}{\partial \tau}\right|_T$, and thus can be used to determine the activation volumes in nano-pillar compression experiments through conducting tests at different constant strain rates [118]. Specifically Eq. 5.1 can be re-written to show that [125]:

$$\Omega = k_B T \frac{d \ln \dot{\gamma}}{d\tau}$$ Eq. [5.2]

We determined the strain rate sensitivity and activation volumes for all of our compression tests at different strain rates, spanning over three orders of magnitude. The experimental data for the flow stress at 10% strain as a function of strain rate for five different diameters is shown on a log-log plot in Figure 5.5a. In Figure 5.5a, the slopes of the curves correspond to the strain rate sensitivity, *m*. Noticeably, at high strain rates $\dot{\varepsilon} \geq 10^{-1} s^{-1}$, corresponding to power-law behavior for all diameters tested (Figure 5.4a), all pillar diameters show an increasing rate dependence with decreasing diameter, with *m* ranging between ~.027 and ~.057, all over 5x greater than bulk single crystalline copper (~.006) [126]. This finding suggests that as the size is reduced, not only does the strength increase, but the strain rate dependence of FCC materials emerges and increases, as well. Furthermore, at intermediate strain rates $\dot{\varepsilon} < 10^{-2} s^{-1}$, the two smallest diameters: 75nm and 125nm show a discrete transition to a much stronger rate dependence, ~0.11, than the *m* at the three larger diameters 0.027 - 0.04 suggesting a transition to a different deformation mechanism. The precise choice of transition strain rate is difficult to determine due to the inherent stochastic response of these compression

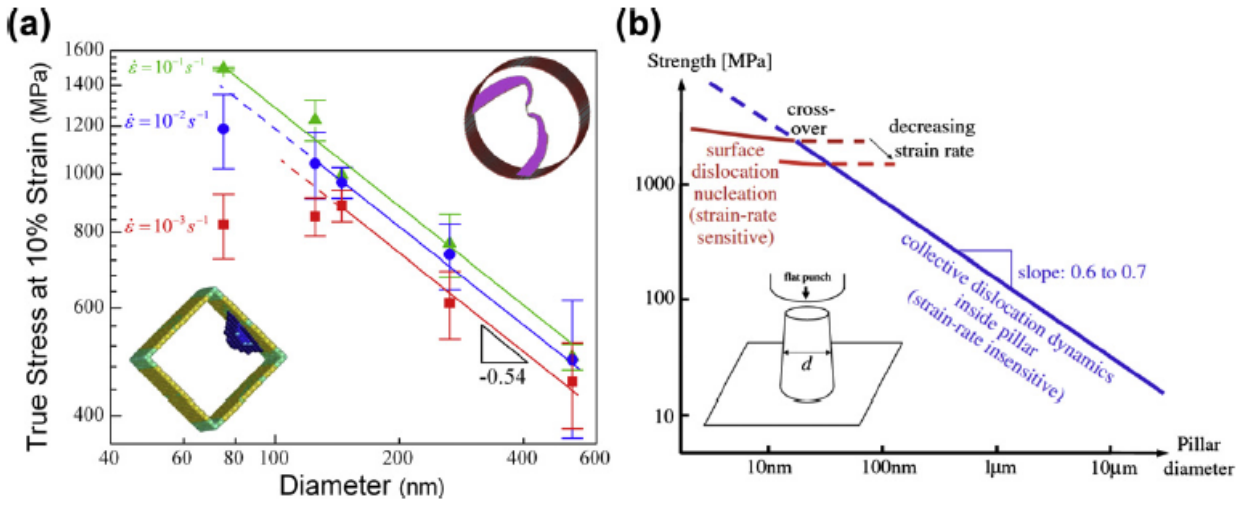

Figure 5.4 (a) Strength as a function of diameter for three different strain rates (log-log scale). Trend lines denote power-law strengthening where plasticity is governed by collective dislocation dynamics. Inset shows atomistic simulation of two single-arm sources sharing a pinning point [127]. At the transition diameter, specific to each strain rate, the mechanism changes to surface source nucleation, as reflected in a deviation from the power-law strengthening. Bottom left inset shows atomistic simulations of a surface source (reprinted with permission from APS)[81]. B) Theoretical predictions by Zhu et al. showing a nearly identical trend (reprinted with permission from APS)[81]

tests. A first approximation of the transition strain rate for a given diameter was estimated from Figure 5.4a. Subsequently, best fits of the stress vs. strain rate data were determined as common mechanisms are assumed to maintain similar trends in both strength and strain rate sensitivity with size.

It may be possible to gain insights into the microstructural plasticity mechanisms responsible for this surprising strain rate sensitivity by analyzing the activation volume. The experimental results of the activation volume, along with error bars corresponding to the accuracy of the fit, for each diameter at high strain rates, $\dot{\varepsilon} \geq 10^{-1} s^{-1}$ are plotted in Figure 5.5B. This plot reveals a trend of smaller pillars having smaller activation volumes. The best fit of the activation volume as a function of pillar diameter data on a log-log plot has a nearly linear slope of ~0.97, implying that the Ω scales linearly with pillar diameter D. Notably, the activation volume here lies between $9.6b^3$ and $62b^3$, a range that is larger than that predicted for SS operation with the exception of the 75nm diameter pillars. The large error bars for the two smallest diameters in Figure 5C correspond to the limited range of strain rates over which this regime was experimentally measured. Figure 5C shows a similar plot for the activation volume at slower strain rates, $\dot{\varepsilon} \leq 10^{-2} s^{-1}$, and illustrates that the two smallest diameters have activation volumes of $\sim 6b^3$ and $\sim 7.3b^3$, approximately 50% and 40% smaller than activation volumes at faster strain rates,

with magnitudes expected for surface source nucleation: 1-10b^3 [81]. The range of activation volumes expected for conventional bulk sources are plotted for comparison and completeness [118].

5.4 Discussion

5.4.1 Influence of Sample Fabrication on Mechanical Properties

To date, the vast majority of experiments on FCC pillars have been performed on samples fabricated by the use of Focused Ion Beam (FIB) [67]. Pillars fabricated via this methodology exhibit size-dependent strengths, and the mechanisms responsible for this strengthening have been a heavily debated topic [67]. One of the major points of contention has been the influence of the FIB fabrication technique on nanopillar strength [2, 9, 18, 59, 61, 82, 95, 128-134] as the FIB introduces damage into the surface of the pillar by forming dislocation loops and surface amorphization [18]. Damage of this type is a known source of strengthening in bulk single crystals suggesting that FIB-fabricated pillars maybe be stronger than bulk [18]. Thus, as the relative surface area to volume ratio in pillars increases with decreasing pillar diameter, these ion damage effects become more adverse. Further studies of the effects of the FIB damage and dislocation structure evolution through Laue microdiffraction [129-133, 135], x-ray microdiffraction [128, 134], and in-situ TEM [28] have provided valuable insight into the role FIB-induced microstructural damage plays in a pillar's mechanical response.

Several initial investigations of pillars produced without the FIB have produced pristine uniaxial samples that deform in tension and compression at near-theoretical strength [2, 57, 59]; however, it has been shown that initially pristine Mo-Al-Ni eutectic alloys undergo a significant decrease in strength after exposure to the FIB or pre-strain as a result of increasing damage/dislocation density [61]. Effects of pre-strain are not limited to this system and in fact have been observed in FCC Au [20].

Among others, the current authors have recently shown that it is the initial dislocation density rather than the fabrication technique that drives the size effect in FCC metals [20, 25, 26, 82, 95]. In those experiments, similar arrays of Cu nano-pillars as those used here were produced via electron beam lithography and electroplating. These pillars as fabricated contained initial

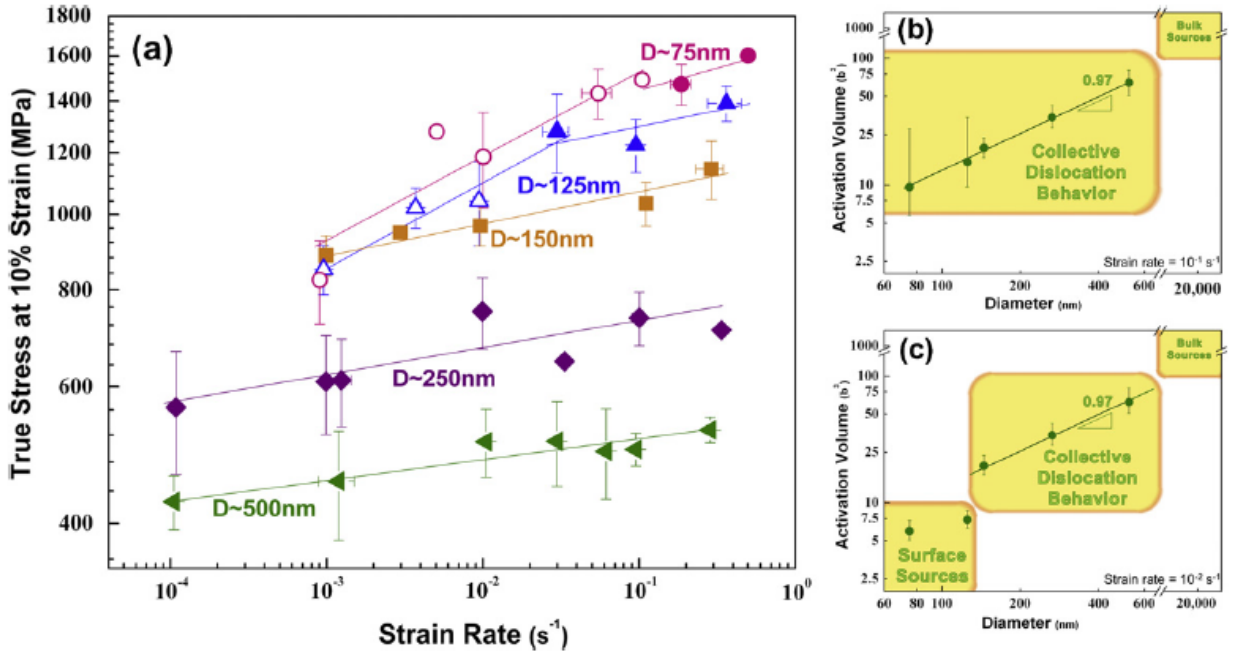

Figure 5.5(a) Flow stress at 10% strain as a function of strain rate for five different pillar diameters shown around each data set. The extracted activation volumes for each diameter at strain rates of (b) 10^{-1} s^{-1} and (c) 10^{-2} s^{-1}. These activation volumes may correspond to two distinct plasticity mechanisms: surface dislocation nucleation vs. collective dislocation dynamics

dislocation densities of ~10^{14} m^{-2} [82]. These dislocation densities are in the high end of the range of dislocation densities reported in FIB-fabricated FCC pillars: 10^{12} m^{-2} and 10^{14} m^{-2} [20, 24, 25, 82]. Examples of these electroplated pillars shown in Figure 5.1b,c. These pillars, which have never been exposed to the FIB, demonstrate an identical size-dependent strengthening trend as all FIB-produced FCC pillars with similar initial dislocation densities [82]. This finding is consistent with previous work on BCC-alloy systems showing that the pillar strength is a strong function of the initial dislocation density. A key finding here is that as a result of similar strength relationships with diameter, we expect the observed trends here to apply to FIB fabricated FCC pillars; however, at the moment, fabrication limitations makes producing sufficiently small pillars within the transition size range overly cumbersome. We also note that while several investigations into the effects of the FIB on the previously reported size-dependent regime, we know of no investigations into how FIB-damage may enhance or diminish the observed transition seen here.

5.4.2 Nano-scale Crystalline Plasticity: Dislocation Starvation

A characteristic feature of the plastic deformation in pillars with non-zero initial dislocation densities is the stochastic nature of the intermittent strain bursts, corresponding to discrete dislocation avalanches [23, 32, 94]. In large systems, these avalanches are the result of collective dislocation motion; however, as pillar diameters decrease to the deep sub-micron regime, dislocation sources will be required to sustain plastic deformation, as dislocations will more readily annihilate at a free surface as seen in both *in situ* [28] and post-deformation TEM [82] without forming extensive dislocation networks. For example, in a 300nm tall pillar, 10% of nominal axial plastic strain in a <111> oriented Cu pillar would require ~125 dislocations to reach the free surface in order to carry that plastic strain. In the materials tested here, a 100nm diameter pillar has an estimated initial dislocation density of $\sim 10^{14}$ m^{-2} corresponding to only a few dislocations initially residing within the pillar. For instance, in a 100nm diameter pillar, a single 2nm dislocation would result in a dislocation density of $\sim 10^{12}$ m^{-2}; whereas, a dislocation extending the diameter would result in a dislocation density of $\sim 10^{14} m^{-2}$. This suggests that in these small diameter pillars dislocation avalanches must have an increasing contribution from simultaneous source operation, as the initial dislocation density is far from sufficient to carry the required plastic strain.

The increasing influence of source operation in these small pillars does not suggest that the dislocation density will vanish after appreciable plastic strain. These pillars are ~<111> oriented, resulting in one <111> slip plane normal to the loading direction thus having no resolved shear stress on that plane. Post deformation TEM studies on these pillars show that within the deforming region only dislocations lying in this slip plane remain in the pillar resulting in a non-zero dislocation density [82].

5.4.3 Choice of 10% Flow Stress and Impact on Activation Volume

We chose to report flow stress at 10% strain because in these small samples the determination of yield point is ambiguous and for the copper pillars tested here, there is, in general, no global hardening in the stress-strain response as illustrated in Figure 5.3. This lack of global hardening outside the initial plastic region has also been observed in other FIB fabricated copper pillars [14] and suggests that beyond the initial plastic deformation as high as 10% strain, the choice of strain to report flow stress does not affect the power-law slope or the reported strain rate sensitivity. Furthermore, one of the consequences of dislocation starvation is that the internal microstructure should not appreciably

change as a function of strain, allowing the use of the flow stress at 10% strain in estimates of activation volume for either surface sources or single arm sources. In contrast, in samples or sizes where dislocation sub-structures evolve with strain, the deformation mechanisms will evolve with strain, and the choice of characteristic flow stress should be carefully considered.

5.4.4 Surface Source Strength and Activation Volume

While transitions from power-law behavior in FCC metals have not been investigated experimentally, they were recently predicted using a combination of analytical and atomistic theory by Zhu et al. [81]. These authors raised the question of what would happen if surface sources were the dominant mechanism in small volume plasticity [81]. Following their analysis, the nucleation frequency of a surface dislocation source due to an applied stress can be described by Eq. 5.1 where the nucleation frequency corresponds to the resulting shear strain rate of Eq. 5.1. In order to describe the stress for nucleating a dislocation burst, they define a survival probability $f(t)$, which describes the percentage of pillars that have not nucleated dislocation burst by a time t. The change in the survival probability with time can then be described by:

$$\frac{df(t)}{dt} = -\nu f(t) \qquad \text{Eq [5.3]}$$

where ν is the nucleation frequency. This function can be rewritten in terms of uniaxial stress through a linear elastic relation: $\sigma = E\dot{\varepsilon}t$ as pillar compressions show nearly elastic loading between bursts. In order to find the most probable stress at which a pillar will nucleate a burst we look for the maximum in the change of the survival probability. The resulting predicted stress can be written most clearly through a linearized form of the stress dependence:

$$\sigma = \sigma_{ath} - \frac{k_B T}{\Omega} \ln \frac{k_B T N \nu_o}{E \dot{\varepsilon} \Omega} \qquad \text{Eq. [5.4]}$$

The likely stress for nucleating a dislocation from a surface source is then related to two components: the athermal strength, σ_a, and the last term on the right-hand side, describing the thermal contribution. Examining the latter term, the thermal contribution is proportional to $\frac{1}{\Omega}\ln\frac{1}{\Omega}$ showing that for mechanisms with smaller activation volumes, the thermal contribution plays a larger role. It should be noted that this analysis is general for any dislocation source. Furthermore,

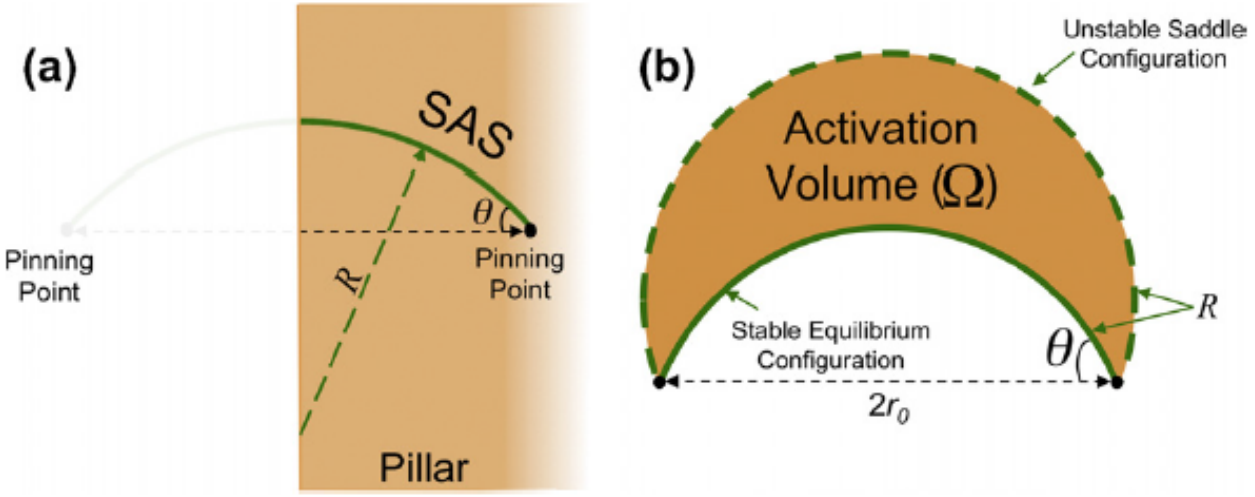

Figure 5.6(a) A schematic of a single-arm source represented as ½ a F-R source. (b) The activation volume is determined as ½ the difference between the stable and unstable equilibrium configurations for a F-R source at a particular applied stress.

in the event of repeated successive bursts, the physics described above holds true as long as the microstructure does not change appreciably with strain. It should be noted that in micro-pillars dislocation sub-structures progressively develop and change with increasing strain, rendering the above analysis inapplicable to these larger samples. Deeply in the sub-micron regime, however, dislocations do not readily form sub-structures, and therefore this analysis should be relevant at all strains.

The linearized form of the strength of a surface source can be used to predict the diameter dependence of surface source operation. Figure 5.4b [81] shows a sketch of the theoretically predicted strength as a function of diameter on a log-log scale, which bears a strong resemblance to our experimental findings (Fig. 5.4a). Both of these plots convey that larger pillars strengthen in a power-law fashion whose slope is relatively independent of strain rate, or thermal contributions, suggesting that the power-law dependence is proportional to the athermal strength. However, as the diameter decreases, a competition between the power-law and SS-dominated plasticity arises, where the weaker of the two governs the overall response. Based on the atomistic FENEB simulations the activation volume for partial dislocation nucleation was found to be 1-10b^3 corresponding nucleation from a sharp corner, 1b^3, to an atomically smooth surface, 10b^3. Their atomistic predictions suggest a transition diameter in the range of 10nm to 100nm, depending on strain rate [81]. This predicted diameter range and strain rate sensitivity of the transition diameter overlap favorably with our experimental results suggesting that in sufficiently small samples, surface nucleation of dislocations

may be the dominant plasticity mechanism. This transition to partial dislocation nucleation has also been observed in tensile tests of Cu thin-films and single-crystal Au, illustrating that similar mechanisms govern plasticity in all small-scale crystalline samples, irrespective of the sample geometry [64, 136, 137].

In order for the reasonable agreement found in Figure 5.4 in both trend and magnitude between our experimental data and this atomistic work, the experimental results and atomistic simulations must reflect similar values in both the athermal strength and activation volume. The agreement in the activation volume has been shown above, suggesting these similarities likely hold true in at least the limited region accessed by our experiments. This further suggests that surface sources are controlling the deformation of the smallest pillars tested at the slowest strain rates.

5.4.5 Size-Dependent Strength and Transition Diameter

Previous compression tests on similarly produced electroplated pillars have resulted in a size dependence with a power-law exponent of ~0.63 [82] similar to the ~0.54 reported here. Notably, the previous compression tests were all conducted at a constant displacement rate of 2 nm/s as opposed to a constant strain rate as done here. The aspect ratio in both sets of experiments corresponds to a ~3:1 height to diameter resulting in an increasing strain rate with decreasing pillar diameter and, therefore, height in tests performed at constant displacement rates. As a result, the ~0.63 exponent is, in fact, artificially high in relation to constant strain rate tests. Correcting for the changing strain rate during these tests would bring the two power-law slopes into an even closer agreement.

The observed deviation from power-law strengthening at the sub-micron pillar diameters has not been experimentally observed before since most experiments to date have been performed on larger pillars and/or not at constant strain rates [3, 4, 9, 11, 19, 23, 32, 36, 67, 82]. This finding emphasizes the non-trivial role strain rate plays in the determination of the strength, a factor not yet systematically evaluated in FCC nano-pillar experiments. Interestingly, Uchic et al. reported a transition in power-law exponent for several micron-sized Ni_3Al-Ta and speculated that the source to be the self-exhaustion or annihilation of screw dislocations [3].

The lack of strain-rate effect on the power-law slope demonstrates that the mechanism responsible for the power-law is itself insensitive to strain rate, as the strain rate dependence manifests itself as a deviation from the power-law. In order to understand the strain rate-dependence of the power-law behavior, we examine a useful form for small-scale crystalline strength [4, 24, 26]:

$$\sigma = \sigma_o + \frac{1}{2}\mu b\sqrt{\rho} + \frac{\alpha\mu b}{L}\ln\frac{L}{b} \quad \text{Eq. [5.5]}$$

where the first term on the right-hand side corresponds to friction stress, the second term is due to back stresses from dislocation-dislocation interactions, and the last term originates is from the single arm source strength, where α is a constant prefactor corresponding to the character of the dislocation line [50]. Noticeably, none of the terms above are expected to be strain rate dependent. However, we note that the above equation only takes into account athermal effects, rendering its ability to describe the thermally activated processes discussed here inadequate. As mentioned previously, Zhu's analysis is general for any dislocation source. If we apply Zhu's analysis [81] to understand the thermally activated nature of single-arm sources, we notice that the athermal strength (1st term Eq. 5.4) corresponds to Eq. 5.5. The remaining term in Eq. 5.4, the thermal contribution, is proportional to $\frac{1}{\Omega}\ln\frac{1}{\dot{\varepsilon}\Omega}$. We have shown here that the measured activation volume is almost linear with diameter suggesting that the thermal contribution would be proportional to $\frac{1}{D}\ln\frac{1}{\dot{\varepsilon}D}$. If the source length, *L*, in Eq. 5.5 and the pillar diameter, *D*, are linearly related, then both the thermal and athermal components of a SAS would have nearly the same size-dependent behavior as their size dependencies would be dominated by the prelogarithm $1/D$ dependence. This added thermal contribution to Eq. 5.5 would not substantially change the observed power-law slope which reflects the diameter dependence of the power-law seen in Figure 5.4a. Furthermore, the addition of the thermal contribution would include the correct trend in the strain-rate dependence: a decrease in the strain rate rigidly shifts the power-law to lower stresses. We note that the expected source length for a pillar is not precisely linear with its diameter; rather it will be a function of the dislocation density [26]. Furthermore in order to truly account for the thermal contributions in the mechanisms of nanopillars within the power-law regime, both atomistic and discrete dislocation simulations would be required to accurately capture the correct physics and the relevant length scales and timescales.

5.4.6 Activation Parameters

The range of strain rates explored in our experiments corresponds to a relatively narrow range of activation energies. The activation energy available to any mechanism is $Q = nk_BT$ with n is of the order of the logarithm of total number of atomic vibrations during a test. In our experiments, this gives n~37 to 28 based on the strain rates of ~10^{-4} s^{-1} to 1 s^{-1}, and corresponds to a limited accessible

energy range of ~0.95eV down to ~0.72eV [118, 138]. All of the activation volumes we computed correspond to this relatively narrow energy range. Further exploration of the details of the activation energy versus applied stress would require atomistic simulations and further experiments including those over a range of constant temperature.

5.4.7 Expected Trends in Single Arm Source Activation Volume

In order to determine whether the observed nearly linear trend in the SAS activation volume versus diameter at fast strain rates, $\dot{\varepsilon} \geq 10^{-1} s^{-1}$, is reasonable, we developed a simple phenomenological model that assumes the main change in activation volume with pillar diameter is contributed through the SAS operation. This assumption is based on the idea that the length of a SAS is a strong function of the pillar diameter; whereas, other collective dislocation behavior is to expected here to be independent of sample diameter. This phenomenological model approximates a SAS as ½ a Frank-Read source, shown schematically in Figure 5.6a. In this case, the activation volume and energy of a SAS would correspond to those of a ½ FRS.

Following Nabarro's derivation for the activation volume of a FRS [138], there are two components to the activation volume. The first corresponds to the classical description of the activation volume of a bowing dislocation segment between two perfectly immobile pinning points. The second component accounts for the finite strength and thus the motion of said pinning points. This latter component was introduced in order to reconcile Cottrell-Stokes Law with Frank-Read Source operation [138]. The required strength for a SAS to multiply dislocations and thus govern plasticity in nano-pillars is determined by the motion of a SAS around its stationary pinning point [50]. While simulations and experiments have shown that SASs are not immortal [25, 79, 139], the strength of a pinning point is not expected to be a strong function of the pillar diameter especially in large pillar diameters, but rather of its proximity to the free surface. However, the length of a SAS is a strong function of diameter, thus in our attempt to capture the trend in activation volume we focus here only on the contribution from the bowing of a dislocation line between two infinitely strong pinning points.

At a given applied shear stress, a dislocation segment pinned by two immobile pinning points has two equilibrium positions corresponding to the same radius of curvature, as schematically shown in Figure 5.6b. In order for a FRS to produce a new dislocation, a certain amount of thermal energy is required to move the dislocation segment between the stable and unstable equilibrium positions. The

activation volume is then defined as the geometry of the volume difference between these two configurations:

$$\Omega(\tau, r_o) = b(A^* - A_i) = b(\pi R^2 - 2A_i) \quad \text{Eq. [5.6]}$$

Generally, dislocation multiplication from a Frank-Read source is an athermal process, where the thermal component represents less than ~0.1% of the athermal strength for typical line lengths [138, 140]. As a result, the distance between the two equilibrium positions is very small. Eq. 5.6 can then be simplified by rewriting the geometry of the dislocation segment in terms of the stress necessary to bow the dislocation segment through an angle θ: $\tau = \frac{\mu b \sin\theta}{2r_0}$ and the athermal strength of a FRS: $\tau_{ath} = \frac{\mu b}{2r_0}$ [65]. In the limit where τ is close to τ_{ath} and taking the dominant term, the resulting activation volume is approximately:

$$\Omega(\tau, r_o) \approx b r_o^2 \sqrt{\frac{2}{\tau_{ath}}(\tau_{ath} - \tau)} \quad \text{Eq. [5.7]}$$

The activation energy is then the integration of the parabolic dependence between source strength and activation volume near athermal strength [141, 142]: $Q \approx \frac{2}{3}(\tau_{ath} - \tau)\Omega$ and fixed in the narrow range described previously. We arrive to the following approximate scaling of the activation volume of SAS with its athermal strength: $\Omega \propto \tau_{ath}^{-5/3}$.

Figure 5.4a shows that in the range of power-law strengthening for different strain rates, the absolute pillar strength increases with strain rate; however, the power-law exponent remains relatively insensitive to the strain rate. This suggests that the trend in athermal strength with diameter reflects the commonly reported power-law. As a result, we write the activation volume as a function of diameter as $\Omega \propto D^{-5n/3}$. Comparing the diameter dependence of the activation volume to the experimental data presented here, we find that $\Omega \propto D^{0.9}$, close to the experimentally obtained exponent of 0.97. To date, FCC micro-compression tests have a range of reported values for *n*, with the majority between 0.5 and 0.7 resulting in a range of possible exponents, 0.83-1.16, relating the activation volume to the pillar diameter. Despite the simplicity of this model, the combination of our experimental findings and those predicted by the model indicates that SASs strongly contribute to the size dependence of part of the strength in larger, micron-sized pillars. It should be noted that while this phenomenological model

captures the relative trend, it does not accurately predict the magnitude of the observed activation volumes. The activation volumes suggested by this simple model are in the range of $\Omega > 400b^3$ which as expected reflect values for FRS operation. The lack of agreement in the magnitude of the activation volume shows that while this simple model reflects the activation volume's diameter dependence, there remain important open questions as to the other sources of thermal activation in FCC nanopillars and questions the applicability of classical theories like Nabarro's to small-scale plasticity.

It should be noted that the above model does not take into account the image force or any extra thermal contribution from the nearby free surface. Simulations have shown that the effects of the image stress are negligible for the sources longer than ~250b, implying that the image force effects may only come to play a role in the smallest diameter pillars: D ~75nm [143, 144]. Furthermore, the complete athermal strength of a single arm source has a logarithmic dependence on the dislocation source length, 3rd term of Equation 5.5 which - while a much smaller contribution than the inverse source length dependence - may account for some discrepancy between the experimental results and the model [64, 119, 136, 137, 143, 144]. Also as noted by Nabarro the motion of the pinning points may contribute substantially to the thermal activation of a double-pinned source [138]. An alternate approach to determine the expected dependence of the activation volume with diameter would be to examine the expected source length with varying pillar diameter. This was done analytically by Rao et al. [143]; however, that model implicitly requires the knowledge of the dislocation density and distribution at each pillar diameter which is unknown here [26]. The approach taken above subsumes all of the information regarding the dislocation density and distribution into the diameter dependence on strength, which we suggest is proportional to the observed power-law.

5.5 Summary

We demonstrate a notable effect of both strain rate and sample size on the compressive strength of single crystalline Cu nano-structures. By determining the activation volume for each pillar diameter and strain rate, we observe a clear transition in the slope of strength vs. strain rate for the two smallest diameters: 75nm and 125 nm while these slopes remain constant for larger pillars. Further, we report a deviation from ubiquitously reported power law size-dependent strength for smallest pillar diameters and at slowest strain rates, as predicted by theory. Based on our experimental findings, existing atomistic simulations and theory, we postulate that this strain rate sensitivity arises from the operation of surface dislocation sources of highly thermal nature. We believe that these findings may provide

further insight into small-scale plasticity and facilitate the layout the full extent of size effects, as well as the corresponding governing deformation mechanisms.

Chapter 6: Influence of a Hard Surface Coating on Strength and Deformation Behavior

The strength in sub-micron pillars is governed by two distinct mechanisms: surface source nucleation in small pillars at slow strain rates and single arm source multiplication at large pillars and fast strain rates. In order for either of these mechanisms to continue to control the pillar strength, the existing and newly produced dislocations must be able to escape at the free surface. In this chapter, adapted from Jennings et al. (*Acta Materialia,* 2012) Ref [69], we apply a hard coating to the pillar free-surface through atomic layer deposition in order to hinder dislocation escape and change the operating deformation mechanisms. We find that in the case of 250nm-diameter pillars, the pillars experience increased strength along with enhanced dislocation storage. Furthermore, hysteresis in the unloading and reloading cycles throughout the test demonstrate the Bauschinger effect: explained through a simple intuitive analytical model as the result of dislocation pile-ups and their resulting back-stresses.

6.1 Introduction

Current understanding of size-dependent strength in nano- and micro-scale crystals is centered around the idea that their overall strength is determined by the stress required to operate dislocation sources [3-9, 12-14, 20, 23, 24, 27, 34-36, 40, 62, 64, 66, 67, 82, 83, 89, 100, 117, 130, 132, 145]. The nature and type of these dislocation sources is a subject of extensive debate; however, one commonality amongst these theories is that the free surface's ability to absorb dislocations is a necessary condition to transition into the source-controlled regime. Two commonly discussed dislocation sources at these length scales are (1) spiral, or single arm sources (SAS), where additional dislocation segments are generated from a rotating "arm" at a single pinning point [4, 25, 26, 117, 143, 146] and (2) surface source (SS), whereby partial dislocation loops emanate from a free surface [8, 31, 81, 117, 147, 148]. The predicted stresses required to operate an SAS in a pillar have been theorized to be a major contributor to the size-effect [25, 26, 76, 149]. Recent reviews on this topic can be found in references [62, 64, 66, 67].

As mentioned above, it is the dislocations' propensity for escape at the free surface in nanocrystals that enables the shift in governing plasticity mechanism from forest hardening to source-activation dominated. Hence, intentionally preventing mobile dislocations from annihilating should result in a very different mechanical behavior. Several research groups have investigated the effects of

passivation layers on the mechanical behavior of free-standing small-scale metallic structures, albeit most of these were concerned with suspended thin film geometries [150-152]. Few reports discuss the results of uniaxial compression experiments on single crystalline, FIB-machined fcc pillars, uniformly coated with hard passivation [105, 153]. This scarcity of literature on the mechanical deformation behavior of coated pillar geometries partly stems from the challenges associated with creating conformal coatings on such high-aspect-ratio nano-scale structures, rendering many of the well-established techniques utilized in micro-fabrication, like evaporation and sputtering, unsuitable. One of the earlier reports by Greer et al. reported the compressive behavior of 500nm -900nm diameter, single crystalline gold pillars conformally coated with Al_2O_3,deposited via atomic layer deposition, ALD [153]. More recently, Ng and Ngan conducted compressions on micron-sized, $1\mu m < D < 6\ \mu m$, single-crystalline aluminum pillars with anion-beam-aided deposition of a W-Ga alloy coating [105]. Both sets of experiments revealed a substantial increase in strength as well as in the amount of hardening. For example, 500nm-diameter Au nano-pillars showed a flow stress increase of 1.5x at 10% strain as compared with their uncoated counterparts [153] while the ~6μm-diameter Al pillars demonstrated increased strengths as large as 2.5x in measured at 2% strain [105]. Post-mortem TEM images in the aluminum experiments revealed a significant build-up in dislocation density, which the authors deemed as a key cause for the observed size-induced strengthening and post-yield hardening. Furthermore, both groups noticed a change in the stress-strain signature from stochastic, jerky flow ubiquitously present in crystalline pillars to smooth, continuous flow in the coated samples. Finally, these experiments revealed that the coating on Al pillars in the micron-size range did not fully suppress the size-effect although the power law exponent was reduced from 0.9 for the uncoated pillars to 0.5 for the coated ones [105].

Of course, experiments alone cannot provide sufficient insight into the physical origins of the observed behavior. To that end, dislocation dynamics (2D and 3D) simulations have been utilized to examine the influence of a passivation layer on crystalline pillar geometries [146, 150, 154]. These simulations reveal a significant, approximately a full order of magnitude, build-up in dislocation densities, leading to higher flow stresses and hardening rates [146, 150, 154]. Furthermore, the amount by which crystalline strength increases as a result of passivation is found to be strongly dependent on pillar diameter, initial dislocation configurations, coating strength, and the affinity of mobile

dislocations for cross-slip. Interestingly, the simulations also find the presence of a size-effect, with the power law exponent being within the range reported for uncoated fcc materials [146, 154].

Before pillar geometries, studies on the effects of passivation on the mechanical behavior of small-scale metallic structures were performed through experiments and simulations on free-standing thin films. For example, the effects of 80nm-thick Si_3N_4/TaN passivation layers on unsupported thin Cu films with thicknesses between 300nm and 1μm were examined by Xiang et al via bulge testing [151, 152]. These authors found a similar strength increase relative to the unpassivated films as in the pillar compression tests [151, 152]. However, in addition to a strength increase, passivated thin films also displayed a Bauschinger effect, which increased with overall pre-strain, a phenomenon not yet investigated in pillars. Generally, the Bauschinger effect describes the phenomenon where the flow stresses upon forward (for example, tension) and reverse (i.e. compression) are non-equivalent [150-152, 155, 156] and is usually manifested by a hysteresis in the stress-strain curves. The magnitude of this deviation is the recovered plastic strain. 2-dimensional DD simulations have attributed the emergence of Bauschinger effect to the reverse movement of dislocations that had piled up during loading, i.e., "back stresses" [150-152, 156].

In this work, we explore the role of a hard conformal coating on the mechanical deformation of electroplated single crystalline Cu nano-pillars with diameters deeply in the sub-micron regime. We focus our investigations on samples with initial diameters between 75nm and 1000nm, conformally coated with a ~5-25nm of Al_2O_3/TiO_2 deposited via atomic-layer deposition (ALD) [153]. We perform uniaxial compression tests with several unloading-reloading cycles at regular strain intervals to explore the Bauschinger effect in pillar geometries. We analyze the evolved microstructure and dislocation configurations via post-compression TEM and discuss the specific impact of the coating on the observed stress-strain behavior. Finally, we explain (1) the higher strengths found in our coated samples in the framework of single arm source-based theory and (2) the emergence of Bauschinger effect by developing a dislocation theory-based simple analytical model.

6.2 Experimental

We fabricate single crystalline copper nano-pillars with diameters ranging from 75 nm to 1000nm via templated electroplating [68] and coat them with 5-25nm thick conformal layers of Al_2O_3/TiO_2 via atomic-layer deposition (ALD). In the pillar fabrication process, vertical cylindrical pores with diameters of the desired pillars are developed in a polymethylmethacrylate (PMMA) template spin

coated onto a seed Au thin film on Si substrate by electron beam lithography. This template is then placed across from a Pt-coated anode in a $CuSO_4$ solution, whereby applying a voltage results in plating single crystalline Cu into the pores. The details of this electroplating procedure have been reported in chapter 2 and in Ref. [68]. The mechanical properties of the exact pillar arrays tested here were recently reported in Chapter 5 Ref. [117]. An SEM image of a representative 200nm pillar is shown in Figure 6.1a. We have also included a weak-beam dark-field TEM image of an uncoated pillar (Figure 6.1b) produced by an identical fabrication process to demonstrate that these pillars are single-crystalline with a non-zero initial dislocation density, $\rho \sim 10^{14} m^{-2}$[117]. Prior to compression tests, those pillars suitable for mechanical testing were identified in an SEM (FEI Nova 200) and marked via focused e-beam deposition of 7 μm-diameter, 1μm-thick tungsten rings.

6.2.1 Atomic-Layer Deposition

Depositing a thin conformal hard coating on high-aspect ratio structures is non-trivial, with ALD being particularly suitable for these types of coatings as it offers atomic-level control of the depositing species one monolayer at a time. Figure 6.1c shows a schematic of this process for an initially uncoated copper pillar whose surface is terminated with oxygen atoms. In the first step (1), a precursor gas is added into an ALD system where the precursor bonds with the oxygen to form a monolayer of the corresponding oxide. The following purge step (2) removes the remaining extra precursor as well as any additional reaction products from the chamber. This surface layer is then functionalized through reaction in a plasma (3) to produce a reactive oxygenated surface. The final step (4) is another purge step to remove the remaining reaction products. This process is repeated until the desired thickness is achieved. All reactions in our process were performed in an Oxford OpAL ALD system (Oxfordshire, UK); whereby 3nm of alumina was deposited with a precursor of trimethyl aluminum (SAFC Hitech, Allentown, PA) and the remaining thickness is titania formed from a titanium tetra-iso-propoxide precursor (SAFC Hitech).

The initial 3nm-thick Al_2O_3 layer was deposited first (1) with a reactant dose of precursor of trimethyl aluminum for 30ms at 120C. This was followed by (2) a 2 second purge followed by (3) a total of 6 seconds in a 300W plasma, 2 seconds for gas stabilization and 4 seconds for plasma power on. Finally, (4) the last purge step also lasted two seconds [70]. This process was repeated until the 3nm layer was complete. The following TiO_2 layer was added with a titanium tetra-iso-propoxide precursor at 200C. The remaining thicknesses of 2nm at pillar diameters, D, 75nm-150nm; 7nm at

D~200nm, and 22nm at D ~ 500nm- 1000nm, respectively, were deposited via a process similar to the alumina deposition [71]. In both of these procedures, a remote oxygen plasma functionalized the surface with oxygen atoms such that the surface was identical to the initial conditions. It is expected that oxygen atoms and ozone are the most likely reactive species as there was a showerhead separating the plasma from the substrate.

We deposited coatings of ~5nm thick alumina/titania for 75nm, 125nm, and 150nm-diameter pillars; ~10nm thick for 200nm-diameter pillars, and ~25nm thick for 500nm and 1000nm-diameter samples. This choice of coating thicknesses stems from the constant relative area fraction of roughly 17% relative to the copper pillar diameter, with the exceptions of the smallest and largest pillar diameters - 75nm and 1000nm - which have area fractions of ~25% and ~10%, respectively.

In order to determine the number of cycles necessary for a precise thickness, we performed test depositions on Si and measured the resulting films with ellipsometry. For the pillar samples, we assessed the resulting coating thickness and integrity by analyzing bright-field TEM images of a representative passivated pillar, with the particular example of an as-fabricated and coated 200nm pillar shown in Figure 6.1d. In this image, the bright halo surrounding the pillar is the ~10nm thick Al_2O_3/TiO_2 coating deposited via the described ALD process, and is clearly conformal, i.e., having nearly identical thickness at each pillar location. Figure 6.1e shows a representative SEM image of a coated 200nm nano-pillar immediately before a compression test.

6.2.2 Mechanical Tests

Uniaxial compression tests were performed in an Agilent (Santa Clara, CA) G200 nanoindenter with the commercially acquired Berkovich diamond tip milled into a 7 micron diameter circular flat punch. As our recent work unambiguously demonstrated a substantial strain rate dependence in identical Cu nanopillars [117], we performed our compression tests in nominal strain rate control, i.e., maintaining an ostensibly constant strain rate of 10^{-3} s^{-1}. This nanoindenter is inherently a load-controlled machine, and therefore strain rate control is achieved through a software controlled feedback loop on displacement. Unloading segments were performed at the same nominal strain rate at increments of 2% strain throughout the test in order to elucidate the presence or absence of a Bauschinger effect. After compressions, nanopillars were first examined in the SEM in order to correlate the observed mechanical behavior with deformed pillar morphology. In order to correlate the real-time deformation behavior with the stress-strain curve, several compression tests were performed *in situ* inside

SEMentor, a custom-built nanomechanical testing instrument comprised of SEM (FEI Quanta 200 FEG) and a nanomechanical module similar to nanoindenter (Nanomechanics Inc., Oak Ridge, TN))[36]. Post-deformation TEM images of selected pillars after deformation were used to examine the defect-driven microstructural evolution.

6.3 Results

6.3.1 200nm-diameter Pillars:

Figure 6.2a shows the compressive engineering stress-strain curve of a coated, 200nm diameter pillar with a zoomed-in inset showing the first 4% of strain. As evident from the stress-strain curve, the initial loading is nearly elastic, followed by two displacement bursts, commonly understood to correspond to dislocation avalanches [93, 94, 157]. This type of signal, nearly elastic loading followed by displacement bursts, is characteristic of nano-crystals' deformation as evidenced by a very similar signature in the compressive stress-strain curve of an identical but not coated 200nm diameter Cu nano-pillar, Figure 6.2b. Interestingly, we observe the stochastic signal in the compressions of both coated, Figure 6.2a, and uncoated, Figure 6.2b, samples, a finding in contrast to the majority of Ng and Ngan's compression tests on micron-sized coated Al samples [105] and those by Greer, et al [153]. Our *in situ* SEMentor tests reveal that the first large burst frequently coincides with cracking and subsequent delamination of the coating, an example of which is shown in Figure 6.3.

We use two different metrics to estimate the strengths of the coated pillars: (1) the flow stress at the first observed displacement burst and (2) the flow stress at a "final" strain, i.e., where

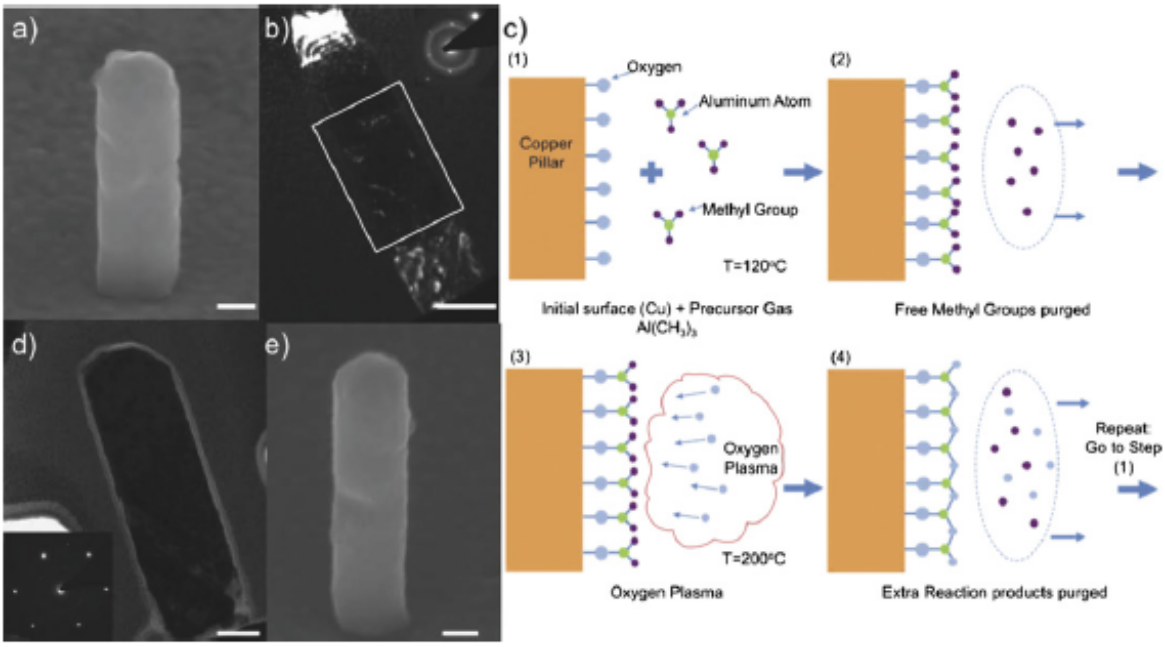

Figure 6.1 Morphology and microstructure of single crystalline electroplated Cu nano-pillars before and after the coating deposition. a)SEM image of a 200nm-diameter sample. b) TEM image of an as-fabricated pillar (weak-beam dark-field conditions). The bright lines inside the white box correspond to individual dislocations (Reprinted with permission from [8], Copyright (2010) by The American Physical Society). c) Schematic of the ALD deposition process showing the details of each monolayer formation. d) Bright-field TEM image clearly showing the conformal passivation layer, and e) SEM image of a typical 200nm-diameter coated pillar. All scale bars are 100nm and all SEM images taken at 52° tilt.

the flow behavior can be characterized as "steady-state". Due to the geometric imperfections in the pillar tops, distinguishing the first burst corresponding to the overall pillar deformation and a local feature in the pillar top due to roughness is challenging. Therefore, determining strength based on methodology (1) requires defining the burst after $e = 0.02$ and setting a threshold for the burst extent, $\Delta e \geq 0.002$. These values were chosen based on extensive analysis of numerous stress-strain curves and deformation videos. The second methodology describes the final, rather than initial, strength measurement. In coated pillars, this corresponds to the maximum stress prior to the extensive, often-catastrophic strain burst due to the cracking of the coating, which usually occurs at strains between 0.02 and 0.06. Since the uncoated pillars do not have such a maximum stress, in order to effectively compare their "final" strengths with those of the coated pillars, we define their "steady-state" stresses as flow stresses at an appreciable strain of ~10% since they have virtually non-existent hardening in that region. This steady-state strength can be viewed as an estimate of

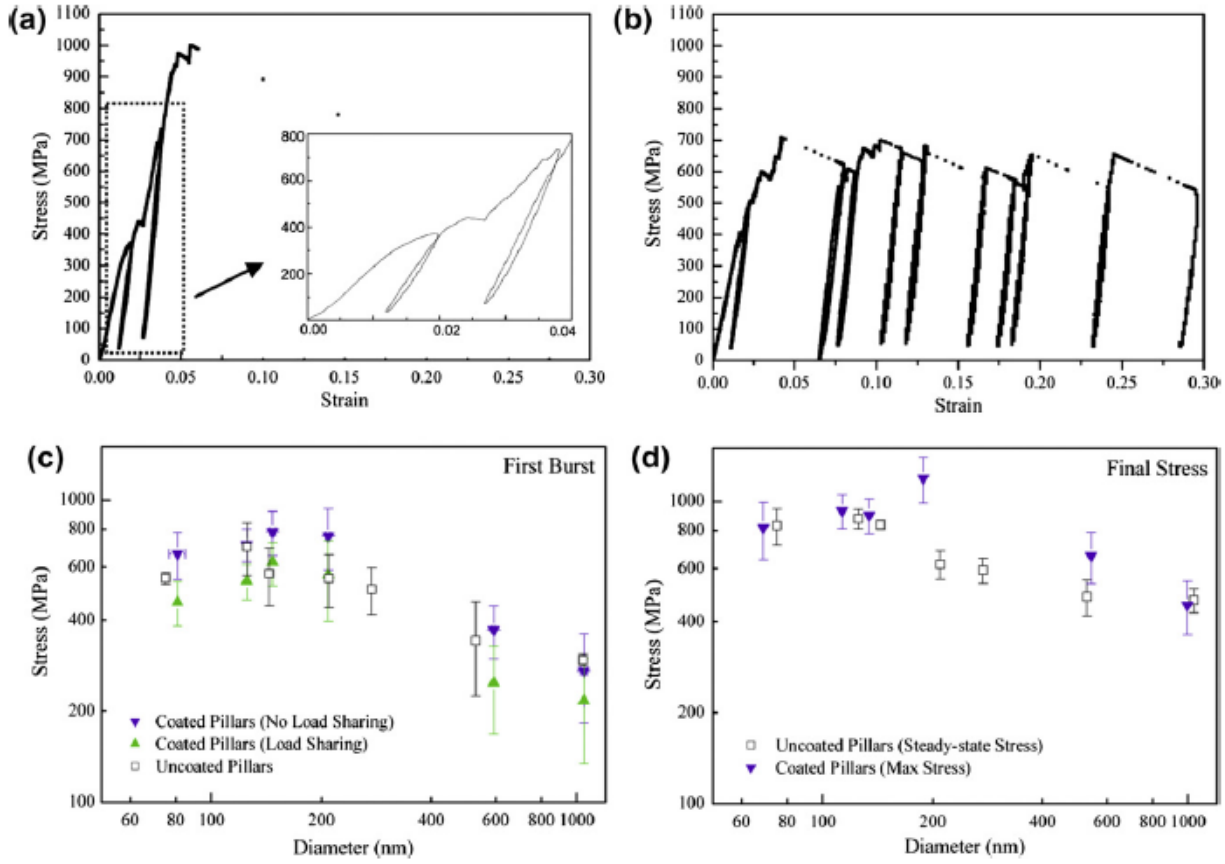

Figure 6.2 Engineering stress-strain curves of (a) a coated 200nm pillar with inset revealing the zoomed-in region of the initial 4% of deformation and (b) an uncoated 200nm pillar. Log-log plots of flow stress at (c) first burst and (d) final strength vs. pillar diameter in coated and uncoated pillars. Axis scales are intentionally equivalent.

the average stress required to continuously produce and release dislocation avalanches. Utilizing these two methodologies, we observe the average initial burst strengths for the coated vs. uncoated 200nm-diameter pillars, to be quite similar: the coated pillars reach 590 ± 148MPa whereas the uncoated pillars reach 549 ± 110 MPa. However, their "final" strengths differ substantially: the average maximum strength achieved in the coated case is 970 ± 170 MPa and the steady-state strength in the uncoated sample is 619 ± 66 MPa, a difference of 56%.

6.3.2 Models & Size-Dependent Strength

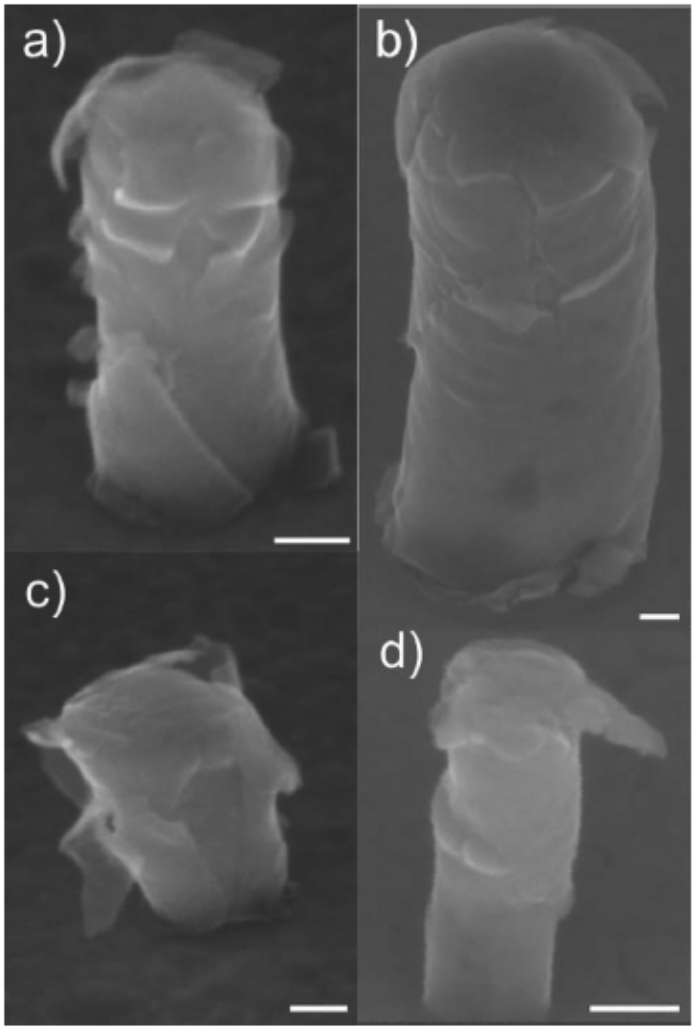

Figure 6.3 Post compression SEM images of coated pillars with diameters of (a,c) 200nm, (b) 500nm, and (d) 150nm. All scale bars are 100nm and images taken at 52° tilt.

Figure 6.2c shows the engineering stress range for the first burst (methodology (1)) as a function of pillar diameter. For the uncoated samples, we re-analyzed the raw data reported in Ref. [117] according to this described methodology. For the coated pillars, we provide the estimates of the stress in Cu with and without load sharing with the coating. Details of these methods are provided in the supplementary information [158]. We plot both extremes in Figure 6.2c, with the error bars corresponding to the standard deviation. It is clear that for all pillar diameters, the uncoated vs. coated samples show little discernible difference in strength of the initial burst, suggesting that the coating has little effect on the initial dislocation avalanche. In contrast, Figure 6.2d conveys a notable difference when comparing the same pillar compressions taken at the maximum stress for coated pillars and the "steady-state" stress for uncoated pillars. We only plot the no-load sharing results since prior to attaining this maximum stress, typically found at 10% strain, the pillar has usually already undergone some deformation, which led to cracking of the coating. We find that pillars with the largest diameter of $1\mu m$ show no difference between coated and uncoated samples; while the 500nm-diameter coated pillars are 37% stronger than the equivalent-diameter uncoated samples, and the 200nm-diameter pillars exhibit a dramatic increase, 93%, in strength over the as-fabricated counterparts, a result similar

to

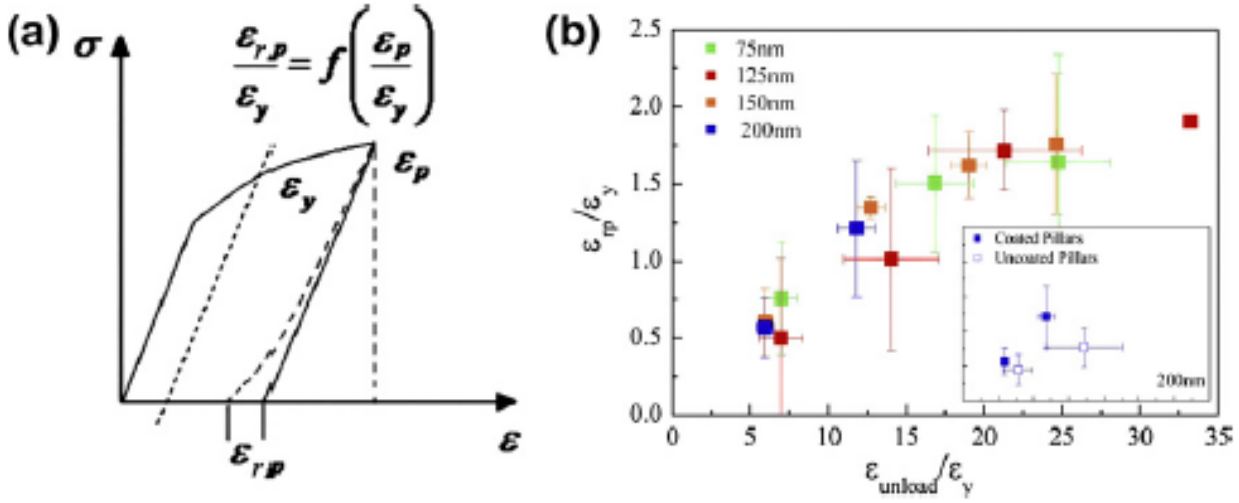

Figure 6.4 Schematic illustrating methodology for measuring reverse plastic strain based on unloading-reloading hysteresis loops. (b) Reverse plastic strain normalized by yield strain as a function of unloading strain normalized by yield strain for each pillar diameter. Inset: Comparison of reverse plastic strain for 200nm coated vs. uncoated pillars. Axes scale in (b) and inset is identical.

Ng and Ngan's work on Al who report an 80% increase for 1.2μm-diameter pillars[105], and to Greer, et al's work on Au who observed a 50% increase at 500nm pillars [153]. Similarly to 1 micron-diameter pillars, the three smallest diameters: 150nm, 125nm, and 75nm also show no change in their strength between coated and uncoated samples, a point addressed in the Discussion section.

6.3.3 Bauschinger Effect

All compression tests contained several unloading-reloading segments prescribed at intervals of 2% nominal strain (Figure 6.2a,b). We observe that these reversals in the loading direction are manifested by hysteresis loops in the stress-strain curves, which allow us to measure the amount of recovered plastic strain, ε_{rp}, following the procedure outlined by Xiang et al. and schematically illustrated in Figure 6.4a [152]. In this work, the recovered plastic strain is measured by subtracting the difference between the initial unloading slope and the measured unloading segment at a common stress-level of ~60MPa chosen in order to measure the release of the preceding internal build-up of dislocations at a common, constant applied stress. This common stress is non-zero to maintain contact between the indenter tip and the pillar top throughout the test. We plot the recovered plastic strain normalized by the yield strain, ε_y, calculated as $\varepsilon_y = {}^{\sigma_{1st\ burst}}/_{E_{<111>}}$ where $\sigma_{1st\ burst}$ is the stress at the first burst

and $E_{<111>}$ is elastic modulus in the pillar's orientation: <111>, as a function of applied strain, also normalized by the yield strain, for all successful compressions up to a catastrophic strain burst, shown in Figure 6.4b. This graph clearly indicates that the recovered plastic strain increases with pre-strain for all pillar diameters, a finding in agreement with similar studies on thin films [152]. Also shown in the inset in Figure 6.4b is the same plot for the uncoated vs. coated 200nm pillars provided for comparison. Concurrent evaluation of the uncoated vs. coated cases reveals – perhaps surprisingly - that both the coated and uncoated pillars possess a nonvanishing recoverable plastic strain that increases with applied strain; however, we find that the coating significantly amplifies this effect by a factor of ~2. Hence, we find that the coated pillars demonstrate a definite increase in recovered plastic strain leading to the presence of the Bauschinger effect.

6.4 Discussion

Our experiments reveal three main observations: (1) Coated 200nm single crystalline copper nano-pillars sustain stresses up to 93% larger than their uncoated counterparts at equivalent diameters prior to failure; (2) stress-strain curves of coated pillars contain discrete, intermittent strain bursts; and (3) coated pillars exhibit a Bauschinger effect that increases with increasing pre-strain. In order to explore the origins of these phenomena, microstructural analysis via TEM is performed on cross-sections of coated pillars after deformation.

6.4.1 TEM Microstructure

The key distinction between the experiments presented here and the plethora of ones existing today is that the dislocations are intentionally prevented from escaping at the free surfaces by the hard passivation layer. Therefore, we first examine whether the dislocations are, indeed, being trapped inside the pillar after compression tests. Figure 6.5 shows a bright-field TEM image with the inset containing the corresponding diffraction pattern (DP) of a 200nm-coated pillar. These images clearly verify that the dislocations were trapped inside the pillar as indicated by the formation of complex, dense dislocation networks, and even sub-grains. Further, the notable streaking of the individual diffraction spots in the DP serves as evidence of extensive plastic deformation and the

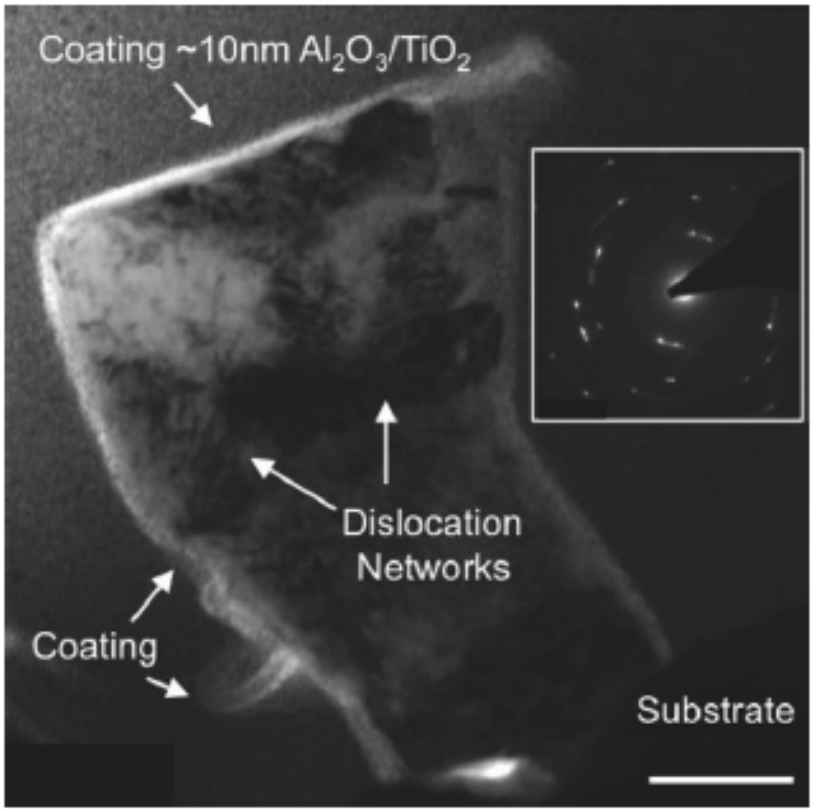

Figure 6.5 Bright-field TEM image of compressed 200nm-diameter coated pillar showing dense dislocation networks and the fractured coating. Diffraction pattern in inset clearly shows streaking in the diffraction spots.

presence of multiple different crystal orientations [159]. While a build-up of dislocation density has been observed in larger, micron-sized $D > 1000$ nm samples and at shear strains larger than 10% [24]; these sub-grains are markedly different from what is seen in the uncoated pillar compressions [24, 28, 82]. Furthermore, the deformation of uncoated single crystalline fcc nano-pillars, those with diameters deeply in the sub-micron regime, $D \leq \sim 200$ nm, is generally characterized by a notable decrease in the mobile dislocation density upon deformation, and therefore never forming dislocation sub-grains [14, 28]. This dense dislocation microstructure in post-mortem coated pillars agrees well with those in the W-coated Al micro-pillars, suggesting that the coating results in the global dislocation density build up as it traps any mobile dislocation traveling towards the outer surface at the pillar-coating interface [105].

6.4.2 Strengthening from Dislocation Storage

As Figure 6.5 clearly reveals a significant build-up of dislocations in the coated *D*~200 nm Cu nanopillars, we now concern ourselves with the question of whether the evolved dislocation density is a reasonable explanation for the observed increase in flow stress, as suggested by Ng and Ngan [105]. Estimating the dislocation density directly from the TEM images shown in Figure 6.5 is virtually impossible as the dislocations are densely packed in localized regions, i.e., sub-grain

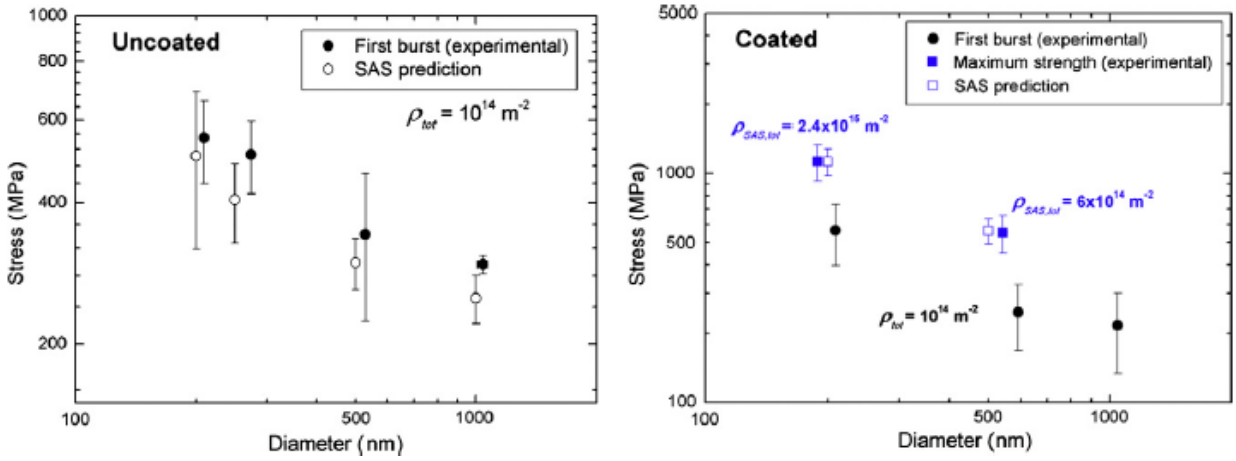

Figure 6.6 Log-log plot of (a) Experimental data for uncoated pillars (closed circles) vs. single-arm source (SAS) model predictions (open circles) for stress at first burst as a function of diameter. Error bars correspond to standard deviation. Initial dislocation density shown is drawn from TEM analysis of uncoated pillars. (b) Coated experiments (blue, closed squares) vs. single-arm source model (blue, open squares) for maximum stress as a function of pillar diameter. Different simulated initial dislocation densities are shown. Black, closed circles show experimentally measured stresses at first burst.

boundaries. Therefore, we provide an alternative procedure for quantifying the dislocation density in strained pillars based on the single arm dislocation source model by Parthasarathy et al., describing the size-dependent strength of micro- and nanopillars [24, 26, 160, 161]. Several existing studies have convincingly demonstrated that single arm sources control plasticity of fcc nanopillars with diameters greater than ~200nm [25, 26, 149]. As a result, a model based on the operation of single arm sources, may be appropriate to estimate the dislocation density increase in our coated pillars for the samples with diameters of 200nm and 500nm.

Building upon analytical models for single arm sources [24, 26, 160], the general equation for overall shear stress in a small-scale sample is comprised of the lattice friction stress (first term on RHS in Eq. 6.1), the elastic interactions stress (2nd term on the RHS in Eq. 6.1), and the line tension stress (last term in Eq. 6.1):

$$\tau_i = \tau_o + 0.5\mu b\sqrt{\rho_{tot}} + \frac{\mu b}{4\pi\lambda_i}\ln\left(\frac{\lambda_i}{b}\right) \qquad (6.1)$$

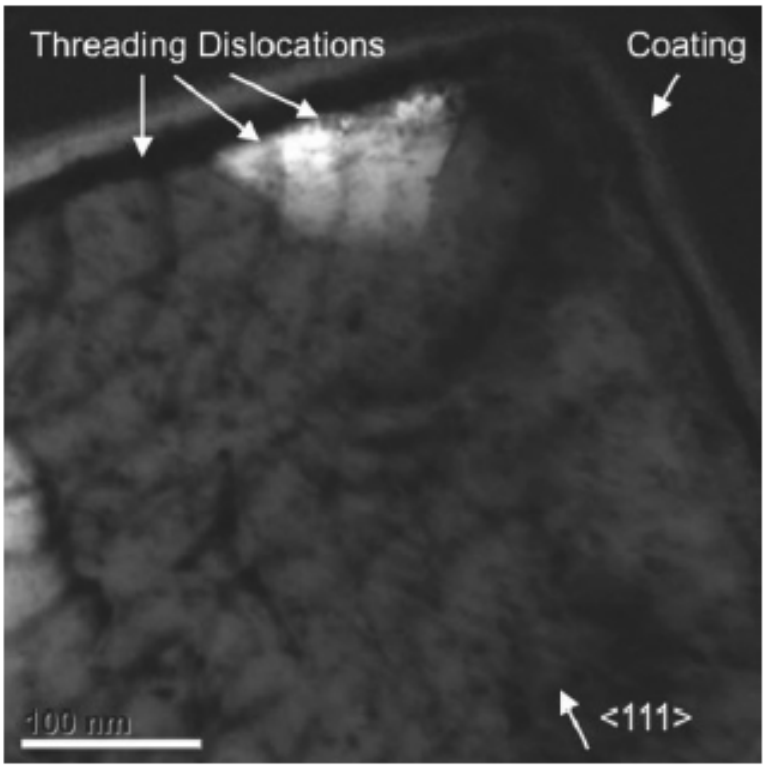

Figure 6.7 Bright field TEM image of the top right corner of an as-coated 500nm-diameter pillar before deformation. Regularly-spaced threading dislocations emanate from the coating-pillar top interface.

where τ_i is the resolved shear stress for the activation of the i^{th} single arm dislocation source, τ_0 is the lattice friction stress, μ is the isotropic shear modulus, b is the magnitude of the Burgers vector, and ρ_{tot} is the total dislocation density: material and microstructural parameters with identical applicability in the framework of classical bulk dislocation theory [50]. On the other hand, λ_i is a parameter relevant to single arm sources in pillars, as it represents the shortest distance between the source's pinning point and the free surface within the same elliptical slip plane. Further details of the model can be found in the supplementary information [158].

First, we explore the applicability of the model to our experiments by estimating the strength of the first burst in uncoated pillars from the initial dislocation previously reported for as-fabricated electroplated copper pillars: $\rho_{tot} = 10^{14} m^{-2}$ [82]. These results, plotted in Figure 6.6a, show excellent agreement between the model and experiments, and therefore we extend the model to solve the reverse problem – i.e. to estimate the dislocation density in the coated *D*~200 nm pillars when they attain their maximum strength. When the coated pillars reach the maximum stress, the coating partly cracks and delaminates as observed in in-situ compression tests, Figure 6.3. The coating cracking allows for normal slip processes to proceed in these localized regions, as with uncoated nanopillars, suggesting that this model is still applicable to calculate the maximum strength and the corresponding dislocation density in coated nanopillars. Here we use the no load-

sharing analysis, i.e., in the situation where the coating is discontinuous in several locations, since the cracked coating is unable to support any significant load. To find the dislocation density in the coated pillars at maximum stress, we increment the density by the amount $\Delta\rho_{tot} = 10^{14}$ m^{-2} until the calculated strength reaches the measured no-load-shared maximum strength: ~1129 MPa for D~200 nm (see Figure 6.2d). At this strength, the model predicts a dislocation density of 2.4×10^{15} m^{-2}, a value ~24 times larger than that observed for the uncoated pillars. This dislocation density is also a typical density of dislocation sub-grains [162], which agrees with our TEM observation of D~200 nm pillar. We also performed this calculation for coated nanopillars with D~500 nm, whose maximum strength is ~552 MPa (assuming no load-sharing). The necessary dislocation density to sustain these stresses would be 6×10^{14} m$^{-2,}$ or a factor of 6 higher than that in the uncoated pillars. Therefore, this model estimates a significant increase in dislocation density upon compression as a result of the coating, a finding in qualitative agreement with the TEM image. Figure 6.6b explicitly shows the increase in dislocation density in the plot of diameter vs. strength for D~200 and 500nm pillars.

In this plot, the initial dislocation density of ~10^{14} m^{-2} in the as-fabricated 200nm samples may seem high, however this is an inevitable consequence of the very small pillar volumes – i.e. even a single dislocation loop of ~ 7 atoms in circumference leads to a jump in dislocation density from 0 up to ~10^{11} m^{-2}. Indeed, the number of dislocation segments in such samples is estimated to be only 9. Given these few potential dislocation sources, an extensive build-up of dislocations and their organization into complex structures (as observed experimentally, see Figure 6.4) may seem unreasonable. However, recent 3D dislocation dynamics simulations deem such a significant dislocation density increase in coated nano-pillars feasible and provide microstructure-based arguments [146, 154]. In their work, Zhou and LeSar showed that when dislocations are able to cross-slip, it occurs more frequently in the coated pillars compared with the uncoated ones because dislocations in the latter can easily escape at the free surface. In coated pillars, however, the initially mobile dislocations pile up at the surface-coating interface, thereby facilitating cross-slip through back-stresses. Cross-slipped dislocations, in turn, can serve as subsequent dislocations sources, producing additional dislocations on other slip planes. Hence, we may expect the formation of sub-grains, from an extensive build up of dislocations, commensurate with our post-compression TEM analysis (Figure 6.4), as well as with Ng and Ngan's work on Al micropillars [105]. The significant build up of dislocations will likely result in local stress heterogeneities, which may substantially influence the

operation and availability of dislocation nucleation sources. While investigating the local strain throughout pillar deformation is beyond the scope of this work, a more in-depth discussion on this topic can be found in Refs. [13, 130, 132, 156, 163]

6.4.3 Hoop Stress and Coating Failure

The analytical model described above estimates the required dislocation density for pillar diameters of 200nm and 500nm responsible for the observed strength increase (Figure 6.2d). The choice of only these two diameters stems from our discovery that the remaining pillar diameters –i.e. 75nm, 125nm, 150nm, and 1000nm do not exhibit any strength difference relative to the uncoated pillars. In order to investigate this observation, we first examine the three smallest pillar diameters, all sharing the same nominal coating thickness of ~5nm. However, while the area fraction of the coating in these smaller pillars: 75nm (~25%), 125nm (~17%), and 150nm (~15%) is larger than or similar to pillar diameters of 250nm (~17%) and 500nm (~17%), the absolute thickness of ~5nm appears to be insufficient to effectively trap dislocations. Pillars within this small size range, 75nm to 150nm, have been shown to exhibit a deviation from the size effect at the strain rate of $\dot{\varepsilon} = 10^{-3}s^{-1}$ used to perform these experiments. In the work of Jennings et al. [117] this shift in size effect was ascribed to the activation of surface dislocation sources, a process that is expected to be strongly influenced by the surface stress state. While investigating this topic in-depth is outside of the scope of this work, a subject for a future study is to examine the range of possible coating thicknesses sufficient to affect the dislocation nucleation mechanisms inside the pillar.

In larger pillars with diameters of 200nm, 500nm, and 1000nm the post-deformation SEM images consistently show axial cracks in the coating suggesting that the coating fails due to loading along the circumference of the pillar, i.e., hoop stresses. Assuming that the coating can be described as a thin walled pressure vessel, the hoop stress in the coating can be found by: $\sigma_{hoop} = F\frac{D}{2t}$ where F is the pressure normal to the coating, $D/2$ is the pillar radius, and t is the coating thickness. Examining the equation for the hoop stress, we notice that for the 200nm, 500nm, and 1000nm pillars, the geometric factors, $D/2t$, are ~10,10, and 20, respectively. The factor of 2 increase in 1000nm pillars relative to 200nm and 500nm may cause the coating to fracture prior to dislocation build up, thus generating no additional strengthening due to the coating for these 1000nm pillars. Furthermore, the presence of the hoop stress in pillars is an example of the differences between experiments on coated

thin films and coated pillars. Due to the geometric differences between these experiments: two-dimensions (thin films) versus three-dimensions (pillars), thin films do not have a hoop stress and therefore the coating will not fail under the same conditions, stress and relative coating thickness. Interestingly, we see regularly spaced threading dislocations in the as-coated 500nm pillars shown in a bright-field TEM in Figure 6.7. These threading dislocations likely emanate from misfit dislocations exist at the interface suggesting a complex stress state at the pillar-coating interface. Details of these threading dislocations can be found in the supplementary information [158].

6.4.4 Discrete Burst Stress-Strain Signature

As seen in Figure 6.2a and 6.2b coated pillars' stress-strain signature is characterized by rapid strain bursts, similar to that in uncoated pillars. This result stands in contrast with the results in previous compression tests on coated pillars [105, 153], where Ng and Ngan observed continuous stress-strain curves in the majority of their tests [98]. However, they also reported that the smallest pillars, D<1.2um, with thin coatings resulting in area fractions less than 0.26, also contained intermittent displacement bursts and displayed increased strength. These two reports suggest that a combination of the pillar diameter and the coating thickness controls the stress-strain signature. Simulations by El-Awady et al. [97] corroborate this result through demonstrating that weaker coatings lead to larger strain bursts and a jerky stress-strain behavior; whereas stronger coatings promote shorter and slower strain bursts, leading to a continuous deformation response. The combination of experimental and simulations results suggest, as may be expected, that coating thickness and coating strength are synonymous when discussing transitions between jerky stress-strain behavior and continuous flow.

6.4.5 Bauschinger Effect

6.4.5.1 Experimental Results

Another consequence of the hard coating is the sample's ability to recover plastic strain upon unloading, an example of the Bauschinger effect, as illustrated schematically in Figure 6.4a. In a regular unloading-loading segment in compression (or tension), the stress-strain curve will trace the same exact path during unloading and then reloading demonstrating purely elastic behavior; however, in the coated pillars compressed here, during unloading, the curve deviates from this purely elastic behavior as some of the "permanent" strain is reversed, a Bauschinger effect. Figure 6.4b demonstrates the extent of this reverse plastic strain for all the unloading-reloading cycles as a function of applied strain for coated pillars with diameters between 75nm and 200nm prior to a catastrophic burst, frequently

occurring before 10% strain. Interestingly, these measurements demonstrate that: (1) the magnitude of the Bauschinger effect normalized by yield strain appears to be independent of diameter, and (2) the amount of recovered plastic strain increases with increasing pre-strain, similar to that seen in previous experiments in polycrystalline copper thin films and simulations [150-152]. Comparing the observed Bauschinger effect in the experiments performed here and those previously reported for passivated thin films, we find that the magnitude of the reverse plastic strain in our experiments is larger by a factor of 4 to 5. This difference in magnitude may be due to a number of factors associated with different experimental setup, including: (1) while the critical thicknesses of the pillars (75nm to 200nm) and thin films (350nm to 900nm) are similar, the geometries are significantly different; (2) the pillars are single crystalline; whereas, thin films are polycrystalline with a grain size on the order of ~400nm [152] resulting in many internal grain boundaries in thin film geometries; (3) the strain domain over which both experiments were reported are different: 0.2% to 1% in thin films and 2% to 10% in pillars; (4) the loading geometries: bulge testing (thin films) and uniaxial compression tests (pillars) as well loading conditions: strain rates and experimental constraints are different; (5) and finally different stress states: thin films have a 2-D stress state (plane strain) in contrast to a 3-D stress-state in pillars [151, 152]. Larger pillars with diameters of 500nm and 1000nm demonstrated no observable Bauschinger effect even though in the case of 500nm, the pillars exhibit strengthening (Figure 6.2d). Conversely, pillars with diameters between 75nm and 150nm demonstrate a clear Bauschinger effect but no observable strengthening (Figure 6.2d). These two results suggest that strengthening in pillars and the Bauschinger effect are not necessarily coupled.

In order to establish the baseline for the emergence of Bauschinger effect in our compression tests, we also conducted similar experiments on the as-fabricated 200nm Cu pillars. The inset of Figure 6.4b shows similar analysis for the uncoated pillars (open symbols), as compared with the coated 200nm pillars (closed symbols). While the measured hysteresis in these uncoated pillars is non-zero, it is less than that found in coated pillars by a factor of 2, demonstrating that the coating has a clear influence on the amount of recovered plastic strain. The non-negligible Bauschinger effect exhibited by the uncoated pillars in our experiments is in close agreement with that observed through discrete dislocation dynamics (DD) simulations of the compression of *un*-passivated sub-micron pillars with material properties (shear modulus, Burgers vector, and Peierls barrier) similar to that of single crystalline copper. In those DD simulations, similar initially high dislocation densities, ~10^{14} m^{-2}, result

in the build-up of dislocations [156]. A mechanism for such a build-up in our experiments may be explained by the presence of slip planes perpendicular to the pillar loading axes, and hence experience no resolved shear stress upon compressing the pillars along their <111> direction [82]. As a result, the dislocations residing in this plane cannot be considered as mobile, as shown in the post-deformation TEM image [117]. The interactions between such dislocations and those traveling in the active, inclined slip planes, resulting in the creation of pinning points and locked segments, may contribute to the observed Bauschinger effect.

6.4.5.2 Analytical Model

Investigating the role of the coating as a source of hysteresis deeper, we developed a simple 1D analytical model based on dislocation theory that predicts the emergence of hysteresis from dislocations piling up against the hard coating. Recent 3D DD models on coated nano-pillars considered the cases of (1) an impenetrable coating and (2) dislocations able to break through the coating [146, 154]. However, samples in these simulations were loaded monotonically and thus did not explore the loading-unloading hysteresis. Similar 2D simulations of thin films with an impenetrable coating showed smooth hardening and a Bauschinger effect accompanied by hysteresis loops [164, 165]. Each of these studies incorporates varying aspects of the broad complexity of this problem. As an alternative approach, we consider an approximate problem in hopes of offering physical intuition for the Bauschinger effect. Hence, the aim of this model is not to act as an exact numerical comparison, but rather as a physically founded qualitative complement to the experimental results.

Starting with a cylindrical pillar, we isolate a resolved slip-plane and consider it initially containing only a dislocation source offset from the center with a given strength, τ_{source}. When activated, i.e., when the applied stress exceeds this strength, the source emits a dislocation loop, and has no short-range interaction with the dislocations it emits throughout the simulation. Viewed

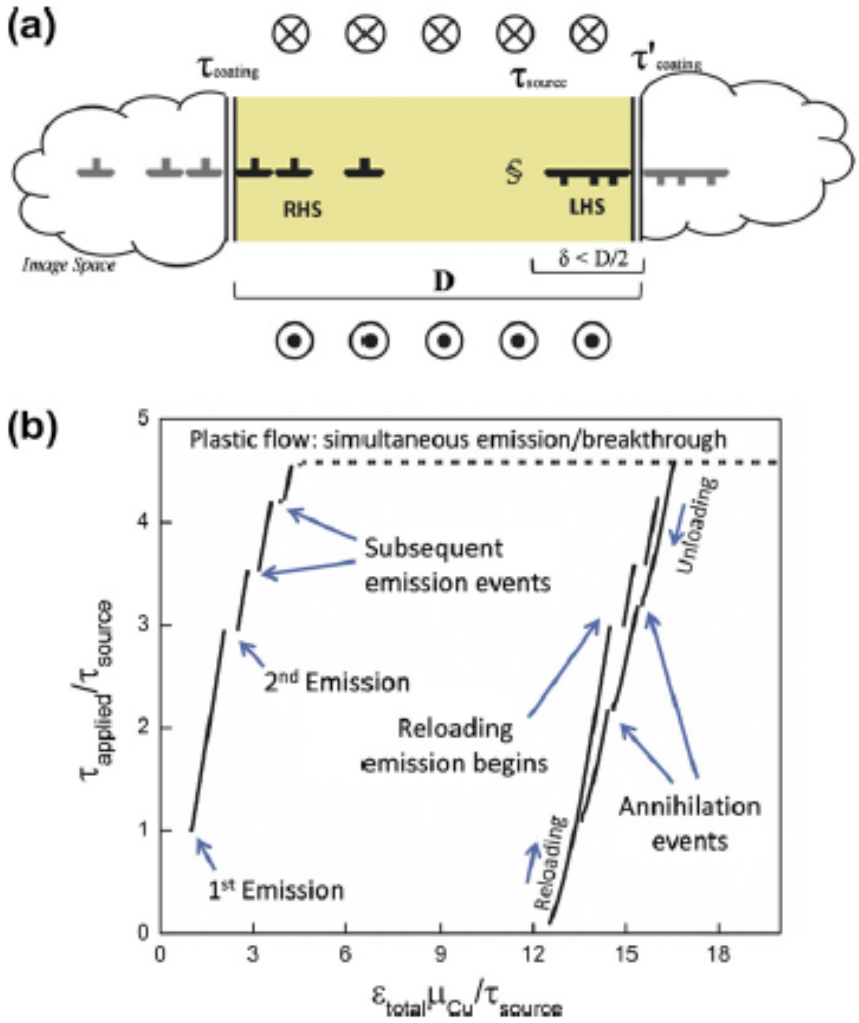

Figure 6.8 a) A 2-dimensional schematic showing pillar geometry for the analytical model. Yellow region corresponds to the pillar cross-section, and cloud-like regions on both sides represent dislocation image space. Dislocations are treated as screw-type and shown as $\perp$ or $\top$ depending on dislocation orientation. Section sign corresponds to the dislocation source, and grayed-out dislocations in the image-space represent image dislocations. For screw-type, the applied shear vectors directed into and out of the page are shown above and below the plane. b) Shear stress normalized by the source strength vs. dimensionless strain parameter generated by the analytical model with material properties representative of Cu: $\mu_{Cu} = 48$ GPa and $b = 0.256$ nm.

along a cross-section of the plane, the resulting loop is seen as two oppositely oriented segments on either end of the slip plane, as shown in Figure 6.8a. As this slip plane is isolated we do not consider interactions with other slip-planes or 3-dimensional processes such as cross-slip. At the boundary of the domain is the coating with given strengths $\tau_{coating}$ and $\tau'_{coating}$ on either side whose actual values may depend on elastic modulus or lattice mismatch, coating thickness, and orientation of the

dislocation and interface [166]. The strengthening of these collective interactions represents the Koehler barrier strength that sets a threshold stress by which dislocations are allowed to pass through the coating [167]. Here we have taken $\tau_{coating} = \frac{4}{3}\tau'_{coating} = 4\tau_{source}$, values comparable to those used in previous coated pillar simulations [146]. The difference in coating strength is reasoned from the variation seen in coating thickness and possible variations in its bonding strength that naturally arise during ALD deposition on a non-atomically smooth pillar surface. Figure 6.8a shows the geometrical diagram of the described setup. Details of the calculation can be found in the supplemental section [158].

Figure 6.8b shows the stress-strain curve resulting from the model, where the strain is a summation across 10 identical slip planes. Starting with the emission of the first loop, the loading curve is marked by discrete events, each corresponding to source activation. This continues, as the traveling dislocations are piled up against the coating. Eventually continuous plastic flow (with no hardening) begins, where the applied stress is sufficiently high such that both source emission and coating penetration occur simultaneously. Plastic deformation continues until the unloading, where the dislocations move back towards the center of the domain and annihilate when two oppositely oriented dislocations are in proximity of each other. The applied stress is then increased, and a clear deviation of the reloading curve from the unloading curve is apparent. This hysteresis loop is only seen when a coating strength is applied at the boundary. In exploring this models' virtues and limitations we see that as expected, the model shows no difference in stress-strain curves between unloading vs. re-loading directions for the case of free surfaces, which suggests that the Bauschinger effect is caused entirely by the presence of the coating. In contrast with earlier DD simulations on uncoated sub-micron copper-like pillars that exhibit a Bauschinger effect [156], this model treats each dislocation source as independent, i.e., the dislocations produced from one source do not interact with dislocations from a different source. As a result, during either the loading or unloading phase of the hysteresis loop in Figure 6.8b, the deviation of the stress-strain curve from linear elasticity is a result of the emission and movement of dislocations (plasticity gained) or relaxation and annihilation of dislocations (plasticity recovered). Considering an increase in coating strength, more dislocations will be stored within the coating and thus greater deviation. We would then expect to see an increase in hysteresis with an increase in coating strength. These modeling results are encouraging in that they

appear to capture behavior seen experimentally in a model that is not computationally expensive and can be interpreted through classical dislocation theory.

6.5 Summary

We demonstrate a nano-fabrication methodology for creating 75 nm to 1000nm diameter electroplated single crystalline Cu nano-pillars coated with a conformal 5nm-25nm layer of Al_2O_3/TiO_2. Uniaxial compression experiments indicate that plasticity commences via intermittent strain bursts, with coated pillars generally exhibiting (1) higher strengths over their as-fabricated counterparts and (2) hysteretic loops during unloading/re-loading, whose magnitude increases with pre-strain. Microstructural analysis reveals large dislocation networks in post-compressed coated pillars as compared to the significantly reduced mobile dislocation densities in un-coated pillars. We explain the ~600MPa increase in strength and deformation-induced dislocation storage up to densities of $2.4x10^{15}$ m^{-2}, in 200nm-diameter nanopillars, an order of magnitude increase over as-fabricated samples, through a modified single-arm source strength model. Finally, we develop a 1-dimensional dislocation theory-based analytical model, which reveals the emergence of Bauschinger effect with a simple application of a penetrable coating.

Chapter 7: Heterogeneous Dislocation Nucleation from Surfaces and Interfaces As Governing Plasticity Mechanism in Nano-scale Metals

Previous chapters have shown two different operating mechanisms in single crystalline electroplated copper pillars. At slow strain rates, 10^{-3} s^{-1}, pillar diameters 150nm and above show a size-dependent strength similar to previous reports. Below 150nm, the size effect vanishes, as the strength transitions to a relatively size-independent regime dominated by surface source nucleation. In this chapter, adapted from Ref. [168], the experimental results presented in previous chapters are discussed in the framework of recent *in situ* TEM experiments observing both deformation mechanisms in pillars and thin films on flexible substrates - single arm source operation in larger samples and partial dislocation nucleation from stress concentrations in smaller structures. Several proposed models for surface dislocation nucleation are discussed and compared with experimentally measured quantities: strain rate sensitivity and activation volume in order to gain insight into the governing physics,

7.1 Introduction

In both the sub-micron and micron pillars, several groups have proposed that collective dislocation behavior is responsible for the size effect, with the principal mechanism arising from the operation of truncated dislocation sources, also known as single arm sources, whose strength scales as $\frac{\ln L}{L}$ where L is their pinned segment length [4, 24, 26, 62, 64, 67, 75, 143]. The average pinned segment length has been shown by several authors to decrease with decreasing pillar diameter or film thickness leading to higher strengths in smaller-sized structures[26, 169]. This mechanism has been demonstrated through analytical models [4, 24, 26], dislocation dynamics (DD) simulations in 2- and 3-dimensions[64, 78, 79, 170, 171], and through *in situ* transmission electron microscopy (TEM) testing of Au thin films [172] and Al wires [25].

Few reports have been published on assessing metallic strengths with critical sample dimensions on the order of ~100nm and below, and those that exist reveal a relatively size-independent response of flow strength in both pillar [2, 117] and thin film geometries [137, 172], sometimes deforming at nearly-theoretical strengths [2]. In-situ TEM investigations have postulated a plasticity mechanism transition from single arm source operation to partial dislocation nucleation from

free surfaces and interfaces near ~100nm in size [31, 172]. Also, several groups have noticed a transition from size-dependent strength above ~100nm to relatively size-independent strength below ~100nm [117, 137]; a transition predicted by Zhu et al as a result of the emergence of partial dislocation nucleation as the dominant plasticity carrier [81]. These experiments are corroborated with the results of molecular dynamics (MD) simulations, which also suggest that at these very small length scales, dislocation nucleation from surfaces and interfaces controls deformation [81, 115]. While numerous computational studies of nanowire deformation exist, the focus of this report is to present our experimental findings on the deformation of sub-600nm single crystalline Cu nano-pillars and then relate these results in the context of reported experimental investigations of nanowire and thin film deformation. The state of the art overview concerning plasticity in small-scale metallic systems can be found in four recent reviews on small-scale plasticity [62, 64, 66, 67].

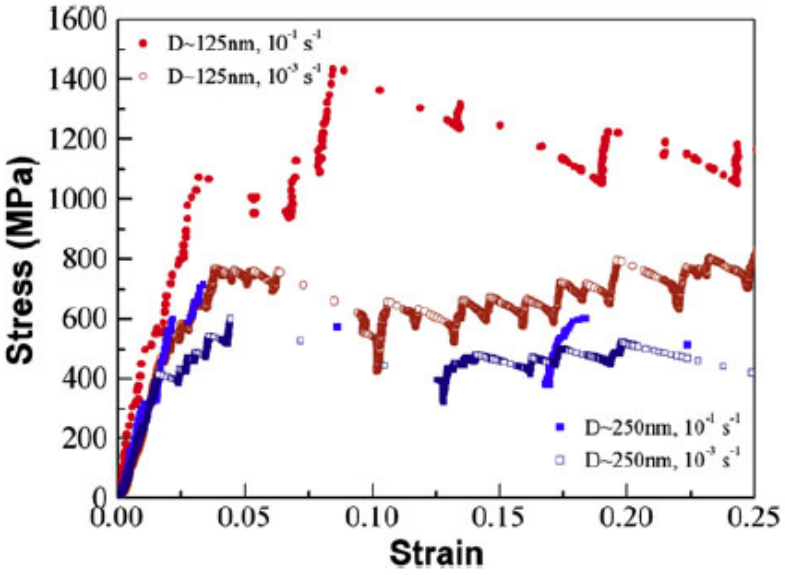

Figure 7.1 Representative stress strain curves for two different electroplated Cu pillars with diameters 125nm and 250nm. Two different strain rates: 10^{-1} and 10^{-3} s^{-1} are shown for each pillar diameter[1].

Here, we compare our results showing the nucleation of partial dislocations ~100nm Cu electroplated pillars with those reported for similar-thickness thin films on compliant substrates. We discuss this deformation behavior in the framework of previously reported *in situ* TEM investigations, which clearly illustrate that in these small structures, partial dislocations preferentially nucleate from local stress-concentrations. We highlight the variety of nano-mechanical testing sample fabrication routes reported to date and their resulting initial microstructures, which have been found to have a significant impact on deformation behavior [2, 31, 59-62, 64, 66-68, 82, 89, 100, 117, 145]. We compare our experimental results to the existing models

that attempt to explain heterogeneous

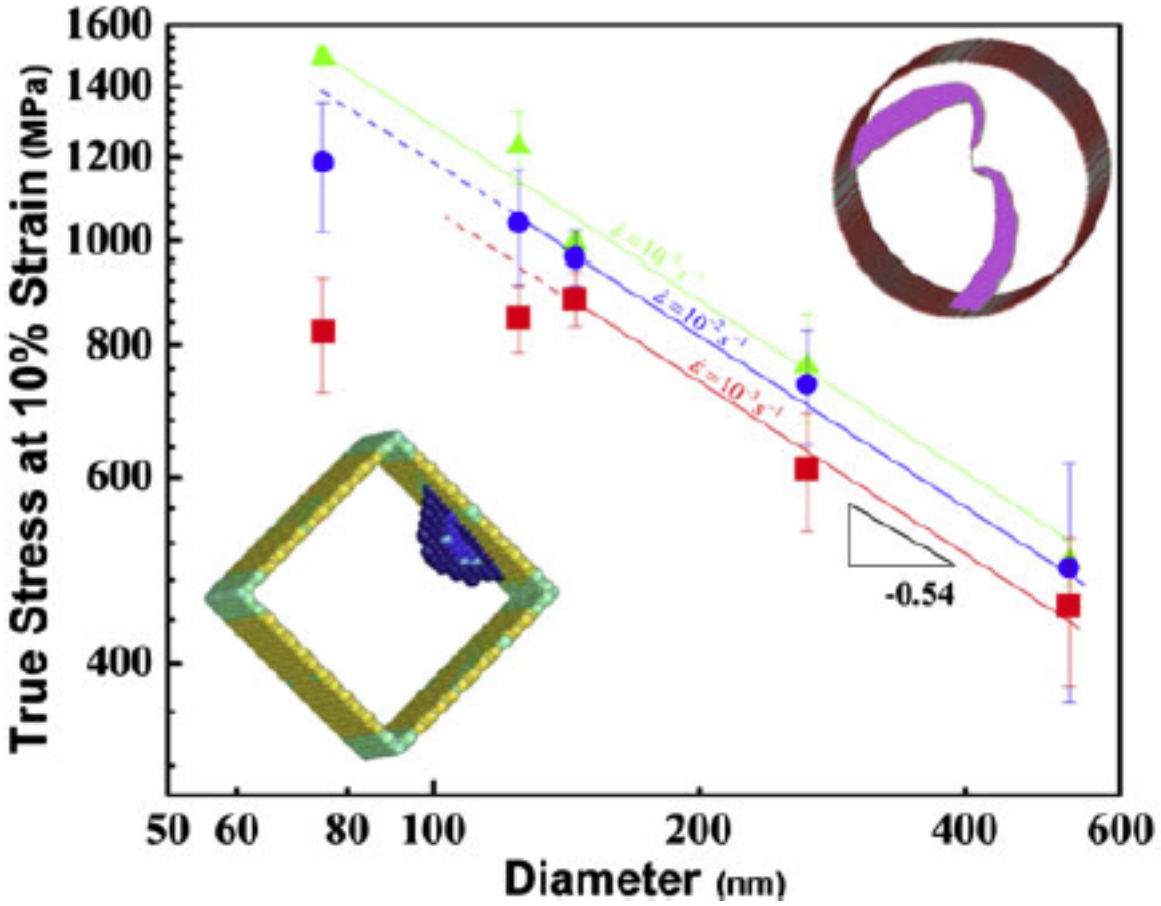

Figure 7.2 True stress at 10% strain versus pillar diameter at three different strain rates: 10^{-3}, s^{-1}, 10^{-2}, s^{-1}, and 10^{-1} s^{-1}. Bottom left inset is an atomistic image for surface source nucleation from a free surface in a square pillar (from Ref [81]). Top right inset is an atomistic image of two single arm sources in a circular pillar (from Ref [127]).

dislocation nucleation in pillar and thin film geometries. Further, we use the measured experimental activation volumes to test the applicability of these models to the deformation of our Cu nano-pillars.

The following Results and Data Analysis section are restated from Section 5.3 and 5.4 respectively, for the reader's convenience.

7.2 Results

Representative stress-strain curves for the compressions of pillars with diameters of 125nm and 250nm can be seen in Figure 7.1. There are two stress-strain curves for each pillar diameter,

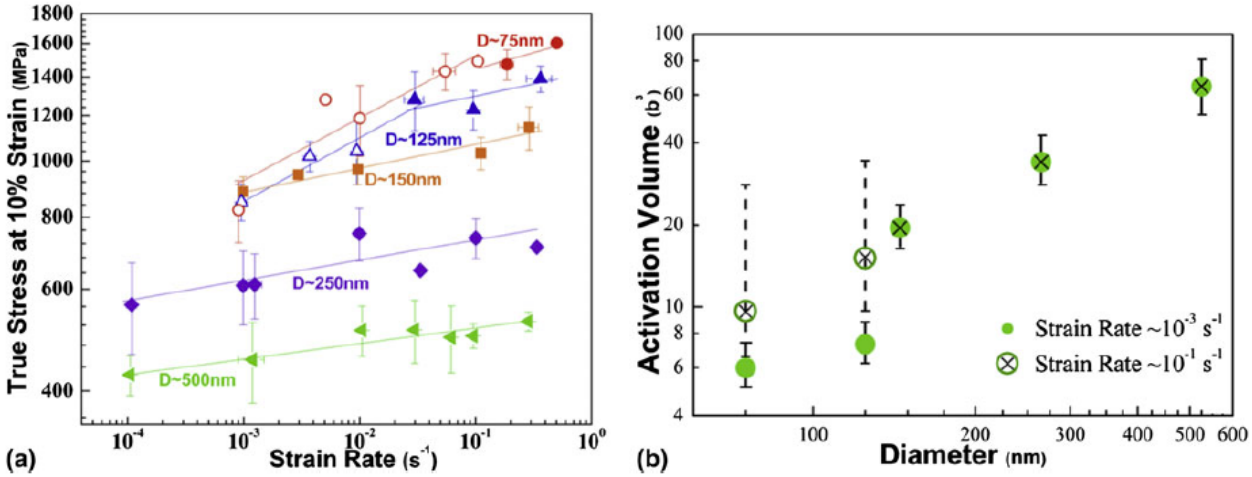

Figure 7.3(a) Log-Log plot of stress at 10% strain versus strain rate for 5 different pillar diameters: ~500nm, 250nm, 150nm, 125nm, and 75nm. Lines are fits to the strain rate sensitivity, *m*. Data re-plotted from Ref 25 with permission from Elsevier. (b) Log-log plot of activation volume versus diameter at two different strain rates denoting the change in activation volume for the smallest diameters.

corresponding to compression tests at two different strain rates: 10^{-3} s^{-1} and 10^{-1} s^{-1}. These four curves have a typical stochastic signature with intermittent strain bursts and are examples of two global trends found in Figure 7.2 and 7.3. The first is that at a constant strain rate, smaller pillars reach higher strengths, and the second is that for a constant diameter, faster strain rates result in higher strengths. Further examples of these curves can be found in Ref. [82]. The stress-strain behavior in these pillars is similar to that reported in other literature on pillar compressions in similar instruments[62, 64, 67].

Figure 7.2 shows a log-log plot of the strength at 10% strain versus pillar diameter for 5 different samples with diameters between 75nm and 525nm, deformed at different constant strain rates spanning four orders of magnitude. Examining the strength as a function of pillar diameter at the slowest strain rate accessible for all pillar diameters, 10^{-3} s^{-1}, we find that the largest pillar diameters $D \geq 150nm$ obey a power-law with the slope of -0.54 similar to ubiquitous reports in the literature on the size-dependence of FIB-fabricated pillars [62, 64, 66, 67]. Furthermore, at small sizes $D < 150nm$

the strength versus size appears to flatten out relative to diameter suggesting that there is a transition to a different deformation mechanism. The transition diameter is defined here as the smallest pillar diameter whose strength can be accurately defined through the power-law scaling seen in larger pillars. At the strain rate of 10^{-3} s^{-1} this transition diameter is ~150nm. We find that this transition diameter is a strong function of strain rate, with faster strain rates resulting in smaller transition diameters [117]. For example for strain rates between 10^{-3} s^{-1} and 10^{-1} s^{-1} the transition diameter shifts from D~150nm to D~75nm or smaller as seen in Figure 7.2 and Ref 25 [117].

7.3 Data Analysis: Measurement of Activation Volumes

In order to explore the strain-rate dependence, the current authors measured the strain rate sensitivity, *m,* from the phenomenological dependence of stress on strain rate: $\sigma = \sigma_0 \dot{\varepsilon}^m$. The results at each pillar diameter can be seen in Figure 7.3a, a log-log plot of flow stress at 10% strain versus applied strain rate, where the lines correspond to the fits of *m*. There is considerable scatter in the measured strength of small volume pillars [62, 64, 66, 67]. As a result, we assume here that each type of stress versus diameter signature seen in Figure 7.2, either size-dependent behavior in larger pillars or relatively size-independent behavior in smaller pillars, corresponds to a single strain rate sensitivity regime, taking into account this inherent scatter in these types of measurements. The three largest pillar diameters consistently have strengths well described by power-law behavior and as a result, a single value of *m* is measured across the range of strain rates tested. This value of *m* increases from ~0.027 at 500nm to ~0.04 at 150nm. At the two smallest diameters, two fits for the strain rate sensitivity are plotted, with the transition diameter inferred from Figure 7.2. At slow strain rates, the strain rate sensitivity dramatically increases from 0.04 in 150nm diameter pillars to ~0.11 in both 125nm and 75nm pillars. At high strain rates, the increase in strain rate sensitivity is more subdued, corresponding to again ~0.04 at 150nm and ~0.057 at 125 and 75nm.

This strength versus strain-rate data can be used to estimate experimental activation volumes associated with nano-scale plasticity in these structures. The activation volume is measured by assuming the shear strain rate is controlled through a dislocation nucleation process, consistent with previous reports in the literature [81, 98, 147, 173], and can therefore be described by an Arrhenius form:

$$\dot{\gamma} = \dot{\gamma}_o \exp\left(\frac{Q - \tau\Omega(\tau, T)}{k_B T}\right) \tag{7.1}$$

where $\dot{\gamma}_o$ is a constant prefactor, Q is the energy barrier, τ is the resolved shear stress, k_B is Boltzman's constant, and T is the temperature. The activation volume, $\Omega(\tau,T)$, is defined as a change in the activation energy with applied stress. We assume here that the resolved shear stress dominates the deformation mechanism such that the activation volume can be described as $\Omega(\tau,T) = \left.\frac{dQ}{d\tau}\right|_T$. Rearranging this equation for activation volume results in:

$$\Omega(\tau,T) = k_B T \frac{d\ln\dot{\gamma}}{d\tau} \tag{7.2}$$

which can be measured from the stress dependence on strain rate at a constant temperature.

The data in Figure 7.3a represents ~150 successful compression tests with each point having error bars containing on average ~5 data points. The activation volumes as a function of diameter can be found in Figure 7.3b, where they are plotted for two different strain rates, 10^{-1} s^{-1} and 10^{-3} s^{-1} represented by 'X's and 'O's respectively. At the faster strain rates, 10^{-1} s^{-1}, the activation volume scales linearly with diameter, as recently reported by Jennings et al. [117] and as might be expected for single arm sources [117]. It should be noted that while the observed linear trend is in reasonable agreement with this theory, the predicted and observed magnitudes are substantially different implying the need for further improvements in theoretical investigations. Slower strain rates demonstrate a drop in the activation volumes for the two smallest pillar diameters to below $10b^3$ [117]. These two diameters, 75nm and 125nm, also experience a deviation from the commonly observed power law, transitioning to a size-independent strengthening regime, suggesting a deformation mechanism transition.

7.4 Discussion

7.4.1 Experiments on Nanowire Deformation

Electroplating copper pillars is not the only fabrication route developed to study size-effects in FIB-less geometries. For example, Buzzi et al. and Dietiker et al. both used an embossing method on Ag [89] and Au [145], respectively, whereby a patterned Si template was pushed into a square platelet of the desired material at elevated temperatures. The metal is then formed into the mold, producing pillars with diameters ranging from ~150nm up to several microns [89, 145]. The resulting pillars had different crystallographic orientations, with the smallest pillars D<200nm in Au and D<500nm in Ag being single-crystalline. Larger pillars were a mix of single crystalline and polycrystalline. The results of these experiments show a clear size-effect similar to FIB-fabricated pillars [89, 145]. In fact, Dietiker et

al shows no substantial difference between Au pillars produced by the FIB and those produced through the embossing method [145].

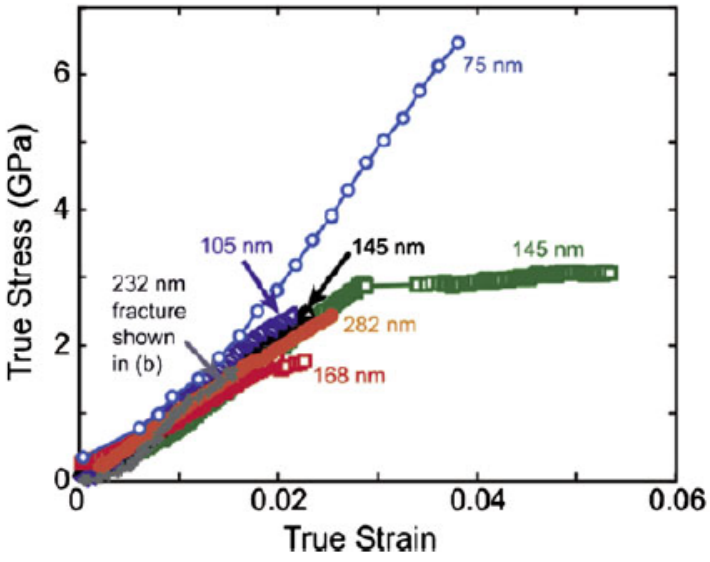

Figure 7.4 Stress-strain curves from tensile tests of pristine single crystalline copper nanowires performed by Richter et al. Ref. [2] Stress-strain curves show very high strengths, on the order of 2-6 GPa.

Richter et al. grew pristine [110]-oriented copper nanowires through vapor-liquid-solid method with diameters between 75nm and 400nm [2]. In contrast to pillars produced through electroplating, these nanowires result in an equilibrium Wulff shape, with atomically smooth side surfaces and virtually non-existent initial dislocations, resulting in a similar microstructure as the micron-sized, wires originally investigated by Brenner [57]. Similar to Brenner's now-classical results on Cu whiskers, these nanowires were pulled in tension and exhibited very large strengths: 2-6 GPa and failed predominantly via brittle fracture [2]. The size dependence of these wires has been described through Weibull statistics, calculating the probability of finding a defect on the surface or in the wire volume, which would lead to brittle failure [64]. Stress-strain behavior demonstrating the large strengths and subsequent fracture in Richter et al.'s nanowire experiments can be found in Figure 7.4.

Uniaxial compression experiments were also performed on Mo-alloy pillars, also produced without the FIB through eutectic solidification [59-61]. As grown, these square pillars contain zero initial dislocation densities, and SEM micrographs appear to have pristine surfaces. As a result, these pillars have a size-independent strength under compression as they all attain nearly theoretical strengths at all sizes [59-61].

What emerges is that in the pillar and nanowire tests, there is a clear distinction in the mechanical behavior and deformation between the initially pristine samples and those that contain defects: dislocations and non-atomically smooth surfaces. The truly and nearly pristine samples attain

strengths that are very high and nearly size-independent, while those with defects have lower strengths, with considerable scatter in their measured values. In the former, the failure is catastrophic at near theoretical strengths. In contrast, pillars with initial defects show a mechanism transition: larger samples deform at strengths according to the widely observed power-law and smaller diameters deform at a relatively size independent strength that is significantly lower than the ideal strength [174]. Several groups have performed in-situ TEM investigations in order to understand the origins of the deformation mechanisms unique to one-dimensional nano-pillar and nanowire geometries. These investigations revealed two different mechanisms: the operation of single arm sources [25] in larger pillars and wires and partial dislocation nucleation in smaller pillars [31]. In the former, 460nm-wide single crystalline Al wires with rectangular cross-sections were cut by the FIB from non-pristine single crystalline Al films on polyimide substrates. An unobstructed view of the Al wire was obtained by selectively fracturing the polyimide around the viewing area. Tensile straining of these wires unambiguously demonstrated the sequential nucleation of concentric dislocation half-loops emanating from an operating single arm source. Tests at higher strain rates revealed a build up of dislocation density, as the dislocation generation rate exceeded their annihilation rate [25]. Investigations into thinner wires were limited due to the stability of the samples after processing.

On the opposite end of the size spectrum, in very small Au nanowires with diameters of 10nm and below, high-resolution transmission electron microscopy (HRTEM) investigations revealed neck formation and partial dislocation emission under tensile loading [31]. These nanowires were produced through the reduction the of AuCl (oleylamine) complex on the TEM holder. The Au NWs were loaded into the TEM and attached to a Au substrate through compression cold-welding [31], a process whereby two crystals of the same material bond together without the introduction of external heat such that no interface exists at the "weld" site [124]. These Au nanowires have a very complex surface comprised of low-energy {111} facets [137]. During tensile tests on [001]-oriented wires, partial

dislocations were noticed to nucleate at local stress

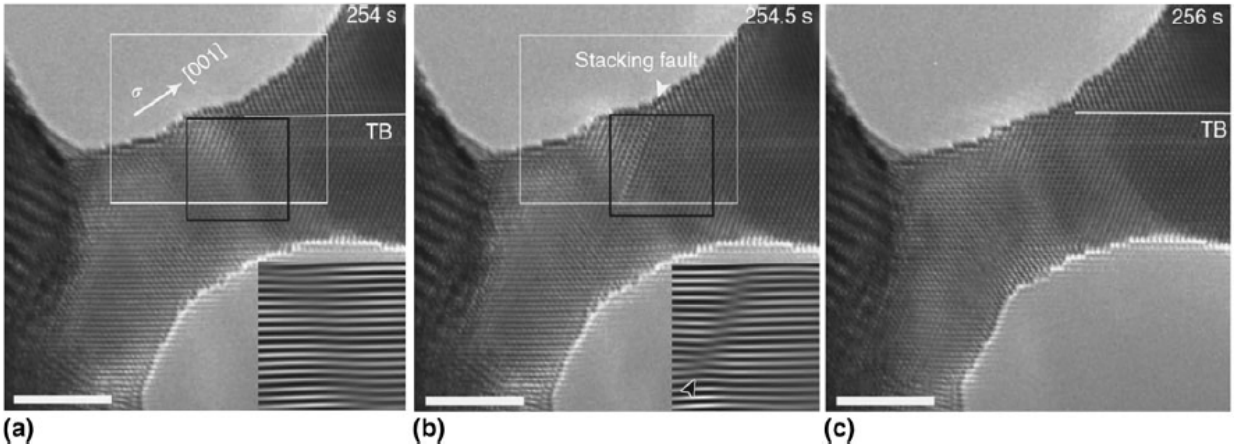

Figure 7.5 High-resolution TEM image of a [001] gold nanowire in tension. (a) Before and (b) after leading partial dislocation nucleation. Inset in (a) and (b) show Fourier-filtered images of the stacking sequence highlighting the stacking fault. (c) After trailing dislocation nucleation. Scale bar is 3nm

concentrators like slip offsets along the wire surface. A series of HRTEM images showing the time progression of these partial dislocation emissions can be found in Figure 7.5. Figure 7.5a shows that the initial atomic structure contains surface steps and a twin boundary, TB, intersecting the surface. Figure 7.5b shows the stacking fault left behind after the leading partial dislocation has nucleated, and Figure 7.5c displays the disappearance of the stacking fault after the trailing partial dislocation is nucleated. Nanowires with [110] loading orientations were also tested and favored twinning as their deformation mechanism. The authors ascribe this preference for twinning to the large Schmid factor difference in the leading versus trailing partials in [110] tension. The result may be the preference for the repeated nucleation of leading partials on adjacent slip planes as opposed to the nucleation of trailing partials.

Analyzing the HRTEM images, the authors were able to capture local stress and strain information at the specific site the partial dislocation nucleates. Significantly, the authors find that the local stress at the nucleation site is generally higher than the rest of the pillar demonstrating the important role that stress concentrations have in the nucleation of partial dislocations. For example, the leading partial dislocation shown in Figure 7.5b nucleated at the intersection of the surface and the twin boundary. Furthermore, in contrast to bulk materials, the dislocations nucleated in these small wires immediately pass through the wire diameter and escape at the opposite surface. This type of

dislocation starvation has also been shown in other *in situ* TEM investigations [14, 28] and also in MD simulations of circular gold nanowires [99].

7.4.2 Experiments on Thin Film Deformation on Flexible Substrates

As described above, the unique deformation mechanisms found in 1-dimensional pillar and nanowire geometries arise due to the reduced sample sizes. It is useful to discuss the deformation mechanisms in 2-dimensional structures, i.e. thin films, whose thicknesses are reduced to nanoscale dimensions. Most mechanical tests on single crystalline, as opposed to polycrystalline thin films, have been conducted for samples on stiff substrates, which have been shown to greatly influenced the observed mechanical response [175, 176]. In order to discuss the deformation mechanisms inherent to small-scale single crystals with minimal added constraining effects of the substrates, here we focus on tensile tests of single crystal Au thin films on flexible polyimide substrates [137, 172]. These thin gold films were prepared by first growing an epitaxial Au film on a single crystal of NaCl followed by the deposition of polyimide on top of the Au layer. Subsequently, the seed NaCl layer was dissolved in water, resulting in the "upside-down" Au film on a flexible substrate. The resulting test samples were [001] oriented, 5mm wide, 8mm long, and ranged from 30nm to nearly 1um thick. These samples were not pristine, but contained several initial dislocations, as well as a small number of growth twins and pores in samples with thicknesses below 50nm as a result of the growth process. Further details of the sample preparation procedure can be found in Ref. [137, 172].

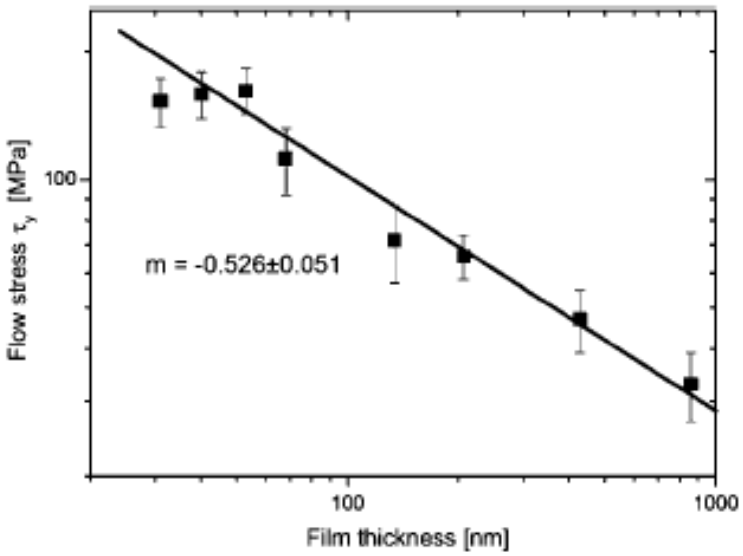

Figure 7.6 Resolved shear stress for flow stress at 0.5% strain for single crystalline gold thin films on polyimide substrates.

Films with thicknesses ranging from ~30nm to ~868 nm were tested in tension along the [001] direction. Tensile tests were performed by applying a displacement in steps from 30um to 90um up to a total length of 1000um, and the total strain was measured via a laser extensometer. In between each extension, Laue patterns were obtained with an exposure time between 15s and 120s in order to determine the complete stress state in the films. As a result of the different testing methodology, constant strain-rate comparisons are difficult. In contrast to pillar compressions, the resulting stress-strain curves of the films are quite smooth and exhibit no noticeable bursts, likely due to the film's much larger length and width as compared to pillars [137]. The resulting flow stresses at 0.5% strain are plotted as a function of film thickness in Figure 7.6, which shows a log-log plot of stress as a function of thickness. The flow stress reported here is the resolved shear stress on the perfect dislocation slip direction (111)[1-10]. These authors find that for larger film thicknesses, t>60nm, the strength follows a power-law with the exponent n~-0.53, similar to that seen in FIB fabricated pillars and quite close to that seen in larger electroplated copper pillars. Similarly to the electroplated copper pillars, when the film thickness decreased below a critical value, in this instance t~60nm, the films' strengths remained constant or even decreased with decreasing film thickness [137],

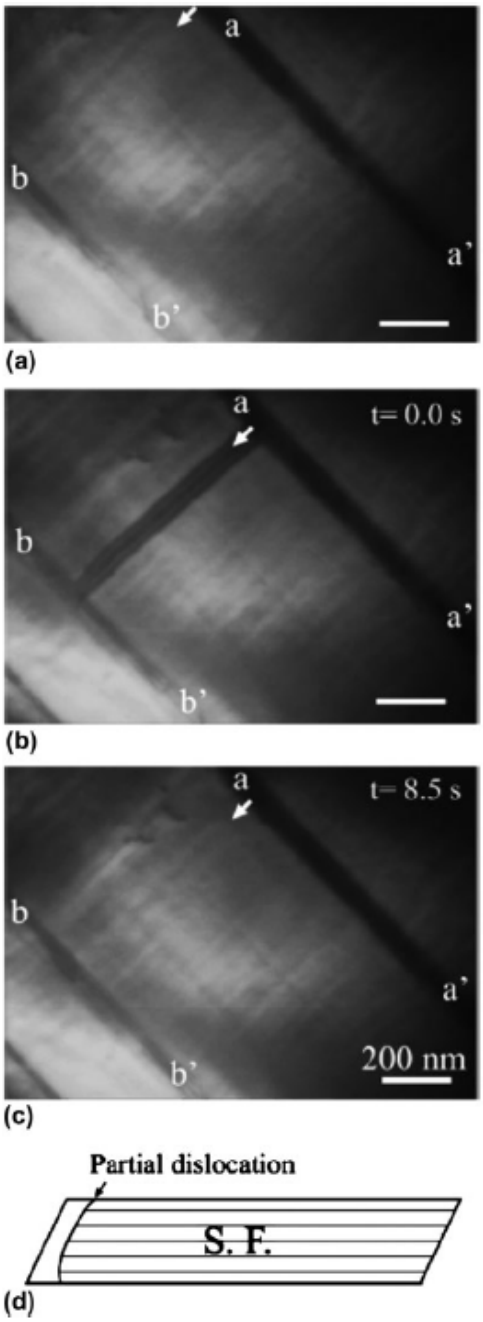

Figure 7.7(a)-(c) Successive TEM images of partial dislocation nucleation. (a) Initial state. (b) 0.4 seconds after initial state showing a stacking fault extending between twins a-a' and b-b'. (c) 8.5 seconds later the stacking fault closes. (d) Schematic of nucleation process

In order to understand the origins of the deformation mechanisms in thin films, Oh et al. performed in-situ TEM tensile tests on similar single crystalline gold samples supported by polyimide substrates[172]. In those experiments, 5 different film thicknesses between 160nm and 40nm were tested, and the resulting size-dependent behavior is also measured outside the TEM via XRD and the results are similar to that seen in Figure 7.6 [172]. In these experiments, thicker films, $t \geq \sim 80nm$ obey a power law with the exponent ~ -0.5 while thinner films deform at a relatively size-independent flow stress. In contrast to the ex-situ experiments discussed above, these films are subject to additional thermal effects due to the polyimide layer heating up during electron beam exposure [172]. These researchers found that samples with the larger film thicknesses, t>80nm, deformed via multiplication and glide of perfect dislocations. Frequently though not always, these perfect dislocations were observed to deposit interfacial segments at the Au/polyimide interface, a deformation mechanism characteristic of thin films on stiff substrates as demonstrated in the Matthews, Blakeslee, Freund, and Nix model[175, 176]. At large strains, this deposition of threading segments leads to the so-called "cube glide", or glide of [001] dislocations. Also, the authors see evidence of ample dislocation emission from single arm sources pinned at grown-in defects, in this instance growth twins or epitaxial gold nanoparticles. Single arm sources are also seen through *in situ* tests of pillar geometries [25] and have been shown to manifest in a size-dependent yield stress [4, 24, 26, 67, 78, 170].

In thinner films, $t \leq \sim 80nm$, the glide of threading dislocations still contributes to deformation; however, these dislocations no longer deposit interfacial segments. Furthermore, the authors note that partial rather than perfect dislocation nucleation becomes the dominant deformation mechanism, whereby these partial dislocations predominantly nucleate at stress concentrations at the internal interfaces: square pores, twins, and surfaces defects, produced during film growth. An example of partial dislocation emission at a twin boundary is shown in Figure 7.7. Figure 7.7a, shows the crystal prior to dislocation emission while Figure 7.7b shows the stacking fault after the leading partial has nucleated and passed through. The time difference between Figure 7.7a and 7.7b is 1 frame or 0.4 seconds, an amount of time sufficient to obscure the mechanistic details. Figure 7c shows the trailing partial emitted from the same location 8 seconds later and the subsequent annihilation of the stacking fault [172].

7.4.3 Dislocation Starvation

These and several other *in situ* TEM investigations in pillars and thin films have provided insight into how the behavior of individual dislocations changes as a function of size [14, 28]. Separate *in situ* investigations have shown that not only does the individual dislocation behavior change, but also the collective dislocation behavior changes with critical thickness. As the critical length scale decreases, dislocations no longer tend to form substructures; instead they readily escape at free surfaces, which result in the crystal becoming starved of dislocations [14, 28]. This concept of dislocation starvation was first introduced by Greer and Nix to explain the deformation behavior of nanoscale Au pillars [8] and post-deformation TEM behavior on nanoscale samples has suggested its operation [8, 82]. Most convincingly, this phenomenon was demonstrated during *in situ* TEM compressions of Ni pillars with diameters at or below~200nm [28]. In those experiments, the dislocations likely produced by the FIB damage and escape the sample resulting in a significant reduction of the dislocation density in a process coined as "mechanical annealing" [28]. A similar set of in situ TEM compressions performed by a subset of the same team of researchers also observed this phenomenon in smaller [001] oriented copper pillars [14]. In these experiments, strengthening after the yield point was associated with a decreasing dislocation density. The authors postulate that as a result of fewer dislocations being present in the pillar, higher strength dislocation sources are required to sustain deformation. The lack of dislocation multiplication via double cross-slip processes and substructure formation, as would be the case in bulk crystal deformation, is unique to this nanometer length scale and increases the likelihood that dislocation nucleation from alternative sources contributes substantially to deformation. In pillars and thin films, a prime candidate as an alternative source of dislocation becomes heterogeneous dislocation nucleation as the surface to volume ratio increases with decreasing pillar diameter or film thickness.

Thin film geometries have only one dimension reduced to the nanometer scale, their thicknesses, and therefore might be expected to also experience dislocation starvation; however, the constraints imposed by the supporting substrates lock the mobile dislocations into the film, thereby hindering starvation effects [137, 172]. In addition, extensive cross-slip has been observed during *in situ* experiments on thin films, which may further effect starvation.

7.4.4 Dislocation Starvation Model.

A model based on the balance between nucleation and annihilation rates of dislocations at surfaces in circular pillars was recently developed by Nix and Lee [147]. This relatively simple phenomenological model describes the physics of pillar compressions through a kinetic law:

$$\dot{\gamma} = \frac{1}{\mu}\frac{d\tau}{dt} + \rho_m b\bar{v} \tag{7.3}$$

where $\dot{\gamma}$, is the shear strain rate, , μ corresponds to the shear modulus, $\frac{d\tau}{dt}$ is the shear loading rate, b is the Burgers vector, $\bar{v}$ is the average dislocation velocity, and ρ_m is the mobile dislocation density. Eq. 7.3 describes the shear strain rate as composed of two terms corresponding to the elastic-loading term and the subsequent plastic deformation term. Through the comparison of the rates of dislocation nucleation and annihilation at a free surface, these authors derive an equation for the stress required to maintain a constant shear strain rate as:

$$\tau_{ss} = \tau_{th}\left(\frac{\dot{\gamma} b}{\pi \omega_o D}\right)^m \tag{7.4}$$

Where τ_{ss} corresponds to the steady state applied shear stress, τ_{th} is the theoretical shear stress, D is the pillar diameter and ω_o is the nucleation frequency at the theoretical shear stress [147]. Notably, the stress here depends on both the pillar diameter through D^{-m} and on the strain rate as $\dot{\gamma}^m$ suggesting that as pillar diameter becomes smaller or the strain rate increases, higher stresses will be required to maintain steady state deformation. Further, the size dependent strength and strain rate dependence are linked through the exponent m. In larger pillars, where the size-dependent strength obeys a power-law with exponent between -0.5 and -1.0 the resulting value of the strain rate sensitivity of 0.5 to 1, unreasonably large values for FCC metals.

Applying this analytical framework to our experiments on Cu nano-pillars, we see good agreement in regards to the expected strain rate sensitivity and diameter dependent strength. Substituting our experimentally determined strain rate sensitivity of ~0.1 for the 125nm and 75nm pillar diameters at the slowest strain rates of 10^{-3} s^{-1} into Eq. 7.4 we find the corresponding strength dependence on diameter of ~-0.1 a reasonably weak strength dependence on diameter, which compares favorably with our smallest samples, as well as with the results of investigations presented here and other theoretical works [81, 117, 137, 172]. While this phenomenological model accurately

captures the correlation between strain-rate dependence, size, and strength, it cannot explore the details of dislocation nucleation. Therefore, we next discuss atomistic models that attempt to capture the physics and the stresses required for partial dislocation nucleation.

7.4.5 Partial Dislocation Nucleation Models

Two different models for heterogeneous nucleation of dislocations in FCC metallic thin films and pillars have been reported [81, 137, 172]. Despite the differences in sample geometries between these models and our samples, it is reasonable to expect that the governing mechanisms in both small-scale structures are similar.

7.4.6 Classical Dislocation Source Model

The model recently published by Chen et al. provides an estimate for the transition diameter between perfect and partial dislocation nucleation at grain boundaries in nanocrystalline Al [177]. The shear stress to expand a partial dislocation with the Burgers vector b_p and the stacking fault energy γ_{SF} is correspondingly written as:

$$\tau_p = \frac{2\alpha\mu b_p}{D} + \frac{\gamma_{SF}}{b_p} \tag{7.5}$$

The stress to expand a perfect dislocation loop is:

$$\tau_N = \frac{2\alpha\mu b_N}{D} \tag{7.6}$$

Here, τ_p is the resolved shear stress to operate a partial dislocation source, α is a coefficient, between 0.5 and 1.5, reflecting to the orientation dependence of the line energy, μ is the shear modulus, b_N is the perfect Burgers vector, and $D/2$ is the critical radius for this dislocation source where D is the critical length scale, originally grain size [177] but recently extended to film thickness [137, 172]. This simple model compares the strength to operate a Frank-Read source emitting a perfect dislocation loop versus a partial dislocation and an accompanying stacking fault as function of the critical length scale. By setting Eqs. 7.5 and 7.6 equal to each other, these authors find the critical length scale for the transition.

$$D = \frac{2\alpha\mu\left(b_N - b_p\right)b_P}{\gamma_{SF}} \tag{7.7}$$

This model has been extended more recently to single crystalline Au films [64, 137, 172] to explain the observed transition in strength as a function of film thickness, as seen in Figure 7.6. This partial

dislocation nucleation model captures the trend in observed strength reasonably well [64, 137, 172, 177]. However, in the case of Au thin films on polyimide this model overpredicts the stresses by a factor of > 2 which the authors hypothesize may be due to defects enabling lower strengths for partial dislocation nucleation [137]. Frank-Read and single arm source operation requires the existence of a pinned dislocation segment; however, in single crystals, partial dislocation nucleation appears to operate in the absence of such sessile dislocation segments. In fact, as shown previously, the existing in situ TEM studies suggest that partial dislocations nucleate at external surfaces or internal interfaces [31, 172]. In the absence of a pinned dislocation segment, the critical length scale, *D*, is not necessarily associated with the film thickness. Rather, atomistic and analytical models studying homogeneous nucleation [178] and heterogeneous dislocation nucleation [81, 179, 180] showed much smaller critical dislocation loops, with the critical radius on the order of a few nanometers. Such a small critical radius further suggests an important contribution from thermal effects. Including thermal effects would result in lowering the strength necessary for dislocation nucleation, an effect possibly manifested as the larger transition diameter found in in-situ thin film studies versus ex-situ tests.

7.4.7 Heterogeneous Dislocation Nucleation

Zhu et al recently investigated the probabilistic nature of thermally activated surface dislocation nucleation through the development of a general analytical model[81]. This model requires the knowledge of the thermal activation parameters: activation energy and activation volume, in order to make predictions regarding specific nucleation processes. These activation parameters were then determined through fixed end nudged elastic band, FENEB, method, in square Cu nano-pillars [81]. In their analytical model, the nucleation frequency, ν, of a given site is taken to have an Arrhenius form as in Eq. 7.1 where ν is substituted for shear strain rate, $\dot{\gamma}$. Then, in order to describe the probabilistic nature of thermal activation, they define a survival probability, $f(t)$, as the fraction of a set of pillars that have not nucleated a dislocation by a time t. The change in $f(t)$ is related by the nucleation frequency, ν, through: $\frac{df(t)}{dt} = -\nu f(t)$. The most probable time that a nanowire will nucleate a dislocation can then be found by finding the maximum of $\frac{df(t)}{dt}$. The resulting equation describes the most likely time at which a pillar will nucleate a dislocation; however, in experiments, a

more relevant measure is applied stress. The survival probability analysis can be rewritten in terms of the applied stress by relating time and stress through the elastic modulus and applied strain rate: $\sigma = E\dot{\varepsilon}t$. Rearranging the above and linearizing the result for clarity we find that the activation stress can be represented as:

$$\sigma = \sigma_{athermal} - \frac{k_B T}{\Omega} \ln \frac{k_B T N \nu_o}{E \dot{\varepsilon}_e \Omega} \tag{7.8}$$

Here, the first term, $\sigma_{athermal}$, corresponds the athermal stress, or the stress required to nucleate a dislocation at zero temperature. The second term comprises the thermal contribution to nucleation stress where: k_B is Boltzman's constant, T is temperature, N is the number of equivalent nucleation sites, ν_o is the atomic vibration frequency, E is the Young's modulus, and $\dot{\varepsilon}_e$ is the

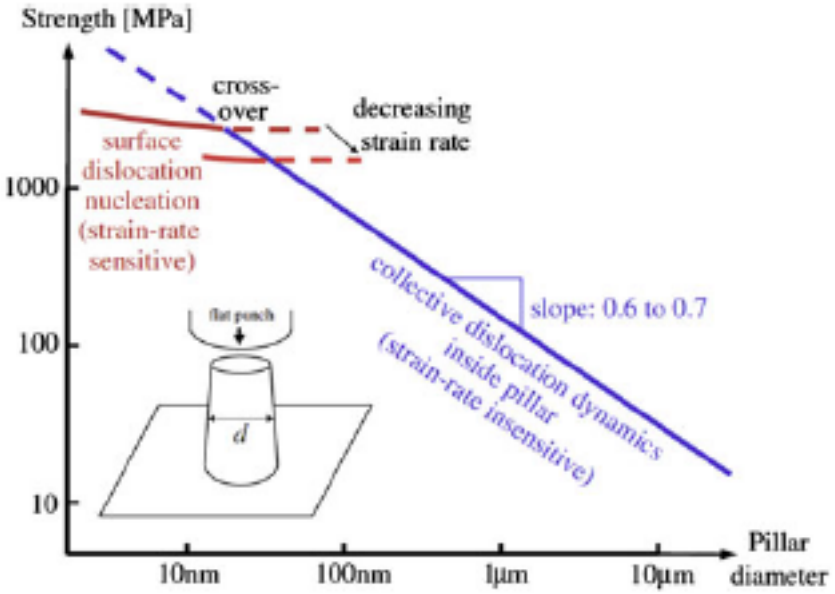

Figure 7.8 Log-Log plot of strength versus diameter showing the predicted transition from collective dislocation dynamics to surface source nucleation

applied strain rate. This term is dominated by the constant prefactor outside the logarithm, and will be large at high temperatures and small activation volumes.

Zhu et al. [81] determined the activation parameters for surface source nucleation in an initially perfect square [001] Cu wire through an atomistic FENEB calculations. The predicted size-dependent stresses are shown in Figure 7.8. The expected size effect due to partial dislocation nucleation is quite

weak with the exponent of ~0.1 to 0.2 related to the number of equivalent sites N inside the logarithm. This weak size-effect reflects well the observed trend in experimental literature on thin films [64, 137, 172] and, more recently, in pillar compressions [117]. Furthermore, they estimate the transition diameter to be between 10-100nm and to depend on strain rate, both of which are in reasonable agreement with our experiments on pillars and those discussed on thin films. These authors' calculations find the activation volumes for surface source nucleation to be within the range of 1-10b^3, which extends a range from nucleation at a sharp corner (~1b^3) to the flat side of the nanowire (~10b^3) [81]. These small activation volumes correlate well with the ones we find in our pillar experiments as seen in Figure 7.5 in Ref [117] and result in a large thermal contribution to strength as seen in Eq. 7.8.

The two models above, the classical source model and heterogeneous dislocation nucleation model, differ in their assumption of the state of the crystal prior to partial dislocation nucleation. The classical source model assumes the pre-existence of a pinned dislocation segment; whereas, the heterogeneous nucleation model does not. As a result of this assumption the expected activation volumes of the two processes are drastically different. The classical source model is Frank-Read type model and would therefore likely result in an activation volume on the order of 100b^3 to 1000b^3 [118, 140, 142, 181]; whereas, the heterogeneous nucleation model results in activation volumes between 1b^3 and 10b^3 is in good agreement with our pillar compressions [117]. This discrepancy between the activation volumes of the classical source model and the measured activation volumes suggests that the heterogeneous dislocation model may be a more-accurate depiction of the nucleation physics during pillar compressions.

7.4.8 Effects of Imperfections on Dislocation Nucleation

TEM studies on partial dislocation nucleation have highlighted the role that various defects play in dislocation nucleation. This is most obvious in the case of thin films where dislocations preferentially nucleate at square voids, as they serve as sites of stress-concentrations during tensile experiments[137, 172]. Furthermore, partial dislocation nucleation at twin boundaries has also been observed in both thin films and nanowires [31, 172]. This preference for nucleation at stress-concentrations has also been observed in recent MD simulations of bulk nano-twinned copper [182] and twinned nanowires [115]. In large-scale MD simulations of a bulk nanotwinned sample, dislocation emission is strongly preferred at the intersection of twin boundaries and grain boundaries, which are characterized by local

stress concentrations [182]. Similar results were found in MD simulations of twinned nanopillars, where partial dislocations preferentially nucleated at the intersection of the twin boundary and the nanowire surface [115]. This last type of stress concentration has been observed experimentally in gold nanowires, as shown in Figure **7.**5. Further, in these *in situ* experiments, the pillar surface is characterized by the intersection of distinct {111} planes resulting in a faceted surface along the nanowire length promoting nucleation through stress concentrations at the kinks in nanowire surface and surface steps [31]. All this evidence for the preference of heterogeneous dislocation nucleation at inhomogeneities also corroborates the work of Richter et al. [2]. In the absence of surface defects or internal dislocations, failure via brittle fracture is more energetically favorable than dislocation nucleation from a pristine surface.

In our pillar tests, the surface roughness also likely acts to change the local surface stress state. In tension, surface roughness may be expected to create stress concentrations similar to a crack tip with the initial crack length controlled by the local roughness; however, the experiments presented here were performed in compression, likely posing a more subtle influence of surface roughness on the local stress state. Tensile tests on similar electroplated copper pillars showed deformation through immediate necking [100]. Comparisons of these same pillars under both tension and compression did not demonstrate a tension-compression asymmetry suggesting that in these pillars the surface roughness did not act as a crack tip, further emphasizes the subtle influence the surface roughness may play [100].

It should be noted that the strengths of these pillars always showed size-dependent strength; however, the effects of a constant displacement rate, as opposed to a constant strain rate, and the relatively few samples tested precludes a definitive conclusion. Further, as the critical dislocation nucleation radius is on the order of a few nanometers [81, 179, 180], variations over these small distances such as individual surface steps may play a key role in determining a material's resistance to heterogeneous dislocation nucleation.

7.4.9 Partial Vs. Perfect Dislocation Nucleation

Our discussion up to this point has been dominated by heterogeneous partial dislocation nucleation at internal surfaces or interfaces. The preference for partial dislocation nucleation as opposed to perfect dislocation nucleation is due primarily to the low stacking fault energy of the materials tested so far: Au and Cu. In low stacking fault materials, perfect dislocations readily split into ribbons bounded by the

leading and trailing partials as this configuration has a lower energy. In metals with high stacking fault energies, perfect dislocations dominate deformation as the energy does not decrease through the separation of partials. The details of this preference for perfect versus partial dislocation nucleation have been discussed in the MD simulations of nanocrystalline materials, where it has been shown that the choice between perfect and partial nucleation depends critically on the complete generalized stacking fault curve [183]. As a result of low stacking fault material's ability to lower their energy by splitting into partials, it is not surprising that partial rather than perfect dislocation nucleation has been observed. Further experimental and theoretical investigations into FCC metals with high stacking fault energies – like Al or Ni - will help elucidate the specific role stacking fault energy plays in nano-scale plasticity

7.5 Summary

We discuss the role of heterogeneous nucleation of partial dislocations at local stress concentrators found on the surfaces and interfaces of nano-sized pillars and films on plastic deformation. Our experiments on single crystalline Cu nano-pillars, as well as other experimental studies on thin films demonstrate a transition in size-dependent strength when the critical length scale dips below ~100nm. At this size, the strength becomes independent of size and deviates from the commonly observed power law. *In situ* TEM tests on thin films and nanowires reveal the likelihood that this observed transition results from a change in preference from perfect dislocation multiplication through internal source operation to partial dislocation nucleation from local inhomogeneities on the surfaces and interfaces like voids, twin boundaries, and surface roughness. These findings help explain the lower strengths for pillars and thin films containing initial defects in contrast with the much higher strengths exhibited by pristine and nearly pristine small-scale geometries. We finally discuss the combined strain rate and size-dependent experimental data in the context of several models concerning partial dislocation nucleation and combined through comparisons of activation volumes.

Chapter 8: Atomistic Simulations and Continuum Modeling of Dislocation Nucleation and Strength in Gold Nanowires

The strength of metallic nanopillars with diameters ~100 nm and below has been shown through compression tests, *in-situ* TEM, and atomistic simulations to be likely controlled by surface dislocation nucleation: a thermally activated process that is sensitive to both temperature and strain rate. Simple continuum models have had limited success due to their inability to account for this thermal nature. As a result, understanding of dislocation nucleation has largely proceeded through atomistic simulations, which assume little of the governing nucleation physics. However, most of these models are limited to very high strain rates due to the short molecular dynamics time scales, which may influence both the observed strength and failure mechanism.

As a result, understanding of the strength necessary for surface nucleation at experimental temperatures and time scales is limited. In this chapter, adapted from Ref. [184], the strength for dislocation nucleation in pristine gold nanowires at experimental temperature and strain rate is estimated through a combination of atomistic chain-of-states energy barrier calculations and transition state theory. This combination of chain-of-states atomistics and transition-state theory also allows for the investigation into the competition between thermally activated dislocation nucleation and other proposed failure mechanisms from MD simulations such as elastic and structural instabilities.

These atomistic simulations are able to provide reasonable, quantitative estimates of nanowire strength; however, alone, these simulations provide limited insight into the governing physics. In order to understand the observed trends in nucleation site preference, an analytical model of dislocation nucleation is used to show that the dislocation character, screw vs. edge orientation, dictates the nucleation site.

8.1 Introduction

The interest in strength of small structures has increased dramatically since the discovery by Uchic et al. [3] that focused ion beam (FIB) machined single crystalline metals show a clear size-dependent flow stress. This has led to observations that the strength in single crystal metals scales with the diameter of the pillar raised to an exponent between -0.6 to -0.8 [9, 10, 28, 32, 82]. The most prominent theory describing strengthening with decreasing pillar diameter is the activation of single arm sources [97, 170, 185-187] (or truncated Frank-Read sources) in pillars that range between 200 nm and several microns.

On the other hand, atomistic simulations and *in situ* TEM analyses [31, 122] demonstrated that in the very small nanowires, dislocations nucleate from free surfaces. These observations have led to the interest in when plasticity dominated by single arm sources transitions to dislocation nucleation from free surfaces (surface sources) [81, 168, 188]. The presence of two competing mechanisms has also created much interest in experimental measurements of the strength of true nanowires [2, 31], defined here as wires with diameters D <100 nm. In these samples, direct evidence of surface nucleation is attained at very high stresses.

In atomistic simulations, there has been significant interest in the plasticity of metal nanowires [53, 189] primarily using molecular dynamics. These simulations have focused on understanding the criteria for dislocation nucleation [121, 188, 190, 191], competition between slip and twinning [122, 192], as well as the strength of the wires [121]. As a result of these computational studies, many different theories have emerged to describe the strength of the nanowires including classical nucleation theory [81, 121], surface layer strength [191], and surface wrinkling [188]. Furthermore, since most of these simulations are carried out using high strain rate molecular dynamics with rates between $10^7\ s^{-1}$ and $10^{10}\ s^{-1}$, it is unclear which mechanism would occur at experimental strain rates, which are typically between $10^{-4}\ s^{-1}$ and $10^{-2}\ s^{-1}$ [9, 31, 117]. Similarly, the high strain rates in MD simulations obscures the applicability of discussions of the competition between deformation twinning and slip. For a more-detailed discussion of the plasticity and strength of nanowires, the reader is recommended to read [193].

The purpose of this study is to investigate dislocation nucleation in gold nanowires using atomistic simulations in order to understand the effects of loading geometry (surface facets and loading orientation), loading conditions (tension versus compression) and strain-rate effects with a focus on experimentally relevant strain rates. The energetics of dislocation nucleation are investigated by computing the energy barrier as a function of stress for two orientations, <100> and <110>, as well as both tension and compression and prism geometries. Transition state theory is used to estimate the strength of the wires and is compared against instabilities reported in the literature and those observed in our direct MD simulations. Finally, we use an analytical continuum model to gain insight into the nature of dislocation nucleation and the applicability of the Schmid law in describing dislocation nucleation. The continuum model is able to capture the competition between the energy

associated with the character of the dislocation and the total line length which helps explain the choice of nucleation sites.

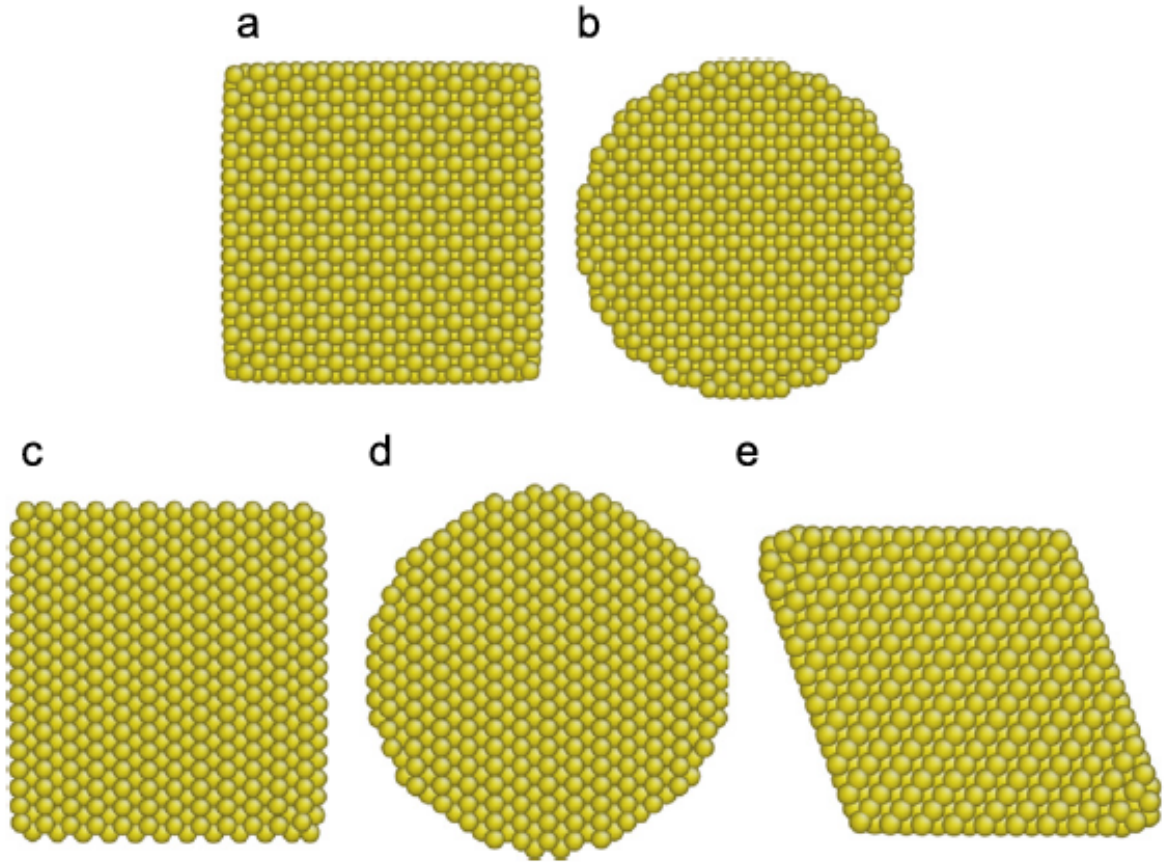

Figure 8.1 The five different cross-section nanowires considered in this study: (a) a (100) square wire with {100} side surface, (b) a (100) with a circular cross-section, (c) a (110) square prism with {100} × {110} cross-section, (d) a (110) circular prism and (e) a (100) rhombic prism with {111} side surfaces

8.2 Atomistic Simulations of Dislocation Nucleation

This work focuses on understanding the orientation, loading direction and surface facet effects on the strength of gold nanowire at experimentally relevant time scales. To capture orientation effects, we will look at two orientations: the <100> and <110>, two high-symmetry directions. For the atomistic simulations, we use nanowires that are approximately 5 nm in size and 15 nm in length with periodic boundary conditions along the wire length. This simplifies the problem since each nucleation site along the nanowire length is equivalent. For the <100> orientation, we include surface facet effects by considering both a square nanowire with {100} side surfaces and one with a circular cross section, as shown in Figure 8.1. For the <110> nanowire, we consider a square nanowire with {100} × {110}

side surface, a circular wire, and a rhombic wire with {111} surfaces also shown in Figure 8.1. Finally, for loading direction effects, we consider both tension and compression of the nanowires.

Homogeneous dislocation nucleation [50, 194-197] and heterogeneous nucleation from free surfaces [81, 121, 198] have been studied extensively. The methods of studying nucleation include simple continuum models [178], Peierls-Nabarro [194], phase-field models [195], molecular dynamics [121, 190], and chain of states methods using atomistics [81]. In this paper, a chain-of-states method is applied to study dislocation nucleation using the Foiles embedded-atom-method (EAM) potential [53]. Additionally, an analytical continuum model is used to bring additional insight often lost in direct atomistics.

8.2.1 Interatomic Potential

In order to accurately capture the nucleation of dislocations in gold, an appropriate interatomic potential must be used. For this purpose, we utilize the EAM Foiles potential for gold [53], which has been shown to represent structural properties of gold well. An additional benefit of this potential is it has been used in several studies of plasticity in gold nanowires previously [53, 122, 199] and therefore the potential's representation of nanowire plasticity at high strain rates is well documented.

Table 8.1 lists many of the relevant properties of the potential including the lattice constant, a_o, the cohesive energy, E_{coh} and the elastic constants, C_{11}, C_{12}, C_{44} and B. Notably, the intrinsic and unstable stacking fault energies (γ_{isf} and γ_{usf}) should be very important for characterizing dislocation nucleation[200] and agree well with DFT calculations for gold. Table 8.1 includes the unstable twinning energy γ_t, the unstable twinning energy, γ_{ut}, and the surface energies of the {100}, {110}, and {111} surfaces: γ_{100}, γ_{110}, and γ_{111}. Also listed in Table 8.1 are the surface stresses f_x^n with the superscript denoted the free surface and the subscript denotes the direction if it is anisotropic. The general agreement between the structural properties predicted by the EAM Foiles potential and the relevant experimental and *ab initio* data suggests this EAM potential should do a reasonable job of representing dislocation nucleation in gold nanowires and nanopillars.

Table 8.1 The relevant physical predictions of the EAM Foiles potential for gold compared to experiments and first principles data

Property	Units	EAM	Experiments	First Principles
a_o	Å	4.08	4.08 [201]	4.06 [96], 4.07 [202], 4.12 [203]
E_{coh}	E_v	3.93	3.93 [204]	
B	GPa	166.67	166.67 [205]	168 [96]
C_{11}	GPa	186	186 [205], 195, and 179 [206]	202 [202], 200 [207]
C_{12}	GPa	157	157 [205], 166, and 149 [206]	174 [202], 173 [207]
C_{44}	GPa	39	42 [205], 42, and 43 [206]	38 [202], 33 [207]
γ_{100}	J/m^2	1.31	1.51 [208], 1.50 [209]	1.62 [210], 1.63 [211]
γ_{111}	J/m^2	1.09		1.39 [210], 1.28 [211], 0.705
γ_{110}	J/m^2	1.18		1.75 [210], 1.70 [211]
γ_{isf}	mJ/m^2	31	32 [212], 33 [213]	32 [214], 27 [203], 44 [215]
γ_{usf}	mJ/m^2	102	N/A	124 [214], 94 [203], 110 [216]
γ_{ut}	mJ/m^2	117	N/A	135 [216]
$2\gamma_t$	mJ/m^2	31	30 [50]	52 [216], 42 [215]
f^{100}	J/m^2	2.10	1.15 [217], 3.2 [218]	4.6 [219]
f^{111}	J/m^2	2.88		2.77 [220], 2.56 [221]
f_{100}^{110}	J/m^2	2.19		
f_{110}^{110}	J/m^2	2.88		

8.2.2 Molecular Statics Simulations

In order to understand plasticity in metallic nanowires, it is useful to consider the stress-strain curves of the wires as well as the mechanisms of failure of the nanowires using direct molecular dynamics and molecular statics. In molecular statics (MS), the atoms positions are relaxed to a local energy minimum using the conjugate gradient method while in molecular dynamics (MD) the positions of the atoms follow Newton's equations of motion. These results can be used to compare against predictions from

transition state theory as discussed later in the text. For gold nanowires, the stress-strain curves have

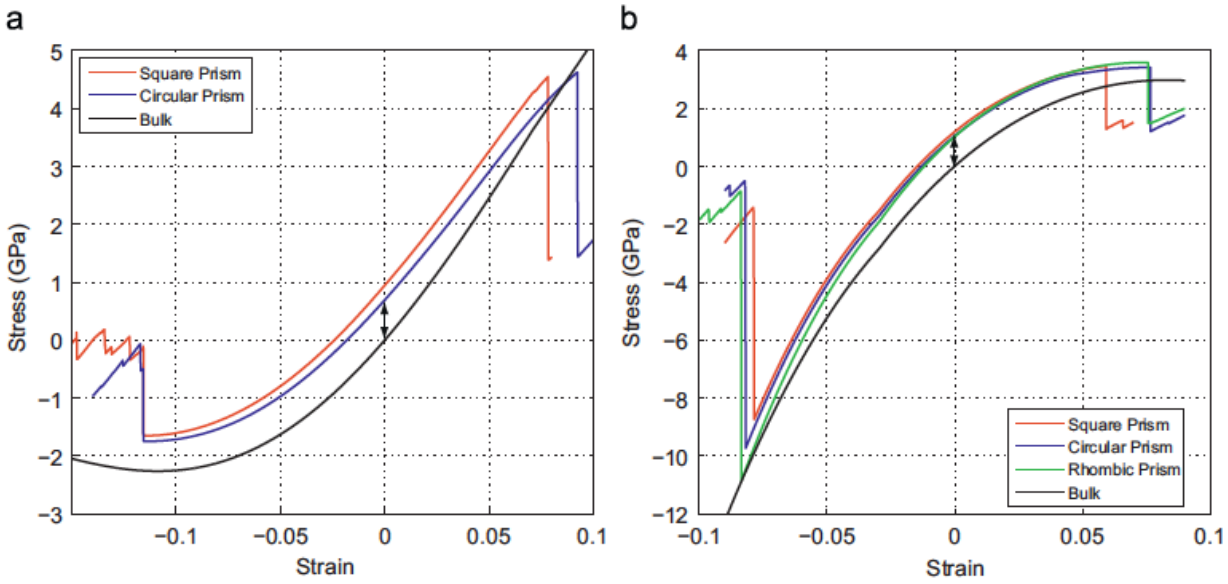

Figure 8.2 The stress-strain curves of (a) (100) and (b) (110) oriented nanowires. The data represents tension and compression tests run at different times from a starting engineering strain of 0.0 relative to the unrelaxed length at the bulk lattice constant, but appended back-to-back. The black arrows show the offset in the stress-strain curve caused by the surface stresses.

been reported previously [121, 188, 190, 191] for some orientations and loading directions. Figure 8.2 shows the engineering stress-strain curves of the nanowires for the EAM Foiles potential computed from MS in both tension and compression by a succession of straining of the atomic box and subsequent atomic relaxations. The initial length used to compute the engineering strain is the length of the crystal carved out of the bulk lattice without relaxation. This means at zero strain, there is a non-zero stress caused by the surface stress as shown in Figure 8.2. Both tension and compression are run independently but are represented as a single curve. For reference, the stress-strain curve for the bulk material in the appropriate directions are included for comparison. We have also performed 0.01K MD simulations, which agree with the molecular statics stress-strain curves, although they show more rounding near the failure point.

For <100> tensile loading, the stress-strain curve is relatively linear and failure occurs via spontaneous dislocation nucleation. For compression in the bulk, we see that the stress strain curve reaches a maximum around 10 percent strain, which has been reported before and corresponds to a phase transformation [190], and decreases after that. As previously reported [190], classical Euler buckling may be responsible for controlling the plastic deformation, due to the vanishing tangent

Young's

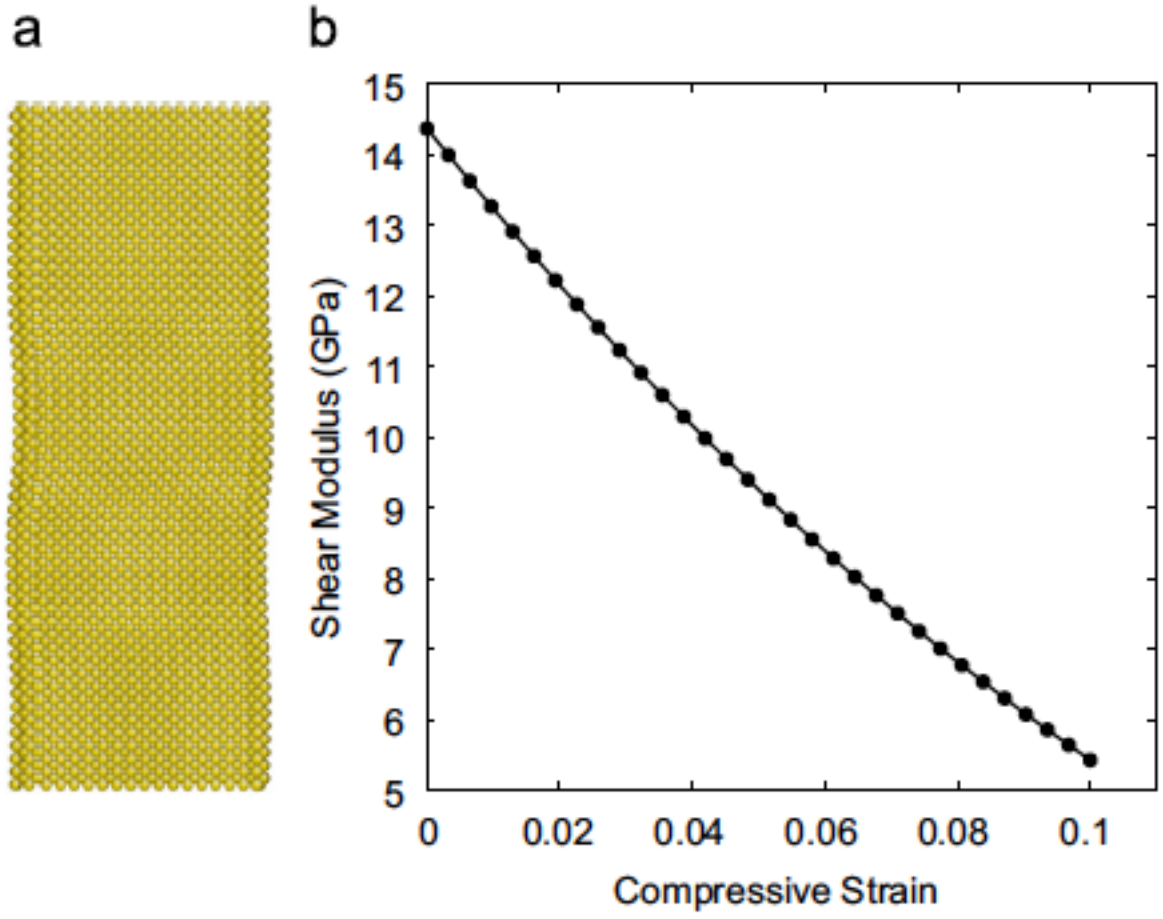

Figure 8.3(a) Buckling during compression of a (110) nanowire prior to dislocation nucleation. (b) Variation of the shear modulus in the [110] in the bulk crystal as a function of uniaxial compression along the $[\bar{1}10]$

modulus, with dislocation emission occurring during post-buckling. Our simulations of the <100> orientated nanowires, both using conjugate gradient and 0.01K MD, do not show any buckling in the <100> but rather spontaneous dislocation nucleation prior to the stress reaching its maximum value. A very similar behavior is observed for <110> tension with the stress-strain curve reaching a maximum resulting in an elastic instability from the vanishing of the tangent modulus. This may not be surprising since <100> compression and <110> tension are directly linked via reorientation caused by twinning [122, 199]. While classical buckling is not expected since the loading is tensile, the vanishing of the tangent elastic modulus still signals an elastic instability. Our MS and MD show standard dislocation nucleation just prior to this instability.

For <110> compression we observe a buckling failure in the lateral <110> direction, as shown in Figure 8.3. The shear modulus in this direction decreases dramatically with the applied load which is consistent with previous reports [190]. However, due to the very small aspect ratios of these pillars, classical beam buckling analysis including Euler theory are inadequate to describe the buckling observed here. Following buckling, we see dislocation nucleation from the free surface which presumably is enabled by the changing surface morphology. Thus, buckling controls the strength of the nanowires for the <110> direction in compression at low temperatures and high strain rates.

To summarize, the MD simulations show a combination of buckling followed by dislocation nucleation for the <110> in compression and dislocation nucleation without buckling for all other cases. However, in the <100> compression and <110> tension cases, the nucleation correlates well with the vanishing of the tangent Young's modulus. With these observation in mind, the simulations are carried out at low temperature and high strain rates. Thus, the question of how nanowires fail at experimental strain rates still remains. It is still unclear if either classical buckling will occur or if standard dislocation nucleation from free surfaces will dominate. It is important, then, to consider the strain-rate-dependent nature of dislocation nucleation by computing their activation energies. Since elastic and structural instabilities should not be strain rate dependent, we can compare the nucleation stresses of thermally activated dislocation nucleation against these instabilities to determine which is dominant at experimental strain rates.

8.2.3 Energy Barriers to Dislocation Nucleation

Dislocation nucleation is a thermally activated process with a well-defined activation energy that has been computed extensively using continuum theory [50, 194, 195, 198, 222]. Most of these studies conclude that homogeneous dislocation nucleation requires stresses that are much higher than values observed in experiments of bulk metallic crystals and are therefore not significant contributors to plastic deformation in metals. However, in submicron metallic single crystals, the flow stress increases dramatically and dislocation nucleation from free surfaces becomes a candidate mechanism. In this section, we compute the energy barriers to dislocation nucleation from free surfaces using atomistic simulations.

The energy barrier for nucleation is computed using a chain-of-states methodology where the initial state is a nanowire compressed to a specified strain and the final state is the same nanowire under the same total strain with a dislocation in it. The dislocations are created by a cut-and-relax

process to create a representative dislocation on the desired slip plane. However, since the stresses in

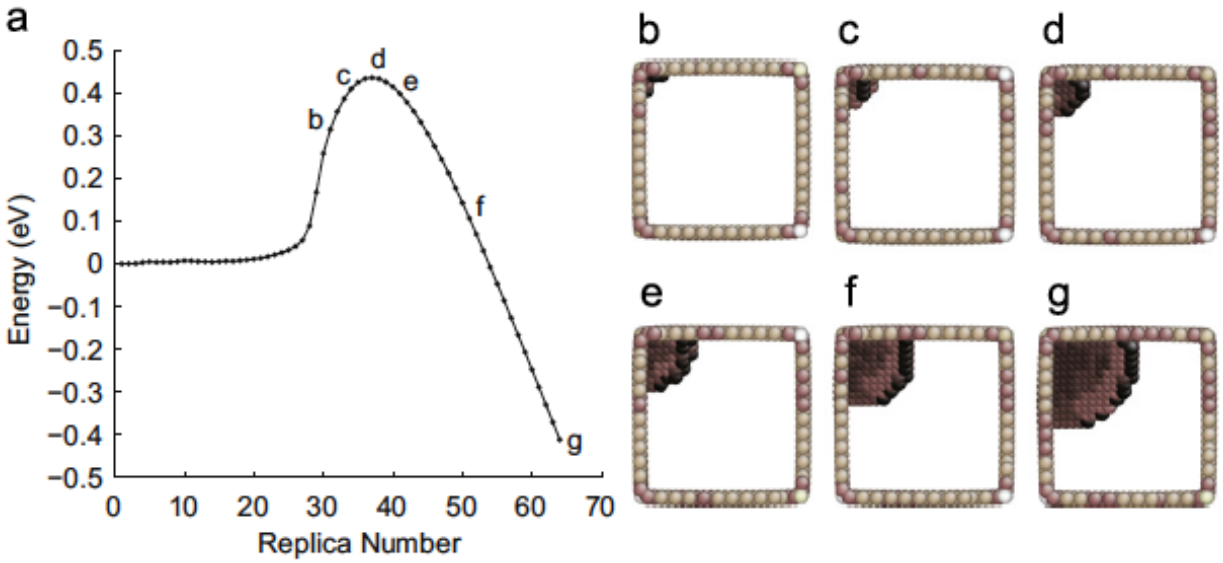

Figure 8.4 An example of the energy barrier calculations for dislocation nucleation in a gold nanowire. The nanowire has a nominal side length of 5nm and the applied stress is 0.66 GPa. (a) The computed energy barrier curve as a function of replica number. (b)-(g) Different instances of the dislocation during the nucleation process; corresponding energies are shown in (a). Atoms are colored according to their centro-symmetry parameter [197].

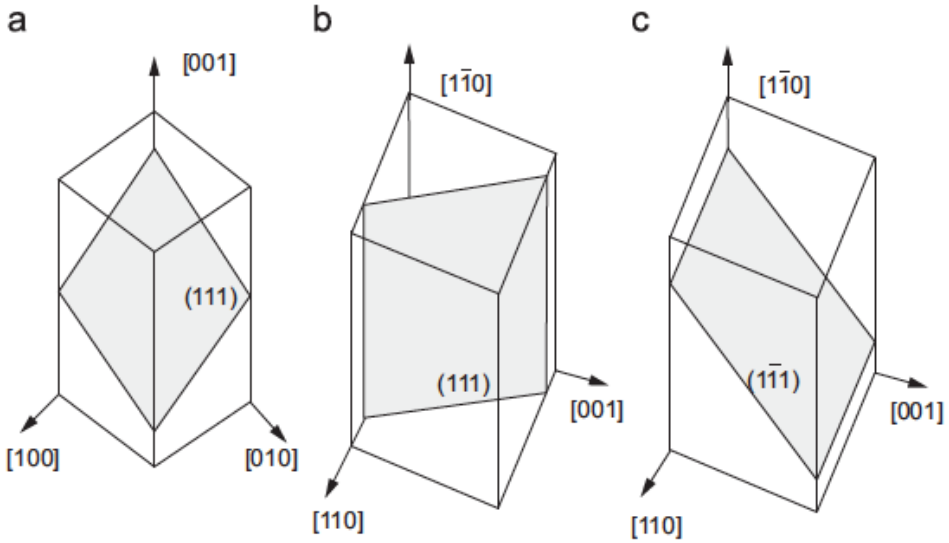

Figure 8.5 Examples of the three distinct slip planes in the (100) and (110) square pillars. (a) A [001] pillar with {100} side surfaces. The (111) plane intersects the pillar surfaces creating both obtuse and acute corners. The three other slip planes can be obtained by successively rotating the slip plane about the pillar by 90◦. (b) A $[1\bar{1}0]$ square pillar with {110} × {100} side surfaces highlighting the (111) plane which contains the pillar axis. The other equivalent slip plane, the $(11\bar{1})$, can be generated by rotating the (111) plane by 70.5° counterclockwise about the pillar axis. (c) A $[1\bar{1}0]$ square pillar with {110} × {100} side surfaces highlighting the $(1\bar{1}1)$ plane which is inclined to the pillar axis. The other equivalent slip plane can be generated by rotating the $(1\bar{1}1)$ plane by 180° about the pillar axis.

these simulations are high, the energy barrier is quite low compared to the nearest metastable state and therefore traditional methods that require metastable configurations for both end states are inefficient. To this end, we use the free end string method [223] which is a generalization of the string method to allow one of the ends to move. This is similar to the free end nudged elastic band method used by other authors [81]. For these simulations, the fixed end of the string is the defect free wire, which is a metastable state, and the free end is the nanowire with a dislocation, which is unstable. These simulations are carried out with 64 images, or states, along the path which ensures an accurate representation of the reaction pathway and are carried out at zero temperature.

Figure 8.4 shows an example of one of our energy barrier simulations. The gold wire is oriented <100> with {100} side surfaces creating a square geometry, which has been studied extensively in the literature. The energy barrier in this calculation, for an applied stress of 0.66 GPa, comes out to be 0.45 eV and the critical dislocation nucleus, as shown in Figure 8.4d, is small even compared to the small ~5 nm pillar.

In order for the calculations to be meaningful, the selected nucleation path must capture the lowest energy dislocation nucleation process in the nanowire. This requires an intelligent choice for the different dislocation configurations used in the energy barrier calculation process. An FCC crystal has four different {111} slip planes and three partial dislocations per slip plane, not all of which are necessarily equivalent. Let's first consider the <100> nanowire that has a square cross-section with {100} side surfaces. We note that the crystal has a fourfold symmetry axis along the <100>, and the geometry of the nanowire obeys this symmetry due to its square cross-section. Thus, each of the four slip planes are equivalent. This conclusion can also be obtained by inspecting each of the different slip planes individually. An example of a square <100> pillar with {100} side surfaces highlighting one of the {111} slip planes is shown in Figure 8.5a. By the same argument, the <100> pillar with a circular cross-section has even higher symmetry, also rendering each of the slip planes equivalent. Therefore, it is sufficient to consider only one of the four slip planes. However, the location of nucleation on this one slip plane still must be determined. This can be done by using the string method and picking a stacking fault as the end state. During the relaxation of this particular configuration, the minimum energy path determines the location where the dislocation will naturally nucleate. This nucleation location is then used in subsequent calculations where the free end is a much smaller dislocation loop providing the necessary resolution of the minimum energy path.

For the <110> pillar, the (110) direction is associated with a dyad axis giving two distinct types of slip planes for the square, circular and rhombic cross-section pillars. Since slip occurs on {111} planes and the specific (110) direction aligned with the axis of the pillar lies on two of those {111} planes, those two slip planes have zero resolved shear stress and zero Schmid factor. An example is shown in Figure 5(b) for a square pillar with {110} × {100} side surfaces. This means these two slip planes are irrelevant. Thus, one only needs to consider one of the two degenerate slip planes with non-zero Schmid factors which are illustrated for a square pillar in Figure 8.5c. Thus the problem is again reduced to looking at the barrier to dislocation nucleation on a single slip plane.

8.2.3.1 The <100> Orientation

In FCC crystals, slip via partial dislocations is direction dependent due to the stacking fault energy surface on the {111} planes resulting in two distinct type of partial dislocations, the leading and trailing partial. As suggested by the choice of names, the leading partial must precede the trailing partial in both slip and nucleation. After leading partial nucleation, the trailing partial may or may not nucleate. The preference for trailing partial nucleation is strongly influenced by the relative Schmid factors between these two partial dislocations. If the Schmid factor for the leading partial is lower, we expect the trailing partial to nucleate immediately as the energy barrier to trailing partial nucleation would be smaller than leading partial nucleation. If the Schmid factor for the trailing partial is lower, we expect the nucleation of only the leading partial dislocation. Both expectations have been confirmed in MD simulation [122, 224]. Thus, the rate limiting step is the nucleation of a leading partial dislocation from the surface which we will investigate here.

Table 8.2 Schmid factors for dislocation nucleation in nanowires

Orientation	Loading Type	Leading Partial	Trailing Partial
<100>	Tension	0.24	0.47
	Compression	0.47	0.24
<110>	Tension	0.47	0.24
	Compression	0.24	0.47

If we choose the slip plane in particular to be the (111) as shown in Figure 5(a), then the three partial dislocations are the $\frac{a}{6}[11\bar{2}]$, $\frac{a}{6}[1\bar{2}1]$, and $\frac{a}{6}[\bar{2}11]$, where a is the lattice parameter. The $\frac{a}{6}[11\bar{2}]$ is the leading partial in compression and consequently the trailing partial in tension while the

$\frac{a}{6}[1\bar{2}1]$ and $\frac{a}{6}[\bar{2}11]$ are the leading partials in tension and trailing partials in compression. Table 8.2 lists the relevant Schmid factors of the leading and trailing partials for tension and compression of the <100> nanowires. The nucleation sites in the nanowire depend on the specific geometry of the slip plane which is controlled by how the slip plane intersects the free surfaces of the pillar, as shown in Figure 8.5. For our <100> pillars, we are considering both a square pillar with {100} side surfaces and a pillar with a circular cross-section. The geometry of the (111)-slip plane of a (100) pillar with {100} side surfaces is shown in Figure 8.6a. Also shown in the figure are two potential nucleation sites for the leading partial dislocation in compression. The two sites can be distinguished easily because one is acute, 60^o, and the other is obtuse, 120^o. As shown in Figure 8.6a, the Burgers vector is perpendicular to the acute corner and parallel to the obtuse corner. Thus, if the dislocation nucleates from the acute nucleation site, the dislocation would be close to edge in orientation which has a higher energy per-unit-length. By contrast, the dislocation nucleated from the obtuse angle would be near the screw orientation and have a lower energy per-unit-length. This suggests that the choice of nucleation sites would be a balance in energies; the acute angle would have shorter line length but higher energy per-unit-length and the obtuse angle would have larger line length but a lower energy per-unit-length. Our atomistic simulations, which agrees with all previous calculations [81, 121], shows that nucleation occurs from the obtuse angle under compression.

For the circular prism, as shown in Figures 8.6c,d, we see a similar behavior. In this geometry, the {111} slip plane intersects the circular prism creating an ellipse with a minor axis of the same radius as the original pillar and the major axis has a length elongated by $1/\cos\varphi$, where φ is the angle between the {111} plane normal and the (100) loading axis. The leading partial dislocation now has the opportunity to nucleate anywhere on the ellipse. However, the two competing extremes are nucleation from the "obtuse" side and the "acute" side as either screw-like or edge-like, respectively. It is no surprise then that the dislocation nucleates in the screw-like orientation under compression just as it did in the square prism. For the case of tension, there are two different leading partials that can nucleate as shown in Figures 8.6e-h. We note in this case that the dislocations nucleate in the acute corner for both the square and circular prism (as shown in Figures 8.6f,h. The locations of nucleation in this case are not surprising since the location minimizes line length and the dislocation character is almost screw.

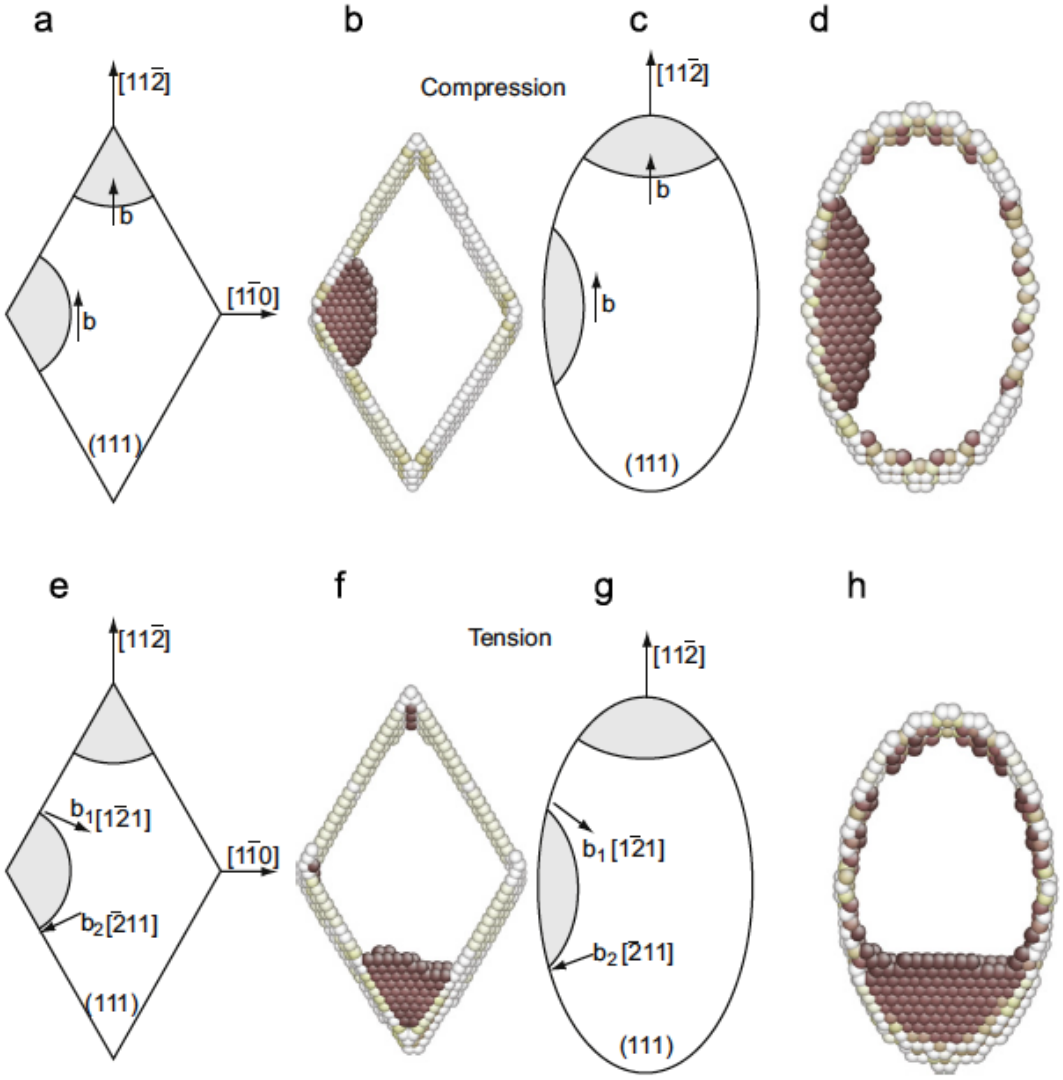

Figure 8.6 The geometry of slip in (100) nanowires. (a) The {111} slip plane of a square nanowire with {100} side surfaces showing two potential source sites in compression. (b) The actual nucle- ation site in the nanowire under compression as predicted by our atomistic simulations. (c) The (100) nanowire with a circular cross-section with two potential nucleation sites in compression. (d) The actual nucleation site as predicted by our atomistic simulations. (e) The {111} slip plane of a square nanowire with {100} side surfaces showing two potential source sites in tension. (f) The actual nucleation site in the nanowire under tension as predicted by our atomistic simulations. (g) The (100) nanowire with a circular cross-section with two potential nucleation sites in tension. (h) The actual nucleation site as predicted by our atomistic simulations. Note that all of the dislocations shown here are super critical in size, but are used to make the figures clearer.

The energy barriers from these simulations for both geometries are shown in Figure 8.7a,b for both tension and compression. From these plots, we can see that the circular prisms are always stronger than the square prisms, in agreement with previous MD simulations [224]. One of the key

differences is the line length of the dislocation: a dislocation nucleating from the same site in a circular pillar will have a longer line length and thus will have a higher energy barrier than one nucleated in a corner. This is corroborated by simple continuum models, discussed in the next section, which shows that circular prisms are always stronger than the square ones and the difference is the line energy of the dislocation.

The activation volume, which is important for understanding the temperature and strain rate sensitivity of thermally activated processes in plasticity, is defined as the negative of the derivative of the activation energy:

$$\Omega \equiv -\frac{dE_b}{d\sigma} \tag{8.1}$$

The activation volume has units of volume and is physically interpreted as the volume of all the atoms involved in the activated process, which in this case is heterogeneous dislocation nucleation. We can interpret the activation volume for dislocation nucleation as the Burgers vector times the area swept out by the nucleating dislocation, which can be derived directly from our continuum models in Section 8.3. For comparison, the activation volumes for plastic processes in bulk FCC metals typically lie between $100 - 1000b^3$ [225].

The activation volume can be computed numerically from Figures 8.7a,b if desired. However, the numerical differentiation is not very accurate and so we choose to fit a curve to the activation energy versus stress curve and analytically take the derivative which produces smoother values of the activation volume as well as provides an interpolation for the activation energy. While cubic splines may be a popular choice, we choose to fit the data with the following function:

$$E_b = A\left[1 - \exp\left(\alpha\left(1 - \frac{\sigma}{\sigma_o}\right)\right)\right] \tag{8.2}$$

where A, α and σ_o are fitting parameters. The functional form was chosen to represent some features of energy barrier curves for dislocation nucleation one expects from intuition. First, it has an athermal limit, σ_o, at which the energy barrier and activation volume are zero. Second, it predicts a monotonically decreasing energy barrier and activation volume as a function of the applied stress up to that athermal limit. Finally, this particular functional interpolates all of the energy barrier data in our paper well with correlation coefficient values of 0.97 or greater. The activation volume from this functional form is:

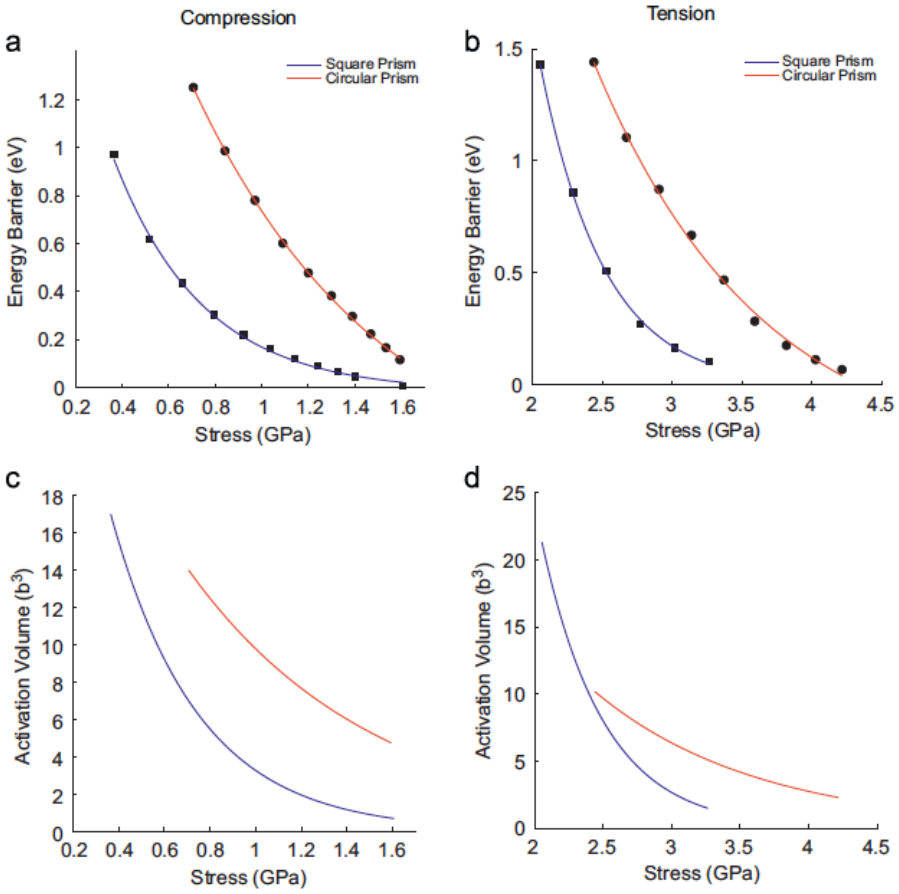

Figure 8.7 The activation energy of dislocation nucleation in (100) gold nanowires for (a) compression and (b) tension. The activation volume, determined from the derivative of the curve fit, is shown in (c) for compression and (d) for tension. The circles and squares are the atomistic data points for circular and square prisms, respectively.

Table 8.3 The fitted parameters for the energy barrier and activation volume compared with athermal critical stress (σ_{ath}) values from molecular statics simulations. The fitted value σ_o and the athermal strength from molecular statics σ_{ath} agree well except for the (110) orientation where σ_{ath} corresponds to buckling. The R^2 value is reported for the curve fit as an indicator of the quality.

Orientation	Loading Direction	Cross-section	A (eV)	α	σ_o (GPa)	σ_{ath} (GPa)	R^2
<100>	Compression	{100} × {100}	-0.0168	5.05	1.92	1.65	1.00
<100>	Compression	Circular	-0.452	2.19	1.79	1.75	1.00
<100>	Tension	{100} × {100}	-0.082	9.68	4.41	4.54	1.00
<100>	Tension Compression	Circular	-0.3670	3.64	4.34	4.64	1.00
<110>	Compression	{100} × {110}	-0.0019	7.37	18.4	8.74	0.97
<110>	Tension	Circular	-0.0095	5.88	21.8	9.73	0.99
<110>	Tension	{100} × {110}	-0.487	7.57	3.46	3.46	1.00

$$\Omega = \frac{A\alpha}{\sigma_o} \exp\left(\alpha\left(1 - \frac{\sigma}{\sigma_o}\right)\right) \tag{8.3}$$

When the activation energy is zero, $\sigma = \sigma_o$, which is sometimes interpreted as the athermal strength of the material. Furthermore, σ_o is a fitting parameter determined from a least squares fit of our data and may have error due to both the fitting procedure and the assumed functional form. Furthermore, we have the athermal strength, σ_{ath}, from our molecular statics simulations. The fitted value, σ_o, agrees will with the molecular statics in all cases except for the <110> compression when the wires fail by buckling as shown in Table 8.3. The curve fit of the activation energy is shown in Figure 8.7a,b and the corresponding activation volume in 8.7c,d. The fit of the data is generally quite good and the parameters for the fit can be found in Table 8.3. The activations volumes, shown in Figure 8.7c,d vary from $1 - 20b^3$ where $b = {}^{a}/_{\sqrt{2}}$, which is in agreement with previously reported activation volumes of surface sources [81]. The variation of activation volumes with respect to the applied load shows that the critical dislocation radius is a function of the applied stress. The larger the applied stress, the smaller the critical radius of the dislocation nucleus. It is also worth noting that not only are the activation energies of circular prisms greater than square ones, but so are the activation volumes. This suggests that circular prisms are generally stronger but may be slightly less strain rate sensitive.

8.2.3.2 The <110> Orientation

As previously mentioned, slip in a <110> oriented nanowire will occur on one of two degenerate slip planes (Figure 8.5c). The other two that make up the four slip planes have zero resolved shear stress and do not contribute to plastic deformation (Figure 5b). If we again limit ourselves to consider specifically a [011] nanowire and the (111) slip plane, the three partial dislocations on this slip plane are again the $\frac{a}{6}[11\bar{2}]$, $\frac{a}{6}[1\bar{2}1]$ and $\frac{a}{6}[\bar{2}11]$. The leading and trailing partial dislocations are reversed from the <100> nanowires: the $\frac{a}{6}[11\bar{2}]$ is the trailing partial in tension and leading partial in compression while the $\frac{a}{6}[1\bar{2}1]$ and $\frac{a}{6}[\bar{2}11]$ are the leading partials in tension and trailing partials in compression.

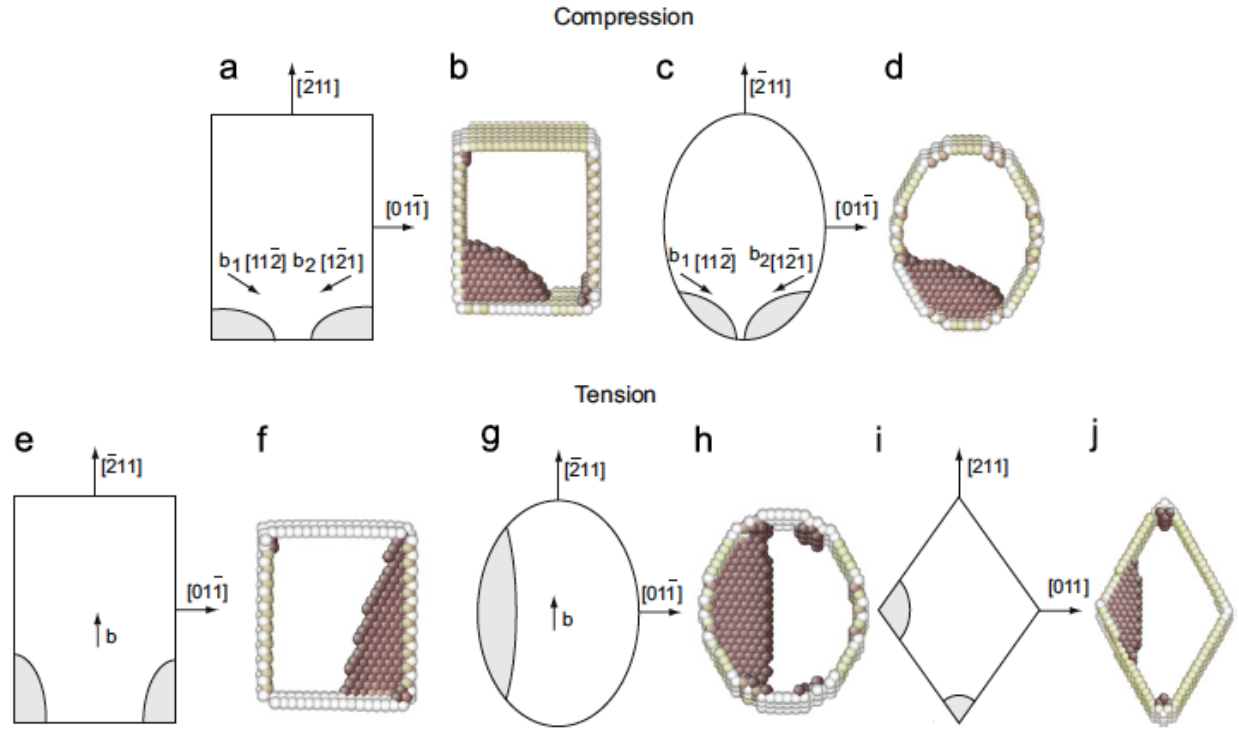

Figure 8.8 The geometry of slip in (110) nanowires. (a) The {111} slip plane of a square nanowire with {100} × {110} side surfaces showing two potential source sites in compression. While the two sites appear equivalent, the energy barriers are different if the Burgers vectors are the same. (b) The actual nucleation site in the nanowire under compression as predicted by our atomistic simulations. (c) The (110) nanowire with a circular cross-section with two potential nucleation sites in compression. (d) The actual nucleation site as predicted by our atomistic simulations. (e) The {111} slip plane of a square nanowire with {100} side surfaces showing two potential source sites in tension. (f) The actual nucleation site in the nanowire under tension as predicted by our atomistic simulations. (g) The (110) nanowire with a circular cross-section with one potential nucleation sites in tension. (h) The actual nucleation site as predicted by our atomistic simulations. (i) The (110) nanowire with a rhombic cross section illustrating the two potential nucleation sites and (j) the actual nucleation site as predicted by our atomistic simulations. Note that all of the dislocations shown here are super critical in size, but are used to make the figures clearer.

Figure 8.8 shows a geometric representation of nucleation sites compared against the actual nucleation sites in the <110> nanowires. We observe again that the nucleation site is the one that appears to reduce line length as well as maintain an orientation close to screw. This agrees with the trends observed in <100> nanowires. As an example, the rhombic <110> nanowire in tension (Figure 8.8i,j) shows nucleation that looks very similar to the square nanowire in compression, where the two Burgers vectors and Schmid factors are the same and the geometries are similar. The circular <110> nanowires in tension and compression show the similar profiles to the circular (100) nanowires with the opposite loading direction. The slight differences between the shape of the <110> compression and <100> compression may have to do with the eccentricity of the ellipsoidal slip planes.

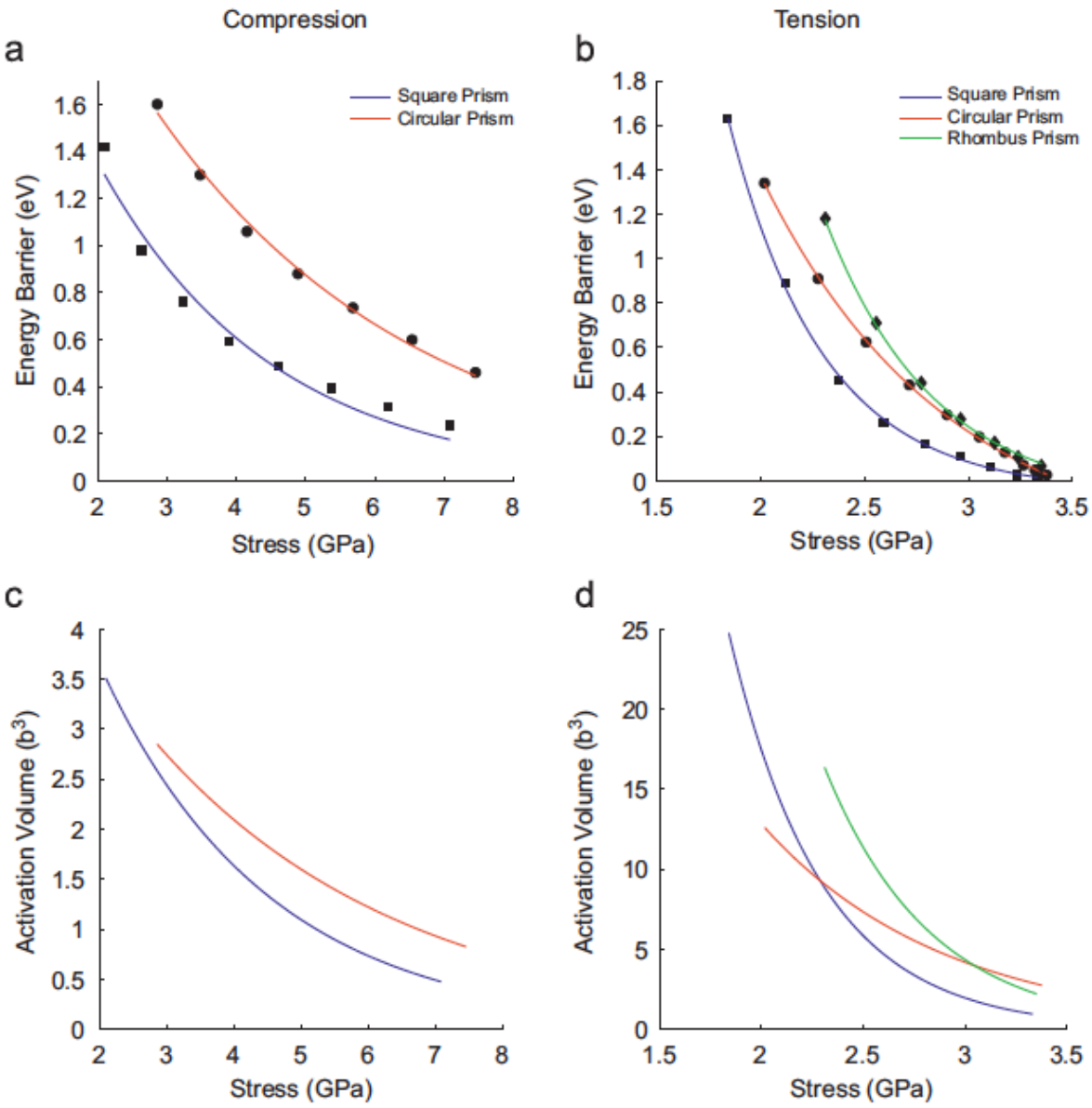

Figure 8.9 The activation energy of dislocation nucleation in (110) gold nanowires for (a) compression and (b) tension. The activation volume, determined from the derivative of the curve fit, is shown in (c) for compression and (d) for tension. The circles, squares, and diamonds are the atomistic data points for circular and square and rhombic prisms, respectively.

The <110> rhombic nanowire data for compression is not shown although energy barrier calculations were performed. This is partially due to the nature of the nucleation showing conflicting results. For stresses ~ 6 GPa (energy barrier of 1.0 eV), our results show a stable dislocation nucleating from the free surface. However, higher stress calculations actually show homogeneous

nucleation in the center of the nanowire, which agree with our low temperature (0.01 K) simulations, although these dislocations nucleate while the nanowire is undergoing an elastic instability. This is a strange result at first, however unusual behavior of <110> nanowires with {111} side surfaces in compression was reported before by Park et al. [122]. They observed in gold (using the same potential), nickel, and copper that line defects did not nucleate in their simulations. While our results are different, showing line defects nucleating, the unusual nature of our results suggests that reporting a single energy barrier curve would be inappropriate. In order to fully explore this phenomenon a range of mechanisms would need to be explored through the string method to and a set of energy barrier curves would need to be reported.

Figure 8.9 shows the energy barrier curves and activation volume curves or <110> nanowires in tension and compression. The Schmid factors for the leading partials in compression are about half that of the leading partials in tension. We note that this signature appears again in the energy barrier curves with the compression barriers being larger than those in tension. Furthermore, the activation volumes in compression are much lower than those in tension with the compression activation volume is less than $4b^3$ while the tension data has values well above $10b^3$. These results also support the notion that the square prisms are weaker than the circular prisms. The circular prism and rhombic prism show very similar energy barrier curves converging upon one another at high stresses.

The energy barrier calculations performed here show a complete picture of dislocation nucleation. From the reaction pathways we see that dislocations prefer to nucleate in the screw orientation in order to reduce their line energy. The energy barrier curves show that square prisms are generally weaker than circular prisms, which we hypothesize primarily occurs from the reduction in line length from corner nucleation. The computed activation volumes are small, confirming that nucleation is both temperature and strain rate dependent. A comparison of the fitted athermal strength, σ_o, shows very good correlation with the athermal strength computed from molecular statics, σ_{ath}, except in the case of <110> where buckling is observed in molecular statics rather than spontaneous dislocation nucleation. In the next section, we will use a pure continuum model and repeat our calculations and confirm the role of line energy in controlling nucleation. In Section 4, the energy barrier calculations will be used to predict strengths in gold nanowires.

8.3 Continuum Modeling of Dislocation Nucleation

To better understand the choice of nucleation sites, we construct a simple continuum model to capture the essential mechanics of nucleation. The model is in the spirit of that proposed by Hirth and Lothe [50] (pages 758-760). However, the Hirth-Lothe model does not account for the competition between screw and edge dislocations which is important for understanding the competition among nucleation sites in a nanowire. Therefore, we define the change in Gibbs free energy for nucleation as:

$$\Delta G = \int \varepsilon(\theta) dL + A\gamma - A\sigma bS \tag{8.4}$$

where $\varepsilon(\theta)$ is the energy per unit length of the dislocation which depends on the dislocation orientation, A is the area of the loop, L is the line length of the dislocation, γ is the stacking fault energy, σ is the applied axial stress, S is the Schmid factor, and b is the Burgers vector. For convenience, we take the line energy per unit length as the standard orientation dependent line energy:

$$\varepsilon(\theta) = \frac{\mu b^2}{4\pi(1-\nu)}(1 - \upsilon \cos^2\theta) \ln\frac{r}{r_c} \tag{8.5}$$

where θ is the angle between the line direction defined by L and the Burgers vector b and r_c is an inner cutoff radius used to regularize the elastic energy. To further simplify the calculation, we assume that in every case the dislocation nucleated is an arc with a radius r that spans an angle α. This allows the change in Gibbs free energy to be written as:

$$\Delta G = \int_{-\alpha/2}^{\alpha/2} \int \frac{\mu b^2}{4\pi(1-\nu)}(1 - \upsilon \cos^2\theta) r \ln\frac{r}{r_c} d\psi + A\gamma - A\sigma bS \tag{8.6}$$

where *r* is the radius of the dislocation loop and the relationship between θ and ψ depends on the geometry of the problem. For dislocation nucleation from corners, the area simplifies to $A = \frac{1}{2}\alpha r^2$. For example, one can compute the elastic energy of the dislocation loop from the obtuse angle in Figure 6(a) by setting the angle θ equal to ψ and α equal to 120^o.

From this model, one can determine the energy barrier as a function of the applied stress σ similar to how it is done in atomistics. However, here we directly control the loop radius r, which guides the free energy of the system. From this one can determine ΔG^* and r^*, the maximum free energy and critical dislocation radius, at a given applied stress level σ. The parameters that must be specified are the shear modulus, Poisson's ratio, stacking fault energy, Burgers vector and inner cutoff radius r_c. The stacking fault energy we take to be the value of the EAM potential and the elastic

constants are taken to be $\mu = 25\ GPa$ and $\nu = 0.48$. These values are determined from the anisotropic energy factors as suggested by Scattergood and Bacon [226]: $\mu = \frac{4\pi}{b^2} K_s$ and $\upsilon = 1 - {K_s}/{K_e}$ where K_s and K_e are the prelogarithmic energy factors for a screw and edge dislocation, respectively, for a partial dislocation on the {111} plane computed from anisotropic elasticity theory. The final value that may be ambiguous is the inner cutoff radius r_c which we take to be $1.0b$ for convenience. We note that the choice of r_c can significantly affect the results, however, the purpose here is not to fit our continuum model to our atomistic results but rather gain insight to the nucleation process.

The continuum model also provides a direct physical interpretation of the activation volume. The critical Gibbs free energy, Equation 4, depends on the applied stress explicitly in the last term as well as implicitly through the area and line length due to the stress dependence of r^*. The activation volume is then:

$$\Omega = -\left(\frac{d}{dr}\int \varepsilon(\theta) dL + \gamma \frac{dA}{dr} - \sigma b S \frac{dA}{dr}\right)_{r=r^*} \frac{dr^*}{d\sigma} + AbS \tag{8.7}$$

The term in parenthesis is zero since, by the definition of r^*, it maximizes Equation 4 and so the first derivative is zero. Thus, the activation volume has a very simple physical form:

$$\Omega = SAb \tag{8.8}$$

The Schmid factor appears here because the derivative is with respect to the applied axial stress, and not the resolved shear stress.

Figures 8.10 and 8.11 show the energy barrier and activation volume curves

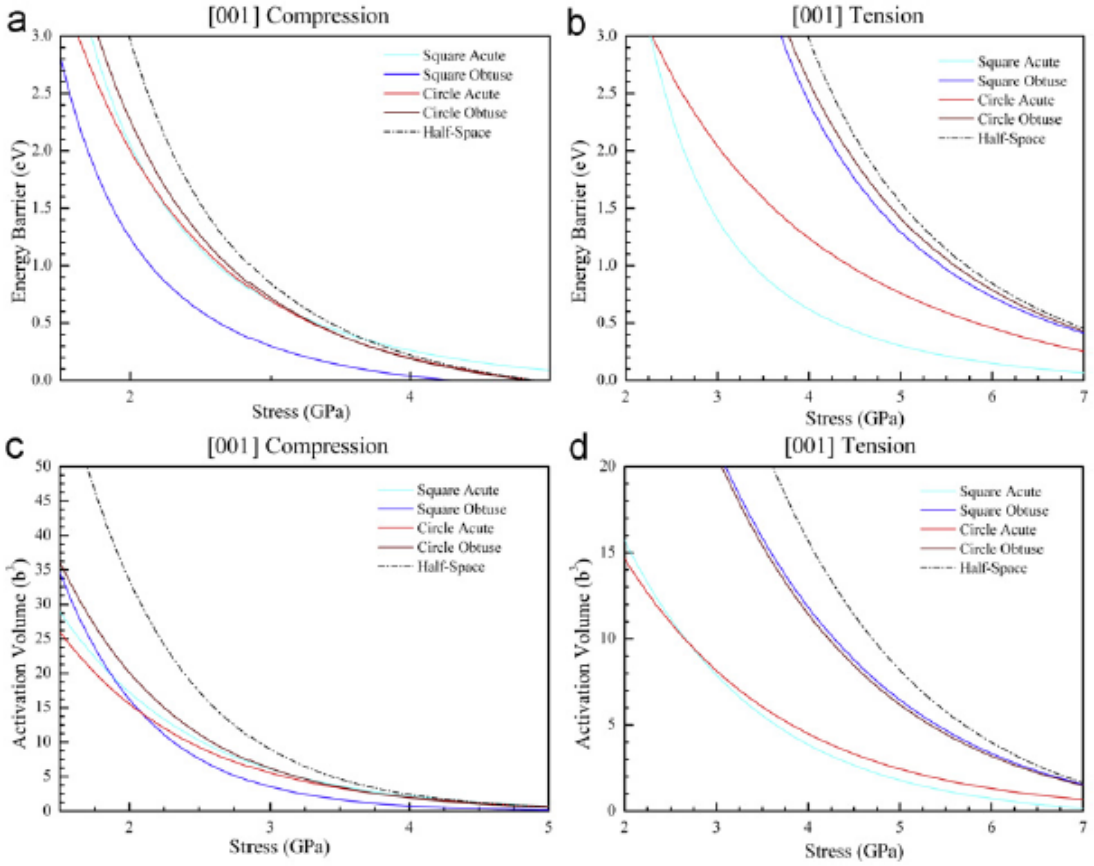

Figure 8.10 The activation energy of dislocation nucleation in (100) gold nanowires for (a) compression and (b) tension using the orientation-dependent line energy. The activation volume, determined from the derivative of the curve fit, is shown in (c) for compression and (d) for tension.

for this simple continuum model. For each square pillar, we compute the energy barrier for nucleation from both corners, the obtuse and acute. Similarly, we compute energy barriers for the obtuse and acute radii of the elliptical slip planes in the circular pillars. For comparison, we also show the energy barrier curves for the nucleation of a circular loop from a half-space. This is done for pillars of <100> and <110> orientations.

We note that, in general, the trends predicted from the simple analytical continuum model agree with the atomistic simulations. For example, square pillars are always weaker than circular ones due to the reduction in line length in the corners of the pillars. The difference can be quite significant

even at 0.8-1.0 eV, showing strength differences of around 1 GPa. The difference in strengths becomes more significant at lower activation energies, which correspond to higher strain rates. The trend of strength as a function of wire orientation and loading is also recovered showing that <110> compression is the strongest, followed by <100> tension. The strengths of the <100> compression and <110> tension are almost identical following trends observed in MD simulations. The ordering of the strengths of the nanowires in the continuum model is largely controlled through the resolved shear stress which explains the successfulness of Schmid's law in characterizing nanowire strength [121].

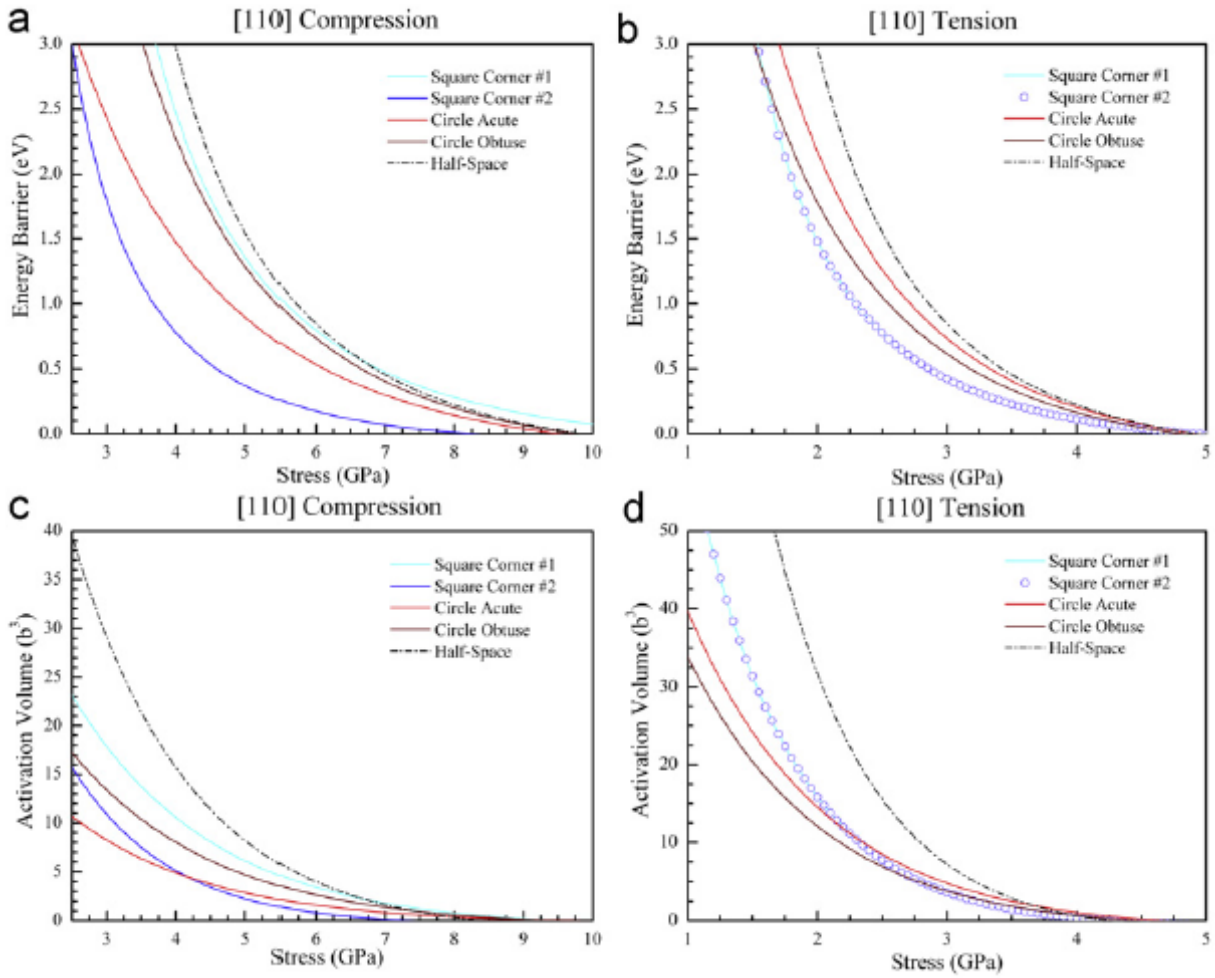

Figure 8.11 The activation energy of dislocation nucleation in (110) gold nanowires for (a) compression and (b) tension using the orientation dependent line energy. The activation volume, determined from the derivative of the curve fit, is shown in (c) for compression and (d) for tension.

The model also confirms one of our previous hypotheses, that the orientation dependent line energy controls the nucleation sites in pillars. Our atomistic simulations show that the preferred nucleation site is the obtuse corner for <100> compression, which is verified by the continuum model in Figure 8.10a which shows the energy barrier to nucleation from the obtuse corner is significantly lower than nucleation from the acute corner. This trend is flipped in tension for both the atomistics and continuum models. For the <110> orientation in tension, the continuum model predicts all four corners to be equal nucleation sites. In compression, both corners can nucleate two different types of dislocations, one that is screw like and one that is edge like and thus it is not surprising the continuum models favors the screw like character from any one of the four corners.

For the circular pillars, the differences are not as significant. This is, in part, due to our treatment of the dislocation loop as a circular arc. This removes a significant part of the orientation dependent energy because the loop is often very close to a half circle. For <100> pillars in compression, the model predicts nucleation from the acute angle at low stress and nucleation from the obtuse angle at high stress, with a transition around 0.5 eV. The atomistics predict nucleation from the obtuse and the dislocation nucleus is clearly not circular, but more elliptical with an exaggerated screw component that likely lowers the energy barrier below that of the acute. For the <100> in tension, the atomistics and continuum both predict nucleation from the acute side. For the <110> orientations the atomistics and continuum model again show agreement predicting acute for compression and obtuse for tension.

This simple continuum model also makes some very interesting predictions when compared to the semi-circular dislocation nucleation from the half space. First, the energy barrier curves of all the circular solutions converge on the half space solution at high stress. This is because, at high stress, the critical dislocation loop radius is much smaller than the curvature of the elliptical slip plane, converging to a half space as the critical radius goes to zero. Second, and perhaps more interesting, is that the nucleation of edge dislocations from the acute corner for <100> compression and from the edge-like corner for <110> tension rise above the half-space solution at very high stress as seen in the light blue curves, square acute, versus the dash dot curves, half space, in Figures 8.10a and 8.11a. This, in particular, is a interesting result because it suggests that at high stress dislocation nucleation from certain corners is not preferred even over nucleation from a flat surface.

Finally, it is worth discussing what such a simple continuum model says about a critical resolved shear stress (CRSS) law and its applicability to dislocation nucleation in nanowires. This nucleation criteria, which has been discussed by several authors in the context of dislocation nucleation [121, 190], is similar to Schmid's law in that it suggests that flow occurs when the shear stress resolved onto the slip plane in the slip direction reaches a critical value. Here, we will interpret the CRSS law to be valid when the energy barrier curves for different nanowires are predicted to be equivalent as a function of the resolved shear stress. This is true, from Equation 8.6, for all orientations/loading conditions if one considers the nucleation of a circular dislocation from a half-space. This would also suggest that the CRSS law would be better obeyed for nucleation at high stresses in circular pillars, since these solutions approach the half space solution at high stress. However, if one were to allow the dislocations to change shape during nucleation, as they most certainly would, this would likely cause deviations from the CRSS law again. This also says that the CRSS law will not work for square pillars since the line energy will depend on the orientation of the surface facets relative to the Burgers vector. These factors are in addition to other reasons that would cause a deviation from the CRSS law such as surface stress, stress-dependent stacking fault energies, and stress-dependent elastic constants that are inherently captured in atomistic models.

Despite the insight gained from this model and its agreement with atomistics, it does not take into account several important features: step formation energy, the unstable stacking fault energy, effects of image forces, core spreading during nucleation, and an allowance for the dislocation line to change shape. All of these terms will influence the magnitude of the stress required for nucleation. Thus, it is surprising and remarkable that such simple physics is able to capture the trends found in atomistics.

In this section, we have shown that a simple continuum model based on the line energy of a dislocation can reproduce much of the trends observed in the atomistic simulations. The square pillars are weaker than circular pillars due to the reduction in line length associated with nucleation from a corner. Furthermore, we can predict the order of strength with respect to pillar orientation and loading type (tension versus compression) which is dominated by the Schmid factor. Further- more, this model also shows that the CRSS law is only valid in the most ideal cases. Finally, the continuum model also gives a direct correlation between the activation volume and a measure of atomic volume.

8.4 Strength and Size Effects

In this section, we attempt to link the energy barriers computed in Section 2 to the strength of the nanowires using classical nucleation theory and compare the values against relevant experiments. Furthermore, since the nanowires computed here are on the order of 5 nm in size, or 25 nm^2 cross-sectional area, we discuss the effects of size on strength and how to estimate strength at larger diameters.

The nucleation rate of a dislocation can be expressed classically as:

$$p = \nu_o N \exp\left(\frac{-E_b}{k_B T}\right) \tag{8.9}$$

where N is the number of nucleation sites, ν_o is the attempt frequency, k_B is Boltzman's constant, T is the temperature, and E_b is the activation energy. However, this expression is valid at constant stress, whereas experiments are usually conducted at constant strain rate. Several authors have already discussed this issue [81, 227] and derived an implicit expression for the stress of the most probable nucleation event. We will summarize the arguments here for completeness. Consider N identical nanowires loaded at constant strain rate $\dot{\varepsilon}$ at a given time t, where f is the fraction of nanowires that have not nucleated a dislocation. The evolution equation for the fraction of nanowires that have not nucleated a dislocation is:

$$\frac{df}{dt} = -pf \tag{8.10}$$

where p is the nucleation rate. Next, one defines the most probable nucleation stress as the stress when

$$\left.\frac{d^2 f}{d\sigma^2}\right|_{\sigma_{crit}} = 0 \tag{8.11}$$

Using Equations 8.9, 8.10, and 8.11 and noting that under constant strain rate that $\sigma = E\dot{\varepsilon}t$ one arrives at an implicit expression for the most probable nucleation stress:

$$\frac{E_b}{k_B T} = \ln\left(\frac{k_B T N \nu_o}{E\dot{\varepsilon}\Omega}\right) \tag{8.12}$$

where E_b and Ω are both functions of σ. A detailed discussion and derivation can be found in Appendix A. If we use a linear expansion of the activation energy with respect to stress, $E_b \approx E_o - \sigma\Omega_o$, one arrives at an approximate expression for the strength:

$$\sigma_{crit} = \frac{E_o}{\Omega_o} - \frac{k_B T}{\Omega_o}\ln\left(\frac{k_B T N \nu_o}{E\dot{\varepsilon}\Omega}\right) \tag{8.13}$$

This expression is useful in understanding functional relationships, however the linear expansions of the energy barrier is only valid in a small range. This may be an acceptable approximation for interpreting experimental results where one varies the strain rate by one or two orders of magnitude. However, it is inappropriate to use it when comparing experiments and MD simulations.

Table 8.4 The predicted strength, σ_{crit}, of the nanowires at 300K at a strain rate of $10^{-3}s^{-1}$ with a 5 nm nominal size

Orientation	Loading Direction	Cross-section	σ_{crit} (GPa)	$\sigma_{crit}S$ (GPa)	$\sigma_{crit}S/\sigma_{ideal}$	$\sigma_{crit}/\sigma_{ath}$
<100>	Compression	{100} × {100}	0.40	0.19	0.10	0.24
<100>	Compression	Circular	0.90	0.42	0.23	0.51
<100>	Tension	{100} × {100}	2.3	0.55	0.30	0.51
<100>	Tension	Circular	2.9	0.70	0.38	0.63
<110>	Compression	{100} × {110}	3.0	0.72	0.39	0.34
<110>	Compression	Circular	4.8	1.15	0.63	0.49
<110>	Tension	{100} × {110}	2.1	0.98	0.54	0.61
<110>	Tension	Circular	2.3	1.08	0.59	0.67
<110>	Tension	{111} × {111}	2.5	1.17	0.64	0.70

Table 8.5 The predicted strength, σ_{crit}, of the nanowires at 300K at a strain rate of $10^{-3}s^{-1}$ with a 100 nm nominal size

Orientation	Loading Direction	Cross-section	σ_{crit} (GPa)	$\sigma_{crit}S$ (GPa)	$\sigma_{crit}S/\sigma_{ideal}$
<100>	Compression	{100} × {100}	1.2	0.56	0.31
<100>	Compression	Circular	1.5	0.71	0.38
<100>	Tension	{100} × {100}	1.3	0.31	0.17
<100>	Tension	Circular	2.3	0.55	0.30
<110>	Compression	{100} × {110}	4.2	1.01	0.55
<110>	Compression	Circular	5.6	1.34	0.73
<110>	Tension	{100} × {110}	1.0	0.47	0.26
<110>	Tension	Circular	1.3	0.61	0.33
<110>	Tension	{111} × {111}	1.5	0.71	0.38

It is worth noting that we have specifically not included the temperature dependence of the energy barrier and activation volume. Our interest in predicting strength in this paper is at 300K.

However, our energy barrier calculations are done at 0K with our interatomic potential. To account for this, Zhu et al. [81] have reduced the activation energy by multiplying by a scaling factor, $\left(1 - {}^{T}/_{T_m}\right)$, where T_m is the surface disordering temperature, but such an approximation has been called into question [228]. Recently, Ryu et al. [229] have investigated the effects of temperature on dislocation nucleation and concluded there are two main effects: thermal expansion and thermal softening, both of which are entropic. However, most interatomic potentials, such as this one, are fit at 0K to experimental (300K) lattice constants and elastic constants. Thus, altering the nucleation rate as Ryu et al. have done for thermal effects will likely overestimate the nucleation rate. For our purposes, we will take our zero Kelvin energy barrier calculations as representative of those for gold at room temperature. Furthermore, we will take the attempt frequency to be the Debye frequency, $\nu_o = k_B\Theta_D$ where $\Theta_D = 170K$. The number of nucleation sites we take to be ~320 since there are ~ 40 sites along the length with 4 equivalent slip planes and two sites on each slip plane for the <100> wires. Similar arguments give $N \sim 200$ for the <110> nanowires.

The equation derived above assumes that the Young's Modulus E is a constant such that the stress is always $\sigma = E\dot{\varepsilon}t$. One can see from Figure 8.2 that this assumption is invalid, especially at high strains. However, for constant strain rate simulations, Equation 8.12 is valid for nonlinear stress-strain relationships if the Young's modulus is replaced by the tangent Young's modulus $E_T \equiv {}^{d\sigma}/_{d\varepsilon}$. This is shown in Appendix A along with the derivation for constant stress rate and the associated critical nucleation rates.

Using the above parameters and our energy barrier curves, we can predict the strength, σ_{crit}, of our nanowires at experimental time scales and temperatures by numerically solving Equation 8.12. The values of these predictions for 300 K at $\dot{\varepsilon} = 10^{-3}s^{-1}$ are shown in Table 8.4. We can compare our predictions with several ways to rationalize the data. For example, it has been argued by Diao et al. [121] that the strength of nanowires would follow maximum shear stress criterion which can be checked by dividing by the Schmid factor. However, our results can be influenced by the surface stress, which creates an internal compressive stress in the nanowire biasing the strength, which we will look at momentarily. The maximum shear stress criteria can be derived by assuming that sliding occurs at some fraction of the ideal shear strength of the crystal. This value we can compute from the slope of the unrelaxed generalized stacking fault energy curve, which we will call τ_{ideal}. The fraction of

$\tau_{ideal}$is also listed in Table 8.4. In addition, we can compare our results to the computed athermal axial stress from molecular statics, σ_{ath}. The maximum shear stress criteria gives significant scatter and normalizing the maximum stress by our computed athermal axial stress reduces that scatter but does not eliminate it entirely. Although our data is affected by size effects, it suggests that a maximum stress criteria cannot explain the results.

In comparison with experimental data, we note that there is extensive literature on the compression of (100) gold sub-micron pillars with diameters as small 200 nm [8-10, 32]. These experiments max out at a compressive stress of 900 MPa, which is at the upper limit of our calculations. This seems rather contradictory since one would expect the nanowires we model, with their perfect surfaces, to represent an upper limit to the strength. However, as noted before, our wires are of order ~ 5 nm and are under significant surface stress. Furthermore, repeating these calculations for larger nanowires might be possible but will be significantly more costly; a 20 nm nanowire will cost 64 times more computational resources than our 5 nm wires. Since we know how the surface stress scales with nanowire size, we can estimate the surface stress contribution as an applied stress and remove it from the calculations. The induced stress by the surface stresses is just the difference between the bulk value of stress and the stress in the nanowire at 0 engineering strain (unrelaxed). This is the chief justification for the use of the axis shown in Figure 8.2. However, the surface has elastic constants as well and therefore changes as a function of the applied strain. Thus, to remove the surface stress completely, it suffices to first order to use the strain from the nanowire energy barrier curves but the stress evaluated using the bulk stress-strain curve. The strengths calculated this way, for a 100 nm nanowire, are listed below in Table 8.5.

This correction produces strengths that make more sense with respect to the compression data of <100> gold submicron pillars. The square and circular pillars exhibit a strength range between 1.2 and 1.5 GPa, representing a potential upper limit to the compression data further suggesting that plasticity in those pillars are not dominated by surface sources.

We note that the surface stress suggests that there is a size effect in nanowire strength. Since surface stress is generally tensile, it will generally induce a compressive stress into the nanowire making them weaker in compression and stronger in tension. Comparing Tables 8.4 and 8.5 confirms this effects as does Figure 8.2. It has also been pointed out that a weak diameter dependence emerges due to the approximate logarithmic dependence of strength on the number of sources. Since the number

of sources scales linearly with the size, this creates and additional size dependence that always strengthens the wire with decreasing size. Thus, in tension, we expect a strengthening with respect to size and in compression there will be a competition between strengthening and softening with decreasing size. The predominant size effect from atomistics of pristine nanowires is associated with the surface stress, which shows little strengthening in wires with diameters greater than 50 nm [188]. Thus, these developments do not explain the size-dependent plastic flow often observed in experiments. Furthermore, these results can be thought of as an upper bound to the strength as pre-existing surface steps are likely sources in many nanowires and pillars. The nature of these sources will likely lower the applied stress required for surface dislocation nucleation [31, 230-233], which is step size dependent, due to the presence of local stress concentrations [231, 234] and further simulation of nanowires with surface steps could provide insight into their impact on strength.

8.5 Discussion

The competition between dislocation nucleation from the free surfaces and buckling exists in molecular dynamics simulations of pillar compression at high strain rates of $10^8\ s^{-1}$. In the <100>, we note that our simulations show nucleation without buckling although buckling has been observed in other simulations using different interatomic potentials for gold. Furthermore, in the <110> compression, our pillars buckle, and dislocation nucleation follows due to changes in the surface morphology, which reduce the energy barrier for nucleation during post buckling. However, since buckling is a structural instability, the critical stress lacks a thermally activated component. Buckling can be weakly temperature dependent through the temperature dependence of the elastic constants. Again, it is worth noting that the interatomic potentials, such as the one used here, are often fit at 0K to the experimentally measured elastic constants at 300K. Therefore, the 0K simulations of buckling are likely relevant to room temperature experiments. Hence, it is always possible that thermally activated nucleation will dominate at higher temperatures and lower strain rates. Our energy barrier calculations support this notion. For our 5 nm nanowires, we see that buckling in the <110> orientation will occur between 9 and 11 GPa, depending on the surface facets while dislocation nucleation at $10^{-3}\ s^{-1}$strain rate and 300K is around 3 to 5 GPa. Thus, high strain rate MD predicts buckling while transition state theory at low strain rates predicts spontaneous dislocation nucleation, which highlights one of the limitations of high strain rate molecular dynamics.

The energy barrier calculations show that, in general, dislocations prefer to nucleate in the screw orientation from pristine surfaces which lowers the dislocation line energy. However, this competes with the line length of the dislocation, making the dislocation nucleation location a balance between the energy associated with its orientation and its line length. Previous molecular dynamics simulations [122] have shown a significant effect on the nanowire prism orientation on the competition between slip via perfect dislocations, partial dislocations and deformation twinning. Our results suggest that one of the main contributing factors is the orientation of the nucleating dislocations relative to the corners of the prisms on the slip planes. This has the potential to significantly alter the location of nucleation and suggests it may contribute to the differences in nucleating perfect dislocations, partial dislocations and twins. The contribution to line energy also shows up in the prism geometry explaining why, fundamentally, that circular prisms are observed to be stronger than square ones [224] even when stress concentrations are not present. Furthermore, it also explains why in <100> wires with {100} side surfaces, the dislocation is always observed to nucleate in the obtuse corner [81, 121, 229] rather than the acute. In many fabricated nanowires, surface steps are likely to exist which may alter the nucleation sites and the predicted strength. However, these results can be used to interpret previous molecular dynamics results and the strengths can be thought of as upper bounds.

The strength of the gold nanowires does not appear to follow a law of maximum resolved shear stress. We note that the Schmid factor does significantly affect the strength generally making the nanowires stronger in orientations / loading directions where the Schmid factors are lower. The nature of a maximum stress condition arises from the original observations of Schmid that showed plastic deformation would initiate on the basal planes of HCP metals when the resolved shear stress reached a constant value regardless of orientation [51]. It is worth noting that this law is only obeyed for basal slip in HCP metals and non-high symmetry loading conditions in FCC metals [51, 235]. Continuum models show that the maximum shear stress criteria is not supported by simple energy barrier curves even when the applied stress on the slip plane is resolved using the Schmid factor except in the very special case of circular loop nucleate from a half space. This arises because the energy of the dislocations depends on the orientation of the dislocation nucleus and, even though work from the applied stress follows a CRSS law, the energy of the dislocation does not. Thus, from our continuum modeling, we should not expect an adherence to a maximum resolved shear stress law.

8.6 Summary

We have demonstrated that the strength of pristine gold nanowires at experimentally relevant time scales is controlled by heterogeneous dislocation nucleation from the free surface. While high strain rate MD simulations and molecular statics simulations do show failure by structural and elastic instabilities in some cases, heterogeneous nucleation is still able to occur at experimentally relevant time and temperature scales because it is a thermally activated process that is both temperature and strain rate dependent.

The chain-of-states method used here for computing energy barriers shows that square prisms are generally weaker than circular prism, a confirmation and generalization of previous findings [224]. However, our results show that one of the major reasons for the reduction in strength is the reduction of the line length of the dislocation nucleus as illustrated by our continuum model. The continuum model is also able to predict, in general, the energetically favorable corners from which dislocations should nucleate through the orientation-dependent line energy. This explains why dislocations in square <100> wires with {100}-side surfaces always show dislocation nucleation from the obtuse corner; the screw orientation lowers the line energy even though the line length is larger.

The continuum model also explains why one would not expect a maximum resolved shear stress model to completely explain dislocation nucleation. For square pillars, the nucleation stress depends on the energy, which depends on the line length and orientation of the dislocation, which can vary from cross-section to cross-section even when the Schmid factors are the same. This is in addition to many other factors that could contribute to the failure of the CRSS law such as stress dependence of both the elastic constants and stacking fault energies that exist in MD simulations.

Chapter 9: Towards an Understanding of Nucleation Strengths in Pristine Nanowires Under Experimental Conditions

In the previous chapter, a chain of states atomistics model was used to predict the energy barrier for surface dislocation nucleation in pristine gold nanowires in different loading directions and surface facets. Those atomistics revealed an unintuitive nucleation site preference for the obtuse over the acute corner in <001>-oriented nanowires under compression. This site preference was accounted for through a simple analytical model incorporating both the character of the dislocation and the geometry of the nucleation site. However, in most cases, the analytical model greatly over predicted the atomistic energy barriers, and on average the predicted strength was a factor of ~2 larger. Here, we further develop the analytical model presented in Chapter 8 in order to develop an intuitive understanding of the physics governing surface dislocation nucleation. The continuum model is validated against the atomistic results from Chapter 8, and shows that by including the full stress tensor-dependent GSF curve and continuum approximations for both the ledge and image energy that these two models can be brought into closer agreement. The potential sources for the remaining error between the continuum model and the atomistic simulations are also discussed.

9.1 Introduction

Originating with the work in micron-sized whiskers by Brenner [57, 58] and demonstrated again more recently in experiments on pristine nanowires [2, 59], dislocation-free single crystals have been shown to attain yield strengths much larger than those measured in single crystals with non-zero dislocation densities. In fact, the strengths for the smallest pristine wires approach a material's theoretical strength due to the fewer available easy surface dislocation nucleation sites in smaller diameter wires [57, 58]. After the initial dislocation nucleation event, Brenner's whiskers contained dislocations and surface roughness allowing the whisker to deform at near bulk strengths [57, 58].

Atomistic simulations have corroborated the high strengths required to nucleate dislocations from nanowire surfaces [81, 118, 121, 123, 224]. However, surface dislocation nucleation is a thermally activated process making is sensitive to both temperature and strain-rate effects, and the accessible strain rates in molecular dynamics, MD, simulations, $\sim 10^{7}$ s^{-1}, are very large compared to experiments, $\sim 10^{-3}$ s^{-1} leading MD simulations to frequently over predict the experimental material strength. Accelerated MD simulations, capable of strain rates of $\sim 10^{3}$ s^{-1}, approach closer to experimental

conditions [236]; however, are still six orders of magnitude off experimental strain rates [149]. In order to overcome the gap between MD-accessible strain rates and experimental strain rates, several authors have performed a combination of chain-of-states atomistic simulations and transition-state-theory to estimate the strengths of pristine nanowires at experimental conditions [81, 178, 184]. However, while both atomistic methods can provide accurate estimates of the nanowire strength at their applied loading conditions, they do not provide any direct insight into the physics governing dislocation nucleation and thus nanowire strength.

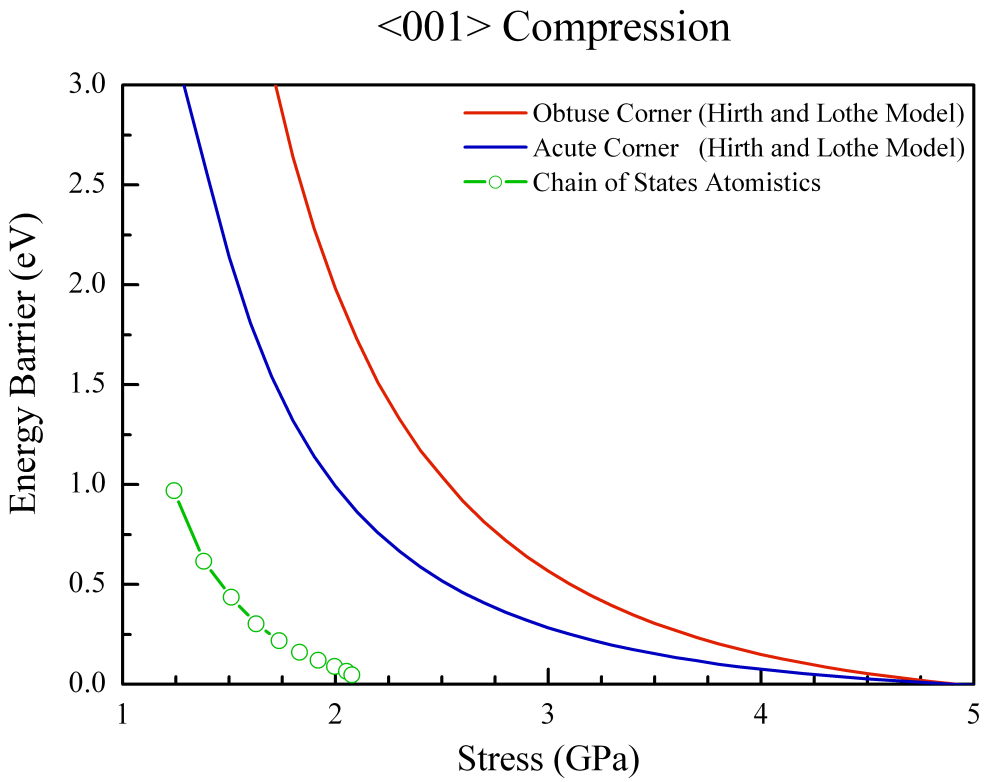

Figure 9.1 Atomistic energy barrier calculation for <001> compression along with classical Hirth and Lothe model showing both the incorrect nucleation site preference and the incorrect quantitative strength.

As a result, several authors have attempted to use analytical models describing the dislocation nucleation process in order to match their atomistic simulations and gain insight into the nucleation process [178, 184, 190]. Classical continuum models of the nucleation process, as discussed in Hirth and Lothe [50], capture the basic physics; however, are insufficient to match either the magnitude or the trend in nucleation site. For example, Figure 9.1 shows the predicted energy barriers in compression for a large, D~100nm, <001>-oriented nanowire at each distinct nucleation site

proposed in Hirth and Lothe[50] along with the atomistic results from Chapter 8. Not only is the energy barrier at least 2x too large, but the observed nucleation site preference is not captured. The inability of this simple model to capture the nucleation site preference inspired the model proposed in Chapter 8; however, while this model is able to reflect the nucleation site preference it still significantly over predicts the nucleation strength.

In this chapter, the analytical model for dislocation nucleation is expanded in order to more accurately reflect the nucleation process in uniaxial tension and compression of <001> and <110> pristine nanowires of different geometries. In order to approach the chain-of-states calculated energy barrier for surface nucleation, we first calibrate our model through the choice of the dislocation core-radius to match the atomistic energy barrier calculations for homogeneous dislocation nucleation under pure shear. We then apply the same model to heterogeneous dislocation nucleation through the introduction of the effects of the image stress, the presence of a surface ledge, and the full stress-tensor-dependent generalized stacking fault curve.

9.2 Continuum Modeling of Dislocation Nucleation

Dislocation nucleation from a surface is a complex process. As a result, we first begin the analysis with a relatively simple case: homogeneous nucleation of partial dislocation in a bulk pristine crystal under pure shear loading along the leading partial dislocation direction. This nucleation process has been shown to be accurately described through a similar analytical model by Aubry et al. in copper [178]. In Section 9.2.1 we use the models employed by Aubry et al. [178] along with chain-of-states calculations of the energy barrier for homogeneous nucleation of a partial dislocation loop in bulk pristine Au under pure shear loading to calibrate the dislocaiton's core radius as well as understand the nucleation process. The atomistics results are shown as green filled squares in Figure 9.2a.

9.2.1 Bulk Pure Shear

The energy barrier required for homogeneous dislocation nucleation can be described through the following general relation [50]:

$$\Delta G = Line\ Energy\ Term + Stacking\ Fault\ Term - Work\ Done \quad (9.1)$$

Aubry et al. used the above framework and apply three increasingly more complex models (named I, II, and III) to understand the nucleation process. In all of these models, the dislocation configuration is assumed to be a circle, and as a result, the line length of the dislocation, L_o, is the circumference of a circle of radius R, while the area swept out by the dislocation loop, A, is the area of a circle. The

simplest model, Model I or ΔG_I, incorporates both line energy for a nucleating dislocation loop and the intrinsic stacking fault energy resulting in a form of:

$$\Delta G_I = L_O \cdot \frac{\mu b^2(2-\nu)}{8\pi(1-\nu)} \ln\frac{R}{r_c} + A \cdot \gamma_{ISF} - A \cdot (\tau b) \tag{9.2}$$

Replacing L_O and A:

$$\Delta G_I = 2\pi R \cdot \frac{\mu b^2(2-\nu)}{8\pi(1-\nu)} \ln\frac{R}{r_c} + \pi R^2 \cdot \gamma_{ISF} - \pi R^2 \cdot (\tau b) \tag{9.3}$$

Here, μ and ν are the averaged anisotropic shear modulus and Poisson ratio, respectively [226], b is the Burgers vector of the nucleating dislocation, R is the dislocation loop radius, r_c is the core radius, γ_{ISF} is the intrinsic stacking fault energy, and τ is the applied shear stress in the direction of the Burgers vector. The core radius is the distance beyond which the dislocation's continuum elastic fields no longer accurately reflect the stress and strain near the dislocation. This length scale is treated here as a fitting parameter in order to best match the atomistics and continuum models. It should be noted that the dislocation line energy used in this work is distinct from that used by Aubry et al. [178]; however, the two forms can be made exactly equal through the choice of the core radius, r_c.

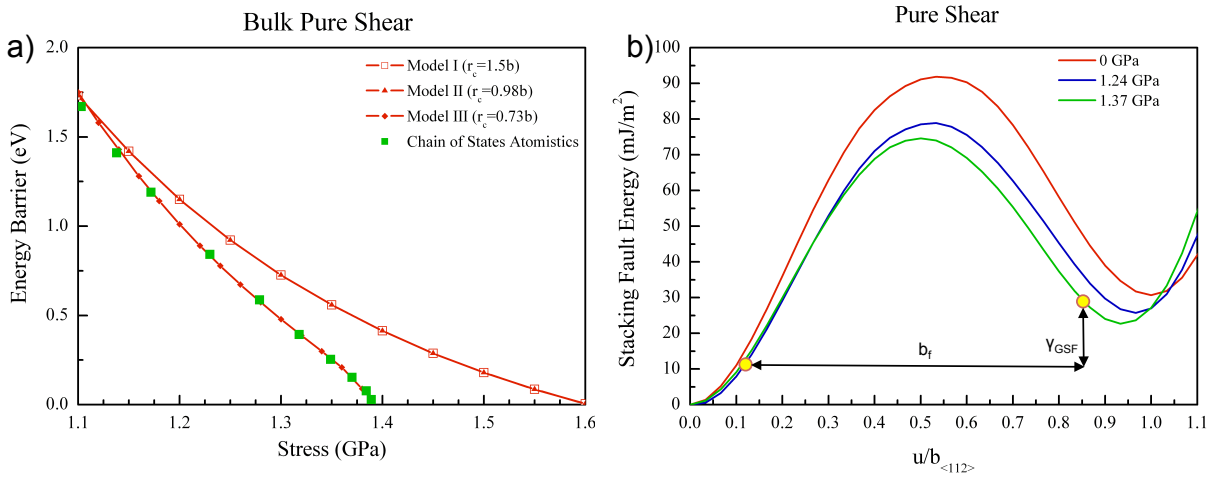

Figure 9.2: (a) Atomistic energy barrier calculation for bulk dislocation nucleation along with continuum models in agreement with results. (b) shear-stress dependent GSF along with schematic of chosen fraction Burgers vector and stacking fault energy

This model is the simplest of the three and uses easily accessible values of the elastic constants, Burgers vector, and stacking fault energy and as a result is frequently used to describe the nucleation process [50, 184, 190]. The resulting energy barrier can be compared with the results from the atomistic simulations and it is found that the corresponding best fit of the core radius is 1.5b. The

results for Model I, red line and open squares, and the atomistics, green-filled squares, are shown in Figure 9.2a. The model reasonable reflects the atomistic energy barrier at low stresses and high-energy barriers; however, as the stress increases the atomistics and model begin to deviate.

Model II distinguishes itself from the previous model by using the full generalized stacking fault curve, γ_{GSF}, and allowing for the nucleating dislocation to minimize its energy through the choice of a instantaneous Burgers vector that is a fraction of the complete partial Burgers vector or $0 \leq b_f \leq 1.0 \cdot b$. In addition, under an applied stress, the atoms will be slightly displaced from their equilibrium position resulting in an increase in energy relative to zero applied stress. The displacement, u_o, along the leading partial dislocation direction can be found through finding the displacement at which the derivative of the generalized stacking fault curve equals the applied stress: $\frac{d\gamma_{GSF}}{du}|_{u_o} - \tau = 0$. The resulting stacking fault energy that replaces γ_{ISF} from Model I is then $\left(\gamma_{GSF}(u_o + b_f) - \gamma_{GSF}(u_o)\right)$. The choice of fractional Burgers vector and the resulting stacking fault energy are shown schematically in Figure 9.2b. The resulting energy for Model II can be written as:

$$\Delta G_{II} = 2\pi R \cdot \frac{\mu b_f^2 (2-\nu)}{8\pi(1-\nu)} \ln\frac{R}{r_c} + \pi R^2 \cdot \left(\gamma_{GSF}(u_o + b_f) - \gamma_{GSF}(u_o)\right) - \pi R^2 \cdot (\tau b_f) \qquad (9.4)$$

Note that the fractional burgers vector influences all three terms in the energy. The best fit of this model uses a core radius of 0.98b and is plotted in Figure 9.2b. Note here that both Model I and II can be brought into reasonable agreement with with one another; however, both models still deviate from the atomistic solutions at large applied strengths. In order to capture the high stress-limit, the stress-dependence of the generalized stacking fault curve is included into Model III. An example of this stress-dependent GSF behavior is shown for Au in Figure 9.2b showing how the generalized stacking fault energy changes as the stress increases. Note that not only does the minimum stacking fault energy decrease, but also it shifts to the left facilitating smaller fractional burgers vectors and thus lower dislocation line energies. The resulting form of the energy barrier is now:

$$\Delta G_{III} = 2\pi R \cdot \frac{\mu b_f^2 (2-\nu)}{8\pi(1-\nu)} \ln\frac{R}{r_c} + \pi R^2 \cdot \left(\gamma_{GSF}(\tau, u_o + b_f) - \gamma_{GSF}(\tau, u_o)\right) - \pi R^2 \cdot (\tau b_f) \qquad (9.5)$$

The best fit for this model is shown in Figure 9.2a and corresponds to an r_c of 0.73b. Including the shear-stress-dependent GSF fully accounts for the atomistic simulations. In future

simulations the Model III r_c is assumed to be a material property and as a result is fixed in the future simulations.

9.2.2 Bulk Uniaxial Loading

9.2.2.1 Leading Partial Dislocation

As opposed to pure-shear loading, uniaxial compression or tension requires that the correct leading partial Burgers vector and accompanying Schmid factor be used. The Schmid factor calculation as well as the origin of the leading and trailing partial dislocation can be seen in Chapter 1 and Figure 1.3 and 1.5b. The Schmid factor for the leading partial dislocation for the full stereographic triangle in tension and compression can be found in Figure 9.3a,b, respectively. Here, there is a clear difference shown for the Schmid factors in tension and compression, an asymmetry that does not occur for perfect dislocations as shown in Figure 1.5. In tension, the highest Schmid factors lie near the <110> pole; whereas, in compression, the largest Schmid factors are at the <001> pole. For comparison, Figure 9.3c shows the stereographic triangle for perfect dislocations. Note that in each of the three cases, the Schmid factor is distinct demonstrating that in order to capture the correct nucleation physics, the appropriate Burgers vector must be used.

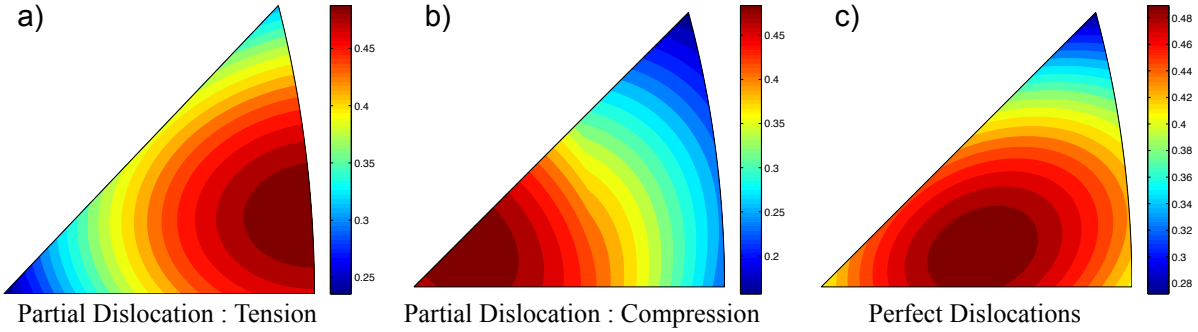

Figure 9.3 Schmid factor plots for partial and perfect dislocations

9.2.2.2 GSF - Uniaxial Loading

Also in contrast to pure shear loading, uniaxial loading results in two additional stress components beyond the resolved shear stress. Several authors [237, 238] have found that these components plays a significant role in determining the GSF landscape and can result in significant changes to the stress required to homogeneously nucleate a dislocation in bulk. Along the same lines, Lee et al. [238] has found that in uniaxial loading, all three stress components influence the GSF as opposed to previous attempts to parameterize the GSF between the resolved shear stress and the slip plane normal stress

[196]. Examples of the uniaxial-loading-dependent GSF curves are shown in Figure 9.4 for: <110> tension, <110> compression, and zero applied stress. Both the tension and compression cases are at similar applied stress: ~1GPa.

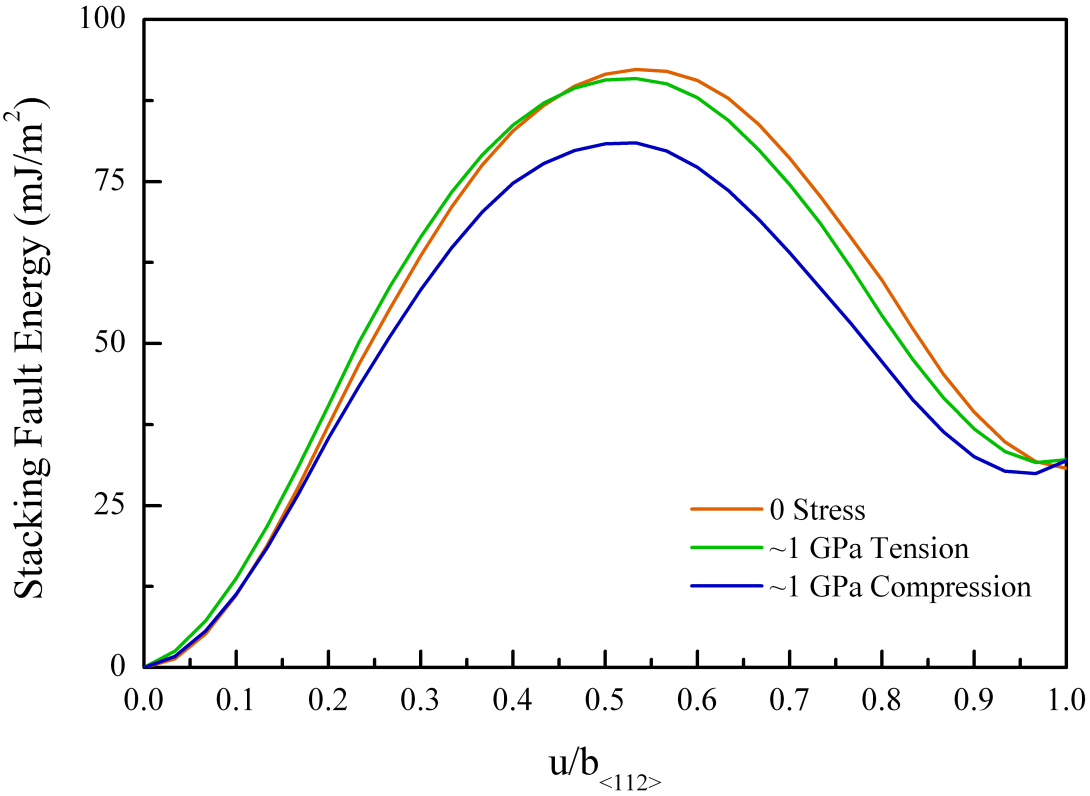

Figure 9.4 Differences in uniaxial-stress dependent GSF in tension and compression

The full stress-tensor-dependent GSF energy as written as:

$$A \cdot \left(\gamma_{GSF}(\sigma, u_o + b_f) - \gamma_{GSF}(\sigma, u_o)\right) \tag{9.6}$$

Note, here that the u_o position is defined the same as previously with the addition of the applied stress is now the resolved shear stress, τ_{RSS}, through $\frac{d\gamma_{GSF}}{du}|_{u_o} - \tau_{RSS} = 0$ where $S\sigma = \tau_{RSS}$. The GSF is affected by the full stress tensor; however, the displacement along the leading partial direction is determined by the stress resolved in the leading partial Burgers vector direction or τ_{RSS}. Due to the influence of uniaxial loading on both the Schmid factor and the stress-dependent GSF curve, the energy to nucleate a dislocation in bulk, uniaxial loading can be written as:

$$\Delta G_{Bulk,Uniaxial} = L_o \cdot \frac{\mu b_f^2(2-\nu)}{8\pi(1-\nu)} \ln\frac{R}{r_c} + A \cdot \left(\gamma_{GSF}(\sigma, u_o + b_f) - \gamma_{GSF}(\sigma, u_o)\right) - A \cdot \left(S\sigma b_f\right) \quad (9.7)$$

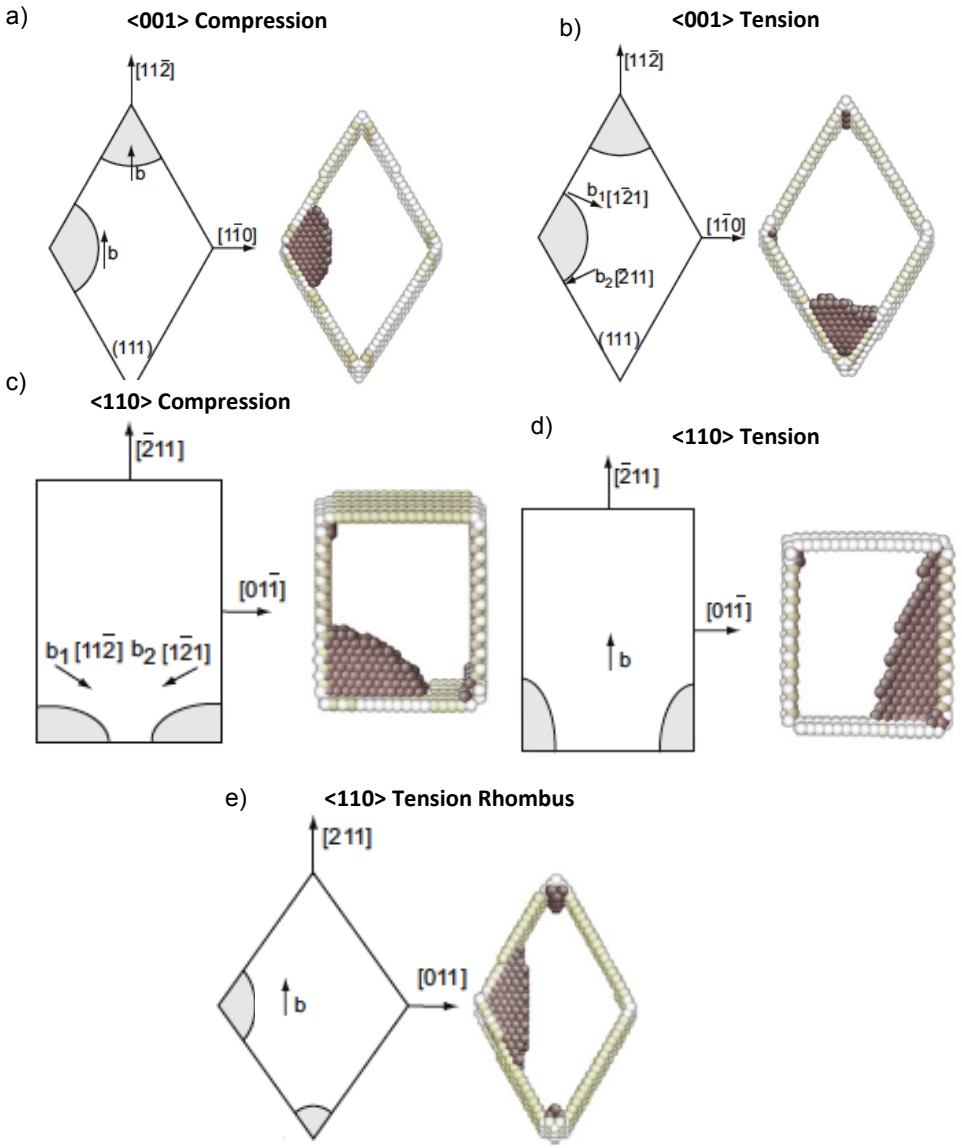

Figure 9.5: Nanowire slip plane schematics along with snapshots of resulting dislocation configurations

9.2.3 Surface Nucleation Uniaxial Loading

Surface nucleation introduces four further contributions to the nucleation barrier: i) the geometry of potential nucleation sites as determined by the slip plane and the nanowire surfaces, ii) the influence of the surface stress caused by small nanowire diameter, iii) the surface ledge produced through nucleation, and iv) the image contributions as a result of the nucleating dislocation's proximity to the surface. These contributions will be added onto the case of bulk uniaxial loading and the resulting analytical model will be employed for five nanowire atomistic energy barriers presented previously: 1) <001> tension and 2) <001> compression with {001}-side surfaces; 3) <110> tension and 4) <110> compression with {001}x{110}-side surfaces; and 5) <110> tension with a rhombus cross-section formed through {111}-side surfaces. The corresponding slip planes for these five cases are reproduced for the reader's convenience in Figure 9.5, and the atomistic energy barriers can be found in Chapter 8.

For simplicity of calculations, the nucleating dislocation in the analytical model is assumed to be a circle with the center of the circle at the corner of the nucleation site. As shown by the configurations of the nucleating dislocations from atomistics, the dislocation is rarely a perfect circle demonstrating that lower energetic configurations for the dislocation line exist. As a result, the energy barrier predicted by the circular dislocation should always be larger than the atomistic results.

9.2.3.1 Nucleation Site Preference

The geometry of possible nucleation sites is chosen by intersection of the slip plane with the side surfaces. As shown in Chapter 8, the preferred nucleation site is due to a combination of both the shape of the corner and the character of the leading partial dislocation. In general, sharper corners are preferred as are sites that nucleate screw-like dislocations[184]. Here the line energy now becomes:

$$Line\ Energy = \int_{-\alpha}^{\alpha} \frac{\mu b_f^2}{4\pi(1-\nu)} (1 - \nu \cos^2(\theta)\, R \ln\left(\frac{R}{r_c}\right) d\psi \tag{9.8}$$

where θ is the angle between the line direction and the Burgers vector and $d\psi$ is the infinitesimal angle between $-\alpha$ and α the half angles of the nucleation site. The preferred nucleation sites along with the orientation of the Burgers vectors are outlined in Figure 9.5.

9.2.3.2 Surface Stress

Not only does the nanowire's shape impact the nucleation, but the nanowire's size also greatly influences the strength through the influence of the surface stress. The surface stress arises because the surface atoms have fewer nearest neighbors than an equivalent atom in the bulk. As a result, the

surface atoms are under large tensile strains that are relieved through inducing compressive strain along the wire axis such that the averaged stress in the wire is zero. The magnitude of the surface stress and the resulting applied compressive axial stress is approximately: $f \sim \frac{4\gamma}{D}$ where γ is the surface energy and is on the order of 1 J/m^2 and D is the wire diameter, ~5nm, resulting in an induced axial compressive on the order of 1GPa, a large fraction of the total strength. In order to account for the surface stress, the energy barrier for the atomistic data have been scaled by the average surface stress as determined through the differences in the bulk and nanowire stress-strain curves found in Chapter 8. The result is that the energy barriers shown in Fig. 9.8 for atomistic simulations are more representative of large nanowires where D~100nm than smaller nanowires.

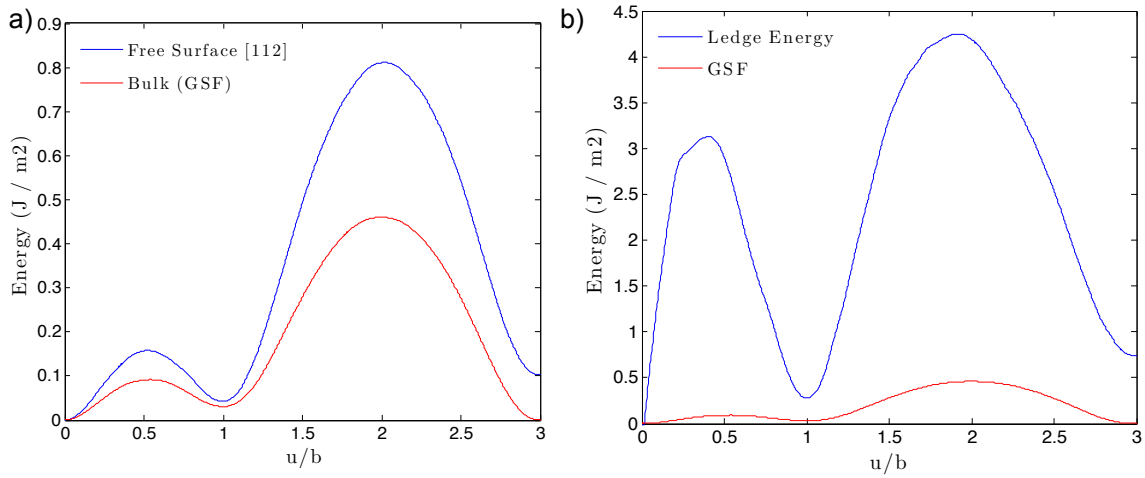

Figure 9.6 Results of ledge energy calculations

9.2.3.3 Surface Ledge

When a dislocation intersects a surface, it leaves a surface ledge corresponding to the dislocation's Burgers vector. In this model, the surface ledge area for a nucleating dislocation is determined through a continuum approach such that behind the dislocation, the nanowire has formed a ledge of magnitude b_f. Note here that the area of the dislocation ledge depends on both the fractional Burgers vector magnitude as well as the orientation of the Burgers vector with respect to the surface. For example, in the case of <001> compression, the dislocation nucleates from the obtuse corner and the produced ledge is inclined 30 degrees relative to the nanowire surface. The resulting ledge area on each side

surface will thus be $Rb_f \sin\frac{\pi}{6}$. The total ledge will be twice this or Rb_f. This area corresponds to A_{Ledge} and is different in each nanowire nucleation site.

The energy of a dislocation ledge is calculated in a manner similar to the calculation of a generalized stacking fault curve; however, in the ledge calculation the (112) face is a free surface. Therefore, as the crystal slips in the [112] direction, a ledge will form on both sides of the crystal. The energy landscape for the case of bulk, the GSF curve, and with a free surface are shown in Figure 9.6a. The extra {111} surface creates a significant in crease in total energy. The associated energy to slip the crystal will be a weighted average between the ledge energy of the created ledge and the stacking fault energy of the bulk stacking fault:

$$E_{Ledge} = \gamma_{Ledge}(u) * 2Lu + \gamma_{GSF}(u) * (W - 2u)L \tag{9.9}$$

Here, E_{Ledge} is the total energy required to slip the top of a simulation block over the bottom, W and L are dimensions of the simulation block area, u is the displacement of the top and bottom blocks, $\gamma_{GSF}(u)$ is the generalized stacking fault curve at zero applied stress, and $\gamma_{Ledge}(u)$ is the ledge energy as a function of the slipped distance. The ledge energy can be found by rearranging the above equation to find:

$$\gamma_{Ledge}(u) = \frac{E_{Ledge} - (W-2u)L\gamma_{GSF}(u)}{2Lu} \tag{9.10}$$

The resulting ledge energy is shown in Figure 9.6b. The stacking fault energy is included for reference. The ledge energy has similar features as the GSF curve; however, the energies are significantly higher reaching ~3 J/m^2 at the first local maximum as opposed to ~0.08 J/m^2 in the GSF curve. Furthermore, at one partial burgers vector away the ledge energy reaches 0.27 J/m^2 and at three burgers vector away the energy rises to 0.75 J/m^2 as opposed to ~0.03 J/m^2 and 0 J/m^2 for the case of a generalized stacking fault curve. The ledge energies found at 1b and 3b are reduced from the {111} surface energy due to the ledge atoms' proximity to other nearby surface atoms. As the ledge distance increases, the ledge is unable to relax its energy as much resulting in the approach of the {111} surface energy at ~1.0 J/m^2.

In total, factoring in the continuum area and the ledge energy at a partial Burgers vector away from the surface leads to the total ledge energy term:

$$A_{Ledge}\,\gamma_{Ledge}(b_f) \tag{9.11}$$

where both the area and ledge energy are functions of the partial Burgers vector.

9.2.3.4 Image Energy

The last contribution included in the model is the reduction in energy from the image stress. The dislocation line energy, as currently written, describes the energy required to nucleate a dislocation in bulk. However, near a free surface, a dislocation's line energy is expected to decrease relative to the bulk as a result of the zero-traction of the free surface [50]. The energy reduction near a free surface is a result of the addition of image elastic fields to maintain the free surface's zero-traction boundary condition.

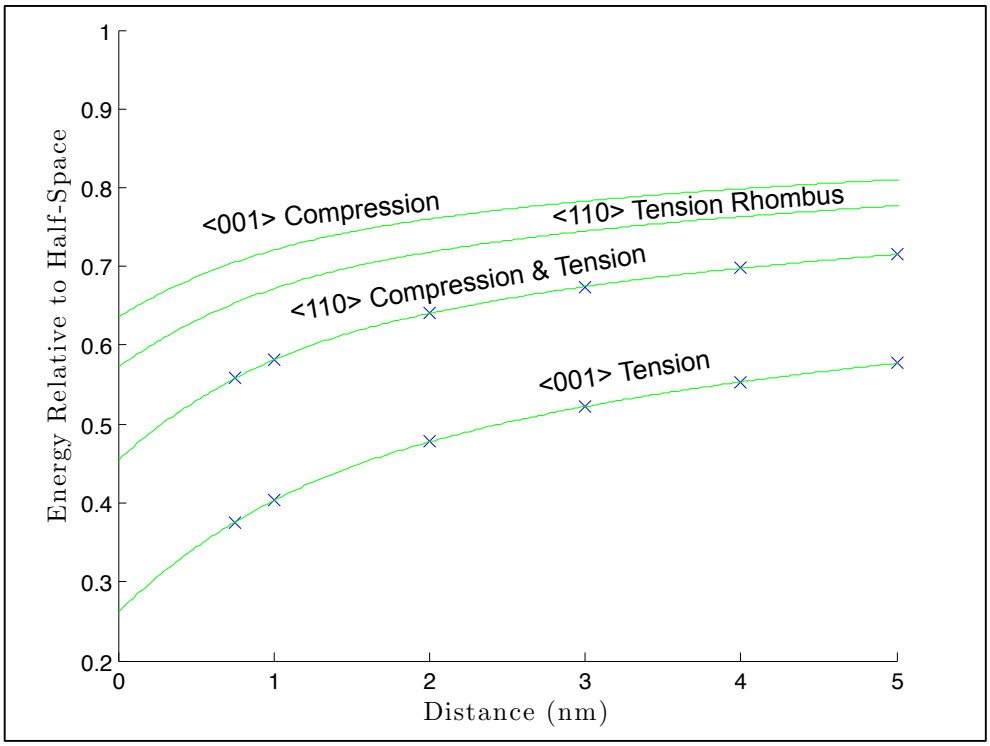

Figure 9.7 Relative energy of a screw dislocation parallel to a corner surface. Energy is relative to the half-space solution.

The full solution for the image field of an arbitrary nucleating dislocation is cumbersome and outside the scope of employing a simple analytical model. However, Beltz and Freund have analytically solved the dislocation line energy for a dislocation nucleating at a half-space and have found a correction factor 'm' inside the natural log in the dislocation line energy. 'm' is found to insensitively depend on the material constants and is equal to ~0.55 for a half space, $\alpha = \pi/2$. The nucleation sites investigated here all have angles narrower than a half-space, and also the line energy may be intuitively

expected to decrease with more acute nucleation sites as the dislocation will see more free-surface relative to the half-space solution. As a result, the question becomes how does 'm' vary with the nucleation site angle. The exact solution is beyond the scope of this work. Here, we investigate two different simple approximations to account for the line energy dependence on the nucleation site.

In the first approximation, we note that in the case of bulk, $\alpha = \pi$, the dislocation line energy is recovered by setting m=1. There are now two values of 'm' at two different nucleation sites, and as a first approximation we take 'm' to vary linearly with the nucleation site angle or

$$m_\alpha = 0.55 + \left(\frac{1-0.45}{\pi - \pi/2}\right)\left(\alpha - \pi/2\right) \tag{9.12}$$

This form of 'm' decreases as the nucleation angle decreases, lowering the dislocation line energy, in line with expectations. The line energy now becomes:

$$Line\ Energy = \int_{-\alpha}^{a} \frac{\mu b_f^2}{4\pi(1-\nu)}(1 - \nu\cos^2(\theta)\, R \ln\left(m_\alpha \frac{R}{r_c}\right) d\psi \tag{9.13}$$

In the second approximation, we numerically calculate the dislocation line energy of a straight screw dislocation parallel to the surface at different distances from the surface. The image dislocations are finite for some of the nucleation angles in question: 180^o($\alpha = \pi/2$), 90^o ($\alpha = \pi/4$) , and 60^o ($\alpha = \pi/6$), and as a result the dislocation energy can be numerically calculated through the strain energy integral inside the crystal. The additional nucleation site angles of 120 degrees, and 109.5 degrees are taken as linear interpolations between the neighboring solutions. Note, that not only is the dislocation orientation with respected to the surface different than the analytical model used here, but also the dislocation line is infinite in one direction possibly resulting in differences from the finite case. As a result, we use the calculations to show the trend in the energy with nucleation site angle. The relative energy of a dislocation at a given corner angle, α, relative to the half-space solution is $\frac{E_\alpha(R)}{E_{Half-Space}(R)}$ and are shown in Figure 9.7. This factor is multiplied by Beltz-Freund solution of the dislocation nucleating at a half-space to show the change in line energy with nucleation angle. The resulting form of the line energy now becomes:

$$Line\ Energy = \frac{E_\alpha(R)}{E_{Half-Space}(R)} \int_{-\alpha}^{a} \frac{\mu b_f^2}{4\pi(1-\nu)}(1 - \nu\cos^2(\theta)\, R \ln\left(m_{\pi/2} \frac{R}{r_c}\right) d\psi \tag{9.14}$$

9.3 Results – Analytical Model vs. Atomistic Calculations

The model employed here includes the approximation for the image energy, the normal stress dependent GSF, the ledge energy and the work done for two different image energy approximations: 'm' and '2d' corresponding to the linear approximation of 'm' with nucleation angle and the relative energy of a straight screw segment at a nucleation site α, respectively.

$$\Delta G_{Surf,m} = \int_{-\alpha}^{\alpha} \frac{\mu b^2}{4\pi(1-\nu)} (1 - \nu \cos^2(\theta)\, R \ln\left(m_\alpha \frac{R}{r_c}\right) d\psi + A \cdot \left(\gamma_{GSF}(\sigma, u_o + b_f) - \gamma_{GSF}(\sigma, u_o)\right) + L_{Ledge}\, \gamma_{Ledge}(b_f) - A \cdot (\sigma S b_f) \quad (9.15)$$

and

$$\Delta G_{Surf,2d} = \frac{E_\alpha(R)}{E_{Half-Space}(R)} \int_{-\alpha}^{\alpha} \frac{\mu b^2}{4\pi(1-\nu)} (1 - \nu \cos^2(\theta)\, R \ln\left(m\pi/_2 \frac{R}{r_c}\right) d\psi + A \cdot \left(\gamma_{GSF}(\sigma, u_o + b_f) - \gamma_{GSF}(\sigma, u_o)\right) + L_{Ledge}\, \gamma_{Ledge}(b_f) - A \cdot (\sigma S b_f) \quad (9.16)$$

The model results for each of the 5 nanowire geometries can be seen in Figure 9.8a-e. Each plot contains six different energy barriers corresponding to: 1) the Bulk-Model has no image stress approximation or ledge energy, 2) and 3) are the 'm' and '2d' image approximations with no ledge energy, 4) and 5) add the ledge energy to the 'm' and '2d', cases respectively, and 6) shows the results from the atomistic simulations that has been scaled for the surface stress.

In general, the Bulk-Model, dashed grey line routinely over predicts the nucleation barrier calculated from atomistics. By incorporating both of the image energy and the ledge, we find better agreement than the bulk-model; however, the improvement is limited as the image energy reduces the energy barrier while the ledge energy increases it resulting in slight net reduction in the energy barrier's relative to the bulk-model. The best agreement between the continuum model and the atomistics is found by neglecting the ledge-energy all together.

We note that the <110> Compression case, Fig. 9.8c, is unique in that the bulk-model under-predicts the atomistics and the inclusion of the ledge and image energy do not improve the result. Furthermore, the <110> Tension Rhombus, Fig. 9.8e, has the most success at replicating the energy barrier curve through the introduction of both the image and the ledge.

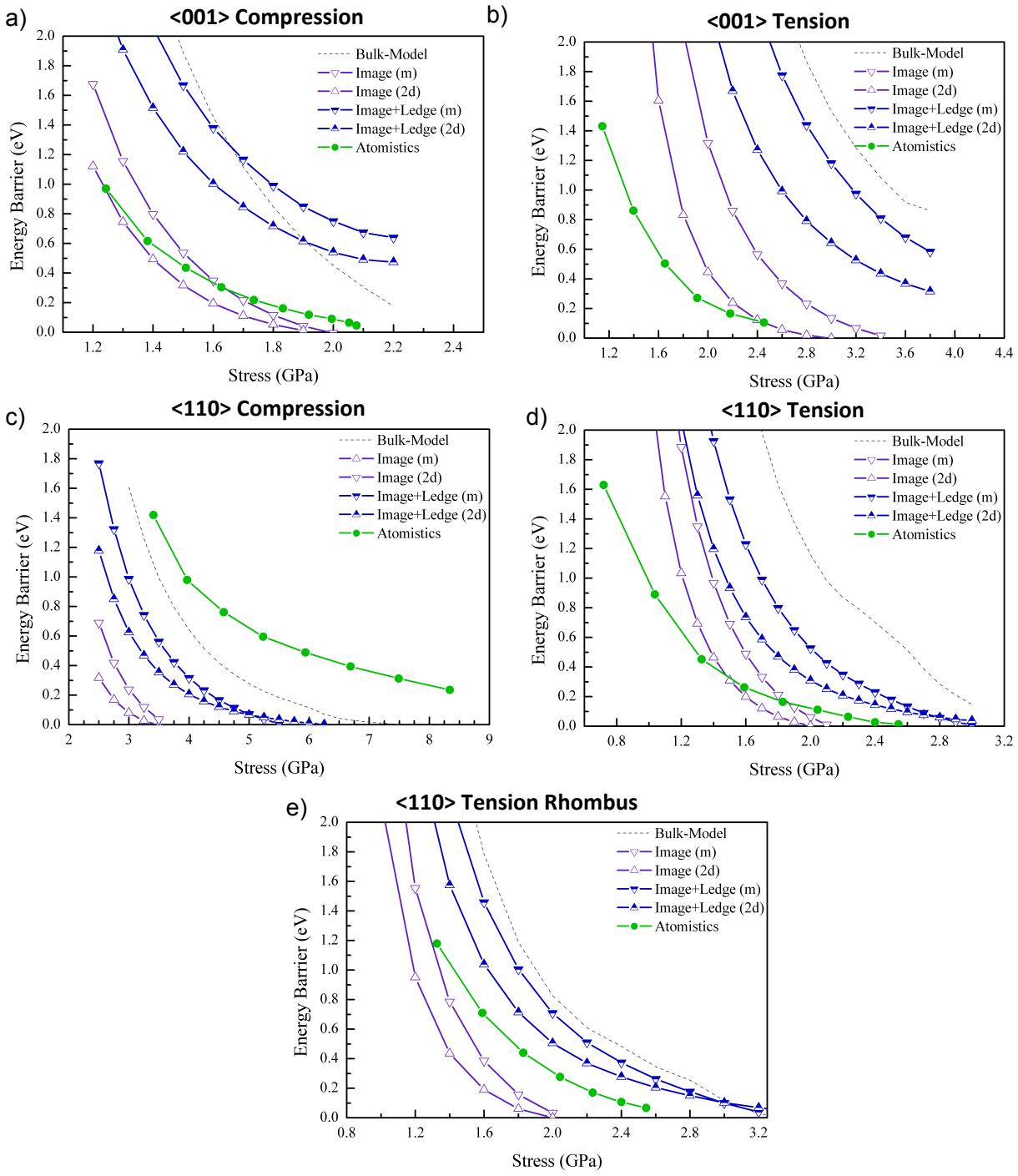

Figure 9.8 Predicted energy barrier curves for each of the 5 nanowire cases along with atomistic results

Table 9.1 and Table 9.2 shows the expected results from experimental tests of 100nm diameter pillars at strain rates of $10^{-3}\ s^{-1}$ and 300K and 2K, respectively, for all of the cases here as well as

classical models from Hirth and Lothe [50]. The calculations here use the same procedure as introduced in section 8.4. The inclusion of the classical model shows the vast improvement that can be obtained in some cases by making simple approximations in the reduced line energy due to the free surface. We find that, excluding the case of <110> compression that the classical model, on average, over predicts the strength by 100%; while, the best approximation: Image (2d), on average, deviates from the observed strength by only 20% showing a large improvement can be made with simple approximation for the image energy while neglecting the ledge contribution.

Table 9.1 Predicted strengths for various analytical models and atomistics at 300K

Stress @ 300K	<001> Comp.	<001>Tens.	<110> Comp.	<110>Tens.	<110>Tens. Rhom.
Image m	1.28	2.02	2.15	1.33	1.27
Image 2d	1.18	1.67	1.76	1.16	1.14
Image + Ledge m	1.65	2.92	2.78	1.59	1.69
Image + Ledge 2d	1.49	2.40	2.44	1.38	1.52
Bulk Model	1.66	3.19	3.23	1.95	1.78
Model 1	1.98	3.03	3.30	2.11	1.86
Atomistics	1.18	1.21	3.53	0.87	1.30

Table 9.2 Predicted strengths for various analytical models and atomistics at 2K

Stress @ 2K	<001> Comp.	<001>Tens.	<110> Comp.	<110>Tens.	<110>Tens. Rhom.
Image m	1.93	3.45	3.61	2.11	2.07
Image 2d	1.91	2.91	3.39	1.99	1.97
Image + Ledge m	2.74	N/A	5.52	3.00	3.35
Image + Ledge 2d	2.87	N/A	6.13	3.36	3.40
Bulk Model	2.29	N/A	7.35	3.17	3.29
Model 1	4.27	8.27	7.95	4.85	4.15
Atomistics	2.11	2.67	10.16	2.60	2.86

9.4 Discussion

Classical models of dislocation nucleation do a poor job of accurately reflecting the physics for dislocation nucleation from a surface. We found through comparisons with atomistic energy barrier curves in Chapter 8 that by incorporating the appropriate geometry of the nucleation site as well as the character of the nucleating dislocation, the correct trends in nucleation site preference could be achieved. Furthermore, in this chapter the continuum model was further refined to reflect details of

the stress-dependent generalized stacking fault curve, the image energy, and the ledge creation, and we find that neglecting the ledge contribution gives the best agreement between the atomistics and the continuum model.

However, error between the atomistics and the analytical model still remains, and in the case of <110> compression, agreement between the atomistics and model are very poor suggesting key physics are still missing from the model. In the below section, we discuss several areas where the continuum model can be improved to better reflect the underlying dislocation physics.

9.4.1 Surface Ledge and Dislocation Configurations

Figure 1.8 shows that for many cases, neglecting the ledge in the energy barrier allows for a reasonable approximation of the atomistic energy barrier; however, on inspection of the atomistic configurations, all of the nanowires show a created ledge suggesting that ignoring the surface ledge is inappropriate. However, several aspects of the nucleation process, not included in this model, may be effectively lowering the ledge energy.

The ledge energy calculation creates a ledge on the (112) face in the [112] direction resulting in two key differences between the nanowire cases here and the ledge energy used in this chapter. First, none of the nanowire surfaces on which the ledge is created are {112} type. Instead, they are either {001}, {110}, or {111} and breaking each of these surfaces to form a ledge will require different energies than a {112} plane. Second, the [112] Burgers vector will be inclined to each surface at an angle relative to each of these surfaces. The result will be a ledge that is very close other surface atoms, allowing the possibility of reductions of the ledge energy through near-neighbor bonding. A similar feature, even at perpendicular ledge relative to the surface, is visible in the first minimum of the ledge energy in Figure 9.6 which is almost 3x smaller than the second minimum at 3b demonstrating that the ledge energy per unit area is smaller at very small ledge displacements likely due to near neighbor interactions across the ledge.

All the continuum models employed here assume that the nucleating dislocation is a circle with the circle's center at the corner of the nucleation site. As can be seen from Figure 9.5, only <001> Compression, Fig. 9.5a, appears close to a symmetric circle while the only other symmetric configuration is <110> Tension Rhombus, Fig. 9.5e. Inspection of these two nanowire cases show that the Burgers vector direction is also symmetric with respect to the surfaces at the nucleation site. The other three cases are the opposite: they have Burgers vectors that have different inclination angles

to each surface at the nucleation site. Furthermore, the preferred dislocation configuration for each site strongly prefers to adopt shapes that minimize the resulting ledge area. For instance, in <110> Tension the dislocation hugs the $(01\bar{1})$ surface, which forms no ledge. The dislocation's preference to minimize ledge area clearly shows that the ledge has a non-negligible energy. Furthermore, the continuum models use of pure circles will lead to over predictions of the energy contribution of the ledge area from high-energy sites.

9.4.2 Image Energy

In order to account for the effects of the image elastic fields on the dislocation energy, two different approximations of the line energy were used. In general, these two approximations give very similar results. However, the Beltz-Freund solution that is used is for the case of a slip plane perpendicular to the surface, a case only satisfied by the $(01\bar{1})$ surface in <110> loading. In all the other cases, the slip plane normal is inclined to the surface normal, which should further reduce the dislocation line energy beyond the approximations used in this model. Another reduction in the image energy comes about due to the small nanowire size. All the atomistic nanowires have side lengths of ~5nm resulting in a further reduction in line energy from the image fields of the dislocation on the opposite side of the pillar.

9.4.3 Transition from Size-Dependent to Surface Nucleation

The analytical models that consider only the reduced line energy from image effects have been shown to be a reasonable approximation of the atomistic energy barrier curves for dislocation nucleation in pristine gold nanowires. Surface source nucleation has also been shown in *in-situ* TEM experiments as well as through mechanical test data to also occur in non-pristine nanoscale structures with sizes below 100nm as seen in Chapters 5 and 7. Here, we compare the predictions of the analytical model with the experimental results of the strength at the first burst, as defined in chapter 6 as well as MD simulations from Cao and Ma Acta Materialia (2008) [224] for in <111> oriented copper pillars with the results shown in Figure 9.9. The nucleation geometry was considered to be a half-space, and as a result should be an upper bound on the nucleation strength. In order to account for the entropic effects, T_m from Section 8.4 was taken from atomistic calculations of Ryu et al. [229].

Figure 9.9 shows that the surface source predicted strength is nearly 10 GPa, similar to that observed in the MD simulations, but a factor of 10 larger than the strengths observed in experiments. The agreement between MD simulations and continuum models is consistent with the above finding

that by neglecting the ledge energy it is possible to get good agreement with atomistic pristine nanowire deformation. The experimentally measured strength has several factors that may reduce the necessary strength to nucleate surface dislocations. First, the electroplated nanowire surface is not smooth and can be seen in TEM images from chapter 3 as well as from SEM images throughout this work providing many easier nucleation sites. Second, these nanowires have non-zero dislocation density which will strongly affect the internal elastic fields in the pillar, especially on the size scale of 100nm and smaller. In summary, the analytical continuum model provides reasonable predictions of atomistic strengths in pristine nanowires; however, significant imperfections exist within experimental samples that will strongly reduce the strength required for nucleation.

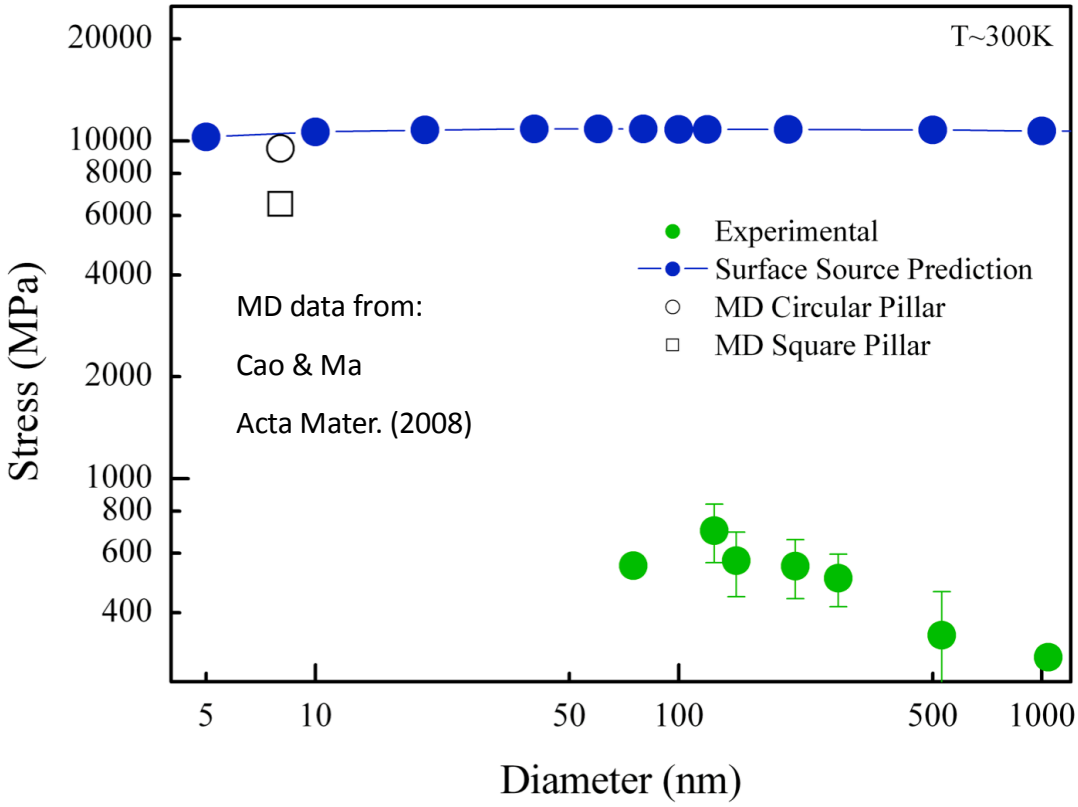

Figure 9.9 Analytical continuum model predictions of <111> oriented copper pillars compared at experimental test conditions compared with MD simulations and experimental results from Chapter 5

9.5 Summary

We have demonstrated that by incorporating a more complete picture of the dislocation nucleation process and also neglecting the contribution from the ledge, reasonable agreement between continuum analytical models and atomistics can be achieved. The reduction in error between the most basic model, Hirth and Lothe, and the best continuum analytical model approximation here shows the error between the predicted strength to be reduced from 100% to 20% with the only necessary input from the atomistics of the full stress-tensor-dependent generalized stacking fault curve. In order to bring these models in closer agreement, we have outlined several additional factors that may explain the low effective ledge energies and/or a further reduction to the line energy as a result of the specific slip plane geometry relative to the pillar surfaces. The predicted nucleation barriers are significantly higher than would be expected from experiments; however, this large discrepancy is likely due to the non-pristine internal microstructure and surface morphology of experimental samples.

Bibliography

[1] Jennings AT, Li J, Greer JR. Acta Mater. 2011;*Accepted*.
[2] Richter G, Hillerich K, Gianola DS, Mönig R, Kraft O, Volkert CA. Nano Lett. 2009;9:3048.
[3] Uchic MD, Dimiduk DM, Florando JN, Nix WD. Science 2004;305:986.
[4] Dimiduk DM, Uchic MD, Parthasarathy TA. Acta Mater. 2005;53:4065.
[5] Frick CP, Clark BG, Orso S, Schneider AS, Arzt E. Mater. Sci. Eng. A 2008;489:319.
[6] Greer JR, Jang DC, Kim JY, Burek MJ. Adv. Func. Mater. 2009;19:2880.
[7] Greer JR, Kim JY, Burek MJ. JOM 2009;61:19.
[8] Greer JR, Nix WD. Phys. Rev. B 2006;73:245410.
[9] Greer JR, Oliver WC, Nix WD. Acta Mater. 2005;53:1821.
[10] Greer JR, Weinberger CR, Cai W. Mater. Sci. Eng. A 2008;493:21.
[11] Kiener D, Grosinger W, Dehm G. Scripta Mater. 2009;60:148.
[12] Kiener D, Grosinger W, Dehm G, Pippan R. Acta Mater. 2008;56:580.
[13] Kiener D, Guruprasad PJ, Keralavarma SM, Dehm G, Benzerga AA. Acta Mater. 2011;59:3825.
[14] Kiener D, Minor AM. Acta Mater. 2011;59:1328.
[15] Kiener D, Minor AM. Nano Lett. 2011;11:3816.
[16] Kiener D, Motz C, Dehm G. J. Mat. Sci. 2008;43:2503.
[17] Kiener D, Motz C, Dehm G. Mater. Sci. Eng. A 2009;505:79.
[18] Kiener D, Motz C, Rester M, Jenko M, Dehm G. Mater. Sci. Eng. A 2007;459:262.
[19] Kiener D, Motz C, Schöberl T, Jenko M, Dehm G. Adv. Eng. Mater. 2006;8:1119.
[20] Lee SW, Han SM, Nix WD. Acta Mater. 2009;57:4404.
[21] Lee SW, Nix WD. Materials Science and Engineering a-Structural Materials Properties Microstructure and Processing 2010;527:1903.
[22] Ng KS, Ngan AHW. Philosophical Magazine Letters 2007;87:967.
[23] Ng KS, Ngan AHW. Acta Mater. 2008;56:1712.
[24] Norfleet DM, Dimiduk DM, Polasik SJ, Uchic MD, Mills MJ. Acta Mater. 2008;56:2988.
[25] Oh SH, Legros M, Kiener D, Dehm G. Nat. Mater. 2009;8:95.
[26] Parthasarathy TA, Rao SI, Dimiduk DM, Uchic MD, Trinkle DR. Scripta Mater. 2007;56:313.
[27] Shade PA, Wheeler R, Choi YS, Uchic MD, Dimiduk DM, Fraser HL. Acta Mater. 2009;57:4580.
[28] Shan ZW, Mishra RK, Syed Asif SA, Warren OL, Minor AM. Nat. Mater. 2008;7:115.
[29] Uchic MD, Dimiduk DM. Materials Science and Engineering A 2005;400-401:268.
[30] Volkert C, Lilleodden E. Philos Mag 2006;86:5567.
[31] Zheng H, Cao A, Weinberger C, Huang JY, Du K, Wang J, Ma Y, Xia Y, X. MS. Nature Communications 2010.
[32] Brinckmann S, Kim J-Y, Greer JR. Phys. Rev. Lett. 2008;100:155502.
[33] Dimiduk DM, Uchic MD, T.A.Parthasarathy. Acta Mater. 2005;53:4065.
[34] Kim J-Y, Greer JR. App. Phys. Lett. 2008;93:101916.
[35] Kim J-Y, Jang D, Greer JR. Scripta Mater. 2009;61:300.
[36] Kim JY, Greer JR. Acta Mater. 2009;57:5245.
[37] Kim JY, Jang DC, Greer JR. Scripta Mater. 2009;61:300.
[38] Kim JY, Jang DC, Greer JR. International Journal of Plasticity 2012;28:46.
[39] Kim JY, Jong DC, Greer JR. Acta Mater. 2010;58:2355.
[40] Schneider AS, Clark BG, Frick CP, Gruber PA, Arzt E. Mater. Sci. Eng. A 2009;508:241.
[41] Schneider AS, Clark BG, Frick CP, Gruber PA, Arzt E. Philosophical Magazine Letters 2010;90:841.
[42] Schneider AS, Frick CP, Clark BG, Gruber PA, Arzt E. Materials Science and Engineering a-Structural Materials Properties Microstructure and Processing 2011;528:1540.
[43] Schneider AS, Kaufmann D, Clark BG, Frick CP, Gruber PA, Monig R, Kraft O, Arzt E. Phys. Rev. Lett. 2009;103.

[44] Byer CM, Li B, Cao BY, Ramesh KT. Scripta Mater. 2010;62:536.
[45] Lilleodden E. Scripta Mater. 2010;62:532.
[46] Frenkel J. Zeitschrift Fur Physik 1924;29:214.
[47] Polanyi M. Zeitschrift Fur Physik 1934;89:660.
[48] Taylor GI. Proc. R. Soc. Lon. Ser. A 1934;A145:362.
[49] Orowan E. Zeitschrift Fur Physik 1934;89:634.
[50] Hirth JP, Lothe J. Theory of Dislocations. New York: John Wiley & Sons, 1982.
[51] Schmid E, Boas W. Plasticity of Crystals: F. A. Hughes Co., 1950.
[52] Taylor GI. Journal of the Institute of Metals 1938;62:307.
[53] Park HS, Zimmerman JA. Phys. Rev. B 2005;72:054106.
[54] Fleck NA, Muller GM, Ashby MF, Hutchinson JW. Acta Metallurgica et Materialia 1994;42:475.
[55] Fleck NA, Muller GM, Ashby MF, Hutchinson JW. Acta Metallurgica Et Materialia 1994;42:475.
[56] Nix WD, Gao H. J. Mech. Phys. Solids 1998;46:411.
[57] Brenner SS. J. Appl. Phys. 1956;27:1484.
[58] Brenner SS. J. Appl. Phys. 1957;28:1023.
[59] Bei H, Shim S, George EP, Miller MK, Herbert EG, Pharr GM. Scripta Mater. 2007;57:397.
[60] Bei H, Shim S, Pharr GM, George EP. Acta Mater. 2008;56:4762.
[61] Shim S, Bei H, Miller MK, Pharr GM, George EP. Acta Mater. 2009;57:503.
[62] Greer JR, De Hosson JTM. Prog. Mater. Sci. 2011;56:654.
[63] Greer JR, Hosson JTD. Prog. Mater. Sci. 2011.
[64] Kraft O, Gruber P, Mönig R, Weygand D. Ann. Rev. Mater. Res. 2010;40:293.
[65] Hull D, Bacon DJ. Introduction to Dislocations. Oxford: Elsevier Ltd., 2001.
[66] Dehm G. Prog. Mater. Sci. 2009;54:664.
[67] Uchic MD, Shade PA, Dimiduk DM. Ann. Rev. Mater. Res. 2009;39:361.
[68] Burek MJ, Greer JR. Nano Lett. 2010;10:69.
[69] Jennings AT, Gross C, Greer F, Aitken ZH, Lee SW, Weinberger CR, Greer JR. Acta Mater. 2012;60:3444.
[70] Goldstein DN, McCormick JA, George SM. J. Phys. Chem. C 2008;112:19530.
[71] Rai VR, Agarwal S. J. Phys. Chem. C 2008;112:9552.
[72] Fultz B, Howe JM. Transmission Electron Microscopy and Diffractometry of Materials. Berlin: Springer, 2001.
[73] Courtney TH. Mechanical Behavior of Materials. Long Grove: Waveland Press, Inc., 2000.
[74] Brinckmann S, Kim JY, Jennings A, Greer JR. International Journal for Multiscale Computational Engineering 2009;7:187.
[75] Rao SI, Dimiduk DM, Parthasarathy TA, Uchic MD, Tang M, Woodward C. Acta Mater. 2008;56:3245.
[76] Rao SI, Dimiduk DM, Tang M, Parthasarathy TA, Uchic MD, Woodward C. Philosophical Magazine 2007;87:4777.
[77] Weinberger CR, Cai W. J. Mech. Phys. Solids 2007;55:2027.
[78] Weygand D, Poignant M, Gumbsch P, Kraft O. Materials Science and Engineering a-Structural Materials Properties Microstructure and Processing 2008;483-84:188.
[79] Tang H, Schwarz KW, Espinosa HD. Acta Mater. 2007;55:1607.
[80] Balint DS, Deshpande VS, Needleman A, Van der Giessen E. Model. Simul. Mater. Sci. Eng. 2006;14:409.
[81] Zhu T, Li J, Samanta A, Leach A, Gall K. Phys. Rev. Lett. 2008;100:4.
[82] Jennings AT, Burek MJ, Greer JR. Phys. Rev. Lett. 2010;104:4.
[83] Volkert CA, Lilleodden ET. Philosophical Magazine 2006;86:5567.
[84] Bei H, Shim S, Miller MK, Pharr GM, George EP. App. Phys. Lett. 2007;91:111915.
[85] Nadgorny EM, Dimiduk DM, Uchic MD. J. Mater. Res. 2008;23:2829.
[86] Moser B, Wasmer K, Barbieri L, Michler J. J. Mater. Res. 2007;22:1004.
[87] Ostlund F, Rzepiejewska-Malyska K, Leifer K, Hale LM, Tang YY, Ballarini R, Gerberich WW, Michler J. Adv. Func. Mater. 2009;19:2439.
[88] Volkert CA, Minor AM. MRS Bulletin 2007;32:389.
[89] Buzzi S, Dietiker M, Kunze K, Spolenak R, Loffler JF. Philosophical Magazine 2009;89:869.
[90] Burek M, Greer JR. Nano Lett. 2009.

[91] Stangl M, Acker J, Dittel V, Gruner W, Hoffmann V, Wetzig K. Microelectronic Engineering 2005;82:189.
[92] Moore TM. Microscopy Today 2005;13:40.
[93] Dimiduk DM, Woodward C, LeSar R, Uchic MD. Science 2006;312:1188.
[94] Csikor FF, Motz C, Weygand D, Zaiser M, Zapperi S. Science 2007;318:251.
[95] El-Awady JA, Woodward C, Dimiduk DM, Ghoniem NM. Phys. Rev. B 2009;80:104104.
[96] Ogata S, Li J, Hirosaki N, Shibutani Y, Yip S. Phys. Rev. B 2004;70:104104.
[97] El-Awady JA, Wen M, Ghoniem NM. J. Mech. Phys. Solids 2009;57:32.
[98] Ng KS, Ngan AHW. Philosophical Magazine 2008;88:677.
[99] Weinberger CR, Cai W. PNAS 2008;105:14304.
[100] Jennings AT, Greer JR. Philosophical Magazine 2011;91:1108.
[101] Gianola D, Eberl C. JOM 2009;61:24.
[102] Jennings AT, Burek MJ, Greer JR. Phys. Rev. Lett. 2010;104.
[103] Cordill MJ, Lund MS, Parker J, Leighton C, Nair AK, Farkas D, Moody NR, Gerberich WW. International Journal of Plasticity 2009;25:2045.
[104] Kelly A, Groves GW. Crystallography and Crystal Defects. India: Longman Group Ltd., 1970.
[105] Ng KS, Ngan AHW. Acta Mater. 2009;57:4902.
[106] Thomas G. Transmission Electron Microscopy of Metals. New York: John Wiley and Sons, Inc., 1962.
[107] Lu K, Lu L, Suresh S. Science 2009;324:349.
[108] Zhu T, Li J, Samanta A, Kim HG, Suresh S. PNAS 2007;104:3031.
[109] Jin ZH, Gumbsch P, Ma E, Albe K, Lu K, Hahn H, Gleiter H. Scripta Mater. 2006;54:1163.
[110] Jin ZH, Gumbsch P, Albe K, Ma E, Lu K, Gleiter H, Hahn H. Acta Mater. 2008;56:1126.
[111] Wu ZX, Zhang YW, Srolovitz DJ. Acta Mater. 2009;57:4508.
[112] Afanasyev KA, Sansoz F. Nano Lett. 2007;7:2056.
[113] Deng C, Sansoz F. Nano Lett. 2009;9:1517.
[114] Deng C, Sansoz F. Acta Mater. 2009;57:6090.
[115] Deng C, Sansoz F. App. Phys. Lett. 2009;95.
[116] Chen ZM, Jin ZH, Gao HJ. Phys. Rev. B 2007;75.
[117] Jennings AT, Li J, Greer JR. Acta Mater. 2011;59:5627.
[118] Zhu T, Li J. Prog. Mater. Sci. 2010;55:710.
[119] Weinberger CR, Cai W. PNAS 2008;105:14304.
[120] Guruprasad PJ, Benzerga AA. J. Mech. Phys. Solids 2008;56:132.
[121] Diao JK, Gall K, Dunn ML, Zimmerman JA. Acta Mater. 2006;54:643.
[122] Park HS, Gall K, Zimmerman JA. J. Mech. Phys. Solids 2006;54:1862.
[123] Gall K, Diao JK, Dunn ML. Nano Lett. 2004;4:2431.
[124] Lu Y, Huang JY, Wang C, Sun SH, Lou J. Nat. Nanotechnol. 2010;5:218.
[125] Krausz AS, Eyring H. Deformation Kinetics. New York: John Wiley & Sons, 1975.
[126] Chen J, Lu L, Lu K. Scripta Mater. 2006;54:1913.
[127] Weinberger C, Cai W. Private Communication.
[128] Maass R, Grolimund D, Van Petegem S, Willimann M, Jensen M, Van Swygenhoven H, Lehnert T, Gijs MAM, Volkert C, Lilleodden ET, Schwaiger R. Appl Phys Lett 2006;89:151905.
[129] Maass R, Van Petegem S, Borca C, Van Swygenhoven H. Mater. Sci. Eng. A 2009;524:40.
[130] Maass R, Van Petegem S, Grolimund D, Van Swygenhoven H, Kiener D, Dehm G. App. Phys. Lett. 2008;92:071905.
[131] Maass R, Van Petegem S, Ma D, Zimmermann J, Grolimund D, Roters F, Van Swygenhoven H, Raabe D. Acta Mater. 2009;57:5996.
[132] Maass R, Van Petegem S, Van Swygenhoven H, Derlet PM, Volkert CA, Grolimund D. Phys. Rev. Lett. 2007;99:145505.
[133] Maass R, Van Petegem S, Zimmermann J, Borca CN, Van Swygenhoven H. Scripta Mater. 2008;59:471.
[134] Budiman AS, Han SM, Greer JR, Tamura N, Patel JR, Nix WD. Acta Mater. 2008;56:602.
[135] Kirchlechner C, Kiener D, Motz C, Labat S, Vaxelaire N, Perroud O, Micha JS, Ulrich O, Thomas O, Dehm G, Keckes J. Philosophical Magazine 2011;91:1256.
[136] Gruber PA, Boehm J, Onuseit F, Wanner A, Spolenak R, Arzt E. Acta Mater. 2008;56:2318.

[137] Gruber PA, Solenthaler C, Arzt E, Spolenak R. Acta Mater. 2008;56:1876.
[138] Nabarro FRN. Acta Metallurgica Et Materialia 1990;38:161.
[139] Weinberger… C. Scripta Mater. 2010.
[140] Estrin Y, Kim HS, Nabarro FRN. Acta Mater. 2007;55:6401.
[141] Christian JW, Masters BC. Proc. R. Soc. Lon. Ser. A 1964;281:240.
[142] Shemensk.Rm. Asm Transactions Quarterly 1965;58:360.
[143] Rao S, Dimiduk D, Tang M, Parthasarathy T, Uchic M, Woodward C. Philos Mag 2007;87:4777.
[144] Pichaud B, Minari F, Kellerhals J. Philos Mag A 1978;38:593.
[145] Dietiker M, Buzzi S, Pigozzi G, Loffler JF, Spolenak R. Acta Mater. 2011;59:2180.
[146] El-Awady JA, Rao SI, Woodward C, Dimiduk DM, Uchic MD. International Journal of Plasticity 2011;27:372.
[147] Nix WD, Lee SW. Philosophical Magazine 2011;91:1084.
[148] Lagos MJ, Sato F, Galvao DS, Ugarte D. Phys. Rev. Lett. 2011;106.
[149] Jennings AT, Li J, Greer JR. Acta Mater. 2011;59:5627.
[150] Nicola L, Xiang Y, Vlassak JJ, Van der Giessen E, Needleman A. J. Mech. Phys. Solids 2006;54:2089.
[151] Xiang Y, Vlassak JJ. Scripta Mater. 2005;53:177.
[152] Xiang Y, Vlassak JJ. Acta Mater. 2006;54:5449.
[153] Greer JR. Materials Research Society Symposium 2007;[0983-LL08-03].
[154] Zhou CZ, Biner S, LeSar R. Scripta Mater. 2010;63:1096.
[155] Aran A, Demirkol M, Karabulut A. Materials Science and Engineering 1987;89:L35.
[156] Guruprasad PJ, Carter WJ, Benzerga AA. Acta Mater. 2008;56:5477.
[157] Friedman N, Jennings AT, Kim JY, Dahmen K, Greer JR, al. e.
[158] Jennings AT. 2012.
[159] Willams DB, Carter CB. Transmission Electron Microscopy. New York, NY: Springer, 1996.
[160] Ng KS, Ngan AHW. Scripta Mater. 2008;59:796.
[161] Lee SW, Nix WD. Philosophical Magazine 2012.
[162] Meyers MA, Chawla KK. Mechanical Behavior of Materials. New Jersey: Prentice Hall, 1999.
[163] Maass R, Uchic MD. Acta Mater. 2012;60:1027.
[164] Nicola L, Giessen EVd, Needleman A. Journal of Applied Physics 2003;93:5920.
[165] Nicola L, Xiang Y, Vlassak JJ, Giessen EVd, Needleman A. Journal of the Mechanics and Physics of Solids 2006;54:2089.
[166] Rao SI, Hazzledine PM. Philosophical Magazine a-Physics of Condensed Matter Structure Defects and Mechanical Properties 2000;80:2011.
[167] Koehler JS. Phys. Rev. B 1970;2:547.
[168] Jennings AT, Greer JR. J. Mater. Res. 2011;26:2803.
[169] von Blanckenhagen B, Arst E, Gumbsch P. Acta Mater. 2004;52:773.
[170] Tang H, Schwarz KW, Espinosa HD. Phys. Rev. Lett. 2008;100.
[171] Senger J, Weygand D, Gumbsch P, Kraft O. Scripta Mater. 2008;58:587.
[172] Oh SH, Legros M, Kiener D, Gruber P, Dehm G. Acta Mater. 2007;55:5558.
[173] Kocks UF, Argon AS, Ashby MF. Prog. Mater. Sci. 1975;19:1.
[174] Lee SW. Private Communicatin. 2011.
[175] Nix W. Metallurgical and Materials Transactions A 1989;20:2217.
[176] Freund LB. Journal of Applied Mechanics-Transactions of the Asme 1987;54:553.
[177] Chen MW, Ma E, Hemker KJ, Sheng HW, Wang YM, Cheng XM. Science 2003;300:1275.
[178] Aubry S, Kang K, Ryu S, Cai W. Scripta Mater. 2011;64:1043.
[179] Beltz GE, Freund LB. Physica Status Solidi B-Basic Research 1993;180:303.
[180] Weinberger CR, Jennings AT, Kang K, Greer JR. 2011;Submitted.
[181] Conrad H. Materials Science and Engineering a-Structural Materials Properties Microstructure and Processing 2003;341:216.
[182] Li XY, Wei YJ, Lu L, Lu K, Gao HJ. Nature 2010;464:877.
[183] Van Swygenhoven H, Derlet PM, Froseth AG. Nat. Mater. 2004;3:399.
[184] Weinberger CR, Jennings AT, Kang K, Greer JR. J. Mech. Phys. Solids 2012;60:84.

[185] Lee S-W, Nix WD. Mater. Eng. Sci A 2010;527:1903.
[186] Motz C, Weygand D, Senger J, Gumbsch P. Acta Mater. 2009;57:1744.
[187] Weinberger CR, Cai W. Scripta Mater. 2011;64:529.
[188] Marian J, Knap J. International Journal for Multiscale Computational Engineering 2007;5:287.
[189] Liang W, Zhou M. Proceedings of the Institution of Mechanical Engineers, Part C: Journal of Mechanical Engineering Science 2004:599.
[190] Rabkin E, Nam HS, Srolovitz DJ. Acta Mater. 2007;55:2085.
[191] Zepeda-Ruiz L, Sadigh B, Biener J, Hodge A, Hamza A. App. Phys. Lett. 2007;91:101907.
[192] Ji C, Park HS. App. Phys. Lett. 2006;89:181916.
[193] Weinberger CR, Cai W. J. Mater. Chem. 2011.
[194] Xu G, Argon AS. Phil. Mag. Letters 2000;80:605.
[195] Xiang Y, Wei H, Ming, E W. Acta Mater. 2008;56:1447.
[196] Tschopp MA, Spearot DE, McDowell DL. Model. Simul. Mater. Sci. Eng. 2007;15:693.
[197] Kelchner CL, Plimpton SJ, Hamilton JC. Phys. Rev. B 1998;58:11085.
[198] Xu G, Zhang C. J. Mech. Phys. Solids 2003;51:1371.
[199] Liang W, Zhou M. Phys. Rev. B 2006:115409.
[200] Rice JR. J. Mech. Phys. Solids 1992;40:239.
[201] Ashcroft NW, Mermin ND. Solid State Physics: Brooks Cole, 1982.
[202] Wang H, Li M. Phys. Rev. B 2009;79:224102.
[203] Wua X-Z, Wanga R, Wanga S-F, Wei Q-Y. Surf. Science 2010;256:6345.
[204] Metal Reference Book: Butterworths, 1976.
[205] Simmons G, Wang H. Single Crystal Elastic Constants and Calcuulated Aggregate Properties: A Handbook: MIT Press, 1971.
[206] Hearmon RFS. Rev. Modern Phys. 1946;18:409.
[207] Mehl MJ, Klein BM, Papaconstantopoulos DA. Intermetallic compounds: Principles and Applications. vol. 1: Wiley, 1994.
[208] Tyson WR, Miller WA. Surf. Sci. 1977;62:267.
[209] Boer FR, Boom R, Mattens WCM, Miedema AR, Niessen AK. Cohesion in Metals: Elsevier, 1988.
[210] Galanakis I, Papanikolaou N, Dederichs PH. Surf. Sci. 2002;511:1.
[211] Vitos L, Ruban AV, Skriver HL, Kollar J. Surf. Sci. 1998;411:186.
[212] Jenkings ML. Philos. Mag. 1976;26:747.
[213] Balk TJ, Hemker KJ. Philos. Mag. A 2001;81:1507.
[214] Ryu S, Weinberger CR, Baskes MI, Cai W. Modell. Simul. Mater. Sci. Eng. 2009;17:075008.
[215] Crampin S, Hampel K, Vvedensky DD. J. Mater. Res. 1990;5:2107.
[216] Bernstein N, Tadmore EB. Phys. Rev. B 2004;69:094116.
[217] Vermaak JS, Kuhlmann-Wilsdorf D. J. Phys. Chem. 1968;72:4150.
[218] Solliard C, Flueli M. Surf. Sci. 1985;156:487.
[219] Fiorentini V, Methfessel M, Scheffler M. Phys. Rev. Lett. 1993;71:1051.
[220] Needs RJ, Godfrey MJ, Mansfield M. Surf. Sci. 1991;242:215.
[221] Kollar J, Vitos L, Osorio-Guillen JM, Ahuja R. Phys. Rev. B 2003;68:245417.
[222] Liu G, Xu G. J. Mech. Phys. Solids 2009;57:1078.
[223] Kang K. Atomistic Modeling of Fracture Mechanisms in Semiconductor Nanowires under Tension. 2010.
[224] Cao A, Ma E. Acta Mater. 2008;56:4816.
[225] Caillard D, Martin JL. Thermally activated mechanisms in crystal plasticity: Pergamon, 2003.
[226] Scattergood RO, Bacon DJ. Philos. Mag. 1975;31:179.
[227] Ngan AHW, Zhuo L, Wo PC. Proc. R. Soc. 2006;462:1661.
[228] Warner DH, Curtin WA. Acta Mater. 2009;57:4267.
[229] Ryu S, Kang K, Cai W. Proc. Nat. Acad. Sci. USA 2011;108:5174.
[230] Zimmerman JA, Kelchner CL, P.A. K, Hamilton JC, Foiles SM. Phys. Rev. Lett. 2001;87:165507.
[231] Li C, Xu G. Philos. Mag. 2007;86:2957.
[232] Karim S, Toimil-Molares ME, Maurer F, Miehe G, Ensinger W, Liu J, Cornelius TW, Neumann R. Applied Physics A: Materials Science & Processing 2006;84:403.

[233] Hara S, Izumi S, Sakai S. J. Appl. Phys. 2009;106.
[234] Brochard S, Hirel P, Pizzagalli L, Godet J. Acta Mater. 2010;58:4182.
[235] Seeger A. Mater. Sci. Eng. A 2001;A319-321:254.
[236] Tiwary P, van de Walle A. Phys. Rev. B 2011;84.
[237] Ogata S, Li J, Yip S. Science 2002;298:807.
[238] Lee SW, Weinberger CR, Jennings AT, Greer JR.

Appendix A: The Critical Nucleation Stress and Nucleation Rate

In this section we derive the critical nucleation rate and nucleation stress for three specific loading conditions: constant strain rate with a linear stress-strain relationship, constant stress rate and constant strain rate with a non-linear stress-strain relationship which is an extension of the derivation presented in [81]. In all three cases, the resulting critical nucleation rates and stresses are very similar and thus this section provides a comprehensive summary of the critical nucleation rates and stresses in loaded pillars.

First consider the equation governing the survival probability of a nanowire as a function of time can be re-written in terms of stress as:

$$\frac{df}{d\sigma}\frac{d\sigma}{dt} = -p(\sigma)f(\sigma) \tag{A.1}$$

Now, we assume that the stress and strain are linear under constant strain rate, $\sigma = E\dot{\varepsilon}t$, resulting in

$$\frac{df}{d\sigma}E\dot{\varepsilon} = -p(\sigma)f(\sigma) \tag{A.2}$$

Taking another derivative with respect to stress gives:

$$\frac{d^2f}{d\sigma^2}E\dot{\varepsilon} = -p(\sigma)\frac{df(\sigma)}{d\sigma} - f(\sigma)\frac{dp(\sigma)}{d\sigma} \tag{A.3}$$

Evaluating the above expression at $\sigma = \sigma_{crit}$ and noting that $\left.\frac{d^2f}{d\sigma^2}\right|_{\sigma=\sigma_{crit}} = 0$ results in:

$$\left.\frac{df(\sigma)}{d\sigma}\right|_{\sigma=\sigma_{crit}} = \left.\frac{dp}{d\sigma}\frac{f(\sigma)}{p(\sigma)}\right|_{\sigma=\sigma_{crit}} \tag{A.4}$$

Both $f(\sigma)$ and $\frac{df(\sigma)}{d\sigma}$ can be removed by combining Equations B.2 and B.4,

$$\left.\frac{dp(\sigma)}{d\sigma}\right|_{\sigma=\sigma_{crit}} = \left.\frac{p^2(\sigma)}{E\dot{\varepsilon}}\right|_{\sigma=\sigma_{crit}} \tag{A.5}$$

Now, noting that $\left.\frac{dp(\sigma)}{d\sigma}\right|_{\sigma=\sigma_{crit}} = \frac{p\Omega}{k_BT}$ (which is obtained by directly differentiating Equation 8. 9)

$$p|_{\sigma=\sigma_{crit}} = \frac{E\Omega}{k_BT}\dot{\varepsilon} \tag{A.6}$$

Substituting in for *p* from Equation 8.9 gives the desired result (Equation 8.12). It is useful, though, to consider the result of Equation A.6. It is convenient to think that in a constant strain rate simulation that the time scale of nucleation, the inverse of *p*, is inversely proportional to the strain rate. Equation B.6 shows an agreement between this physical notion of nucleation and the theoretical

development here.

In many micro-compression experiments, the tests are done neither at constant strain rate or at constant stress rate, but are nominally load controlled with a feedback loop to mimic constant displacement rate. Therefore, it is useful to consider the case of constant stress rate: $\sigma = \dot{\sigma}t$ where $d\sigma/_{dt} = \dot{\sigma}$ is a constant. This does not change the derivation above except that one replaces $E\dot{\varepsilon}$ with $\dot{\sigma}$. And so the nucleation rate is:

$$p|_{\sigma=\sigma_{crit}} = \frac{\Omega}{k_B T}\dot{\sigma}|_{\sigma=\sigma_{crit}} \tag{A.7}$$

and the implicit equation for the critical nucleation stress is:

$$\frac{E_b}{k_B T} = \ln\left(\frac{k_B T N \nu_o}{\dot{\sigma}\Omega}\right) \tag{A.8}$$

The above expression assumes nothing about the linearity of the stress-strain curve.

The original expression for the critical stress, Equation A.12, assumes linearity of the stress-strain curve under constant strain rate. This equation is valid for a non-linear stress-strain curve if E is replaced by the tangent modulus:$E_T \equiv d\sigma/d\varepsilon$. This can be seen by starting with Equation (A.1) and noting that:

$$\frac{d\sigma}{dt} = \frac{d\sigma}{d\varepsilon}\frac{d\varepsilon}{dt} \tag{A.9}$$

Assuming a constant strain rate $\frac{d\varepsilon}{dt} = \dot{\varepsilon}$ we have

$$\frac{d\sigma}{dt} = E_T\dot{\varepsilon} \tag{A.10}$$

Which results in the nucleation rate

$$p|_{\sigma=\sigma_{crit}} = \frac{E_T\Omega}{k_B T}\dot{\varepsilon}|_{\sigma=\sigma_{crit}} \tag{A.11}$$

and the implicit equation for the critical nucleation stress is:

$$\frac{E_b}{k_B T} = \ln\left(\frac{k_B T N \nu_o}{E_T\dot{\varepsilon}\Omega}\right) \tag{A.12}$$

Thus, one simply has to substitute the tangent Young's modulus into Equation A.12 in the case of constant strain rate with a non-linear stress-strain relationship.

Appendix B: Statistics of Dislocation Slip Avalanches in Nano-Sized Single Crystals Explained by a Simple Mean Field Mode

Slowly sheared metallic nano-crystals deform via discrete strain-bursts (slips), whose size-distributions follow power-laws with stress-dependent cutoffs. We extract, for the first time, a scaling collapse of the stress-dependent slip-size-distributions. The obtained universal scaling-function contains infinitely more information than traditional sets of discrete exponents. Both, exponents and scaling-function, agree with mean-field-theory predictions. Our study of 7 materials, 2 crystal-structures, at various deformation-rates, stresses, and crystal-sizes down to 75 nm, attests to the universal characteristics of plasticity.

Introduction: Sheared small-scale crystals deform via a sequence of discrete slips, measurable either as steps in stress-strain curves or as acoustic emission pulses [1-13]. These slips are caused by dislocation slip-avalanches that are due to rapid dislocation nucleation or sudden releases of dislocations from pinned sources. They stop when all slipping dislocation segments have either repinned or annihilated. Recent experiments on the axial compression of micron and sub-micron sized crystals reported that the stress-integrated histograms (distributions) $D_{int}(S)$ of all slip sizes S, from the initiation of compression to pillar failure, follow a power-law $D_{int}(S) \sim S^{-1.5}$ over several decades in slip size, where S is the total axial displacement during an avalanche (see Supplementary Online Material (SOM)). This has been seen in experiments on micron and sub-micron pillars of face-centered cubic (fcc) metals (Cu, Al, Au, Ni), as well as one body-centered cubic (bcc) metal (Mo) [8,9,14-16].

However, the slip statistics are far from understood:

(1) Previous experimental studies focused mostly on fitted power-law exponents, assuming that $D(S) \sim S^{-\kappa}$. But the stress-dependence of slip statistics has not yet been systematically studied in experiments. A simple mean field theory (MFT) model [2] predicts a stress-*dependent* slip size distribution, $D(S,\tau)$, that extends to larger avalanche sizes for stresses τ closer to the failure stress τ_c. This stress dependence is governed by a new "cutoff"-exponent σ describing the stress dependence of the cutoff of the power law regime of $D(S,\tau)$, and a universal scaling function. Here we extract from experiments the traditional exponent κ, the new cutoff-exponent σ, and for the first time also the predicted scaling *function*, which contains infinitely more information than any traditionally used discrete set of exponents. For the first time we succeed in collapsing the experimental avalanche size distributions at different stresses onto a predicted scaling function. The scaling collapse renders more accurate results for more exponents than can be obtained from the traditional power law fits alone [2]. Also, since it constitutes a more stringent test of our theory, it provides convincing experimental evidence that plasticity reflects an underlying non-equilibrium phase transition [1-3], as explained below.

(2) We present a unified understanding of plasticity at nano- and micro scales [10-12]. At first sight plasticity looks different on these two scales. At nano-scales the lattice structure matters: The dislocation dynamics and the criticality-slope, (which we define as

the slope of the stress-strain curve prior to failure at highest strain (Figure 1C)), have been reported to significantly depend on the material's crystal structure at these scales [9-12,17]. Here we show how MFT relates these features to the associated slip statistics. Furthermore we show that the same MFT applies to all crystal structures on both scales, despite the apparent differences observed in experiments.

We thus show that MFT provides a unified explanation for plasticity at nano-scales and micro-scales for different crystal structures. It not only explains the power law exponents of the slip size distributions, but also the stress-dependence of their cutoffs. The model suggests that the scaling behavior is fully analogous to that found near phase transitions, like the liquid gas transition. In equilibrium, temperature and pressure are often "tuning parameters" that need to be tuned to approach the transition where critical power law scaling is seen. The cutoffs of the power law distributions depend on the tuning parameters. Here we show that in our non-equilibrium system, analogous tuning parameters are stress, deformation rate, and sample size. The analogue of an order parameter of the transition is the average deformation rate of the material at a given applied stress. Below the failure stress the material eventually stops deforming, giving it an average deformation rate of zero. Above the flow stress the material deforms continuously until it fails, giving it a non-zero average deformation rate. The model predicts that the flow (failure) stress is a critical point, and near this critical point the systems should show universal (detail-independent) behavior as predicted by the theory of phase transitions and the renormalization group [18]. Thus, plasticity belongs to a large class of other systems that have been treated successfully using these methods, from earthquakes to magnets [19-20].

In summary, in the following we report stress-integrated and stress-binned (i.e. stress-dependent) slip size distributions measured during uniaxial compression of nano-pillars for different values of the tuning parameters. Most importantly, we extract a scaling collapse of the stress-dependent slip avalanche statistics from these experiments and demonstrate agreement of both the exponents and the scaling function with our MFT model. The scaling function contains much more information than the traditionally used critical exponents alone, therefore the scaling collapse constitutes a new and stronger test of the theory than previously possible in the study of nano- and micropillars. The analysis tools and methods applied here to experiments are generally applicable to a much broader set of future experiments on plasticity and slip-avalanche statistics.

***MFT for slow shear*:** Our simple coarse-grained model described in detail in [2] makes robust statistical predictions for material deformation given the following assumptions:

1. A slowly sheared material has weak spots where slip initiates when the local stress exceeds a random local failure stress.

2. Slips occur at length scales that are large compared with the microscopic structure of the material.

3. The material is sheared sufficiently slowly so that avalanches do not overlap in time.

4. The MFT approximation: it is valid to replace the long-range interactions predicted by elasticity with infinite range interactions.

A failed spot slips until the local stress is reduced to a random arrest stress, and then re-sticks. The stress released by a failed spot triggers other elastically coupled weak spots to slip, creating a slip avalanche. In practice, the meaning of assumption 3 is that the avalanches occur much faster than the imposed overall material deformation. We are able to extract detail-independent (universal) analytical predictions [2,18], which give the same results for the scaling behavior as numerical studies of continuum models [19], phase fields [23], phase field crystals [24], discrete 2D dislocation dynamics [3,19,25,18], and full 3D dislocation dynamics simulations [26].

At applied stress τ, the model predicts that the stress-dependent ("stress-binned") distribution $D(S, \tau)$ of slip sizes S follows a power law $S^{-\kappa}$ up to a stress-dependent cutoff size:

$$D(S,\tau) \sim S^{-\kappa} f_S(S(\tau_c-\tau)^{1/\sigma})$$

[2]. Here S is defined by the total displacement during a slip avalanche (see SOM). The exponents $\kappa=3/2$ and $1/\sigma=2$ and the scaling functions $f_S(x)$ is universal [1,2]. In MFT, $f_S(x) = \exp(-Ax)$ where A is a non-universal constant [2]. τ_c denotes the maximum or critical flow stress of the material. The corresponding stress-binned complementary cumulative distribution function (CCDF) scales as

$$C(S,\tau) \sim \int_S^\infty D(S',\tau)dS' \sim S^{-(\kappa-1)} g(S(\tau_c-\tau)^{1/\sigma}) \qquad (1)$$

where $g(x) \equiv \int_x^\infty e^{-At} t^{-\kappa} dt$ is the universal scaling function shown in the inset of Figure 4. MFT further predicts that the stress-integrated histogram $D_{int}(S)$ of slip sizes occurring at all stresses follows a power law (see SOM)

$$D_{\text{int}}(S) \equiv \int D(S,\tau)\, d\tau \sim S^{-(\kappa+\sigma)} \qquad (2)$$

with the exponents' sum, $\kappa+\sigma=2$. The integrated CCDF

$$C(S) \equiv \int_S^\infty D_{\text{int}}(S')dS' \sim S^{-(\kappa+\sigma-1)} \qquad (3)$$

then scales as $C(S) \sim S^{-1}$ in MFT (Figures 2-4). MFT predicts identical stress-integrated power law exponents for fcc nano-pillars (whose stress strain curves end with the virtually-vanishing criticality-slopes), as for bcc metals (with a finite, non-zero criticality-slope) [2,17]. The above predictions apply to slow compression rates where avalanches are well separated in time.

At higher imposed compression rates Ω, avalanches can overlap in time. A general theory [27] predicts that merging of avalanches in time, i.e. activating new avalanches before the previous ones complete, leads to smaller exponent values at higher Ω [27]. For our experiments this implies that at faster compression rates we expect the stress-integrated exponent sum to be $\kappa+\sigma<2$ instead of the $\kappa+\sigma=2$ suitable for the slow compression rates (Figure 3).

Compression experiments on single-crystalline nano-pillars: Experimental load and displacement data were obtained from uniaxial compressions of fcc and bcc single-crystalline, cylindrical nano-pillars with diameters ranging from 75 nm to 1000 nm and aspect ratios (height/diameter) between 3:1 and 6:1 (Figure 1). The experimental procedure outlined in the methods section provided a time series of the applied load, axial displacement, and the slip sizes *S* for each of the pillars tested. The sampling frequency was 25 Hz, and by noting where the distribution of slips changes from power law to Gaussian we concluded that slip identification was reliable down to events as small as O(0.3 nm). The Au, Nb, Mo, Ta, and W nano-pillars were fabricated via focused ion beam (FIB) methodology [9,15,16], and Cu pillars were created via templated electroplating [28], and were compressed at a variety of different prescribed displacement rates. We find that for a slowly increasing applied load, the stress remains approximately constant during each slip, as assumed in the model. In the experiments, this corresponds to the lower displacement rates, where the slip speed is much greater than the externally imposed strain rate [29]. The data were collected on two nanoindenters, one with a very high stiffness of 300 000 N/m, and one with a stiffness of 65 000 N/m; no systematic difference based on machine stiffness was observed.

Figures 2-4 and Figure 5 show stress-integrated and stress-binned complementary cumulative histograms, respectively, for a variety of these experiments. These histograms show the fraction of slips with sizes greater than S as a function of slip size *S*. Since the events are reliably identified, but relatively few in number, the major source of error is statistical. Across the range of materials tested, these cumulative histograms display a power law regime with an exponent close to the theoretical value of -1 (see Figure 2). The data in Figure 2 were collected for large system sizes and at low nominal displacement rates − a regime closest to the scaling regime of the MFT model. These plots show that both fcc and bcc nano-crystals of different diameters and compressed at different displacement rates are characterized by the same power law exponents despite the distinct differences in their dislocation behavior as reported in [9,17]. The materials show slight differences in how the changing nominal displacement rates affect the statistical data.

Figure 3 shows the results for three different nominal displacement rates, varying by an order of magnitude, for 800 nm diameter Au and Mo pillars. The avalanche size distribution for Mo is fairly robust from 0.1 to 1 nm/s, but the magnitude of the fitted scaling exponent of $C(S)$ decreases at 10 nm/s. Au, on the other hand, is much more sensitive to the prescribed displacement rate: the magnitude of the scaling exponent of $C(S)$ decreases with the increasing displacement rate. As discussed in the theory section and in [24], at higher driving rates avalanches tend to overlap in time, thereby reducing the scaling exponents of $D_{int}(S)$ and $C(S)$. Note that due to the limited resolution in time,

two avalanches may not be overlapping but may merely be detected as overlapping; i.e. lower time resolution will enhance the tendency of higher driving rates to effectively merge avalanches. Theory predicts that the amounts by which the exponents change as the displacement rate is increased depend on the material [27], which is corroborated by our experiments. The results of Figure 3 for different nominal displacement rates are thus consistent with the theories of [2] and [27].

We also considered the impact of system size on the slip size distributions. Sufficiently close to criticality, the correlation length associated with the infinite system is larger than the actual sample size in experiments. In this case, the system size (i.e. pillar diameter resolved onto a shear slip-plane) determines the scale of the largest events and, hence, the cutoff of the slip size distribution. Figure 4 shows histograms for Cu for a variety of nano-pillar sizes compressed at the same displacement rate of 2 nm/s. Although the events are comparatively few and the statistical fluctuations are pronounced, the trend of increasing maximum avalanche-size with system size is visible in Figure 4.

Figure 5 shows that the cumulative slip size histograms binned in stress also agree with the model's prediction for $C(S,\tau)$ of Eq. (1) (see SOM). The main figure shows the raw data at four distinct stress bins, while the inset shows a data collapse using the exponents $\kappa-1= 0.5$ and $1/\sigma=2$ predicted by MFT. Stress bins closer to criticality than those shown were not used in the collapse plot due to finite size effects (see SOM). The inset shows that the theoretically predicted collapse function (continuous black line) falls directly on top of the experimental collapse. This analysis of our experimental results reveals that the mean field theory not only correctly predicts the exponents used for the successful collapse, but also provides the correct form for the scaling function [2]. This constitutes the first experimental validation of not only scaling exponents but also a universal scaling function predicted by the simple MFT model. The collapse also confirms the explanation for the stress-integrated power law of -1 for $C(S)$ seen in Figures 2-4.

Discussion: Recent uniaxial deformation experiments and molecular and dislocation dynamics simulations provide insight into the physical nature of dislocation sources, size dependence of material strength, strain rate sensitivity, and amount of hardening [10-12]. The consensus is that these factors vary greatly between fcc and bcc crystals, and from nano- to microscale. The question emerges whether these differences are also manifested by the dislocation slip statistics. Our experiments yield a stress-integrated exponent of $\kappa+\sigma=2$ for the slip size distributions, for both bcc and fcc nano-pillars with diameters between 75 nm and 1 μm, in agreement with the MFT prediction. In contrast, previous experiments on Mo and Au [9,14] have reported a size distribution exponent of 1.5 for samples ranging in size from 180 nm to 6 μm [8]. Our model provides a unified understanding of the statistics in all these cases, as the difference between the observed exponents can be explained as follows:

(1) The compression experiments of [14] on sub-micron samples were performed at relatively higher effective compression-rates (Figure 3), where lower exponents can be explained by the simultaneous activation, and therefore merging, of slip avalanches [27]. We observed significant impact on the exponent for rates as slow as 1 nm/s.

(2) In many micron-sized samples there is a large regime before failure where the stress-strain curve is linear due to hardening [8,11]. Such behavior can be captured by modifying the MFT model to include hardening through incorporating an increased resistance to slip in the course of deformation. In this case, the effective distance from criticality remains constant, and the experiment effectively measures κ rather than $\kappa+\sigma$. Thus the measured value of 1.5 is in accordance with our theory [1, 2, 19, 26, 30].

In the experiments, the applied stress is increased from zero to failure each time a pillar is compressed. Near failure the slip avalanches tend to get large. Consequently, at the highest stresses the slip statistics will be distorted by finite-size effects regardless of the size of the crystal. Therefore stress bins that are too close to failure to be free from finite-size distortions are excluded from the collapse shown in Figure 5 (see SOM).

The successful data collapse of stress-binned slip size data with the theoretically predicted exponents and scaling function serves as a strongest possible experimental verification of mean field theory, which up to this point, had only been confirmed through numerical simulations. Scaling functions contain much more information than a few discrete exponents, so the agreement of the collapse with the predicted scaling function constitutes the most stringent test of the model to date.

In conclusion, this study presents the first universal scaling collapse and scaling function extracted from compression experiments on nanopillars and micropillars. It shows that both the new exponents and the new scaling function of the stress-dependent statistics of strain bursts in slowly deformed crystals agree with predictions from a simple analytical MFT model. The agreement between the model and experiments for a wide variety of metallic nano-crystals subjected to widely varying experimental conditions suggests that a single universality class fully describes discrete crystalline deformation at these small length scales. This holds true under a wide variety of conditions: for pillar sizes ranging from 75 nm to 1 μm, for strain rates less than or on the order of $1\text{x}10^{-4}$ s^{-1}, for different materials including those with fcc and bcc crystal structures. This agreement is observed both in the power law scaling of the event frequency as well as in the stress-dependence of the slip size distributions. This wide applicability of MFT theory means that the same universality class describes small-scale plasticity and is robust against detail-driven differences in dislocation behavior. This robustness is indicative of the broader fact that these analysis methods are highly applicable to other non-equilibrium systems with driving force dependent avalanches [19]. In the context of the renormalization group [2,19] our results imply that the same fundamental properties—symmetries, dimensions, interaction range, etc.—control the statistics of slips in metallic crystals, down to the smallest currently accessible length scales.

Acknowledgements: We thank Dennis Dimiduk, Braden Brinkman, Tyler Earnest, and Matthew Wraith for helpful conversations and acknowledge the financial support of a NSERC Post-Graduate Scholarship (NF), and from grants NSF DMR 03-25939 ITR ("Materials Computation Center") and DMR 1005209 (GT and KD), as well as from NSF Graduate Fellowship (ATJ), NSF CAREER award DMR-0748267 (JRG) and ONR Grant No. N00014-09-1-0883 (JRG).

References

[1] Zaiser, M., Scale invariance in plastic flow of crystalline solids, *Advances in Physics* **55**, 185-245 (2006).

[2] Dahmen, K.A., Ben-Zion, Y. & Uhl, J.T., A micromechanical model for deformation in solids with universal predictions for stress-strain curves and slip avalanches, *Phys. Rev. Lett.* **102**, 175501/1-4 (2009).

[3] Miguel, M.-C., Vespignani, A., Zapperi, S., Weiss, J. & Grasso, J.R., Intermittent dislocation flow in viscoplastic deformation, *Nature* **410**, 667-671 (2001).

[4] Weiss, J., Grasso, J. R., Miguel, M.-C., Vespignani, A. & Zapperi, S., Complexity in dislocation dynamics: experiments, *Mater. Sci. Eng. A* **309-310**, 360-364 (2001).

[5] Richeton, T., Dobron, P., Chmelik, F., Weiss, J. & Louchet, F., On the critical character of plasticity in metallic single crystals, *Mater. Sci. Eng. A* **424**, 190-195 (2006).

[6] Richeton, T., Weiss, J. &Louchet, F., Dislocation avalanches: Role of temperature, grain size and strain hardening, *Acta Materialia* **53**, 4463-4471 (2005).

[7] Weiss J., Lahaie F. & Grasso J.R., Statistical analysis of dislocation dynamics during viscoplastic deformation from acoustic emission, *J. Geo. Res*. **105**, 433-442 (2000).

[8] Dimiduk, D.M., Woodward, C., LeSar, R. & Uchic, M.D., Scale-Free Intermittent Flow in Crystal Plasticity, *Science* **312**, 1188-1190 (2006).

[9] Brinckmann, S., Kim, J.-Y. & Greer, J.R., Fundamental Differences in Mechanical Behavior between Two Types of Crystals at the Nanoscale, *Phys. Rev. Lett.* **100**, 155502/1-4 (2008).

[10] Greer, J. R. & De Hosson, J.T.M**.,** Plasticity in small-sized metallic systems: intrinsic versus extrinsic size effect, *Progress in Materials Science* **56**, 654-724 (2011).

[11] Uchic, M.D., Shade, P. & Dimiduk, D., Plasticity of Micrometer-Scale Single Crystals in Compression, *Annual review of materials research* **39**, 361-386 (2009), and references therein.

[12] Kraft, O., Gruber, P., Mönig, R. & Weygand, D., Plasticity in Confined Dimensions, *Annual review of materials research* **40**, 293-317 (2010) and references therein.

[13] Ngan, A.H.W. & Ng, K.S., Transition from deterministic to stochastic deformation, *Phil. Mag.* **90**, 1937-1954 (2010).

[14] Zaiser, M., Schwerdtfeger, J., Schneider, A. S., Frick, C. P., Clark, B. G., Gruber, P.A. & Arzt, E., Strain bursts in plastically deforming molybdenum micro- and nanopillars, *Phil. Mag.* **88**, 3861 – 3874 (2008).

[15] Kim, J.-Y. & Greer, J.R., Tensile and compressive behavior of gold and molybdenum single crystals at the nano-scale, *Acta Materialia* **57**, 5245 – 5253 (2009).

[16] Kim, J.-Y., Jang, D. & Greer, J.R., Tensile and compressive behavior of tungsten, molybdenum, tantalum and niobium at the nanoscale, *Acta Materialia* **58**, 2355 – 2363 (2010).

[17] Weinberger, C.R. & Cai, W., Surfaced-controlled dislocation multiplication in metal micropillars, *Proceedings of the National Academy of Sciences of the United States of America* **105**, 14304-14307 (2008).

[18] Nigel D. Goldenfeld. *Lectures on Phase Transitions and the Renormalization Group.* Westview Press, 1992.

[19] James P. Sethna, Karin A. Dahmen, and Christopher R. Myers. Crackling Noise, *Nature*, 410(6825):242-250, 2001.

[20] Amit P. Mehta, Andrea C. Mills, Karin A. Dahmen, and James P. Sethna. Universal pulse shape scaling function and exponents: Critical test for avalanche models applied to Barkhausen noise. *Physical Review E*, 65(4):046139, 2002.

[21] Tsekenis, G., Goldenfeld, N. & Dahmen, K.A., Dislocations Jam at Any Density, *Phys. Rev. Lett.* **106**, 105501/1-4 (2011).

[22] Zaiser, M., The 'yielding transition' in crystal plasticity - discrete dislocations and continuum models, *Statistical Mechanics of Plasticity and Related Instabilities*, Provided by the SAO/NASA Astrophysics Data System (2005).

[23] Koslowski, M., Scaling laws in plastic deformation, *Phil. Mag.* **87,** 1175-1184 (2007).

[24] Chan, P. Y., Tsekenis, G., Dantzig, J. Dahmen, K. A. & Goldenfeld, N., Plasticity and Dislocation Dynamics in a Phase Field Crystal Model, *Phys. Rev. Lett*. **105**, 015502/1-4 (2010).

[25] Ispanovity, P. D., Groma, I., Gyorgyi, G., Csikor, F. F. & Weygand, D., Submicron Plasticity: Yield Stress, Dislocation Avalanches, and Velocity Distribution, *Phys. Rev. Lett.* **105**, 085503/1-4 (2010).

[26] Csikor, F.F., Motz, C., Weygand, D., Zaiser, M. & Zapperi, S., Dislocation Avalanches, Strain Bursts, and the Problem of Plastic Forming at the Micrometer Scale, *Science* **318**, 251-254 (2007).

[27] White, R.A. & Dahmen, K.A., Driving Rate Effects on Crackling Noise, *Phys. Rev. Lett*. **91**, 085702/1-4 (2003).

[28] Jennings, A.T., Burek, M.J. & Greer, J.R., Microstructure versus Size: Mechanical Properties of Electroplated Single Crystalline Cu Nanopillars, *Phys. Rev. Lett.* **104**, 135503/1-4 (2010).

[29] Jennings, A.T., Li, J. & Greer, J.R., Emergence of strain rate sensitivity in Cu nanopillars: Transition from dislocation multiplication to dislocation nucleation, *Acta mat.* **59**, 5627-5637 (2011).

[30] Tsekenis, G., Uhl, J.T., Goldenfeld, N. & Dahmen, K.A., Temporal and Finite Size Scaling Properties of Avalanches in Plasticity Exhibit Mean Field Character, submitted to Phys. Rev. Lett. (2012).

Figures

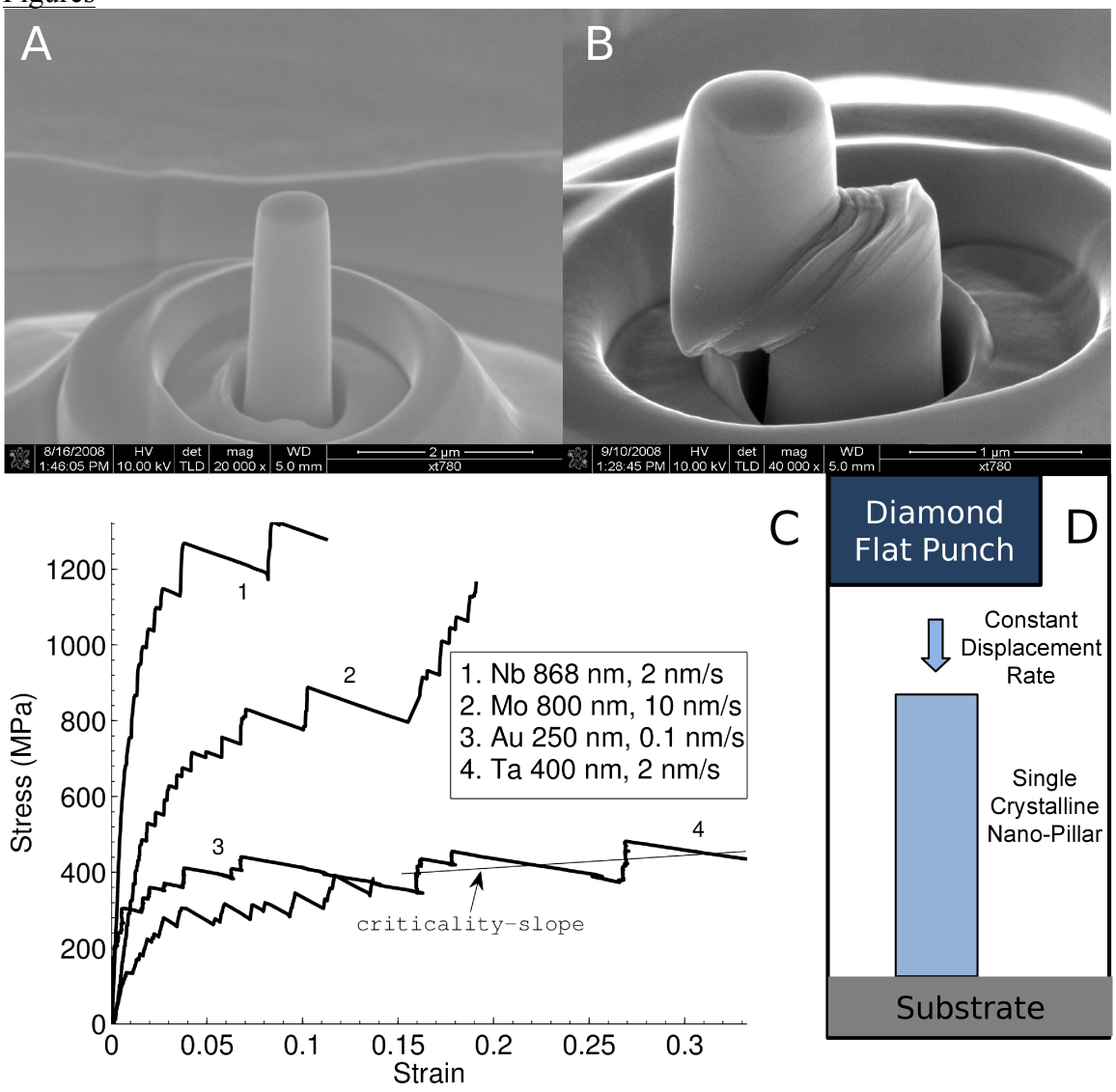

Figure 1: Characteristic experimental results for nano-pillar compression tests. A and B show SEM images at 52º tilt before and after testing, respectively, of a 868nm-diameter Nb pillar. C shows characteristic stress-strain curves (each consisting of thousands of points) for 4 different metals compressed at different displacement-rates. The stress-strain curve for Nb corresponds to the pillar in A-B. The slope of the line fitted to the average stress-strain curve near the critical stress of curve 4 is an example of the "criticality-slope" mentioned in the paper. D is a schematic showing the compression test methodology. For further details on this and all other figures, see SOM.

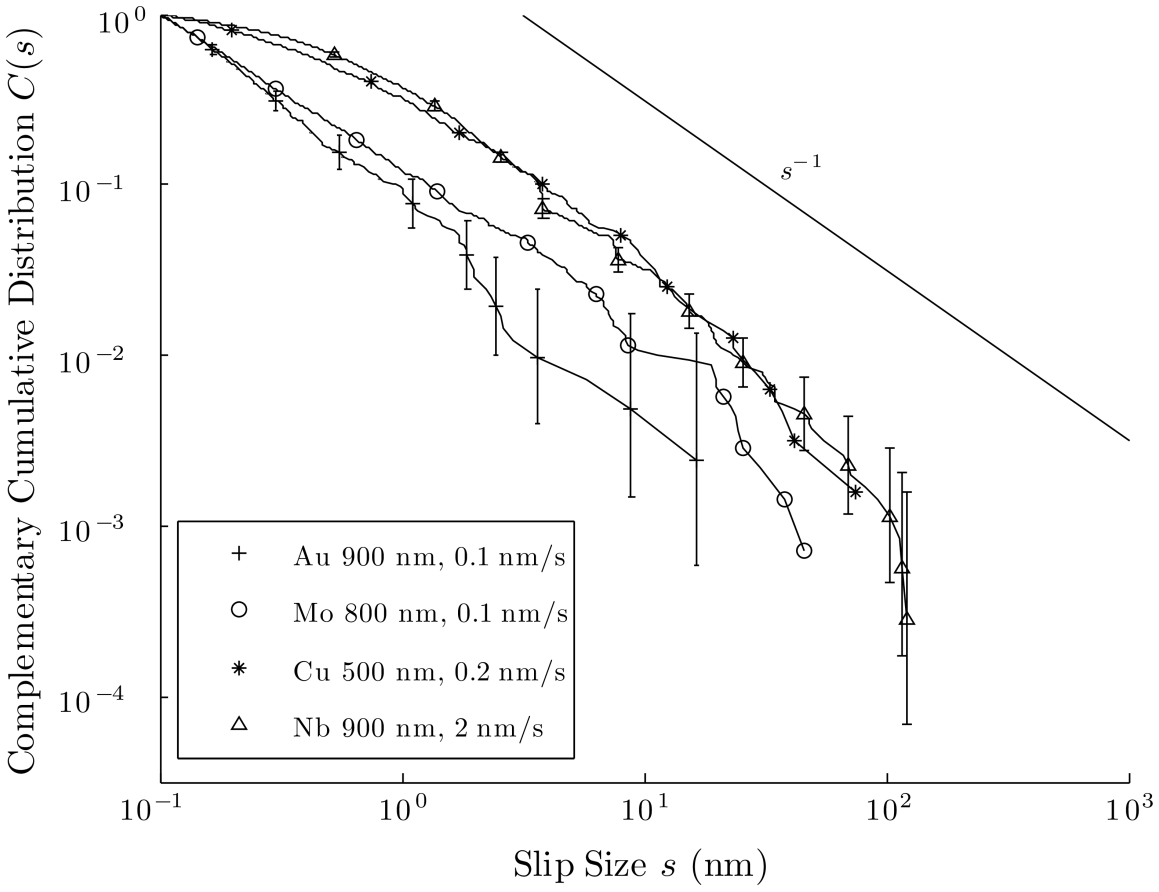

Figure 2: Stress-integrated cumulative histograms C(S) of slip sizes S for uniaxial compression data obtained for various materials, pillar-sizes, and nominal displacement-rates, integrated over all stresses from zero stress to the maximum flow-stress, or "critical stress". The cumulative histograms presented in this figure and others contain one point per observed event, which is generally on the order of hundreds. Errors were found using Bayesian 95% confidence bounds assuming uniform priors; they were placed only on the histograms with the most and least points for clarity. Fitting each curve separately to a power law yielded 2.1±0.1, 1.85±0.1, 1.8±0.2, and 1.9±0.2, in the order given by the legend. The fit was performed using a maximum likelihood estimate; the error was determined by varying the upper and lower bounds of the fitted power law regime. Similar techniques for error bars and exponent fitting were used in all figures.

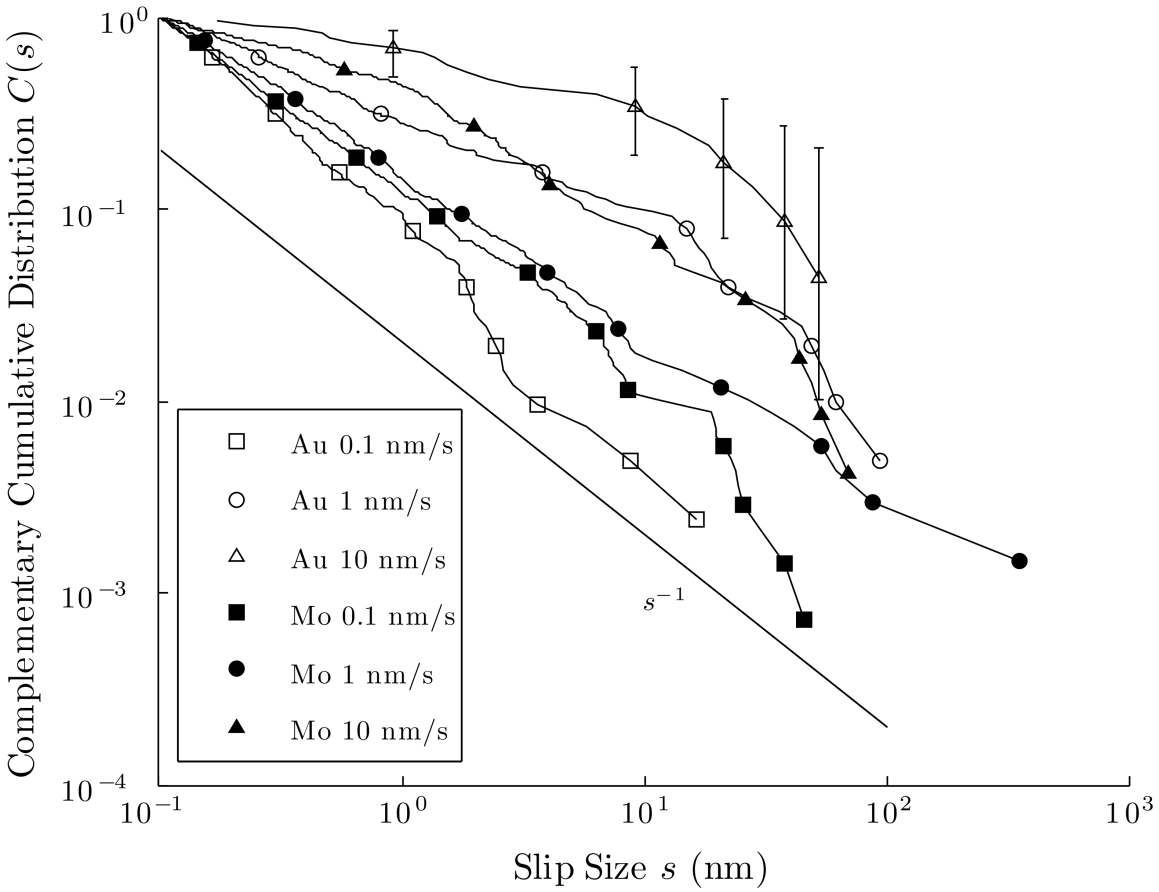

Figure 3: Stress-integrated cumulative histograms C(S) of slip sizes S for uniaxial compression data: comparison of the impact of nominal displacement rate for two different materials, Mo and Au of diameter 800 nm. We can see a clear impact of nominal displacement-rate on the apparent power laws of the cumulative slip size histograms. We quantified this by fitting exponents for the curves shown above: 2.1±0.1, 1.45±0.1, 1.2±0.2, 1.85±0.1, 1.8±0.1, and 1.6±0.3, given in the order of the plots in the legend. Since the model described above uses adiabatically slow displacement rates, in general we should look to the lowest rates to compare with its predictions.

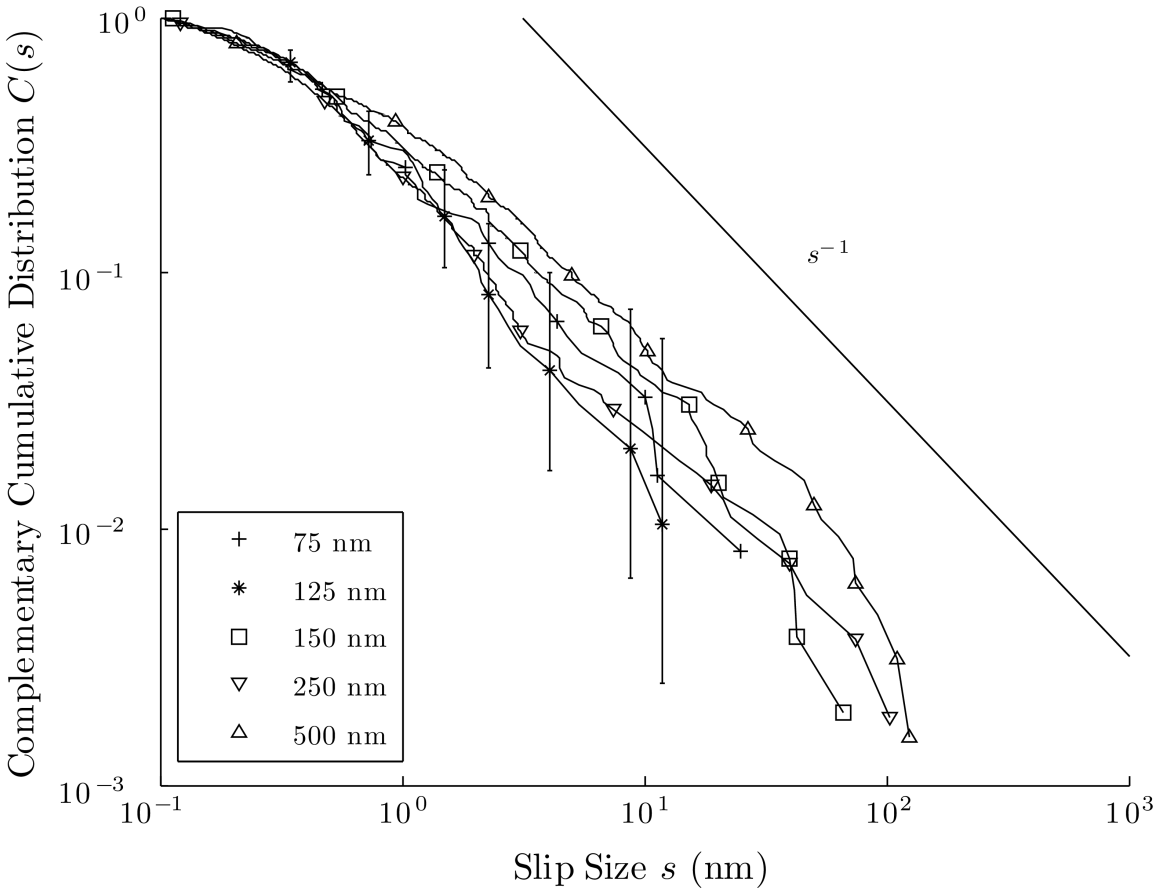

Figure 4: Stress-integrated cumulative histograms C(S) of the slip size S for various sizes of Cu nano-pillars compressed at a displacement-rate of 2 nm/s. Larger pillars tend to have larger maximum slip events. There is an exception for the 125 nm pillars, for which less data was taken. This can be explained by the general fact that, for power law distributions, the expected size of the largest observed slip also increases with the total number of observed slips in the distribution.

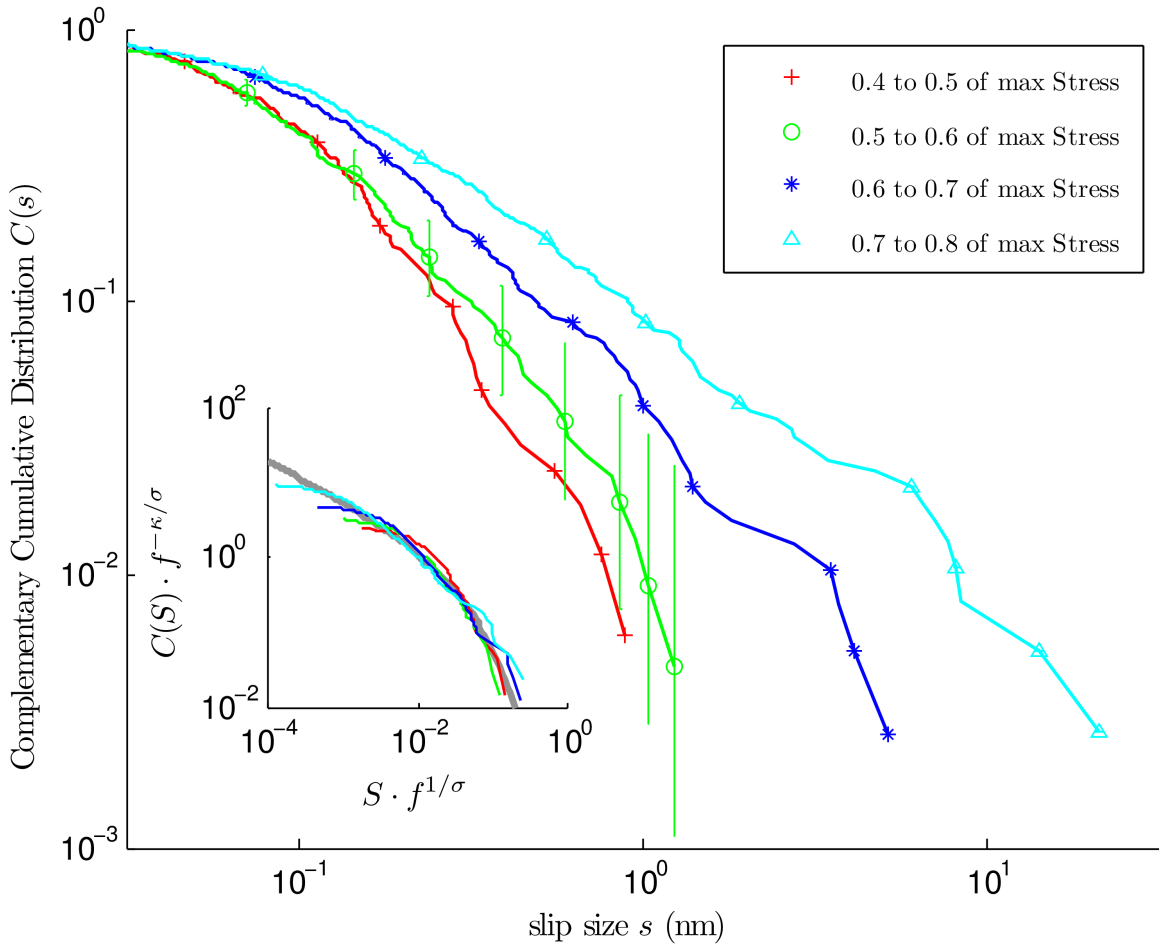

Figure 5: The main figure shows stress-binned cumulative histogram C(S,τ) of slip sizes S as a function of applied stress τ. This histogram includes events from 7 Mo nano-pillars, all of approximate diameter 800 nm, compressed at 0.1 nm/s nominal displacement rate. The events from each pillar are normalized according to their respective maximum stress. The inset shows the collapse; the same data is plotted with rescaled axes. The parameter f is a measure of closeness to criticality, it is given by $f = (\tau_c-\tau)/\tau_c - c'$, where $c' = 0.14$ is an adjustable parameter that compensates for finite system size (see SOM). κ and 1/σ have their MFT values of 1.5 and 2.0 respectively, while the function plotted in grey on the inset shows the predicted universal scaling function based on MFT , $g(x) \equiv \int_x^\infty e^{-At} t^{-\kappa} dt$.

Supplementary Online Material

Materials and Methods

Experiments

Uniaxial compression tests were performed in a G200 Nanoindenter (Agilent Technologies) using the dynamic contact module (DCM) fitted with a 7 micron diameter diamond flat punch. Each compression test was conducted under nominal constant displacement rate ranging from 0.1 nm/s to 1000 nm/s, controlled through a feedback loop method as the nanoindenter is inherently a load-controlled instrument. Compression tests were performed on single-crystalline, cylindrical nano-pillars with diameters ranging from 75 nm to 1000 nm and aspect ratios (height/diameter) between 3:1 and 6:1. Nano-pillars of five different materials were used: Au, Cu, Mo, Nb, and Ta. With the exception of Cu, all nano-pillars were prepared by a subtractive technique using a focused ion beam (FIB) on well-annealed electropolished (100) crystals, which involves milling out the matrix material and leaving the sample in the center [1]. Cu nano-pillars were prepared by electroplating Cu into cylindrical holes patterned by electron beam lithography into PMMA template, as described in more detail in [2]. Examples of a Nb pillar before and after compression along with examples of resulting stress-strain curves are shown in Figure 1 A-C in the main paper, with the schematic depiction of the experiment presented in Figure 1D. Details of these experimental tests and results for Au, Cu, Mo, Nb, and Ta can be found in [2, 3, 1, 4, 5]. A discussion of the displacement rates and the resolution of the measurements is given in [6]. An in-situ uniaxial compression movie combined with instantaneous stress-strain plot is included in the supplementary material.

Data Analysis

In order to identify the slips, the displacement time series $d(t)$ (that is the height of the nano-pillar as a function of time) was numerically differentiated to obtain $V(t) = d(d(t))/dt$. Linear interpolation between discrete measurement times rendered $V(t)$ for arbitrary times t. Slip-sizes were extracted from the fluctuations of $V(t)$ around the mean displacement rate V_{thr}. A slip beginning at time t_1 and ending at time t_2 is defined by

$$\begin{aligned} V(t_1) = V(t_2) = V_{\text{thr}} \quad &\text{and} \\ V(t) > V_{\text{thr}} \quad &\text{for all t with} \quad t_1 < t < t_2. \end{aligned}$$

The size of the slip is $s = d(t_2) - d(t_1)$. This method is consistent with related analyses in [6, 7]. Alternative definitions of the avalanche sizes used in the literature, and the associated avalanche size distribution exponents are discussed below.

Review of Measures of Avalanches

In the experiments described in this paper, avalanches are characterized by a starting time t_{start}, an ending time $t_{\text{end}} > t_{\text{start}}$, and a slip velocity $V(t)$, which is a function of t where $t_{\text{start}} \leq t \leq t_{\text{end}}$. As explained in the main paper $V(t)$ is obtained by differentiating the displacement time series $d(t)$ of the nano-crystal during compression $V(t) = d(d(t))/dt$. In general $V(t)$ is a measure of the collective speed of the dislocations during a slip event. In theory

$$V(t_{\text{start}}) = V(t_{\text{end}}) = 0 \;\text{ and }\; V(t) > 0 \;\text{ for }\quad t_{\text{start}} < t < t_{\text{end}}. \tag{1}$$

In practice our definitions of avalanche beginnings and endings are guided by threshold velocities,

$$V(t_{\rm start}) = V(t_{\rm end}) = V_{\rm thr} \;\text{ and }\; V(t) > V_{\rm thr} \;\text{ for }\quad t_{\rm start} < t < t_{\rm end} \tag{2}$$

with $V_{\rm thr}$ the mean displacement rate in each experiment. There are several ways to characterize the size of such an avalanche. In our work, we discuss avalanche sizes in terms of the total slip displacement S,

$$S \equiv \int_{t_{\rm start}}^{t_{\rm end}} dt\, V(t) = d(t_{\rm end}) - d(t_{\rm start}). \tag{3}$$

In a related theoretical study (see reference [25] in the main paper) we have also used the energy that is released during an avalanche:

$$E \equiv \int_{t_{\rm start}}^{t_{\rm end}} dt\, V^2(t). \tag{4}$$

For each of these quantities, we can use simulations and renormalization group theory to determine the scaling behavior of the probability density functions of the avalanche sizes. The avalanche sizes are distributed according to

$$D(S,\tau) \sim S^{-\kappa} f_S\left(S(1-\tau/\tau_c)^{\frac{1}{\sigma}}\right), \tag{5}$$

where $D(S,\tau)$ is the probability density function of S, τ is the stress, τ_c is the critical stress, κ and σ are universal critical exponents, and $f_S(x)$ is a universal scaling function that drops off exponentially for large values of x. Given this relation, we can derive the distribution of the energies as shown in (Karin A. Dahmen, "Hysteresis, Avalanches, and Disorder Induced Critical Scaling: A Renormalization Group Approach", PhD Thesis, Cornell University 1995) to be

$$D_E(E,\tau) \sim E^{-1-\frac{\kappa-1}{1-\sigma\nu z}} f_E\left(E(1-\tau/\tau_c)^{\frac{2-\sigma\nu z}{\sigma}}\right), \tag{6}$$

where D_E is the density function of the energies, the exponent ν defines the correlation length $\xi \sim (1-\tau/\tau_c)^{-\nu}$, the dynamic exponent z is defined through the scaling of avalanche duration $T \sim \xi^z$, and f_E is a universal scaling function. Another definition of avalanche size used in some reports (e.g. references [3-7] in the main paper) is the peak amplitude A, defined as

$$A \equiv \max_{t_{\rm start} \le t \le t_{\rm end}} \{V(t_i)\}, \tag{7}$$

where the t_i are the times at which the slip velocity $V(t)$ is measured, or the peak amplitude squared

$$E' \equiv \left(\max_{t_{\rm start} \le t \le t_{\rm end}} \{V(t_i)\}\right)^2, \tag{8}$$

which essentially measures the peak acoustic emission energy in an avalanche. There are some advantages to using S and E over A and E', in terms of theory, analysis and experiment.

Distributions of S and E have easily derived scaling forms. A is more complicated, it involves taking the maximum on the set of measured velocities $V(t_i)$ within a given avalanche. Viewed as random variables, the $V(t_i)$ in an avalanche are not independent. This can be seen by looking at the power spectrum (the square modulus of the Fourier transform of $V(t_i)$), which also exhibits a power law (see reference [25] in the main paper). Since the power spectrum is not white noise, the autocovariance function is not a delta function, which implies that the $V(t_i)$ are not independent. This, combined with the complexity of conditioning on the definition of an avalanche (V is zero at the beginning and end of an avalanche, but not in the middle), ensures that the scaling of A is difficult to derive.

A statistical analysis using extremal values like A and E' as opposed to averaged quantities like S and E is disadvantageous. Extremal values have more fluctuations than averaged values, meaning more data will be necessary to see clear convergence of the distributions. Also, S and E provide different information about an avalanche, which can be seen by the fact that D and D_E involve different exponents. This is not

the case for A and E', they are simply related algebraically and provide the exact same information about avalanches.

Finally from an experimental perspective, S and E are associated with more easily observable physical phenomena: S is the total displacement and E is the total released energy of an avalanche. Both can be observed without the need to record the entire time series $V(t_i)$ of each avalanche. A on the other hand requires the observation of the entire time trace $V(t_i)$, for example through acoustic emission experiments (see reference [5] from the main paper). Peak values have less significant interpretations as they do not represent the entire avalanche but just its momentary behavior.

Based on the above arguments we chose S as the best suited definition for the size of an avalanche in the main paper.

Details of Histograms in Main Paper

Here we provide details on the figures provided in the main paper. Recall that Figure 1c in the main paper shows stress-strain curves for various materials, while Figures 2-5 in the main paper show cumulative histograms. Each table below corresponds to one figure, and provides the following details for each plot:

1. the number of pillars used to produce each plot
2. the number of data points in the plot (which is equal to the number of measured avalanches used to create the cumulative distributions)
3. whether the crystal structure of the respective material is face-centered cubic (fcc) or body-centered cubic (bcc)

Figure 1c: stress-strain curves				
Plot Name	Symbol	# of Pillars	# of Data Points	fcc/bcc
Nb 868 nm, 2 nm/s	1	1	6781	bcc
Mo 800 nm, 10 nm/s	2	1	444	bcc
Au 250 nm, 0.1 nm/s	3	1	1049	fcc
Ta 400 nm, 2 nm/s	4	1	1007	bcc

Figure 2: various materials/sizes/rates				
Plot Name	Symbol	# of Pillars	# of Data Points	fcc/bcc
Au 900 nm, 0.1 nm/s	+	1	897	fcc
Mo 800 nm, 0.1 nm/s	○	7	2975	bcc
Cu 500 nm, 0.2 nm/s	⋆	6	1350	fcc
Nb 900 nm, 2 nm/s	△	9	15608	bcc
Ta 800 nm, 2 nm/s	□	7	644	bcc

Figure 3: Au & Mo, 800 nm, various rates				
Plot Name	Symbol	# of Pillars	# of Data Points	fcc/bcc
Au 0.1 nm/s, 0.1 nm/s	□	1	897	fcc
Au 1 nm/s, 0.1 nm/s	○	3	388	fcc
Au 10 nm/s, 0.2 nm/s	△	1	29	fcc
Mo 0.1 nm/s, 2 nm/s	■	7	2975	bcc
Mo 1 nm/s, 2 nm/s	●	5	1444	bcc
Mo 10 nm/s, 2 nm/s	▲	9	352	bcc

Figure 4: Cu, 2 nm/s, various sizes				
Plot Name	Symbol	# of Pillars	# of Data Points	fcc/bcc
75 nm	+	3	146	fcc
125 nm	⋆	2	119	fcc
150 nm	□	9	839	fcc
250 nm	▽	4	684	fcc
500 nm	△	5	2027	fcc

Figure 5: Mo, 800 nm, 0.1 nm/s, binned in stress				
Plot Name	Symbol	# of Pillars	# of Data Points	fcc/bcc
0.5 to 0.6 of max Stress	+	7	243	bcc
0.6 to 0.7 of max Stress	○	7	425	bcc
0.7 to 0.8 of max Stress	⋆	7	409	bcc
0.8 to 0.9 of max Stress	△	7	448	bcc
0.9 to 1.0 of max Stress	□	7	648	bcc
0 to 1 of max Stress	▬	7	2966	bcc

Use of Cumulative Histograms

For a collection of displacement-time series taken at the same experimental parameters (material, size, and nominal displacement rate) we find a collection of N slips of size $S_i, i = 1 \dots N$. We characterize the statistical properties of this collection of slips by computing a histogram. To make an M bin histogram, we choose a set of bin edges $\{e_j\}_{j=1}^{M+1}$. We then plot $\{x_j, y_j\}_{j=1}^{M}$ where

$$\begin{aligned} x_j &= m(e_j, e_{j+1}), \\ y_j &= \frac{n\left(e_j, e_{j+1}, \{S_i\}\right)}{N(e_{j+1} - e_j)}. \end{aligned}$$

Here, m is a function that is generally chosen to be the mean of its arguments, either arithmetic or geometric. The function n is just the number of slips that fall between e_j and e_{j+1}. Note that this normalization guarantees that integrating the histogram numerically across its domain yields 1, imitating the probability density function $D(S)$. Hence when we plot the normalized histograms, we label the x-axis S and the y-axis $D(S)$.

In general, choosing smaller bins allows one to see the distribution with greater resolution. However this reduces the number of counts in each bin and increases noise. Hence a balance is required. The most common choice of edges corresponds to bins of uniform width. However, this is inconvenient for power law distributions. Uniform bins are too large for the small events and too small for the large events because of the rapid decay of the probability density function $D(S)$, leading to a highly uneven distribution of statistical noise.

Instead, for histograms of power-law distributed events, one generally chooses logarithmic binning. This is achieved by choosing $e_j = ar^{j-1}$, for some constants a and r. Generally, the function m is taken to be the geometric mean. We can observe in Figure S1a below that the logarithmic binning is an improvement over the linear binning. However, the tail of the distribution $D(S)$ at large S is still relatively noisy. This is because $(e_{j+1} - e_j) \sim x_j$, but $D(S) \sim S^{-\alpha}$ where in our case $\alpha = \kappa + \sigma = 2$ is the exponent of the integrated avalanche size distribution in equation (2) in the main paper. Thus, in our case the number of counts in the j^{th} bin $n_j \equiv n\left(e_j, e_{j+1}, \{S_i\}\right)$ will scale as $n_j \sim x_j^{1-\alpha} \sim x_j^{-1}$. Hence we still have a dearth of events at the largest bins, and we still have difficulty balancing resolution at the small events with noise at the large ones.

An alternative approach is to avoid the use of bins entirely. Rather than calculate a histogram which attempts to mimic the probability density function (pdf), we calculate a cumulative histogram which mimics the cumulative distribution function (cdf). The cdf is defined by

$$C(S) = \int_{-\infty}^{S} D(S)\, dS.$$

Hence, it is the fraction of events below a certain value. In our case, this is particularly convenient: if our density $D(S) \sim S^{-\alpha}$ is a power law, then $C(S) \sim S^{-\alpha+1}$ is a power law as well. Note that $C(-\infty) = 0$ and $C(+\infty) = 1$. In practice, we actually use the complement of this function $1 - C(S)$, the fraction of events larger than S.

To create a cumulative histogram for $\{S_i\}_{i=1}^{N}$, we begin by sorting the $\{S_j\}$ so that S_1 is the size of the smallest slip and S_N is the size of the largest slip. We then plot $\{x_j, y_j\}_{j=1}^{N-1}$, where

$$\begin{aligned} x_j &= m(s_j, s_{j+1}), \\ y_j &= \frac{N - j}{N}. \end{aligned}$$

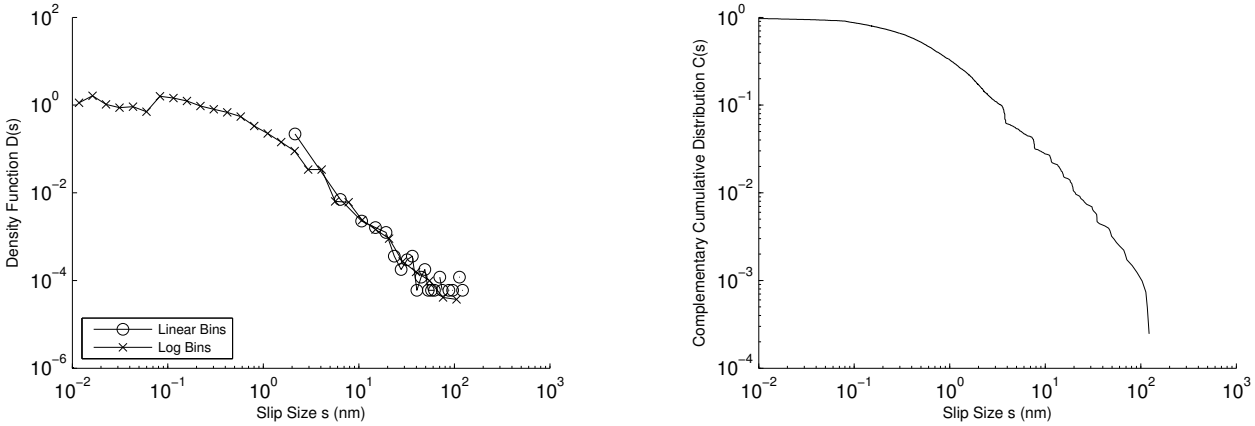

(a) (b)

Figure S1: **a)** The same data plotted in two histograms with different binning. One plot shows linear binning, the other shows logarithmic binning. Notice how the linear binning has poor resolution on small events, and is noisy for large events. The logarithmic binning is much improved, as it is less noisy for the large events. Both binning methods use 30 bins; the number of avalanches collected for the histogram is over 3000. **b)** The same data as in a), now plotted on a cumulative histogram. Excellent resolution and minimal noise clearly show the scaling behavior of the cumulative distribution $C(S)$ from small to large events. Also clearly seen is the cut-off at large events.

Again, m can be either the arithmetic or geometric mean of its arguments. In practice, the $\{S_i\}$ are so closely spaced that this choice has barely any effect on the plot. The y-value ranges from just under 1 to just over 0, as expected. Notice that no binning is necessary here; we avoid the trade-off between noise and resolution. Every single individual event directly impacts the plot, so resolution is maximal. On the other hand, because the distribution is integrated over x the statistical errorbars are reduced compared to the probability density distribution. The reason is that the integration in the cumulative distribution avoids distributing the data among bins with potentially low counts and high statistical error bars. It also avoids the need to justify the choice of number of bins, a parameter that could conceivably impact the perceived power law exponent. Figure S1b shows the cumulative approach applied to the same data as in Figure S1a.

Integrated vs Non-Integrated Exponents

In the section of our paper that summarizes the results of our mean field theory model, we distinguish between distributions that are integrated in stress versus those that are binned in stress. The stress-binned distribution of slip sizes is a function of stress, while the stress-integrated distribution is obtained by integrating the stress-binned distribution over all stresses. The scaling form of the stress-binned distribution is given by

$$D(S,\tau) \sim S^{-\kappa} f_S\left(S \cdot (\tau_c - \tau)^{1/\sigma}\right),$$

where D gives the relative likelihood of observing a slip of size S at stress τ, τ_c is the critical (flow) stress and f_S is the universal scaling function. κ and $1/\sigma$ are universal scaling exponents, with values in mean field theory of 1.5 and 2.0 respectively. However, when we deform a crystal from stress 0 to some stress $\tau_{\max} \leq \tau_c$ and consider the distribution of all the slips that occur along the way, we need to integrate $D(S,\tau)$ over stress to find the integrated form:

$$D_{\text{int}}(S,\tau_{\max}) \sim \int_0^{\tau_{\max}} d\tau\, S^{-\kappa} f_S\left(S \cdot (\tau_c - \tau)^{1/\sigma}\right).$$

Substituting $u = S(\tau_c - \tau)^{1/\sigma}$, we have

$$\begin{aligned} D_{\text{int}}(S, \tau_{\max}) &\sim \int_{S\tau_c^{1/\sigma}}^{S(\tau_c-\tau_{\max})^{1/\sigma}} \frac{-\sigma}{S(u/S)^{\sigma(1/\sigma-1)}} du\, S^{-\kappa} f_S(u) \\ &\sim \int_{S\tau_c^{1/\sigma}}^{S(\tau_c-\tau_{\max})^{1/\sigma}} \frac{-\sigma \cdot S^{-\sigma}}{u^{1-\sigma}} du\, S^{-\kappa} f_S(u) \\ &\sim S^{-(\sigma+\kappa)} \int_{S(\tau_c-\tau_{\max})^{1/\sigma}}^{S\tau_c^{1/\sigma}} du\, \frac{f_S(u)}{u^{1-\sigma}}. \end{aligned}$$

Notice that at the upper bound, the numerator of the integrand is $f_S(S\tau_c^{1/\sigma})$. This is just the scaling function modifying the power law if we evaluate $D(S,\tau)|_{\tau=0}$. At $\tau = 0$ the system is far from criticality and the cutoff size $S_{\max} \sim 1/(\tau_c - \tau)^{1/\sigma}$ of the power law region of $D_{\text{int}}(S,\tau)$ is small. Equivalently for almost all S the scaling function $f_S\left(S(\tau_c - \tau)^{1/\sigma}\right) = f_S(u)$ is also small at $\tau = 0$. Since $f_S(x)$ decays exponentially for large x we can replace the upper bound of integration with infinity and obtain

$$D_{\text{int}}(S, \tau_{\max}) \sim S^{-(\sigma+\kappa)} g\left(S \cdot (\tau_c - \tau_{\max})^{1/\sigma}\right). \tag{9}$$

Note that the universal scaling function $g(x)$ has the same argument as $f_S(x)$, $x = S(\tau_c - \tau_{\max})^{1/\sigma}$, while the distribution exponent has changed from $\kappa = 1.5$ to $\kappa + \sigma = 1.5 + 0.5 = 2.0$. Evaluating this at the critical stress, $\tau_{\max} = \tau_c$, we obtain the distribution of avalanche sizes integrated from zero stress to the critical stress:

$$D_{\text{int}}\left(S, \tau_{\max} = \tau_c\right) \sim S^{-(\sigma+\kappa)} g(0) \sim S^{-(\sigma+\kappa)}, \tag{10}$$

recovering equation (2) in the paper.

In the main paper we use experimental data to verify this prediction of the mean field theory, and test for the exponents $\kappa = 1.5$ and $\kappa + \sigma = 2.0$ for the stress-binned and stress-integrated avalanche size distributions, respectively. Testing the result for the stress-binned distribution $D(S)$ is challenging: the theory describes the distribution of slips that occur at an exact value of stress τ. Since with finite data essentially no events occur at one exact value of stress, it is necessary to bin in stress. If the bins are too large, we are back in the integrated regime. As the bins get small however, obtaining sufficient statistics to generate a meaningful histogram with small statistical error bars becomes more and more difficult. It is therefore necessary to collect large amounts of data to precisely test the predictions for the stress-binned distributions. The result of such an analysis is shown in Figure 5 of the main paper.

Finite-Size Effects

In the model described in [8], the parameter describing the distance of the system from criticality is the stress. Above the critical stress τ_c, the system deforms continuously. For any stress below τ_c, the system will eventually reach a pinned state where it stops deforming. As stress is increased slowly from 0 towards τ_c, the system corresponds by deforming suddenly, transitioning from one pinned state to another. The maximum size of these sudden deformations, or slips, is controlled by the closeness to criticality,

$$S_{\max} \sim \frac{1}{(\tau_c - \tau)^{1/\sigma}}.$$

However, this is all based on a model where the system size is infinite. In a real, finite system, there is always a hard limit to slip sizes based on some parameter of system size:

$$S_{\max} \sim L^{d_f},$$

where L is the linear dimension of the system and d_f is an appropriate fractal dimension.

If we want to see how well the model captures the behavior of the system, we need to take finite-size effects into account. In particular, we need to find a suitable range for the stress where finite size effects do

not distort the scaling form used for the stress-dependent scaling collapse of figure 5 in the main paper. For stresses too far from the critical (failure) stress, the scaling theory does not apply, and for stresses too close to the critical stress, system size dominates the scaling behavior rather than the distance of the stress from the critical stress

To understand how the real system experiences finite-size effects, we consider the average square slip size as a function of stress. As we approach the critical stress, this quantity should diverge as a power law, which can be shwon using the equations from the last section:

$$\begin{aligned}\left\langle S^2 \right\rangle(\tau) &= \int_{S_{\min}}^{\infty} dS\, S^2\, D(S,(\tau)) \\ &\sim \int_{S_{\min}}^{\infty} dS\, S^2\, S^{-\kappa} f_S\left(S\cdot(\tau_c-\tau)^{1/\sigma}\right),\end{aligned}$$

where $S_{\min}$ is the smallest measured avalanche size. Substituting $u = S(\tau_c - \tau)^{1/\sigma}$ we have

$$\left\langle S^2 \right\rangle(\tau) \sim (\tau_c-\tau)^{\frac{\kappa-3}{\sigma}} \int_{S_{\min}(\tau_c-\tau)^{1/\sigma}}^{\infty} du\, u^{2-\kappa} f_S(u).$$

Since $\kappa = 1.5 < 2$ and f_S is of order unity near zero, the integrand is zero for $u = 0$. Now, the lower bound of integration can be thought of as $\frac{S_{\min}}{S_{\max}}$ which is close to zero near the critical stress for large systems. Hence, to calculate the asymptotic behavior we can replace the lower bound of integration with zero. Thus we find $\left\langle S^2 \right\rangle \sim (\tau_c-\tau)^{\frac{\kappa-3}{\sigma}}$.

Figure S2 explains the choice of plots that were used for the collapse in Figure 5 of the main paper. We wanted to use curves that were as close to criticality as possible, but that did not experience finite size effects. Hence we excluded the first two bins which together include events from τ_c to $0.8\tau_c$ as they clearly deviate from the above scaling form due to finite size effects. Thus, to plot the curves shown in Figure 5 of the main paper, we used events from ranges of stresses corresponding to the next 4 points in Figure S2, with 4 equally sized stress bins from $0.8\tau_c$ to $0.4\tau_c$.

Fitting and Error Analysis

To put error bars on our cumulative histograms, we used a Bayesian technique with a 95% confidence interval [9]. Consider a cumulative histogram that has N samples; suppose we are trying to compute the value of the complementary cumulative distribution $C(s)$ at some value of s for which k of the N samples have a value greater than s. Let us refer to $C(s)$ at the s value of interest as p; then p is the probability of a sample being greater than s. Since k of the N samples were greater than s, our best estimate of p is clearly $p = \frac{k}{N}$. We can go farther than this however. The probability of p taking some value given our observation of k (and holding N fixed) is given by

$$P(p|k) = P(k|p) * P(p)/P(k), \tag{11}$$

where P refers to the probability of the contained variable taking on a value, and $|$ indicates a conditional probability. $P(k)$ can be ignored as we are only dealing with one value of k, and thus it is a constant. For $P(p)$, the priors, we assume a uniform distribution on $[0, 1]$. So we have

$$P(p|k) \propto P(k|p) = \binom{N}{k} p^k (1-p)^{N-k}. \tag{12}$$

Normalizing and integrating, we find the cumulative distribution function to be

$$P(p < x|k) = I_x(k+1, N-k+1) \tag{13}$$

where $I_x(a, b)$ is the regularized incomplete beta function. To find error bars, we set p_{low} and p_{high}, the upper and lower error bounds on p, such that

$$I_{p_{\text{low}}}(k+1, N-k+1) = 0.025 \tag{14}$$

$$I_{p_{\text{high}}}(k+1, N-k+1) = 0.975, \tag{15}$$

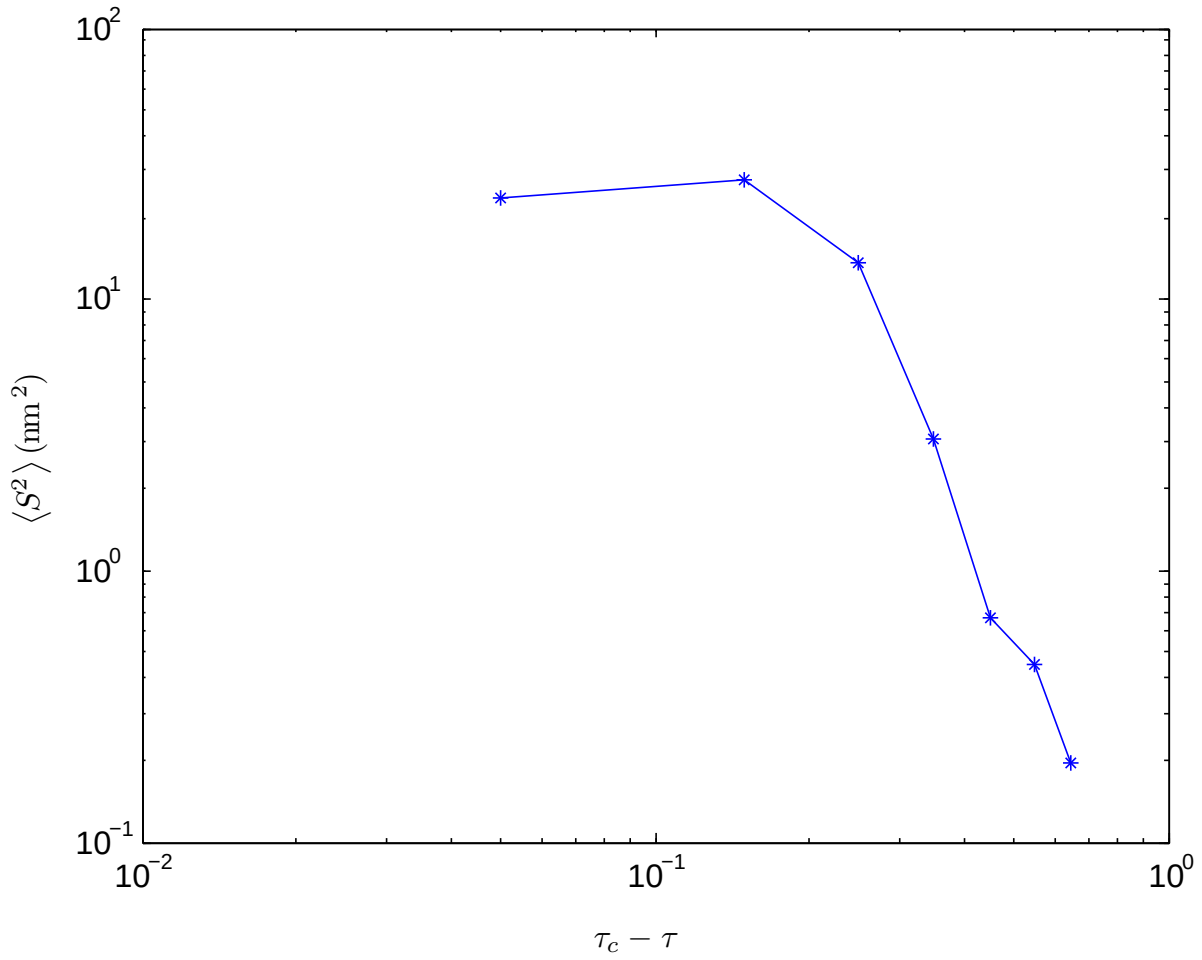

Figure S2: A plot showing how the scale of slips increases as one approaches criticality. $\tau_c - \tau$ is plotted in normalized units where τ_c is equal to 1. For farther distances from criticality towards the right of the graph, there is a consistent, roughly power law increase of event scale with approach to criticality. However, extremely close to criticality this breaks down as the finite system size limits what would otherwise be larger events. Each plotted point comes from averaging over events occuring in consecutive ranges of 0.1 stress in normalized units. So the point closest to criticality is from averaging over all slips that occured at stresses between τ_c and $0.9\tau_c$, the next point from events between $0.9\tau_c$ and $0.8\tau_c$, and so on.

That is, the lower and upper 2.5% of probability, leaving us with a 95% interval in between.

We used a similar approach to estimate the power law exponent α of real data, one that is slightly modified from the approach used by Newman et al [10]. If we assume that data $\{x_i\}$ is distributed as a power law between $x_{\min}$ and $x_{\max}$, and once again assume uniform priors, we have

$$P(\alpha|\{x_i\}) \propto \prod_{i=1}^{N} \frac{\alpha-1}{x_{\min}} \frac{1}{1-S^{1-\alpha}} \left(\frac{x}{x_{\min}}\right)^{-\alpha}, \tag{16}$$

where $S \equiv \frac{x_{\max}}{x_{\min}}$. We now have a probability density on α; we simply pick as our estimate the value of α that has maximum probability. The statistical error in this case from fitting α is relatively small, however α is quite sensitive to the choice of $x_{\min}$. We thus determined the error in α by considering a reasonable range of values for $x_{\min}$ and then using the amount by which alpha varied in that range as the error.

References

[1] Ju-Young Kim, Dongchan Jang, and Julia R. Greer. Tensile and compressive behavior of tungsten, molybdenum, tantalum and niobium at the nanoscale. *Acta Materialia*, 58(7):2355 – 2363, 2010.

[2] Andrew T. Jennings, Michael J. Burek, and Julia R. Greer. Microstructure versus size: Mechanical properties of electroplated single crystalline cu nanopillars. *Phys. Rev. Lett.*, 104(13):135503, Apr 2010.

[3] Ju-Young Kim and Julia R. Greer. Tensile and compressive behavior of gold and molybdenum single crystals at the nano-scale. *Acta Materialia*, 57(17):5245 – 5253, 2009.

[4] Ju-Young Kim and Julia R. Greer. Size-dependent mechanical properties of molybdenum nanopillars. *Applied Physics Letters*, 93(10):101916, 2008.

[5] Ju-Young Kim, Dongchan Jang, and Julia R. Greer. Insight into the deformation behavior of niobium single crystals under uniaxial compression and tension at the nanoscale. *Scripta Materialia*, 61(3):300 – 303, 2009.

[6] Andrew T. Jennings, Ju Li, and Julia R. Greer. Emergence of strain-rate sensitivity in cu nanopillars: Transition from dislocation multiplication to dislocation nucleation. *Acta Materialia*, 59(14):5627 – 5637, 2011.

[7] M. Zaiser, J. Schwerdtfeger, A. S. Schneider, C. P. Frick, B. G. Clark, P. A. Gruber, and E. Arzt. Strain bursts in plastically deforming molybdenum micro- and nanopillars. *Philosophical Magazine*, 88(30-32):3861 – 3874, 2008.

[8] K.A. Dahmen, Y. Ben-Zion, and J.T. Uhl. A micromechanical model for deformation in solids with universal predictions for stress strain curves and slip avalanches. *Phys. Rev. Lett.*, 102(17):175501, 2009.

[9] P. Vermeesch. Statistical uncertainty associated with histograms in the earth sciences. *Journal of geophysical research*, 110(B2):B02211, 2005.

[10] M.E.J. Newman. Power laws, pareto distributions and zipf's law. *Contemporary Physics*, 46(5):323–351, 2005.